Cell Wall Dynamics in the Regulation of Cell Morphogenesis and Growth

Valeria Davì

université PARIS-SACLAY

NNT : 2018SACLS295

Thèse de doctorat

Dynamique de la paroi cellulaire dans la régulation de la morphogenèse et de la croissance cellulaire

Thèse de doctorat de l'Université Paris-Saclay
Préparée à l'Université Paris-Sud

École doctorale n°577 : Structure et Dynamique des Systèmes Vivants (SDSV)

Spécialité : Science de la Vie et de la Santé

Thèse présentée et soutenue à Paris, le 24 Septembre 2018, par

Valeria Davì

Composition du Jury :

M. Olivier Hamant, DR ENS de Lyon (Laboratoire Reproduction et Développement des Plantes)	Président et Rapporteur
M. Mohan Balasubramanian, Professeur Université de Warwick (Département de Sciences Biomédicaes)	Rapporteur
M. Giuseppe Baldacci, Professeur Université Paris-Diderot, CNRS (Institut Jacques Monod)	Examinateur
M.me Florence Chapeland-Leclerc, MC Université Paris Decartes (Laboratoire Interdisciplinaire des Energies de Demain)	Examinateur
M. Alexis Peaucelle, CR INRA, AgroParitech (Institut Jean-Pierre Bourgin)	Examinateur
M. Nicolas Minc, DR CNRS (Institut Jacques Monod)	Directeur de thèse
Prof. Arezki Boudaoud, Professeur Université de Lyon, ENS de Lyon (Reproduction et Développement des Plantes)	Invité

Université Paris-Saclay
Espace Technologique / Immeuble Discovery
Route de l'Orme aux Merisiers RD 128 / 91190 Saint-Aubin, France

Abstract

Cells in nature develop in a wide range of forms, following diverse growth patterns. Despite the importance of these fundamental processes, how cells regulate their growth and morphogenesis is still poorly understood. In this thesis, I explored these processes, focusing my investigations on tip growing walled cells and in particular, by exploiting the fission yeast *Schizosaccharomyces pombe*, adopting mainly a biomechanical approach. To this aim, I first developed novel methods to measure key cell wall mechanical parameters in vivo at a large population scale, which allowed the very first observations of cell wall dynamics. This revealed that the cell wall is softer and highly variable at growing poles, and almost stable and stiffer at non-growing sites. During elongation, there is an interplay between wall mechanics and cell growth, whose active control allows cell expansion while preserving cell integrity. In addition, I observed that there is a strong correlation between cell wall mechanics and cell morphology, and ectopic perturbations of wall properties directly affect shape establishment and maintenance. Together my results show that the regulation of wall mechanics is fundamental in the determination of cell dynamics in tip growing walled cells. Moreover, this suggests that dynamic observation of cell surface mechanics is crucial for a complete understanding of multifactorial and complex processes, such as growth and morphogenesis.

Resumé

Les cellules dans la nature se développent dans un large éventail de formes, suivant divers modèles de croissance. Malgré l'importance de ces processus fondamentaux, la façon dont les cellules régulent leur croissance et leur morphogenèse est encore mal comprise. Dans cette thèse, j'ai exploré ces aspects, avec une approche principalement biomécanique, en concentrant mes investigations sur des cellules à paroi et en exploitant en particulier la levure fissipare *Schizosaccharomyces pombe*. J'ai d'abord développé de nouvelles méthodes pour mesurer les paramètres mécaniques clés de la paroi cellulaire in vivo, ce qui a permis les premières observations de la dynamique des parois cellulaires. Ceci a révélé que la paroi cellulaire est plus souple et très

variable au niveau des pôles de croissance, et presque stable et plus rigide dans les sites sans croissance. Au cours de l'allongement, il existe une interaction entre la mécanique des parois et la croissance cellulaire, dont le contrôle actif permet l'expansion cellulaire tout en préservant l'intégrité des cellules. De plus, j'ai observé qu'il existe une forte corrélation entre la mécanique des parois cellulaires et la morphologie cellulaire, et que des perturbations des propriétés de la paroi affecte directement l'établissement et la maintenance de la forme. Ensemble, mes résultats montrent que la régulation de la paroi est fondamentale dans la détermination de la dynamique cellulaire dans les cellules à parois. Globalement, cela suggère que l'observation dynamique de la mécanique de surface cellulaire est essentielle pour une compréhension complète des processus multifactoriels et complexes comme la croissance et la morphogenèse.

Table of Contents

Aims of the study 5

INTRODUCTION 7

Chapter 1 – General principles of cell morphogenesis 9

1.1 General physical principles regulating living (and non-living) matter 12

1.2 Cell polarity and cell shape 13

1.2.1 Molecular components in cell polarity 14

1.2.2 Cell polarity establishment and maintenance 18

1.3 Cell surface mechanics 20

1.3.1 Surface mechanics of non-walled cells 21

1.3.2 Surface mechanics of walled cells 23

1.4 Mechanosensing mechanisms for shape regulation 25

Chapter 2 – Elongation and morphogenesis in tip-growing walled cells 29

2.1 Mechanics of walled cells 35

2.2 Turgor pressure regulation 41

2.1 Cell wall properties 44

2.1.1 Cell wall composition 44

2.1.2 Cell wall synthesis 48

2.1.3 Cell Wall Integrity pathway 52

2.2 Influence of cell wall mechanics on morphogenesis and growth 54

Chapter 3 – *Schizosaccharomyces pombe*, morphogenesis and growth 61

3.1 Different stages of fission yeast life cycle 64

3.2 Polarity machinery during tip elongation 68

3.3 Turgor regulation 73

3.4 Cell wall properties 74

3.4.1 Cell wall composition 74

3.4.2 Cell wall synthesis 75

3.4.3 Wall integrity pathway 77

3.5 Cell mechanics 79

RESULTS 81

1- Mechanosensation Dynamically Coordinates Polar Growth and Cell Wall Assembly to Promote Cell Survival 83

2- Mechanical Control of Cell Shape and Size in Fission Yeast 85
DISCUSSION 87
METHODS 97
WALLTRACKER 99
WALLTRACKER 2.0 109
ANNEX 1 127
Mechanics and morphogenesis of fission yeast cells 127
ANNEX 2 129
Procede de mesure en temps reel de l'epaisseur de la paroi et ses applications 129
RÉSUMÉ 131
BIBLIOGRAPHY 143

Aims of the study

Cells in nature comes with very different forms and grow with profoundly diverse patterns. These processes are the output of complex genetic and biochemical regulations, which tune local delivery of proteins, synthesis of new material, deformation and remodeling, to ultimately modify the mechanics of the cell surface, in order to acquire a certain shape or expand in a specific manner. However, the complex interplay between all these layers of regulation is still largely unclear.

In most living organisms, from plants to bacteria and fungi, the cell surface is composed of a stiff structure covering the cell boundaries, named cell wall. Those cells are also characterized by a very high internal turgor pressure, which is the driver of growth. Despite the rigidity of their surfaces, walled cells can undergo very dynamic processes of fast-polarized growth, reorientation towards/against stimuli, and acquire profoundly different shapes, both as single cells or in tissues. This suggests that cell walls must continuously modify their structures, to allow for these dynamic processes. Therefore:

what is the dynamical behavior of cell walls?

To answer this question, in my work, I focused on a subset of walled cells, that grow isolated as single cells (e. i. not part of a tissue) by tip extension generating tubular shapes, and in particular, on the rod shaped fission yeast *Schizosaccharomyces pombe*, which among them is one of the best described. So far, mainly because of technological limitations, there was very little access to cell wall dynamics. My first achievement was the setup of novel methods suitable to follow cell wall mechanical parameters in vivo. This allowed, the very first observations of cell wall dynamics, showing that the cell wall is stable at non-growing regions, but highly variable at growing ones. Those results led to the following questions:

How is cell wall dynamics regulated to ensure growth while preserving cell integrity?

In fact, tip growing cells are in a constant precarious condition, because during growth, the deposition of new wall material must constantly balance the internal turgor pressure that without a sufficient support may cause cell lysis. To investigate this aspect, in the first part of my results, I characterized wall dynamics and wall synthesis regulators in wild type cells, as well as in mutants of highly conserved pathways involved in cell integrity maintenance, uncovering an interplay between cell elongation and wall thickness and one mechanism for its regulation.

How do wall mechanical properties influence cell shape?

By exploiting the stereotypical rod shape of fission yeast, in the second part of my results, I investigated the correlation between wall mechanical properties and cell diameter, in different wild type conditions and in tens of mutants defective in diameter or wall synthesis. In addition, I observed diameter changes after perturbation of wall properties, uncovering a putative mechanism for diameter regulation.

The overall aim of this work is to lay the foundation for the understanding of how cell walls are dynamically regulated, and how this can influence fundamental processes, such as growth and shape establishment in walled cells.

INTRODUCTION

Chapter 1 – General principles of cell morphogenesis

In this chapter, I describe the basic principles of cell shape determination. I start by introducing the physiological importance of cell morphogenesis in full organisms and single cells. I then focus on the physical principles that are involved in assembly of both living and non-living matter. Then, I introduce the important principle of cell polarity, the ability of a cell to define local differences in shape, structure or function, based on the local organization of molecular machineries. Thereafter, I focus on the mechanical properties of cell surface, the structure that ultimately confers a defined form. Finally, I describe mechanosensing pathways, involved in the regulation and homeostasis of cell shape, differentiation and response to external perturbations.

Table of contents

Chapter 1 – General principles of cell morphogenesis 9
1.1 General physic principles regulating living (and non-living) matter 12
1.2 Cell polarity and cell shape 13
1.2.1 Molecular components in cell polarity 14
Cytoskeleton 14
Membrane trafficking 15
RhoGTPases 16
1.2.2 Cell polarity establishment and maintenance 18
1.3 Cell surface mechanics 20
1.3.1 Surface mechanics of non-walled cells 21
1.3.2 Surface mechanics of walled cells 23
1.4 Mechanosensing mechanisms for shape regulation 25

Morphogenesis, from the Greek terms "*morphê*", shape, and "*genesis*", creation, literally means the generation of shape. In biology, this term concerns the fundamental question of how biological form and structure are generated, from the rather simple cell level, to the more complex tissues, or the higher order assembly of organs and full organisms.

Already at the cell level we can appreciate that shapes can vary from simple spheres to rods, disks, cubes, branched trees, up to the very complex shapes of protists or diatoms (Figure 1.1). Cell morphology is fundamental, not only for single cell functionality, but also for the correct assembly of tissues and folding of organs, and therefore for the viability of organisms.

Defects in cell shape are associated with loss of function or disease. For instance, the concave shape of erythrocytes confers high plasticity and their ability to flow through very narrow vessels (Figure 1.2A above). Defects in hemoglobin generate the sickle like shape, typical of drepanocytosis (sickle anemia): cells become more rigid, easily undergo hemolysis and can occlude vessels, not being able to deform in small capillaries (Figure 1.2A below) (Pauling et al., 1949). Another example is represented by the very organized cubic cells that, growing in an oriented direction, define a tubular *Arabidopsis thaliana* root, necessary for anchoring and nutrition of a plant (Figure 1.2B above). Inhibition of polarized trafficking in these roots lead to protrusions of several extra fronts of growth and the root will end up being very small and branched, and consequently lowering its overall

Figure 1.1. Drawing of single cell and colonies of protozoa (left) and diatoms (right) from Ernst Haeckel's Art Forms in Nature, 1904.

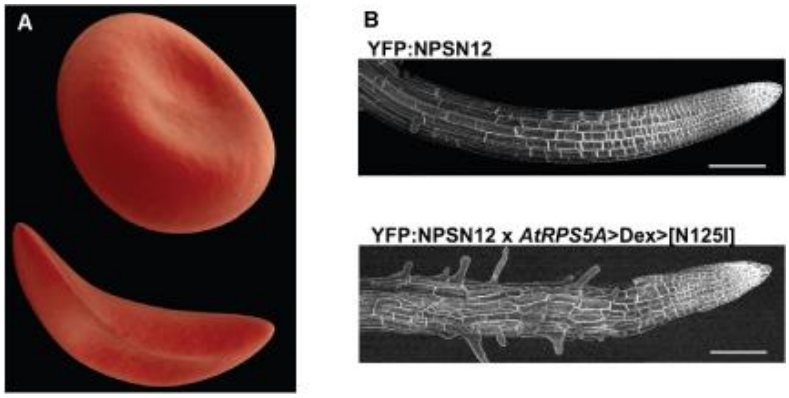

Figure 1.2. Examples of cell shape degenerations. (A) An erythrocyte in normal shape (top) and in sickle anemia (bottom). (B) *A. thaliana* root in a control (top) or after inhibition of polarized exocytosis by RAB delocalized activation (bottom – AtRPS5A dexamethasone inducible promoter, induce RAB activation at root sides). YFP fluorescence in lateral roots expressing the PM marker YFP:NPSN12. Scale bar 100 μm. Adapted from (Kirchhelle et al., 2016).

fitness of the plant. (Figure 1.2B below) (Kirchhelle et al., 2016).

1.1 General physical principles regulating living (and non-living) matter

The variety of shapes in nature is evident and under the eyes of everyone, but the understanding of how these shapes are generated is still fragmentary.

Biological structures are characterized by several layers of organization: at nanometrical scales, macromolecules, such as structural proteins, or lipids, together with enzymatic activity arrange in order to define micrometric structures such as complex lipid bilayers, organelles and cells. Cells interact and organize, forming millimetric tissues, which folds into organs that will ultimately define full organisms. Therefore, the generation of an organism, with precise shape and form, relies primarily on the nanometric interplay of biochemical molecules, enzymatic activity and signaling. Many principles regulating forms of inorganic material are also common in living matter. Two proposed mechanisms that allow for the formation of biological structures are self-assembly and self-organization (Dumont and Prakash, 2014).

Self-assembly is the effect of passive interactions of subunits, that assemble because their association is energetically favorable; there is no consumption of energy and the system can reach an equilibrium. Typical structures generated by this mechanism are nuocleoli, P-bodies or amyloids (Brangwynne, 2011).

Self-organization occurs when subunits interact by dissipating energy; in a living system this energy comes from the metabolism, moving the system out of equilibrium, giving rise to

continuous structural transformations. Examples of self-organized structures are acto-myosin and microtubules networks, that form by dissipating ATP or GTP both during filament growth and movement of motors (Nedelec et al., 1997).

However, these two principles alone cannot explain the very organized and reproducible structures of living organisms. For example, actin can self-organize in filaments, but how can these filaments be localized in the right cell location to promote cytokinesis? To understand how a complex shape is defined in biology we must understand all the layers of regulation that are involved in these phenomena.

1.2 Cell polarity and cell shape

As briefly mentioned before, the ability of a cell to define a specific shape relies, in the first place, on the correct distribution of its components at a biochemical level; this process is named "cell polarity". In other words, cell polarity is the capacity to deliver the correct molecules at the correct place, promoting the definition of a geometric axis, and defining specialized domains of action that can be dedicated to specific tasks.

Cell polarity is prominent in most cell types, from prokaryotes to plants, fungi and mammals. It is essential for a countless number of functions, from growth, to asymmetric cell division, cell migration, extending to embryogenesis, tissue and organ development.

Clear examples are found in tip-growing cells, such as fission yeast, filamentous fungi or pollen tubes of plants: all localize their growth machinery at one or more protrusions, restricting growth to discrete regions of the cell, resulting in rod/branched shaped structures necessary to explore the substrate. Another more complex example of cell polarity is the gigantic cell *Stentor coeruleus*, a trumpet like shaped protist that exhibits a highly polarized and specialized structure, with the larger part covered in cilia, and the smaller developed in a holdfast. In animals, hippocampal neurons elongate from the soma short dendritic protrusions, specialized for synaptic signal reception, and long axon that can releases synaptic vesicles. Cell polarity is also essential for organism development, being involved in embryogenesis and differentiation, as well as in the correct arrangement and functionality of tissue and organs. For example, cells in epithelial tissues possess a distinct polarized internal organization, which defines the assembly of membrane domains, named apical and basolateral: these domains differentiate the functions of the two sides of the tissue and are essential for its correct folding (Figure 1.3).

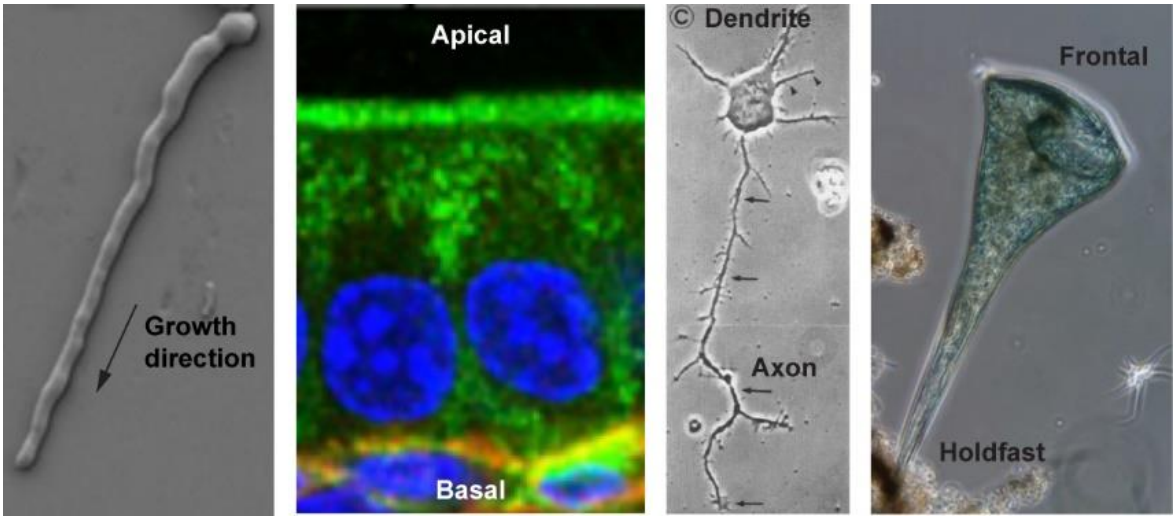

Figure 1.3. Examples of cell polarity. From the left germtubes growth of *Neurospora crassa* (Lichius et al., 2014); immunostaining of small intestinal epithelial cells in WT mice. In green Ezrin, in blue Nuclei, in red laminin (Toya et al., 2016). Cultured hippocampal rat neuron (Dotti et al., 1988). *Stentor coeruleus* cell (From Bill Porter youtube channel). Every image have been adapted from the reference.

1.2.1 Molecular components in cell polarity

At the molecular level, cell polarity is normally defined by two fundamental properties in eukaryotes: the orientation of the cytoskeleton along the polarity axis and the asymmetric accumulation of proteins in discrete regions of the cell (Li and Gundersen, 2008).

Cytoskeleton

Microtubules and actin filaments are the major components of the cytoskeleton. Both polymers are polarized, due to the asymmetric properties of their subunits.

Microtubules are composed of hetero dimers of α- and β-tubulin, which bind head to tail through GTP hydrolysis. Initial nucleation of microtubules occurs at centrosomes or other microtubule organizing centers (MTOCs) that are normally close to the cell center. The so-called minus end of the filament is anchored to those structures, and therefore the polarized direction of microtubules is determined by the regulation of the dynamic polymerization at the plus end. Actin filaments are composed of monomers of globular actin that bind hydrolyzing ATP (Figure 1.4).

Actin nucleation is promoted by actin nucleator factors, such as formins, which nucleate and elongate linear filaments from their barbed ends, or the Arp2/3 complex, which produces branched filaments. Actin nucleation factors can be distributed at the cell surface, therefore their localization is the main mechanism regulating acting orientation for cell polarization (Pollard, 2007).

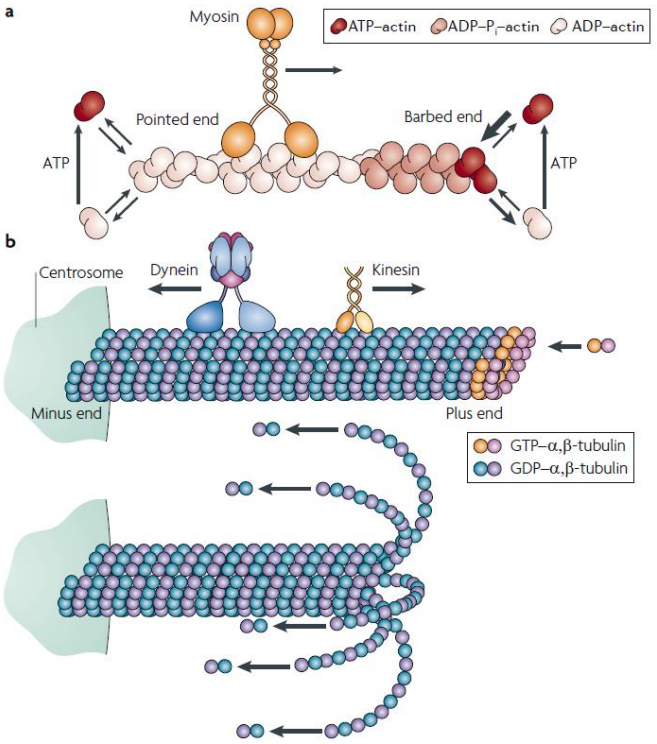

Figure 1.4. Schematic structure of actin filament (a) and microtubule (b), including the dynamic of free polymerization and the direction of molecular motors. In (b) above GTP-dimer stabilize the microtubule structure. Loss of the GTP cap induces de-polymerization (below) (Li and Gundersen, 2008)

Both actin and microtubules are extremely dynamic, with differing polymerization and de-polymerization rates on the two ends of the filaments, both depending on various regulators of elongation that contribute to their dynamism. The ability to reorganize in a fast manner is very important to respond rapidly and locally to arising polarity signals (Li and Gundersen, 2008).

Motor proteins are a class of cytoskeleton-associated proteins highly linked to cell polarity. These proteins can move along the polymer tracks by hydrolyzing ATP. During their "walk", they can carry cargoes, such as molecules, vesicles or organelles within the cell. Microtubule motors include dynein and kinesins. While dynein moves towards the minus end, most kinesins move to the plus end. Actin-associated motors are myosins, which normally moves towards the barbed end (with some exceptions). One example is MyoV that due to its high processivity (ability to be associated to the filament for several steps), can transport cargoes on long distances (Figure 1.4) (Kincaid and King, 2006). Hence, once the cytoskeleton is polarized, it can direct trafficking to specific cellular locations in the cell, promoting or reinforcing polarity.

Membrane trafficking

Polarized accumulation of proteins at specific regions of the plasma membrane can be highly influenced by delivery and fusion of vesicles containing proteins (exocytosis) and internalization

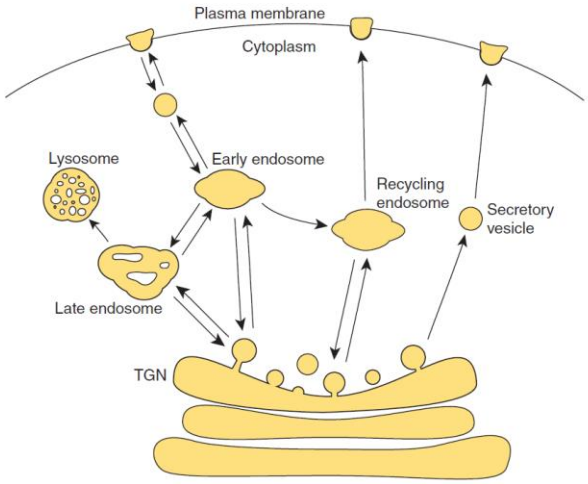

Figure 1.5. Membrane trafficking to and from the plasma membrane. TGN is the trans Golgi network (Orlando and Guo, 2009).

and membrane recycling (endocytosis). For exocytosis, proteins containing vesicles that reach the plasma membrane originate from the trans-Golgi network, or through recycling of previously internalized membranes. They are tethered to specific locations at the plasma membrane by a specific set of proteins, such as the exocyst, an evolutionary conserved octameric protein complex (consisting of Sec3, Sec5, Sec6, Sec8, Sec10, Sec15, Exo70, and Exo84). Tethered vesicles can fuse to the membrane, in a process mediated by SNARE protein complexes.

Proteins at the plasma membrane can be recycled through endocytosis, in a process that creates clathrin-coated vesicles departing from the membrane, which can then be delivered to the endosome either for recycling or for degradation (Figure 1.5) (Orlando and Guo, 2009). Membrane trafficking and cytoskeleton are linked, for example transport from the trans-Golgi network to the plasma membrane can be facilitated by motor-dependent delivery along cytoskeletal tracks (Porat-Shliom et al., 2013); in addition, endocytosis is actin dependent in some organisms, such as budding and fission yeasts (Aghamohammadzadeh and Ayscough, 2009; Basu et al., 2014; Mooren et al., 2012).

Although vesicle traffic is important to generate local domains of polarity regulators, it can be directly modulated by some of those regulators as well; some examples will be given in the next paragraph.

RhoGTPases

In eukaryotes, RhoGTPases, small G proteins part of the Rho family, have emerged as central regulators of cell polarity signaling. Within this family there are Cdc42, Rac, Rho and Rop.

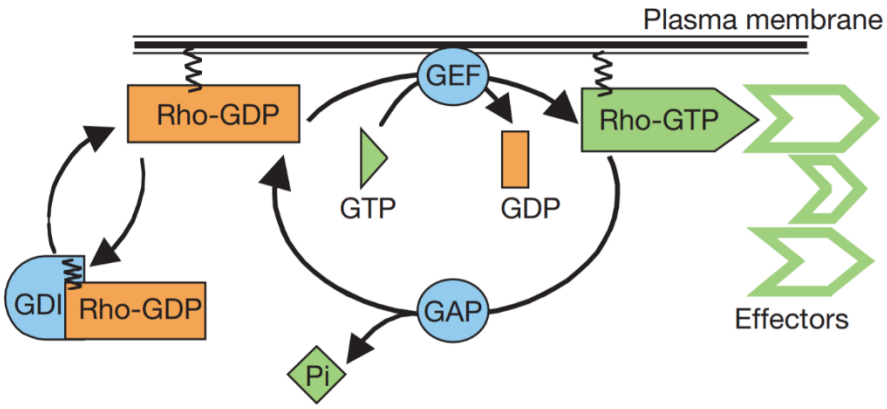

Figure 1.6. Schematic of Rho-GTPase cycle (Etienne-Manneville, 2002)

They are membrane-associated proteins, prenylated at their C-terminus domain. Like all GTPases they can function as molecular switches, being active in their GTP bound state and inactive after GTP hydrolysis. GTPase-activating proteins (GAPs) can promote GTP hydrolysis with a consequent inhibitory effect. GTP exchange-factors (GEFs) on the contrary, can promote GDP-GTP exchange, leading to activation. Moreover, guanine nucleotide dissociation inhibitors (GDIs) can bind to their GDP form, and sequestrate them in the cytosol, by masking their membrane anchoring binding site (Figure 1.6) (Etienne-Manneville, 2002).

RhoGTPases act in very diverse stages of cell shape determinations, interacting directly or indirectly with other molecular players of cell polarity. In both mammals and plants, RhoGTPases can interact with actin structures: Ras can interact with Arp2/3 via the WAVE complex, promoting actin elongation and branching (Basu et al., 2008; Wittmann and Waterman-Storer, 2001; Yanagisawa et al., 2013). During fibroblasts migration, it has been shown that Cdc42 and Rac promote membrane protrusions through actin polymerization, while Rho promotes membrane retraction through actin depolymerization (Etienne-Manneville, 2002). Moreover, Cdc42 can promote directional migration in macrophages (Allen et al., 1998). Furthermore, RhoGTPases can also interfere with microtubules: during cell migration, Rac can indirectly promote microtubule stabilization, while Cdc42 can orient the Microtubule Organizing Center (Wittmann and Waterman-Storer, 2001). There is also proof of direct interactions between RhoGTPases and the secretory pathway: Cdc42 in yeast interacts with Sec3, while in mammals Ral, a small G protein of the Rac family, can interact with Sec5, therefore with the exocyst (Moskalenko et al., 2002; Sugihara et al., 2002). In addition, in mammal zygotes, Cdc42 can interact with Par6, promoting the correct orientation of vegetative and animal poles (Lin et al., 2000). Finally, in fungi

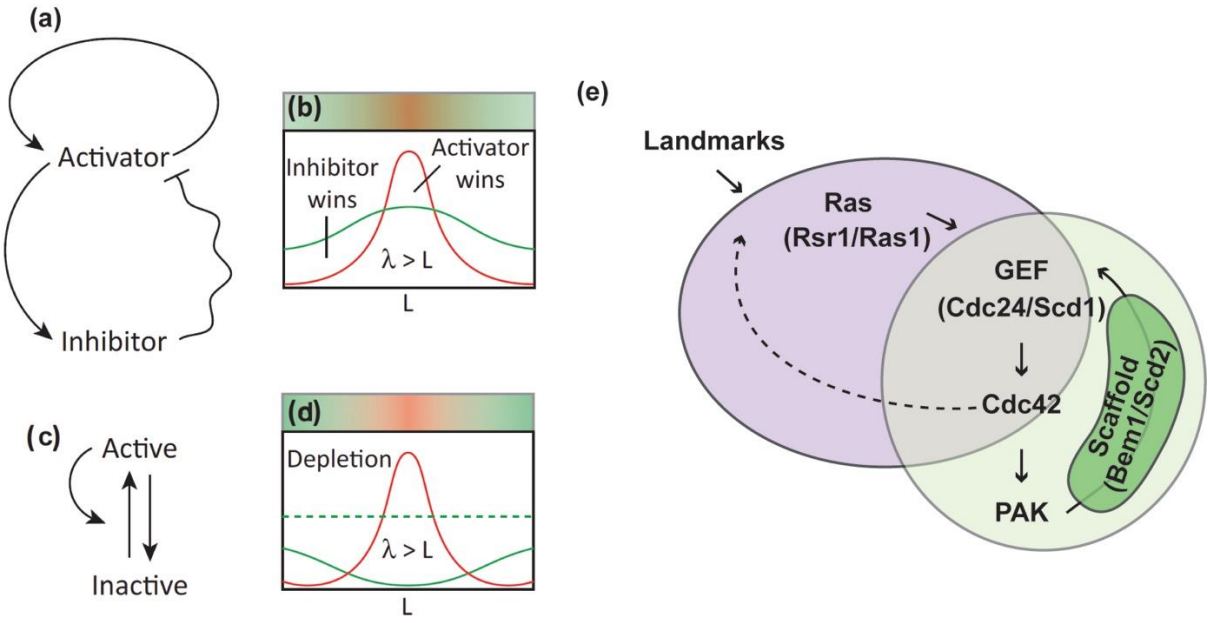

Figure 1.7. Self-assembly. A-D. Pattern formation in chemical systems, with activator/inhibitor (a-b), or with long range inhibition (c-d) Adapted from (Goehring and Grill, 2013). E. Self-amplification of Cdc42 in budding and fission yeasts. Cdc42-GTP can bind a PAK protein, that bind a scaffold protein. The scaffold is also binding a GEF of Cdc42, promoting its further activation. If this happen in the presence of a landmark, can occur at specific location of the cell, through activation of the GEF by the landmark itself. Dotted line is a putative, but yet not described, positive feedback. Adapted from (Martin, 2015).

RhoGTPases control polarized growth, but also the local assembly of cell wall, by the direct regulation of cell wall synthases (Drgonova et al., 1996; Perez and Rincón, 2010).

In conclusion, cell polarization is regulated by a complex communication between different classes of proteins and cellular processes, including cytoskeletal components, membrane recycling and small GTPases, which are mutually regulated and differentially distributed within a cell.

1.2.2 Cell polarity establishment and maintenance

Very often in cells, symmetry breaking, the initiation of cell polarity, occurs in specific areas of the cell surface due to the presence of polarity cues provided by molecules that act as landmarks, by directing RhoGTPases recruitment. However, in several organisms, the depletion of polarity cues may impair the correct orientation of the polarity domain, but does not prevent the formation of polarity domains at random positions. For instance, in *Saccharomyces cerevisiae* the budding pattern is highly conserved: in haploid cells, each new bud will form next to a previous site of budding, a bud scar. This is regulated by the landmark Rsr1 that recruits downstream polarity machinery. However, when Rsr1 is bypassed either by deletion, or by the constitutive activation of

Cdc42 with a $Cdc42^{Q61L}$ allele, cells lose the correct budding pattern, but are still able to bud at random positions (Irazoqui et al., 2003; Wedlich-Soldner et al., 2003). This demonstrates the ability of the system to self-assemble.

The first significant study on pattern self-assembly, is the reaction diffusion model from Alan Turing (Turing, 1953). He proposed that in a uniform starting condition some chemical species, "morphogens", can interact, leading to the formation of new species that have a different rate of diffusion, creating instability. The system will find its equilibrium in very specific and organized patterns.

This theory was later refined by Gierer and Meinhardt (Gierer and Meinhardt, 1972), and included the existence of short-range positive feedbacks, together with long-range negative feedbacks. The positive feedback can be due to activators acting at a short range, while the negative feedbacks caused by inhibitors acting at a longer range. Differences in diffusion between activators and inhibitors, with inhibitors diffusing faster, can lead to patterns formations, such as polarity domains (Figure 1.7 A-B). Moreover the inhibitor can be dispensable, if the molecules diffusion rate varies, moving slow when active and fast when inactive creating an oscillatory dynamic (Figure 1.7 C-D) (Goehring and Grill, 2013; Mogilner et al., 2012).

The best examples of these patterns are found in budding and fission yeasts, during budding in the first one and polarized growth in the second. Cdc42, with or without spatial cue, can form a polarity domain, through the formation of a complex, stabilized by a scaffold protein that can bind both a PAK protein and the GEF of Cdc42. The PAK protein binds Cdc42-GTP, while the GEF activates more Cdc42, providing a positive feedback loop. In *Schizosaccharomyces pombe*, it has been shown that this feedback can be further increased by a low diffusion rate of Cdc42-GTP compared to its inactive form. Moreover, the scaffold diffuses slower when bound to the membrane, than in its cytosolic form, recapitulating the second model represented in Figure 1.7 C-D. (Figure 1.7 E) (Bendezú et al., 2015; Martin, 2015)

To conclude, polarity is established in a self-regulated manner, either at random positions or in specific areas of the cell, when landmarks or external cues are present. An intricate interplay between the cytoskeleton, vesicles trafficking, RhoGTPases regulation and all their possible effectors can lead to the establishment of specialized polarity domains that will orchestrate the building and remodeling of cell structures.

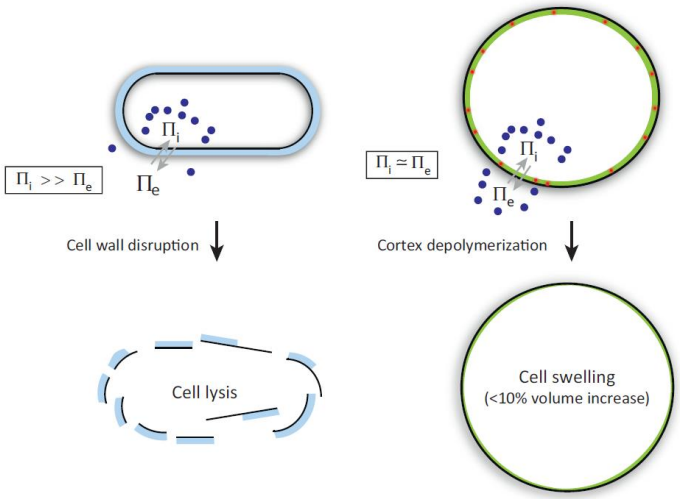

Figure 1.8. The actomyosin cortex versus the cell wall. In walled cells the internal turgor pressure is very high. The cell wall act as a mechanical barrier: its disruption lead to immediate cell lysis. In non walled cells difference in internal and external osmotic pressure is small. Actin cortex still balance the osmotic pressure, but its depolymerization cause only a moderate swelling (From (Salbreux et al., 2012)).

1.3 Cell surface mechanics

Once all the biochemical machinery has been delivered in the right location of a cell, it must polymerize/remodel/rearrange the surface, in order to obtain the correct mechanical properties, to achieve a specific shape.

In fact, as proposed by the pioneering work "On Growth and Forms" in 1917 by D'Arcy W. Thompson, any geometrical structure, even if part of a living system, will follow the mathematical and physical rules of any matter: "cell and tissue, shell and bone, leaf and flower, are so many portion of matter, and it is in obedience to the laws of physics that their particles have been moved, molded and conformed" (Thompson, 1942). He suggested that problems of form are in the first instance mathematical problems, problems of growth are physical problems, and therefore the morphologist must be a student of physical science. One of the main intuition that he had was that, despite the large variety of cell shapes existing in nature, they all follow similar physical principles. He dedicated one entire chapter on the forms of cells, considering them as simple entities comparable to soap bubbles. Like in soap bubbles, surface tension is the leading rule that brings about the minimization of surface area through taking on spherical shapes. By integrating Plateau's work on surface tension, he demonstrated that this rule is not just applicable to soap bubbles but also to many other more complex cell shapes can fall in this definition, under certain physical constrictions. Thompson's work, despite its 101 years and the obvious lack of informations on the

molecular players involved, remains an extremely important milestone in morphology studies, introducing the importance of mechanics, for the complete understanding of morphogenesis.

Thus, to unveil the mechanisms of shape control we need to understand how the cell regulates the mechanical properties and the forces generated at its surface.

In this context, we can divide cells in two families with different boundary composition: walled and non-walled cells.

1.3.1 Surface mechanics of non-walled cells

In most of the non-walled cells, from animal cells to amoeba, the most important regulator of surface mechanics is the actin cortex (Paluch and Heisenberg, 2009). This is a complex thin network made of proteins, located below the plasma membrane. It is mainly composed of actin filaments, parallel to the cell surface, with a mesh size ranging from 20 to 250 nm. Many actin-binding proteins bind to the cortex, among the most important are proteins involved in actin contractility, such as myosin or tropomyosin (Salbreux et al., 2012). The main myosin involved in actin cortex contractility is the non-muscle Myo II, which filaments can associate with each other in an anti-parallel fashion. This allows them to crosslink and slide actin filaments during ATP binding and hydrolysis, directly influencing network contraction (Figure 1.9) (Newell-Litwa et al., 2015).

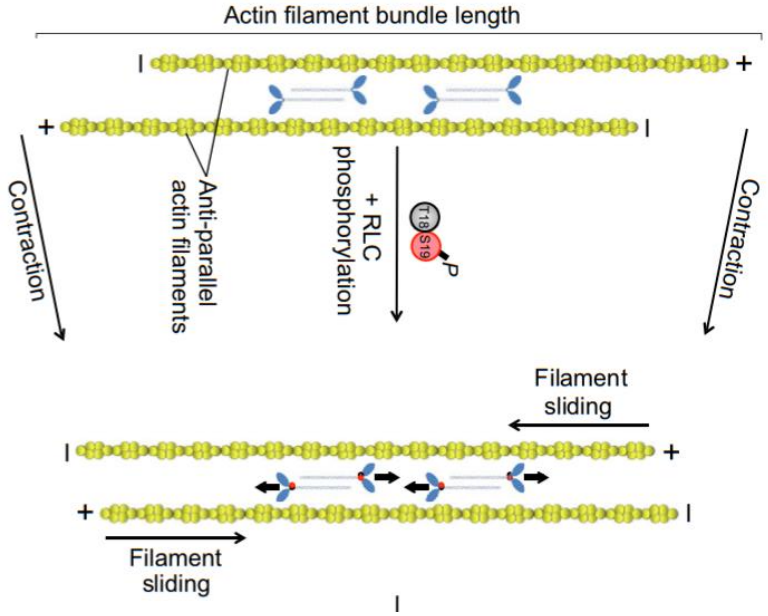

Figure 1.9. Non-muscle myosin II promote sliding of actin antiparallel filaments. Myo II filaments (blue) associate with each other in an anti-parallel fashion, allowing them to crosslink and slide actin filaments past each other. RLC (regulatory light chains) Ser19 phosphorylation increases Myo II ATPase activity, leading to contraction of actin filament bundles, and phosphorylation of both Ser19 and Thr18 increases Myo II ATPase activity, driving the

association of multiple actin filaments into actomyosin filament bundles, often referred to as stress fibers. Adapted from (Newell-Litwa et al., 2015).

The elasticity of the cortex has been estimated to be of the order of 10^3 Pa in cultured fibroblasts (Tinevez et al., 2009) and may balance cell osmotic pressure, in fact, in mitotic HeLa cells cortex depolymerization leads to small increase in cell volume (Stewart et al., 2011) (Figure 1.8 right). One of the key characteristics of the actin cortex, that underlies the biggest difference with walled cells, is its capacity for rapid turnover of its molecules, which allows for rapid remodeling, with a consequent high plasticity of the mesh. Local changes in cortex mechanical properties, particularly in cortical tension, drive cellular deformations, permitting very fast cell shape changes, necessary in these cells for both amoeboid (Charras et al., 2008) or lamellipodial migration (Vicente-Manzanares et al., 2009), rounding for cell division (Stewart et al., 2011), and also for shape modification at the tissue level, such as epithelial contraction (Levayer and Lecuit, 2012; Salbreux et al., 2012). A recent work showed that actin cortex thickness influences surface mechanics, with putative consequences on cell deformation. The authors showed that, in the transition between interphase and mitosis, during cell rounding, actin cortex thickness decreases together with an increase in surface tension. By affecting filament length regulators, actin cortex thickness can increase or decrease, but in both cases tension in mitosis decreases. By coupling this observation with a theoretical model, the authors suggested that only an actin cortex with the right thickness possesses filaments of the optimal length to maximize myosin binding and contractility. This suggests, first, that the length of actin filaments directly influences cortex tension, but also that surface thickness can be an important parameter to study the dynamic of morphogenetic changes (Figure 1.10) (Chugh et al., 2017).

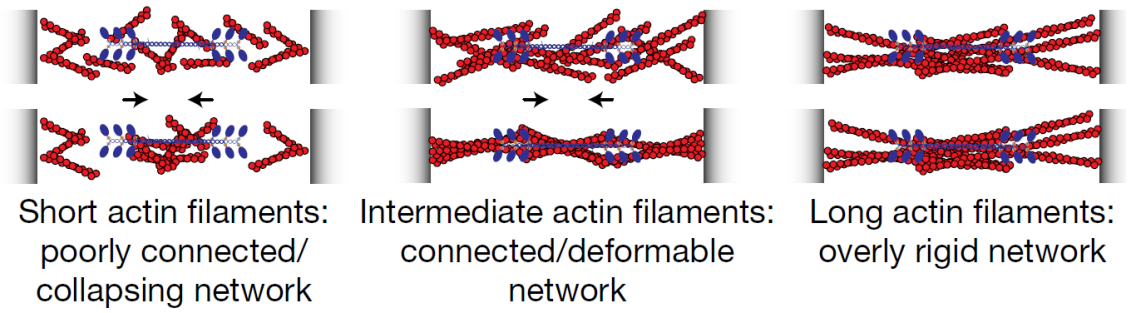

Figure 1.10. Actin filament length influences actin cortex tension. Only intermediate filament lengths, networks are sufficiently connected my Myo II motors for tension generation, and sufficiently compliant to promote tension increase (center). Adapted from (Chugh et al., 2017).

1.3.2 Surface mechanics of walled cells

Cells of plants, bacteria and fungi, have their cells surrounded by a very different structure, the cell wall. The cell wall is composed of different kind of polymers according to cell type, but in general, the main structural components are glucans chains and/or proteins. The first role of the cell wall is to act as a mechanical barrier, balancing the large internal turgor pressure typical of walled cells. Removal of the cell wall lead to immediate cell lysis (Davì and Minc, 2015; Flor-Parra et al., 2013) (Figure 1.8 left). For this reason, cell walls are much stiffer than the actin cortex. Wall elasticity in plants and fungi has been estimated to be on the order of $10^4/10^5$ Pa (Minc et al., 2009a; Steudle and Zimmermann, 1974; Triboulot et al., 1995). Despite the typical rigidity of their surface, walled cells are highly dynamic and can grow in the most variable forms and sizes. Large morphological variations are also observed in bacteria, and their shape has often been used for classification.

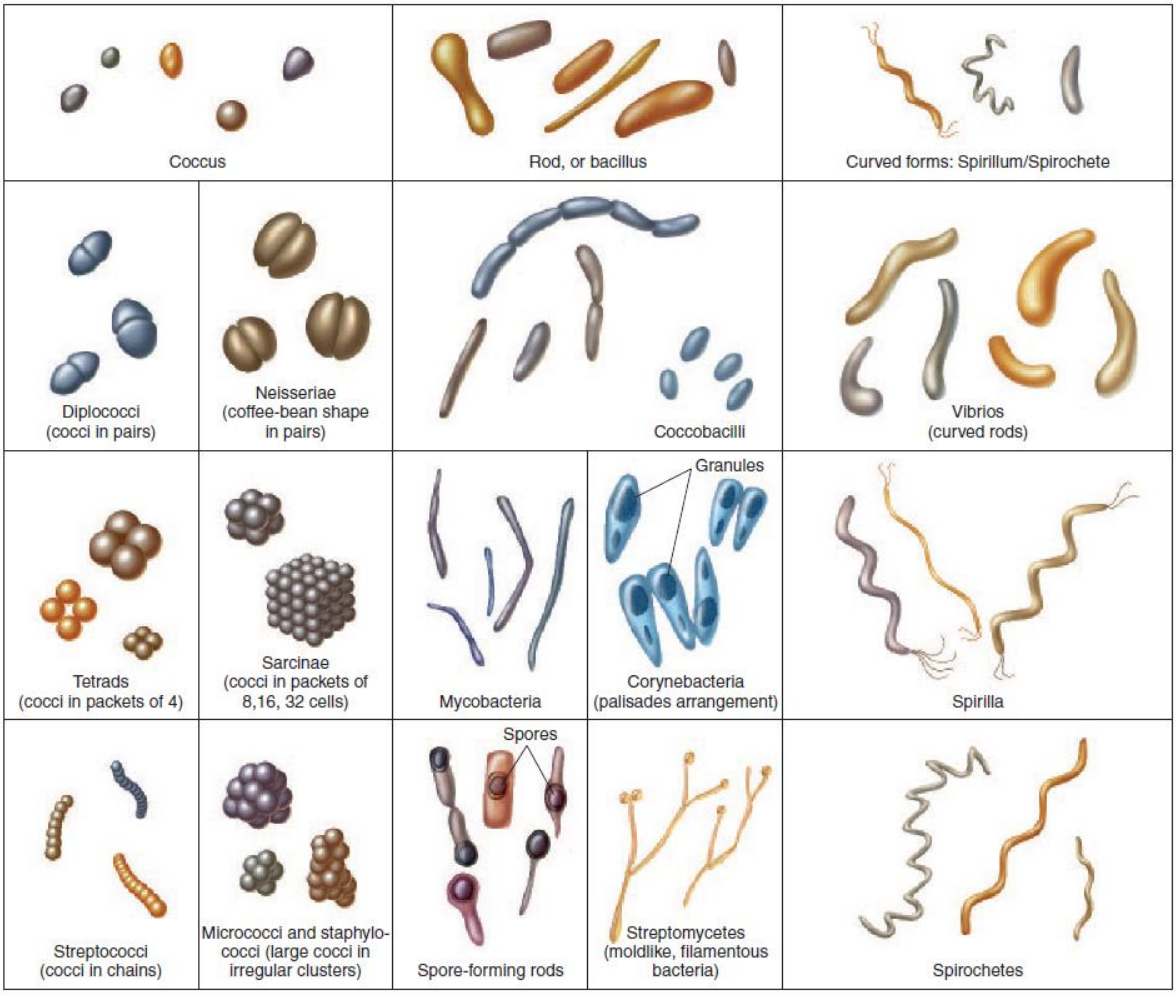

Figure 1.11. Schematic of shape variety in bacteria, not shown in exact scale (Park Talaro and Talaro, 2001).

Spherical/ball shaped bacteria are called cocci, but cocci can also be oval or pointed. Bacilli are rod shaped and variable in length/radius ratio. Plump and short rods are called coccobacilli. Bent rods are normally named vibrios. These simple shaped cells can often grow into multicellular structure, such as chains or squares. Both spirillia and spirochete are characterized by a curved spiral shape, but while the former are rigid, the latter are more flexible. Streptomycetes can grow micelia composed of hyphae, long tubular cells, and develop small rounded spores. The size of bacteria varies from the almost one micron spirillia and spirochete of some *Ricketsias*, to 40-50 μm in length for spirillia and spirochete (Figure 1.11) (Park Talaro and Talaro, 2001).

Plant cells, in tissues, can also acquire very diverse forms. One example, previously mentioned, is the very organized array of cubic and rectangular shape, typical of roots (Figure 1.2B). These cells can be longer than 100 μm in their long axis. Another beautiful example are leaf epidermal pavement cells, where multipolar growth patterns emerge to generate complex irregular cell shapes, that in some species create indentations in their anticlinal cell wall which has been likened to a puzzle piece. The longest axis of these cells can be longer than 50 μm. In the same tissue, much smaller guardian cells surround stomata pores, and are kidney shaped (Figure 1.12) (Ivakov and Persson, 2013).

After synthesis, the wall is deformed by turgor pressure and some enzymatic activity, leading to a very stable structure that is often referred as a shell. This rigid structure literally shapes the cell underneath, as clearly shown by the enzymatic removal of the cell wall in osmo-balanced conditions: the resulting protoplast (cell without wall) totally lose cell morphology becoming round, while often an intact "ghost" shape is left behind, that is nothing but the remnant of the wall (Davì and Minc, 2015; Flor-Parra et al., 2014).

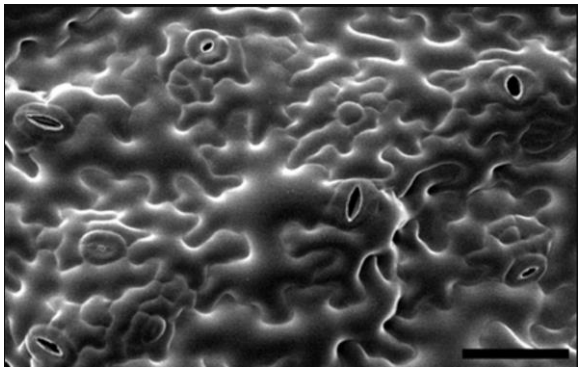

Figure 1.12. Leaf epidermal pavement cells on the abaxial surface (underside) of an *Arabidopsis* cotyledon. Stomata are pores that are surrounded by a pair of kidney-shaped guard cell. Pores appear as black voids in this image. The epidermal surface between stomata is occupied by pavement cells with undulating edges. Scale bar: 50 λm. (Dolan and Langdale, 2004)

Therefore, in a walled cell the correct polarized distribution of wall deposition, the precise control of material properties and the rate of remodeling are key for the definition of a precise cell shape, that will have little margin of change after synthesis, compared to non-walled cells (Cosgrove, 2016; Geitmann and Ortega, 2009). I will discuss with greater completeness, composition, assembly and mechanics of cell walls in the next chapter.

1.4 Mechanosensing mechanisms for shape regulation

In order to generate the correct subcellular structures, a cell must sense and directly control its own shape, not only for the already complex initial shape establishments, but also to control transient or permanent shape changes, to correct for eventual mistakes and to respond to eventual signals from their environment. A generalized view of a morphogenetic program can be oversimplified in the schematic proposed by J. Davies (Figure 1.13), which suggests that the presence of negative feedback is a key principle in morphogenesis (Davies, 2013).

Many mechanosensing feedback regulating morphogenesis and differentiation of specialized structures, have been described in a wide range of organisms, from amoeba, to animal, plants and fungi.

In *Dictyostelium*, during mitotic cell shape change, an active recruitment of myosin II has been suggested to counteract cell shape deformation, to correct for cell asymmetries. This recruitment

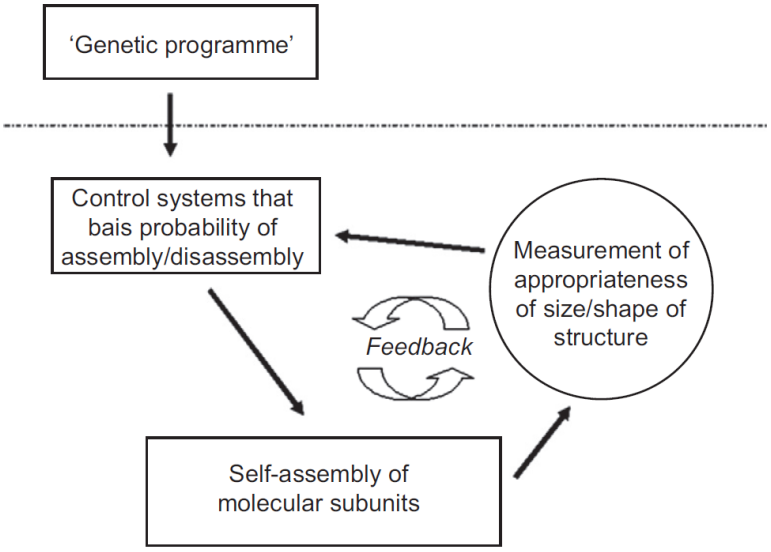

Figure 1.13. A generalized view of a morphogenetic mechanism (Davies, 2013)

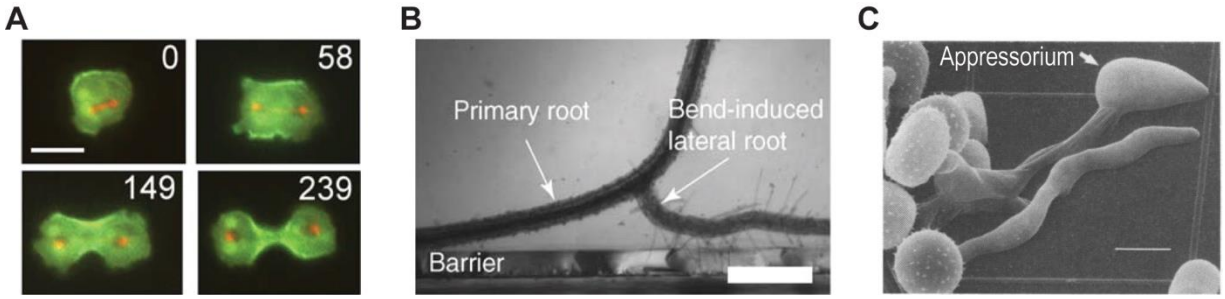

Figure 1.14. Mechanosensing mechanisms regulating morphogenesis and differentiation. A. Redistribution of GFP-MyoII during mitosis progression in *Dyctostelium*. In red RFP-Tub1.Time is in second, scale bar 10 μm (Effler et al., 2006). B. Lateral root formation in *A. thaliana* primary root, induced experimentally by placing a coverslip perpendicular to the axis of growth. Scale bar 500 μm (Monshausen and Gilroy, 2009). C. Scanning electron microcgraph of two germlings of *U. appendiculatus* grown on polystyrene substrate presenting ridges. The appressorium differentiate at site of contact with the ridge. Scale bar 10 μm (Zhou et al., 1991). Images adapted from indicated references.

is also activated after ectopic deformation of the cell surface, suggesting that a mechanosensing mechanism may perceive strain or cell shape, recruiting MyoII to correct for deformation. However, putative mechanosensors involved in this mechanism have not been uncovered yet (Figure 1.14A) (Effler et al., 2006).

In some instances, the signal can come from external cues, as in plants, where lateral root formation can be triggered by mechanical bending of a primary root. After this mechanical stimulus, auxin can redistribute and lead to the emergence of a front of growth. This mechanism can be crucial during growth through the soil: if a root encounters a barrier, it adopts an avoidance response to circumnavigate the obstacle and increase root spreading (Figure 1.14B). Despite this mechanism being known from the early 1900, the mechanosensing mechanism involved in this event remains to be established (Monshausen and Gilroy, 2009).

In the pathogenic fungus *Uromyces appendiculatus*, germ tubes form appressoria, differentiated structures involved in host invasion. Appressoria form only on specific topological areas of leaves, in particular when the germ tube encounters ridges of the height of stomatal guard cells. It has been proposed that, when germ tube/ridge contact occurs, this may activate mechanosensitive ion channels that trigger differentiation (Figure 1.14C) (Zhou et al., 1991).

Although several pathways involved in response to mechanical stimuli have been described or suggested, it is still not clear how these signals are perceived. Some classes of proteins or protein complexes have been identified as mechanosensors, such as ion channels, G proteins coupled receptors (GPRC), complexes linking the extracellular matrix to the cytoskeleton, or trans-wall proteins in fungi. However, the precise mechanical change sensed is not always clear (tension,

stress, strain), as well as the link between sensing and response pathway. Moreover, mechanosensing is often studied under mechanical stress, but cells must sense their boundaries and shape even during physiological conditions, to develop correctly and maintain homeostasis.

Chapter 2 – Elongation and morphogenesis in tip-growing walled cells

In this chapter, I introduce the main focus of my work, which is the morphogenesis of tip growing walled cells. As described below, in these cells the process of growth and shape establishment are tightly linked. I mainly focus on plant pollen tubes and root hairs, on fungal hyphae and tip growing yeasts. I start with a general introduction on tip growth. Then I describe tip growing walled cells from a purely mechanical point of view, introducing the main parameters that influence cell mechanics. Thereafter, I focus on how these cells regulate these mechanical parameters. For instance, I describe how cells regulate their turgor pressure and the properties of their walls. Finally, I summarize several models, both theoretical and experimental, proposed to link wall mechanical properties, growth and morphogenesis. I highlight differences and similarities between these models, their strengths and weaknesses, trying to define a general scenario on which we can base further studies, to better understand the process of tip elongation.

Table of contents

Chapter 2 – Elongation and morphogenesis in tip-growing walled cells 29

2.1 Mechanics of walled cells 35

2.2 Turgor pressure regulation 41

2.3 Cell wall properties ..... **Errore. Il segnalibro non è definito.**

2.3.1 Cell wall composition ..... **Errore. Il segnalibro non è definito.**

2.3.2 Cell wall synthesis 48

2.3.3 Cell Wall Integrity pathway 51

2.4 Influence of cell wall mechanics on morphogenesis and growth 54

Organisms ranging from plants to bacteria and fungi have their cells encased in a stiff structure, the cell wall. This wall, mainly composed of glucans and/or proteins, constitutes the full surface of the cell. One essential role of the cell wall is to prevent lysis, as walled cells are normally under very high internal osmotic pressure that is also the driving force for growth.

As mentioned in the previous chapter (***1.3.1***), in walled cells the structure of the wall is shaping the cell underneath. This is evident by the enzymatic removal of the cell wall in osmotically supported conditions, whereby the generated protoplast loses its shape, becoming round, and sometimes leaves behind the remnants of the cell wall in an intact and defined shape (Davì and Minc, 2015; Flor-Parra et al., 2014).

Similarly, the cell cannot grow without assembly of new wall material, and this assembly may directly influence the direction and velocity of growth. Moreover, during growth, the cell will acquire a new shape that is nothing but the shape of the newly assembled cell wall.

Therefore, in these cells, the process of growth and morphogenesis are tightly linked, and one cannot fully understand how growth and morphogenesis work, without understanding the properties of the cell wall, its composition, mechanics and dynamic regulation.

Tip growing walled cells are interesting models to directly study the links between wall properties, elongation and shape determination. In these cells, the extremely polarized growth typically generates tubular shapes (Figure 2.1).

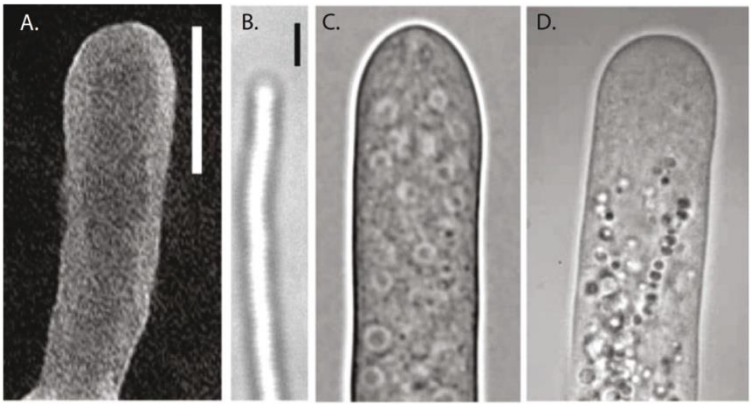

Figure 2.1. Examples of tip growing walled cells. Microbacterial filament from A. *Kitasatospora setae* and B. *Streptomyces coelicolor* A3(2). Bar is 1 μm. C. *Allomyces* hyphal growth. D. Lily root hair. Adapted from (Goriely, 2017)

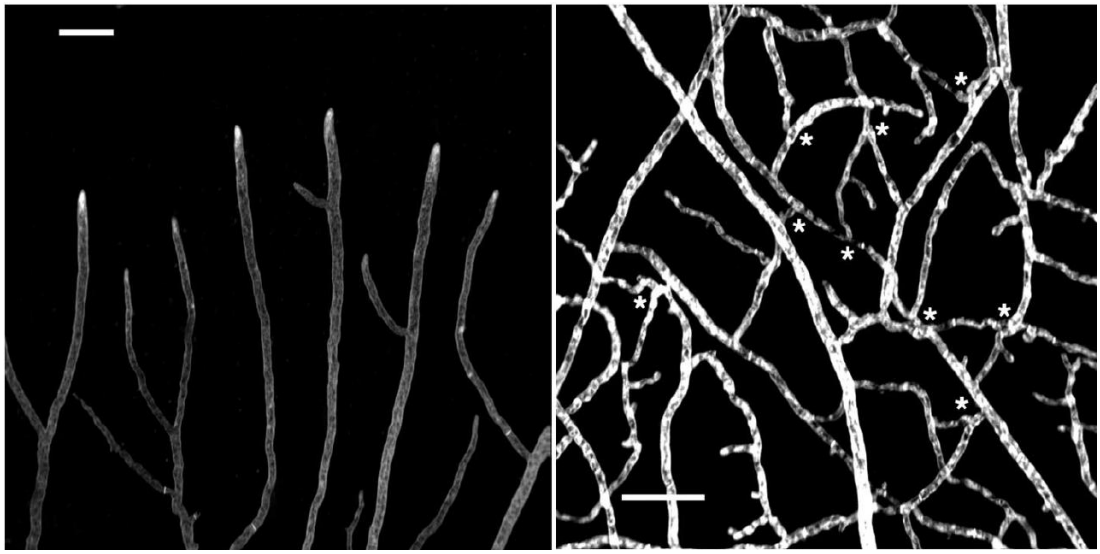

Figure 2.2. Apical and lateral branching in *Neurospora crassa* hyphae. On the right, the central part of the colony presents hyphal fusions (stars). Scale bars 20 μm (Pandey et al., 2004).

Tip elongation is a mechanism that has evolved several times in diverse taxonomic kingdoms (Figure 2.1). It has important physiological functions, to give some examples: in mycelial bacteria as well as in filamentous fungi, tip growth is necessary for the correct spreading of the colony (Flardh, 2003; Sanati Nezhad and Geitmann, 2013). In some fungal pathogens, tip elongation of the hyphae is necessary for host infection (Brand, 2012). Tip elongation is at the base of tropism, the ability of the cell to grow towards (or away from) a specific stimulus (chemicals, light, pheromones). Moreover, tip growth is necessary for root and root hair development, therefore for plant anchorage, and also for fertilization in seed plants, during which pollen can grow a germ tube that explores relatively long distances towards the ovules (Rounds and Bezanilla, 2013).

Despite the structural rigidity of the surface in walled cells, tip growth and morphogenesis are highly variable and dynamic processes. In fact, these are between the fastest growing cells in nature, reaching growth rates up to several tens of microns per minute (Lew, 2011). Growth rate can vary depending on several factors such as nutrients or temperature (Hedhly et al., 2005; Sevilla and Odds, 1986). Even within the same cell, growth rate variation can occur over time, as in pollen tubes, which alternate between phases of stable and oscillatory growth (Pierson et al., 1996; Rojas et al., 2011).

Shapes of growing tubes are highly variable. Diameters vary between species ranging from 10-15 μm of pollen tubes, to less than 1 μm in tip growing bacteria (Figure 2.1). Many filamentous fungi create apical or lateral branches, fundamental for the development of mycelia that often show high

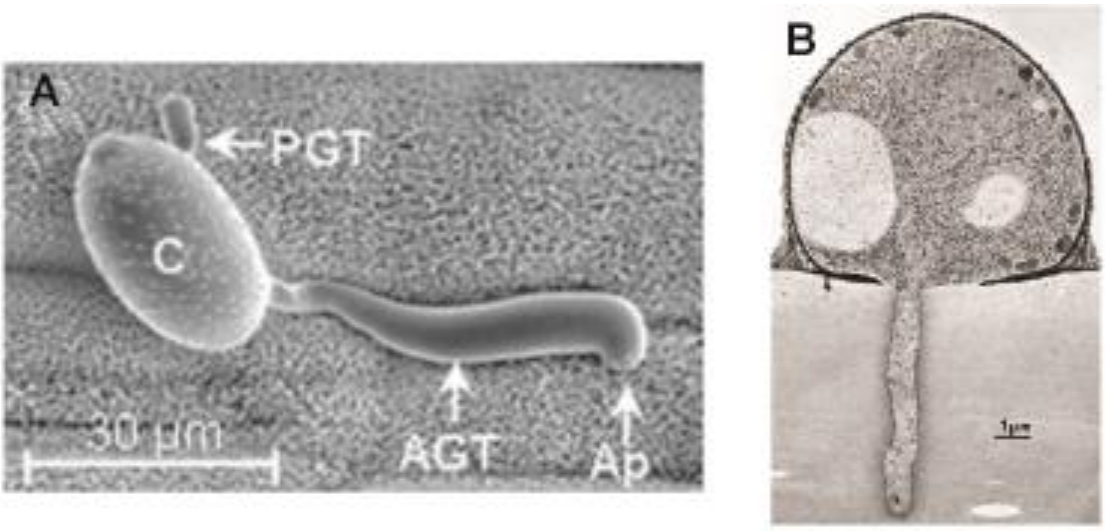

Figure 2.3. Appressoria development. A Cryo-SEM of conidia (C) from *Blumeria graminis f.sp. hordei* growing on barley leaf, developing a primary germ tube (PGT), the secondary appressoria germ tube (AGT) and the appressoria (Ap) (Prats et al., 2006). B Electron micrographs of *Magnaporthe grisea* peg formation from an appressorium, invading cellophane membrane (Deising et al., 2000).

variability in diameter, even within the same colony (Figure 2.2) (Harris, 2008). A single cell can change the direction of growth, hence shape, in response to external cues, such as the presence of chemo-attractant (e.g. pheromone). A beautiful example of how these cells can develop different shapes over growth and differentiation is the generation of appressoria in pathogenic fungi, which are specialized structures involved in host invasion first described by Frank in 1883. They originally develop from conidia, non-sexual spores of fungi, which initially germinate creating a primary thin germ tube, probably used for nutrient uptake. A second germ tube is then elongated, which can swell at the apex, creating a much larger structure that Frank calls an "organ", divided from the germ tube by a septum. This structure tightly adheres to the host surface, develops a penetration peg, perpendicular to the host surface and initiates invasion (***Figure 2.3***) (Bastmeyer et al., 2002; Deising et al., 2000; Prats et al., 2006).

Another process requiring the dynamical behavior of tip growth is cell fusion, an event that entails a large amount of wall digestion and remodeling to allow for plasma membrane fusion. This happens during mating in yeasts, where cells of compatible mating types can fuse to undergo sexual differentiation (Merlini et al., 2013). In some filamentous fungi, like *Neurospora crassa*, both germinating conidia and hyphae can grow towards each other and fuse, a process that has been associated with increased fitness of the mycelial colony (Figure 2.4) (Herzog et al., 2015).

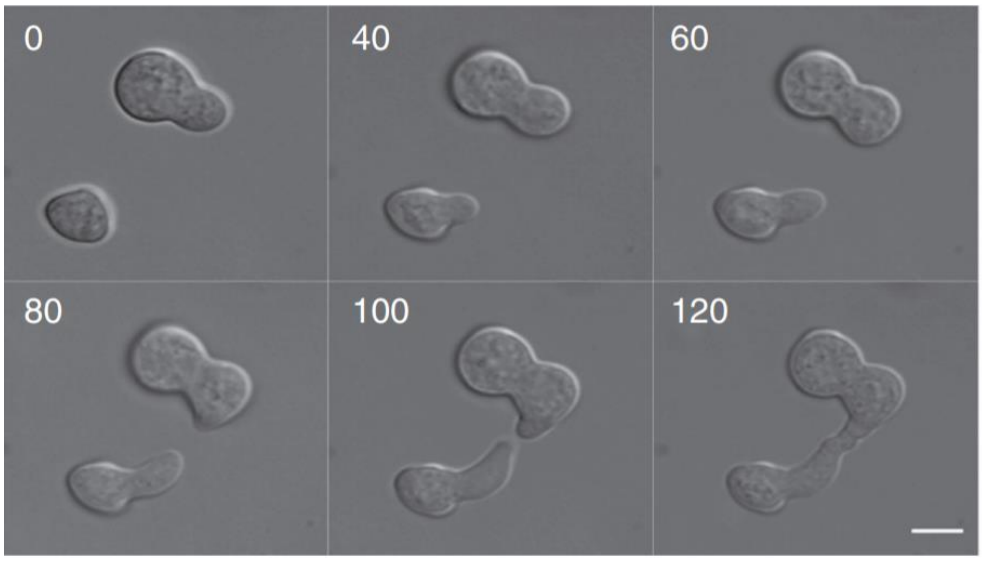

Figure 2.4. Conidia germination and fusion in *Neurospora crassa*. Time is in minutes, scale bar 5μm (Herzog et al., 2015).

Therefore, the cell wall must be continuously remodeled and reshaped to permit all these dynamic changes. Tip growth comes with a very polarized synthesis of wall material that is then remodeled by turgor pressure and in some cases by enzymatic activity. This newly deformed wall is then shifted to the side of the tip, while further new wall is synthesized (Figure 2.5).

Without regulation, tip growth can be dangerous for the cell: errors in synthesis rate or in wall composition can cause for example too soft walls that may be pierced by pressure, and consequently cell lysis and death. Similar effects can be caused by defects in wall extension and turgor pressure. On the contrary, walls that are too hard or when pressure is too low, may also cause growth arrest.

Moreover, polarized synthesis and deformation of wall establishes *per se* the typical tubular shape of tip growing cells (Figure 2.1), suggesting that defects in synthesis and remodeling can cause aberrations in cell morphogenesis.

For these reasons, the process of tip growth is thought to be highly regulated, to allow for the correct balance between turgor pressure, synthesis and remodeling, able to preserve cell integrity and to establish a correct morphology.

In this chapter, I describe growth and morphogenesis of tip growing cells, focusing on yeast, filamentous fungi, pollen tubes and root hair. I first introduce walled cells from a purely mechanical point of view, presenting some of the experimental measurements of their mechanical properties.

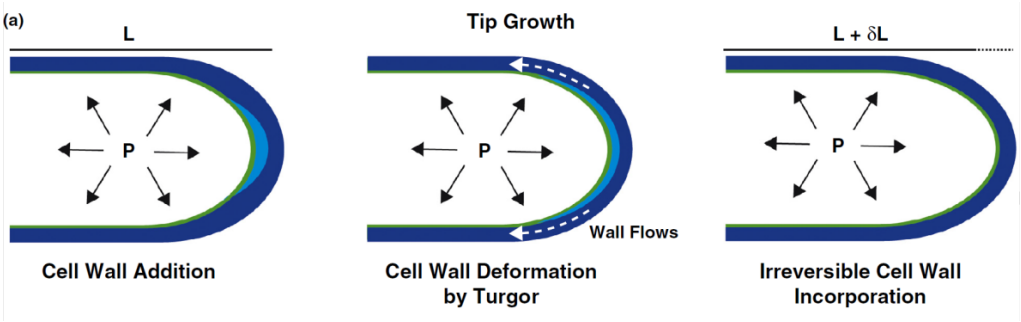

Figure 2.5. During tip growth new wall material (light blue) is deposited at the tip of the cell and then remodeled by internal turgor pressure (P), to be irreversibly incorporated in the structure. Adapted from (Davì and Minc, 2015).

I then focus on how these cells can control their mechanical parameters, for instance by regulating wall properties and turgor pressure. Finally, I outline the different proposed theories to explain how cell wall mechanics can influence growth and shape generation.

2.1 Mechanics of walled cells

The main features that define mechanically a walled cell are the properties of its surface (the wall), and the internal osmotic pressure: these can be seen as the simplest set of components defining cell shape and growth patterns (Figure 2.6).

Walled cells are often compared to balloons. In fact, they are composed of a relatively thin external layer, under tension from high pressure. Turgor pressure is recognized as the driver of growth in walled cells (Rojas and Huang, 2018). This is a hydrostatic pressure, arising from the ability of these cells to increase (or decrease) their intracellular concentration of osmotically active molecules, such as ions, sugars or amino acids. Osmotic adjustment leads to influx (or efflux) of water from the milieu, increasing (or decreasing) turgidity (more insights on turgor pressure regulation in **2.2**). Direct measurement of turgor can be performed by a pressure probe, an oil filled microcapillary directly inserted in the vacuole of studied cells (Green, 1968). Due to the size of this capillary this direct measurements are restricted to large cells, such as giant algae or plant cells, where different studies have reported values between 0.1 and 1 MPa (Steudle and Zimmermann, 1974; Triboulot et al., 1995). In smaller cells, such as yeast and filamentous fungi, turgor pressure can be estimated through indirect approaches, such as Atomic Force Microscopy (AFM) (Deng et al., 2011), osmotic treatments coupled with laser ablation (Atilgan et al., 2015), or elastic deformation of microchambers (Minc et al., 2009a). These different methods gave similar

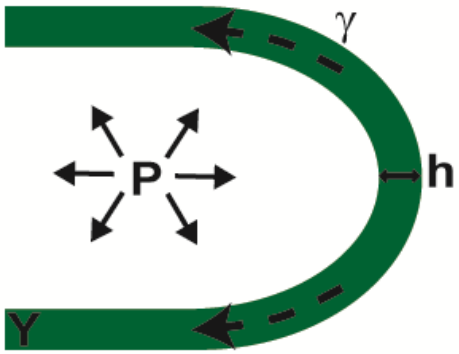

Figure 2.6. Mechanics of tip growing cell. The wall is represented in green. P is the isotropic turgor pressure; Y is the bulk elastic modulus of the wall, while h is thickness. γ represent wall deformation over growth (strain)

estimated values of turgor, in the order of 1-2 MPa for yeasts and filamentous fungi.

Although turgor is the effective driving force for growth and wall deformation, its sole contribution cannot explain the polarized shape of tip growing cells, since its force is equal in all directions (Figure 2.6). Moreover, in lily pollen tubes, oscillations in growth rate can occur without variations in turgor (Benkert and Bentrup, 1997; Zerzour et al., 2009). Therefore, to understand the polarized shape and the mechanism of growth of these cells, the mechanics of their cell wall must be investigated.

In a simplified view, the mechanics of the cell wall can be separated in two independent components, thickness and bulk elastic modulus.

Cell wall thickness does not depend on wall composition and is the most relevant component of wall geometry. Wall thickness is highly variable amongst different organisms. It ranges from few nanometers in gram negative, to tens on nanometers in gram positive bacteria (Vollmer et al., 2008), reaching 100-300 nm in fungi (Ghamrawi et al., 2015; Osumi, 2012), up to 500 nm in tip growing cells of plants (Lancelle and Hepler, 1992). Significant variations in thickness have been reported within species, the extreme of which can be found in lily pollen tube which is in a range of 500 nm (Lancelle and Hepler, 1992; McKenna et al., 2009), while in tobacco the wall measures around 250 nm (Lancelle and Hepler, 1988). Wall thickness also varies in different structures of the same organism, a simple example being the difference between hyphal and conidial wall in fungi, such as in *Scedosporium boydii*, where they present thickness of about 80 nm and more than 200 nm respectively (Figure 2.7) (Ghamrawi et al., 2015). Also growth and metabolic condition can influence wall thickness, as has been observed in pollen grains of pea, in which a thickness increase of two fold is reached between 25°C and 36°C, together with a decrease in germination efficiency

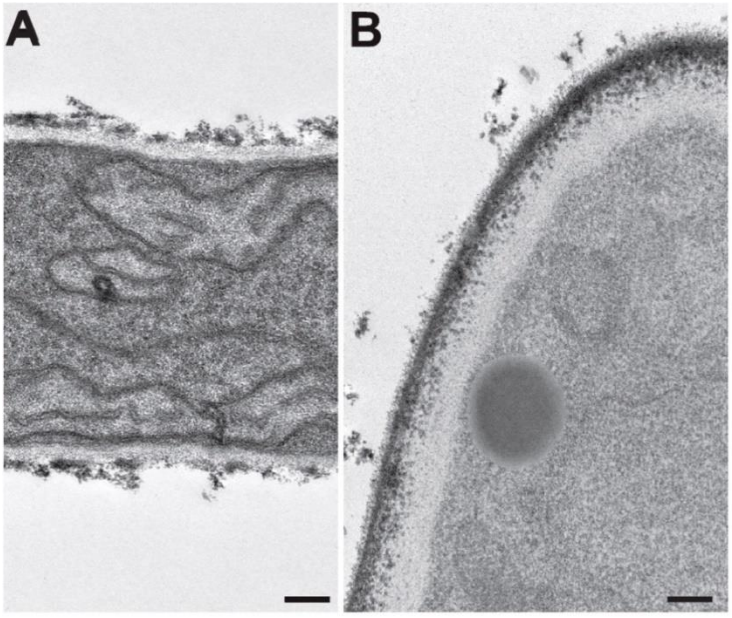

Figure 2.7. Transmission electron micrographs showing thickness and structural difference of the cell wall between hypha (A) and conidia (B) in *Scedosporium boydii* (Ghamrawi et al., 2015).

(Jiang et al., 2015). Similarly, differences in carbon source may affect thickness, for instance in *Candida albicans,* yeasts growing on glucose have a 100 nm thick structural layer of the wall, that halves if cells grow on lactose (Ene et al., 2015). However, so far, observation of the dynamic behavior of cell wall thickness have been highly hindered as thickness is typically below the resolution of light microscopy. The classical method to measure cell wall thickness is Transmission Electron Microscopy (TEM) that is a powerful tool to study the ultrastructure of cells. However, TEM has several limitations for the study of cell wall: first, TEM can be performed only on fixed samples that are afterwards embedded in resins; in these processes, cell structures often shrink and deform, leading to potential aberration in measurements. Second, for observation, samples are sliced by ultra-tomography: a cut out of plane or slightly oblique can lead to mistakes in thickness spatial distributions. Third, and most important, fixation precludes any information on cell wall dynamics. Despite the aforementioned observation of thickness variation, this technological limit is probably at the base of the idea that wall thickness is quasi-constant over time, and this assumption has been used in many models of tip growth. However, there are few attempts to study wall thickness in live. One method is based on the expression of His tagged membrane sensors, engineered to have variable measured length, used as molecular rulers, by coupling single molecule Atomic Force Microscopy (AFM). Only long enough sensors can be detected by the AFM tip.

Through this method the authors could detect thickness variation after enzymatic digestion of the wall, in

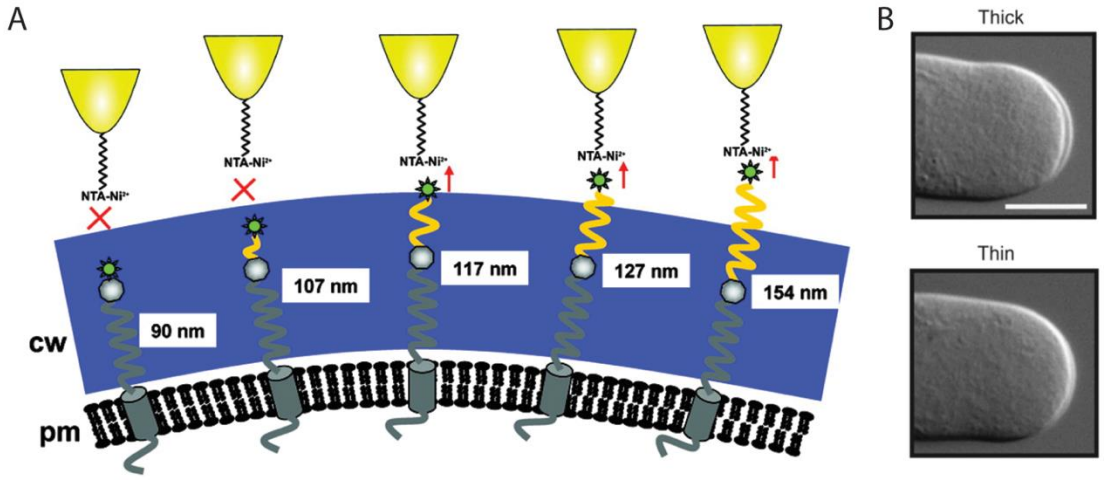

Figure 2.8. Different approaches for live cell wall thickness measurements. A. Schematic of the approach used by Dupres *et al.*: a transmembrane sensor with different length (grey+yellow) is His tagged (green). The AFM tip (yellow), functionalized for His interaction can recognize only sensors with length higher than wall thickness (Dupres et al., 2010). B. DIC images of lily pollen tubes. The sharp gradient in at the front of the tip is used as a direct measure of local wall thickness (McKenna et al., 2009).

budding yeast. However, this approach is particularly complicated, the expected thickness must be known to engineer the right ruler size, and only one molecular ruler can be expressed in one strain, with the consequence of hiding local variation below the size of the molecule. Moreover, modified expression of sensors may have an impact on wall integrity and alter its properties (Figure 2.8 left) (Dupres et al., 2010). The second study exploited the thick cell wall of lily pollen tubes (500 nm): thickness variations can be detected by difference in DIC images. This analysis showed that during oscillating growth of pollen tubes, apex thickness also oscillates in a range between 400 and 800 nm, with phases of thickening preceding fast growth (Figure 2.8 right) (McKenna et al., 2009). Despite the limitation of this method being only applicable to very thick walls, it is clearly evident that thickness is a highly dynamic parameter of wall mechanics that should be considered as such in the studies of dynamic behavior of walled cells. More technological advancements are needed to measure this parameter in a live experimental setting.

The bulk elastic modulus, or Young modulus, is an intrinsic property of the material, directly related to its composition and independent of geometry, and has units of pressure. For the cell wall, this modulus can directly depend on glucan properties, polymers length or cross-links. An evident proof of cell wall elasticity has been observed in *S. pombe* cells, where cells forced in bent shape

in microchambers can come back to their normal rod shape within seconds, if they pop out of the well (Minc et al., 2009a; Minc et al., 2009b).

A classical method to measure wall elastic modulus is AFM. This has been applied on isolated cell walls, or on intact cell surfaces, to study cell wall ultrastructure and measure its elastic modulus. However, only very accurate technical approaches can allow for the correct estimation of cell wall elastic modulus in live cells, successfully separating the influence from wall geometry and turgor (Milani et al., 2013). Other indirect approaches have used deformation of elastomeric microchambers (Minc et al., 2009a), or have coupled modeling with cell deformation under osmotic treatment (Abenza et al., 2015; Atilgan et al., 2015), or with estimation of the other mechanical parameters (Goriely and Tabor, 2006). These estimations revealed values of elastic modulus on the order of 10-100 MPa in tip growing cells (Goriely and Tabor, 2006; Minc et al., 2009a; Vogler et al., 2013). Indentation analysis have shown a local softening of the wall at cell tip, in pollen tubes (Geitmann and Parre, 2004; Zerzour et al., 2009), supported also by different composition of the apical area (discussed below **Errore. Il segnalibro non è definito.**). Similar heterogeneities have been reported also for hyphal elongation (Ma et al., 2005) and for the extreme case of polar growth in mating protrusion of budding yeast (Goldenbogen et al., 2016).

Other important mechanical parameters are derived from this initial set, plus cell geometry, for each cell type.

The surface modulus of the cell wall is the product of bulk elastic modulus and thickness. This parameter best represents the "stiffness" of the wall, containing together the information on mechanical composition and geometry.

Surface tension is the tendency of a fluid to acquire the minimal surface area possible. Defined as the force exerted per unit area by the surrounding molecules, in a cell it does not depend on surface properties. Instead, it depends on cell geometry, and in a cylindrical cell it is defined as:

$$\mu = \Delta P R$$

where ΔP is turgor pressure and R is cell radius. As discussed in ***1.3***, non-walled cells modify their surface tension, through actin cortex rearrangement, to permit morphological changes (Salbreux et al., 2012). Moreover, in *Bacillus subtilis*, a gram positive bacteria, it has been recently proposed that membrane surface tension regulates the rate of cell wall synthesis, modulating responses to hypo- or hyper-osmotic stress (Rojas and Huang, 2018). This suggests that some cells can regulate

their homeostasis by controlling this parameter, therefore its estimation may help to understand these strategies.

Surface stress is defined as the ratio of the force acting on a cross-section of the material scaled by the area of the material resisting the force, and in walled cells can be written as:

$$\sigma = \frac{\Delta P R}{h}$$

where h is the thickness of the wall, while the elastic strain of the wall corresponds to its deformation, and can be defined as:

$$\gamma = \frac{\Delta P R}{Y h}$$

where Y is the bulk modulus of the wall (Figure 2.6).

These last two parameters are interesting to understand how cells can balance turgor pressure, by modulating shape and wall mechanical parameters, to maintain homeostasis and integrity. For instance, a recent work proposed that the highly lobed puzzle shape of leaf epidermal pavement cells is the consequence of isotropic growth, and is obtained in order to minimize mechanical surface stress. In support of this model, the authors show that, in early meristems, cells unable to undergo geometrical changes, because of microtubules de-polymerization, increase in size until they burst (Sapala et al., 2018). In another recent work, that will be better discussed in the last paragraph of this chapter, the authors showed that, during polarized growth of mating projections in budding yeasts, cells must sense their strain, in order to maintain cell integrity. In fact, mutants putatively impaired in this sensing can lyse (Banavar et al., 2018).

Therefore, monitoring more complex parameters of surface mechanics can be a good approach to understand how cells maintain integrity, while ensuring growth and expansion.

To summarize, tip-growing cells have very peculiar mechanical properties, with turgor pressure up to 1-2MPa, and elastic moduli similar to that of rubber. We can compare their mechanical properties to that of a bike tire. In these cells, growth and wall deformation are driven by turgor, while shape is ultimately determined by the mechanics of the cell wall. Cells adopt different strategies, by modulating surface mechanics, for the maintenance of their homeostasis.

Despite current knowledge being sparse and incomplete, estimations of cell mechanical parameters start to give an idea of wall asymmetries that may regulate tip growth expansion, and they have been used in several theoretical and experimental models that attempt to explain tip growth and shape determination. I focus on these works in the last paragraph of this chapter. For a better

understanding of mechanical parameter regulation, in the next paragraph, I describe how cells establish and modulate turgor and wall structure.

2.2 Turgor pressure regulation

Turgor pressure is the mechanical driver of cell growth, therefore, it is not surprising that cells carefully regulate it. Furthermore, many walled cells are sessile, and they can be subjected to massive and uncontrolled change in environmental osmotic conditions. For example, floods can cause hypo-osmotic stress, with consequent increase of water intake and risk of cells bursting. On the other hand, a microorganism that is growing on a fruit can be subjected to hyper-osmotic shock, as soon as the fruit starts to dry and its concentration in sugars increase to saturation levels. This causes turgor reduction, water efflux and cell shrinkage, all conditions deleterious for growth. Similarly, drought or pathogen infections can cause water exit and turgor loss. Moreover, modulation of turgor pressure is fundamental for several physiological functions, for example, to breach the hosts interior, in appressoria, pressure can increase up to 8MPa before penetration (Howard et al., 1991). Dynamic changes in turgor are also associated to organ movements in plants, as well as circadian movements of leaves (Beauzamy et al., 2014; Forterre, 2013).

To contrast osmotic stress and/or to modulate pressure under physiological conditions, walled cells have developed diverse signaling cascades to tune the concentration of intracellular osmolytes, in order to control the water content. So far, the best described system is the HOG MAP kinase cascade in *S. cerevisiae* (Figure 2.9). This pathway, is not essential for growth in standard

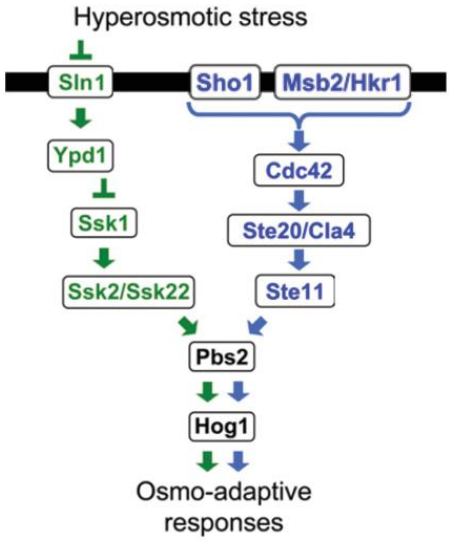

Figure 2.9. HOG pathway in *Saccharomyces cerevisiae* (Saito and Posas, 2012).

condition, and is mainly involved in hyper-osmotic stress responses and can be activated by two different upstream signaling. The first one starts with the transmembrane protein Sln1, which presents both histidine kinase HK) and receiver (REC) domains. HK has been suggested to be active under normal osmotic conditions, and can phosphorylate REC. This can phosphorylate the small protein Ypd1 that transfers the phospho-group to Ssk1. The HK domain of Sln1 can be inactivated by osmotic increase, but also by decreasing temperature or by DMSO treatment, suggesting that its activation is sensitive to variation in plasma membrane fluidity (Hayashi and Maeda, 2006; Panadero et al., 2006). Sln1 inactivation leads to de-phosphorylation of Ssk1, which can bind and activate the two homologous MAPKKK, Ssk2 and Ssk22. These activate the MAPKK Pbs2 leading to activation of the MAPK Hog1. The second pathway starts with the activation of the transmembrane protein Sho1, by the two putative osmosensors Msb2 and Hkr1, two highly glycosylated proteins, serine/threonine rich. Their mechanism of activation is not clear, but after osmotic increase, they activate Sho1. This induces the activation of the PAK-like proteins Ste20 and Cla4, inducing their association to the small GTPase Cdc42. Activated Ste20 and Cla4 can activate the MAPKKK Ste11 that activate Pbs2, as in the Sln1 path. These two pathways, mechanistically different, are functionally redundant and the lack of functionality in one of them is at least partially compensated by the other (Saito and Posas, 2012). Once activated, Hog1 is transported into the nucleus where it can regulate transcription. The major strategy to adapt to increased osmolarity is to increase intracellular osmolytes. The main osmolyte produced by *S. cerevisiae* is glycerol, through the glycerol-3-phosphatases (Gpp1 and Gpp2) and glycerol-3-phosphate dehydrogenase (Gpd1), enzymes up-regulated by Hog1. Lack of these enzymes causes a severe decrease in viability under osmotic stress (Hohmann, 2002). Accumulation of glycerol activates a negative feedback on Hog1 activation that reaches its basal level of activation 30 minutes after the stress (Hao et al., 2007).

The HOG pathway is highly conserved in fungi, and in some cases, it has roles implicated in non-stressed conditions. For example, in the wheat pathogen *Fusarium graminearum*, deletion of homologues of kinases in the *Sc*HOG cascade, cause high sensitivity to osmostress, but also defects in hyphal growth, branching and pathogenesis (Zheng et al., 2012).

Plants developed several pathways to modulate osmotic conditions. Activation of MAP kinase cascades, such as MAPK3-4-6 pathways in *Arabidopsis thaliana*, have been described under hyper-osmotic stress (Sinha et al., 2011). Other pathways involve the accumulation of abscisic acid

(ABA), a key hormone in plants involved in diverse stress responses, that induces the activation of a series of effectors, that finally promotes the transcription of stress responsive genes (Fujita et al., 2004; Yoshida et al., 2014). In plants, pressure can be tuned by modulating the concentration of diverse osmolytes, like carbohydrates or amino acids. One key amino acid is proline, which accumulates in tissues after drought or external salt increase, independently of other amino acids concentration (Beauzamy et al., 2014; Delauney and Verma, 1993).

Another strategy that cells have to modulate their turgor is to regulate water and solute flow. Aquaporins are a large family of plasma membrane channels, described in all living kingdoms. They are involved in passive transport of water, glycerol and other small uncharged molecules and ions. These channels are not constitutively open and their function can be controlled by post-translational modification, such as phosphorylation (Chaumont et al., 2005). They play important roles in osmoregulation. For instance, in *S. cerevisiae*, after turgor reduction, the aquaglyceroporin Fps1 is closed in a mechanism dependent on Hog1, to prevent glycerol outflow (Siderius et al., 2000).

The response to hypo-osmotic stress has been well described in budding yeast. Decrease of external osmolytes causes cell swelling and consequent increase of cytosolic calcium that induces the activation of the cell wall integrity pathway (See 2.1.3). This promotes the opening of Fps1, promoting glycerol release (Ahmadpour et al., 2014). The mechanism of cytosolic calcium accumulation is not clear in budding yeast, while in fission yeast and other fungi homologues of bacterial mechanosensitive channels (MSCs), localizing at the endoplasmic reticulum (ER) have been proposed to modulate calcium release after cell swelling, and may be activated by increased tension (Nakayama et al., 2014; Nakayama and Iida, 2014). In general, MSCs are involved in response to hypo-osmotic stress in bacteria: they are membrane-spanning protein complexes that form a gated macromolecular pore, and if open they can allow diffusion of ions with large (MscL) or small (MscS) conductance. It has been demonstrated that their activation simply relies on increased tension in the plasma membrane (Perozo et al., 2002), and contributes to the cell volume regulation against hypotonic challenge, thus working as a safety bulb to protect cells from osmotic rupture (Sokabe et al., 2015; Wilson et al., 2013). MSCs are conserved in all kingdoms of life. It has been recently shown that in *A. thaliana* MscS like proteins localizing in the plastids, help in the maintenance of the morphology of this organelle, which appears to be under constant hypo-osmotic stress during normal plant growth (Veley et al., 2012).

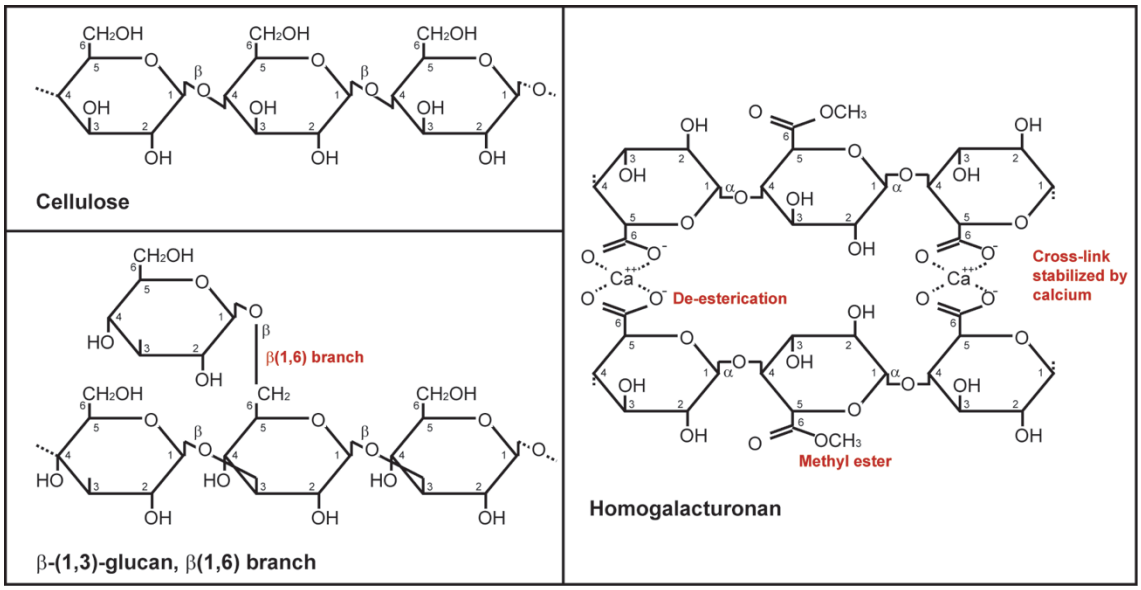

Figure 2.10. Chemical composition of some of the most important structural polysaccharides composing cell walls. Refering to the text, cellulose is the main component of root hairs; homogalacturonan is the main pectin, structural core of pollen tube wall; β-glucans are the main structural components if fungal cell walls.

2.1 Cell wall properties

2.1.1 Cell wall composition

Cell walls in plants and fungi are mainly composed of polysaccharides. These are chains of monosaccharides units, bound by glycosidic linkages. For example, β-glucans are created through beta linkages between carbon 1 of one D-glucose monomer and carbon 3 of the following monomer. Chains can also branch, for instance, in β-glucan, the OH group of carbon 6 can create a glycosidic bond with a free anomeric carbon of a new D-glucose monomer or chain. Parallel chains can also interact through lateral modifications, such as in homogalacturonan, where de-methyl-esterified groups can interact through divalent calcium cations, creating cross linked parallel bundles. Chains of different natures can bind one another: also this interaction is referred to as cross linking. (Figure 2.10, Figure 2.11).

A complete description of cell wall composition in different organisms can be extremely complex. In fact, in different species and organisms, the wall can have considerably different composition, and even in the same organism, different structure may show profound variations.

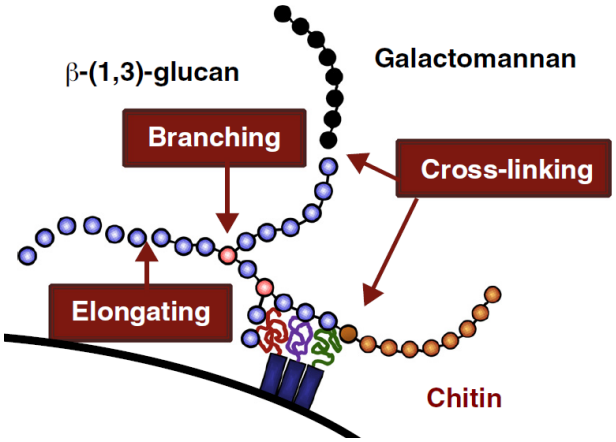

Figure 2.11. Schematic of fungal wall synthesis. Monosaccharides are elongated in chains and eventually branched and cross linked. In black the plasma membrane, in blue with colorful tails are synthases. Galactomannan is synthesized in the Golgi and transported to the cell surface (Latge and Beauvais, 2014).

For sake of simplicity, I will here present a general overview of cell wall composition in plants root hair and pollen tubes, and in filamentous fungi and yeast, without entering in the details of the particular species.

In plants, cell walls are composed of two layers: the primary wall is a thin extensible layer that is normally associated with growth; the secondary wall is synthesized below the primary wall, normally thicker and multilayered; it is characteristic of cells that are no longer expanding.

Both pollen tubes and root hair present only primary walls in the expanding region. The secondary wall, when present, is confined to the tubular part (Figure 2.12) (Mollet et al., 2013).

In root hairs, the cell wall is mainly composed of cellulose, β-(1,4)-glucan (Figure 2.10), which is the principal component of both primary and secondary walls. Interestingly, ultrastructural studies have shown that at the tip of the hair, cellulose microfibrils are short and randomly arranged, while in the tubular part long microfibrils they are highly ordered and oriented transversely to the axis of growth (Akkerman et al., 2012; Newcomb and Bonnett, 1965). In addition, a class of intra wall proteins, the extensins, are essential for correct wall structure and morphology. Extensins seem to play a structural role, and they have been suggested to be implicated in cell wall self-assembly. Pectins and hemicellulose are also present, embedded within cellulose matrix, but their structural role has not been deeply explored. (Galway, 2006; Mendrinna and Persson, 2015; Park et al., 2011; Velasquez et al., 2011).

Despite pollen tubes being, as root hairs, tip-growing cells of plants, their cell wall composition is profoundly different. The main components of their cell walls are pectins. These are complex polysaccharides, as the most diffuse homogalacturonan (HG), α-(1,4)-galacturonan (Figure 2.10).

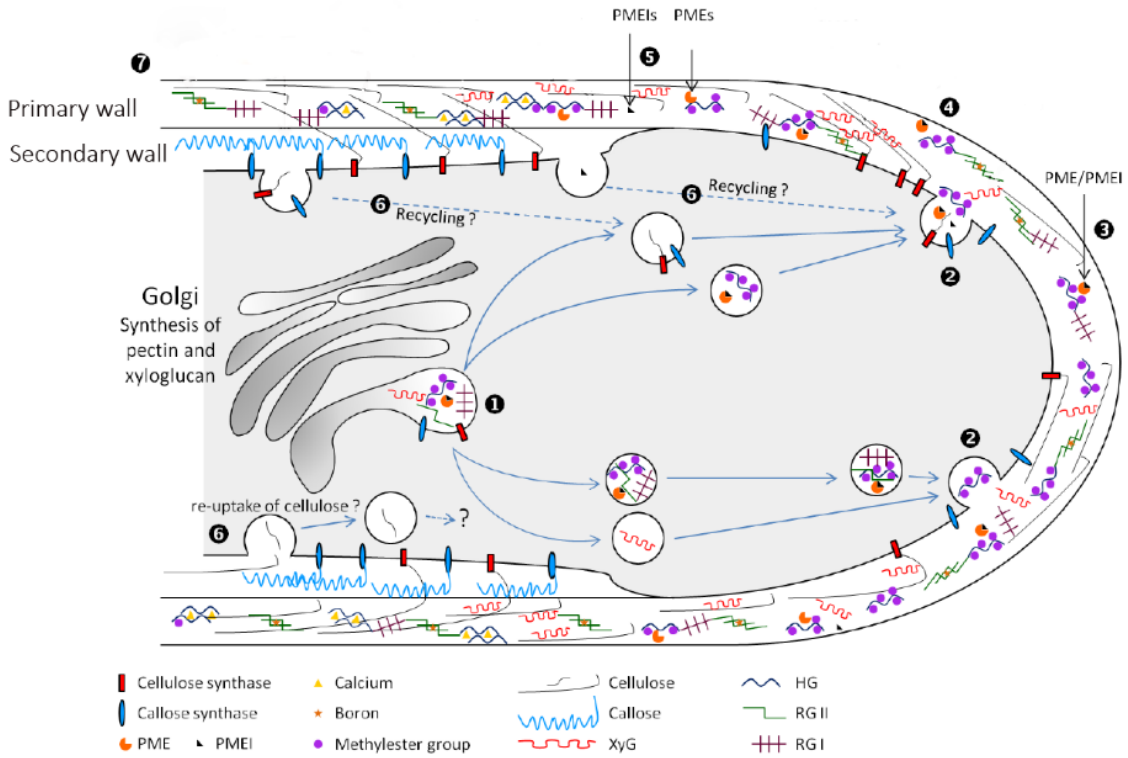

Figure 2.12. Schematic of wall synthesis in pollen tubes. 1- Cellulose and callose synthases, hemicellulose (XyG) and pectins (HG, RG-I, RG-II) in the Golgi, 2- are then secreted to plasma membrane and wall. 3- HG at cell tip remains esterified, thanks to pectin methyl esterase inhibitor (PMI). 4- Other pectins are stabilized by boron (not clear if this happen in the wall or before). 5- release of PMI activates pectin methyl esterase (PME) promoting HG de-esterification and cross-link by Ca^{++}. 6- Callose and cellulose synthase build the secondary wall. 6-7 putative recycling of synthases and cellulose microfibrils. Adapted from (Mollet et al., 2013)

In pollen tubes, esterified pectins are more abundant at the tip, while on the sides they are mainly de-esterified and Ca^{++} cross-linked, suggesting an increase in rigidity. Callose (β-1-3 glucan) is accumulated in the secondary wall, therefore only in the tubular part of the cell. Cellulose is stillpresent, mostly in the tubular part, but it has been observed also at growing tips in slow growing pollen tubes, as in some gymnosperms, suggesting a putative role of cellulose in controlling growth rate (Lazzaro et al., 2003). Finally, hemicellulose is present within the full structure of the primary wall, probably interacting with cellulose, but its structural role is not yet clear (Figure 2.12) (Mollet et al., 2013).

In fungi, there is no distinction between primary and secondary wall, but often the wall is composed of at least two layers: the first is the structural "skeletal" part, close to the plasma membrane, representing the load bearing component of the wall, which resists turgor. The second is the external heterogeneous layer, which can be involved in specific physiology of the species (sensing, adhesion, host infection) (Gow et al., 2017).

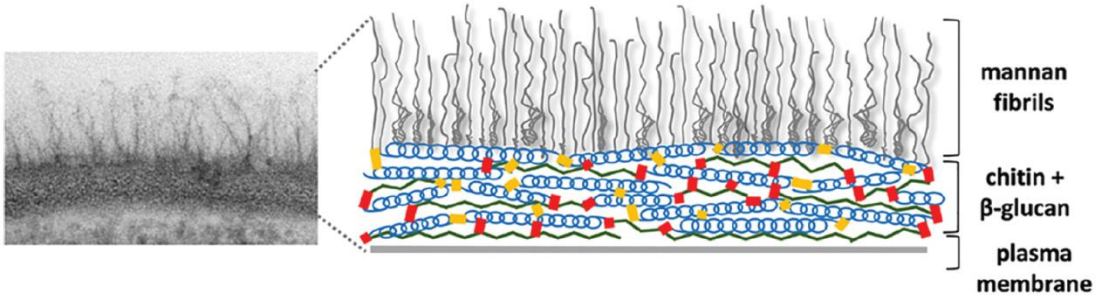

Figure 2.13. Transmission Electron micrograph and schematic of *Candida albicans* cell wall. Blue chains represent β-glucans, green chains chitin. Red and yellow squares are cross links. These together form the structural layer. Mannan fibrils correspond to the non-structural layer. Adapted from (Ene et al., 2015)

The components of the structural layer are mainly conserved within species: in all fungi, the major components are β-glucans, in general made of β-1-3 chains, with β-1-6 branches (Figure 2.10). Chitin (β-1-4-N-acetylglucosamine) is highly spread within fungi: when present, it normally creates the first structural layer above the plasma membrane, arranging in microfibrils that contribute to rigidity and integrity of walls. Chitin can cross-link with β-glucans in some species. α-glucans, normally α1-3, are present in many species, where they form an amorphous polymers that, in some cases, seem to be associated with correctly polarized growth (Beauvais et al., 2005). Many proteins are intercalated in the structural layer, but they should not have load bearing functions (Beauvais et al., 2005; Hochstenbach et al., 1998; Katayama et al., 1999). The outer layer is highly variable within species. Many glycoproteins decorate the surface of cell walls, often carrying the GlycosylPhosphatidylInositol (GPI) domain that tethers them to the wall matrix. Mannans, galactomannans, galactoxylomannans and other polysaccharides (depending on species) are bound to these proteins. This layer, non-structural, can have roles in protection from chemical agents, signaling, sensing, or can be functional to anchor the cell to substrata. (Figure 2.13) (Free, 2013; Gow et al., 2017). As in plants, distribution of wall components is different between apical and tubular parts of tip growing fungi. Staining with fluorescent markers specific for diverse wall components, such as calcofluor, are often distributed heterogeneously between tip and sides of both hyphae and rod shaped cells, suggesting already an uneven distribution of some of the components. This has been confirmed first by micro-dissection of hyphal tips and chemical characterization of wall compositions, which revealed a 2-4 fold decrease in chitin content in tubular parts, compared with apices, in three different filamentous fungi, *Basidiobolus ranarum*, *Neurospora crassa* and *Coprinus sterquilinus* (Kopecek and Raclavsky, 1999). Moreover, AFM studies on *Aspergillus*

nidulans, based on typical adhesion forces of chemical compounds, revealed that there are more unmodified β-glucans and chitins in apical tips than in mid hypha, while in mid hypha an increased amount of unidentifiable compounds where detected. The authors propose that these components can be rearranged in polymeric structures of glucans and chitins, conferring modified adhesion forces to these molecules (Lee et al., 2010). These differences in composition may reflect a process of wall maturation, and could be the basis of what drives differences in the mechanical properties discussed in 2.1.

In general, wall composition in each organism is extremely important for their physiological state. Perturbations in wall properties are often associated to defects in cell morphology, growth and more dramatically to cell integrity. I will discuss more deeply this aspect in the next paragraph, while introducing the machineries involved in wall synthesis.

2.1.2 Cell wall synthesis

We can classify enzymes involved in wall building into two classes, synthases and remodeling enzymes. Synthases are involved in the elongation of polysaccharides chains. Remodeling enzymes are involved in the modification of primary chains, allowing cross-links, branching or chain elongation due to the binding of two existing chains. Remodeling enzymes can also have a degrading function, cutting glycosidic links, removing monomers for the extremity of chains (exo-hydrolase), or splitting a chain from its inside (endo-hydrolase). All these enzymes exhibit high functional specificity in substrate and activity. Due to the difference in composition between plants and fungal cell walls, even the machineries of synthesis show several differences.

In plants, many wall components are synthesized in intracellular compartments, mainly in the Golgi. Here synthases, glucanosyl-transferases and other remodeling enzymes, first elongate and then sequentially modify glucan chains until they reach the final composition. Once assembled, these polymers are released in the cell wall matrix through exocytosis. This is the case for hemicellulose and pectins (Kim and Brandizzi, 2014; Oikawa et al., 2013; Wolf and Greiner, 2012). Pectins are delivered in esterified form, and are then de-esterified and cross-linked directly in the wall mesh, by pectin methyl-esterase (PME), being regulated by their inhibitors (PMEI) (Figure 2.12). Modifications of esterification levels in plants can be deleterious for pollen tubes: in *Arabidopsis thaliana*, deletions of pollen tube specific PME, *vgd1* and PME1, generates defects in pollen elongation with tip bursting events and consequently male fertility reduction, indicating that PME activity is necessary for cell integrity (Jiang et al., 2005; Tian et al., 2006).

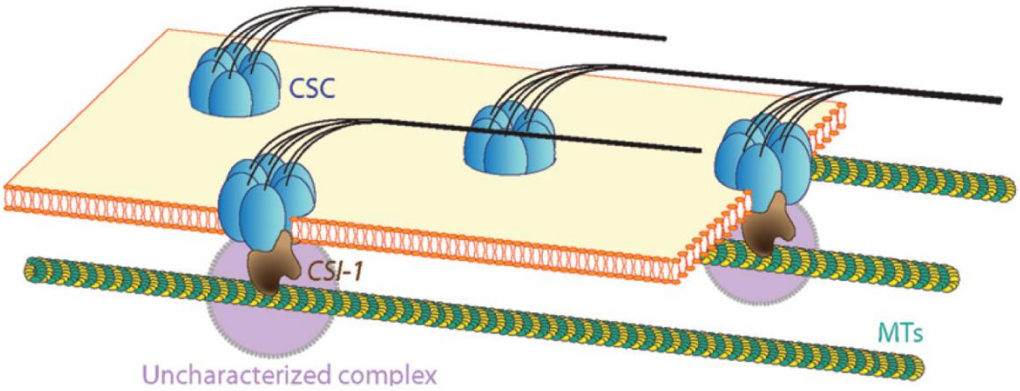

Figure 2.14. Exameric cellulose synthase complexes (CSCs), in the plasma membrane, elongate cellulose microfibrils (black), along cortical microtubule path, to whom they bind through CSI1 and maybe other linkers (pink circle) (Landrein and Hamant, 2013)

Cellulose synthase complexes (CSC) are formed in the ER as rosette-like structures, and delivered to the plasma membrane, where they can directly elongate cellulose fibrils within the wall mesh (Bashline et al., 2014; McFarlane et al., 2014). CSCs move along cortical microtubules, with which they can interact through linkers as CSI1 (and maybe others). Fibers are therefore deposited along microtubule paths that are normally perpendicular to the long axis of the cell (Figure 2.14) (Landrein and Hamant, 2013). Inhibition of CSCs by isoxaben causes tip swelling in conifer pollen tubes, while, more dramatically, inhibition by 2,6-Dichlorobenzonitrile causes pollen tubes and root hair to burst showing once more the importance of correct wall synthesis for cell integrity (Lazzaro et al., 2003; Park et al., 2011).

To allow for tip growth the direction of delivery and synthesis is carefully regulated. For example, in pollen tubes CSC are present only at the tip in primary walls, PME are distributed along the whole cell surface, while PMI are present only at growing tips (Ebine and Ueda, 2015; Mollet et al., 2013) (Figure 2.12). Furthermore, post-translational modifications of wall synthases and generation of protein complexes seem to play an important role for the regulation of these enzymes, but they are not yet very well described (Bashline et al., 2014; Oikawa et al., 2013).

Similar to cellulose synthase complexes, in fungi, synthases of wall structural components normally localize at the plasma membrane. Here, they elongate polymers by vectorial synthesis, which means that nascent chains are extruded in the wall matrix as they are fabricated. In tip growing cells, chitin, β-glucan and α-glucan synthases (when present in each species) bind to the membrane close to the growing apex. They can elongate linear glucan chains. As expected, this

activity is extremely important for both cell integrity and morphogenesis, and most of the genes involved in primary chain synthesis are essential (Gow et al., 2017).

Synthases are transported via exocytosis to the plasma membrane. They are supposed to be inactive, before they reach the plasma membrane, where they form a complex with activators that promote catalysis. β-glucan synthases activation has been thoroughly reported in several fungi: their activity is promoted by the RhoGTPase Rho1 and can therefore be modulated by Rho1 regulators (GAPs and GEFs). The direct regulation of other synthases, as well as of remodeling enzymes, is still not clear. In tip growing fungi, synthases and their regulators are polarized at the growing apex; defects in localization of the synthesis machinery can lead to defect in growth, integrity and morphology, and are often lethal (Bowman and Free, 2006; Latge and Beauvais, 2014; Perez and Rincón, 2010).

Glucanosyl-transferase proteins are wall remodelers, they can catalyze the elongation of β-glucan chains, by binding two shorter polymers. These enzymes are often not essential, but their deletion can cause aberrant phenotypes. For instance deletion of the β-(1,3)-Glucanosyl-transferases Gel1 in *Aspergillus fumigatus* causes abnormal elongation of Conidiophore, a tubular structures containing conidiospores, consequently decreasing virulence (Mouyna et al., 2005). Proteins involved in β-1-6 branching of β-glucans have not yet been described.

Very recent studies have revealed the existence of glucans-transglycosilases, part of the CRH family, involved in chitin-β-glucan cross links, in several fungal species. In *Candida albicans*, three CHR proteins, Utr2, Crh11, and Crh12, have been suggested to modulate wall elasticity, as AFM measurements show a three-fold decrease in Youngs modulus in the triple mutant. Moreover, the triple deletion causes an increase in wall fragility, as cells dramatically lyse under high osmotic treatment (Ene et al., 2015). However, the existence of other cross linkers is unclear.

Glycosil hydrolases (GHs) are another important class of enzymes, involved in wall digestion and remodeling in both plants and fungi. They catalyze the hydrolysis of glycosidic linkages between one or two carbohydrates and another molecule, therefore for wall synthesis they are thought to loosen the structure. Some GHs can also promote the remodeling of the cut chain, catalyzing linkages to other molecules, as to act, in this case, as a remodeler (some of the aforementioned transglycosilase are classified in this family). However here I will focus on enzymes that promote solely digestion. More than 100 families of GH have been described (CAZY, 2018), whom classification is based on substrate specificity.

Many GHs are expressed in pollen tubes, with specificity for almost all wall components, and some of them have been suggested to play important roles in tube elongation (Mollet et al., 2013). For instance, it has been reported that D-gluconolactone and nojirimycin, two GH inhibitors, impede lily pollen tube elongation, suggesting that active cell wall digestion is necessary to sustain tip growth (Kotake et al., 2000). The endo-β-1,4-glucanase *At*GH9C1, is instead important for root hair development in *Arabidopsis thaliana*. *At*GH9C1 is expressed both before hair initiation and during elongation, and a mutant that expresses very low levels of the protein show a dramatic decrease in root hair abundance (del Campillo et al., 2012). This suggests that GH may play role not only in elongation, but also in the initiation of polarized growth.

In fungi, the real importance of glucanases activity is sometimes difficult to assess, because they are highly redundant in the genome (at least 29 in *Aspergillus fumigatus*), and often, the mutation of a single gene does not create evident phenotypes, probably because of compensatory mechanisms (Mouyna et al., 2013). GH are often localized at the site of cell growth, but also at sites of growth initiation, like germinating spores tips and sites of branching, as ChiA, a chitinase of *Aspergillus nidulans* (Yamazaki et al., 2008). In *Candida albicans* β-glucanase activity is important for filamentous growth: the putative β-glucanase CAMP65 is required for hyphal growth, as the null mutant has defects in hyphae formation and consequently lower virulence (Sandini et al., 2007), while on the other hand ectopic administration of β−1,3-glucanase can induce filamentation (Xu et al., 2013). As expected, glucanases are also key enzymes in the process of wall "dissolution", as in septation, to allow for cell separation of fission yeast (better discussed in the next chapter) , or in cell fusions during mating in both budding and fission yeasts (Dudin et al., 2015). For instance in budding yeast, the double deletion of the putative β-glucanases Scw3 and Scw10 shows a decreased fusion efficiency (Cappellaro et al., 1998).

In walled cells, compensatory effects can occur if one or more synthase/remodelers are impaired genetically or chemically, probably due to the functional redundancy of these proteins and the action of stress-activated pathways. For instance, in *C. albicans* and *S. cerevisiae*, inhibition of β-glucan synthesis by Caspofungin, lead to increase of wall stiffness due to increase in chitin (Formosa et al., 2013). In *A. fumigatus* deletion of glucanosyl-transferase Gel1, involved in hyphal wall synthesis lead to expression of Gel7, anorther glucanosyl-transferase normally only involved in conidia development (Zhao et al., 2014).

After synthesis the wall is remodeled by turgor, and the ability to balance deposition with deformation is particularly evident in the phenomenon of "stored growth". Decreased turgor caused by hyper-osmotic stress, inhibits growth. It has been shown, both in plants and bacteria, that under certain circumstances, reestablishing the turgor after plasmolysis induces a period of rapid wall expansion during which the cell or tissue grows to the same size that it would have reached without turgor variation (Acevedo et al., 1971; Proseus and Boyer, 2008; Rojas et al., 2014). It has been suggested that this phenomenon relies on a reservoir of wall material being deposited during plasmolysis, effectively being stored for rapid expansion, after re-pressurization (Proseus and Boyer, 2008). Hence, in these cells the final structure of the cell wall relies on synthesis and deformation, but these two aspects can be in some cases separated.

2.1.3 Cell Wall Integrity pathway

Walled cells have the ability to modulate the wall properties, during physiological events such as growth, but also under external perturbation, such as pathogen infection, osmotic stress, or any chemical or mechanical stress that can damage the wall structure.

The Cell Wall Integrity pathway (CWI) is the principal signaling cascade involved in maintaining the functional integrity of the cell wall. In yeast and fungi, this pathway is well conserved and has

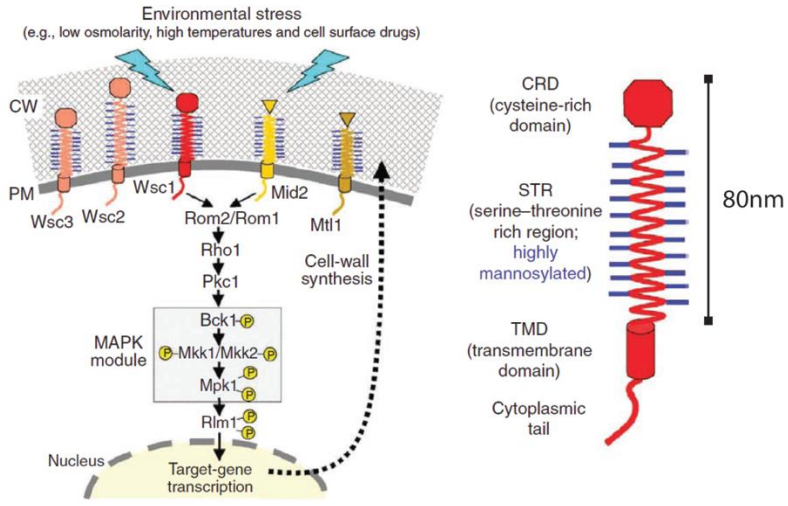

Figure 2.15. Cell Wall Integrity pathway in budding yeast. On the left the main molecular players in the cascade, stimulated by external stress (or physiological wall deformation as in growth), lead to the activation of the stress response. On the right, a schematic of Wsc1, with the STR domain represented as a nano-spring, extruding inside the wall for a theoretical maximum of 80 nm (Dupres et al., 2010). Adapted from (Heinisch et al., 2010a).

been carefully documented in several organisms such as *S. cerevisiae, S. pombe, Candida albicans, Aspergillus fumigatus, Cryptococcus neoformans* and others.

Activation of the signaling cascade starts from trans-wall sensors, which are involved in signaling. These have first been described in *S. cerevisiae* which possesses five different sensors: Wsc1-3, Mtl1 and Mid2. They all have in common a membrane domain with a small cytosolic tail, and a serine-threonine rich domain (STR domain), highly glycosylated, being embedded within the cell wall and having a putative rod like shape. In addition, WSC family presents a cysteine rich domain, which mediates clustering. AFM studies on Wsc1 in budding yeast, shows that the glycosylated STR domain confers a spring like behavior to the protein, suggesting that signals are perceived through mechano-sensing (Figure 2.15) (Dupres et al., 2009; Dupres et al., 2011; Heinisch et al., 2010a; Heinisch et al., 2010b). However, the nature of the signal that is sensed is still unclear (e. g. wall loosening, relaxation, tension).

The putative mechanosensors signal to GEFs, promoting the activation of Rho1 (Philip and Levin, 2001). This activates Protein kinase C that triggers a MAP kinase cascade. Downstream targets of this cascade are wall synthases, actin reorganization, exocyst components, all involved in wall repair or modification. (Figure 2.15) (Cruz et al., 2013; Dichtl et al., 2016; Hamann, 2015).

In plants, data supporting the existence of a CWI are very recent and the understanding of how this can work is still narrow, compared to fungi. In plants, there are no homologues of Wsc or of other sensors present in fungi. Instead, the Receptor Like Kinases (RLKs) are the suggested sensors. They are transmembrane proteins, with a cytosolic kinase domain, and an extracellular domain thought to bind the cell wall, having an affinity for sugars. An example are ANXUR proteins (Anx1-2) in *Arabidopsis thaliana.* The double mutation leads to cells bursting in pollen tubes, while overexpression causes growth inhibition, suggesting the importance of Anx regulation during normal growth (Boisson-Dernier et al., 2013). Other examples are THESEUS, suggested to be involved only after wall damage, and FERONIA, involved in cell elongation, root hair development, salt stress and other factors (Feng et al., 2018). Many responses are activated by these sensors, for example: wall remodeling, pH oscillations, osmotic adaptation, ROS accumulation (that possibly has a signaling role). Many sensors regulate one or more of these responses in different states of tissue development, making the interpretation of their effects more difficult.

To conclude, even in very similarly shaped cells, the biochemistry and the regulation of cell wall composition can be highly variable. However, some features seem to be conserved. For example,

several studies suggest diverse wall composition between tip and tubular extension in the same cell, whereby wall synthesis is confined to the growing apex, and the regulation of synthesis and repair seems to be carefully controlled by dedicated pathways that preserve cell integrity. This confirms the importance of the dynamic regulation in cell wall composition during the dangerous process of cell elongation. However, wall composition and its regulation are directly translated into mechanical properties of the cell wall and it is this structural composition that will ultimately influence shape and growth.

2.2 Influence of cell wall mechanics on morphogenesis and growth

How do cell wall dynamics and mechanics ultimately define cell shape and growth rate?

Many theoretical and experimental works attempted to answer this question. Some of these works focused purely on the mechanical properties of the cell. In Boudaoud, 2003, the author developed a model that considered only mechanical parameters. He explained variations in size in a wide range of cylindrical shaped cells, and predicted tip growth when turgor pressure driven wall remodeling was balanced by the bending of wall fibers (Boudaoud, 2003). Another work observed directions of wall deformation and incorporation, entailing a model that predicts the correct shape of a *S. pombe* under turgor pressure, starting from its plasmolyzed state, and can simulate the curvature change at tips during growth (Abenza et al., 2015).

The difference in composition between tubule and tip, described in pollen tubes (*Errore. L'origine riferimento non è stata trovata.*), together with the aforementioned measurements of asymmetries in wall mechanical properties (***2.1***) have inspired several works. Rojas and coworkers proposed a chemo-rheological model, based on the concept that cross-linked pectins are stiffer than free ones. Their model describes chemical reactions that predict wall loosening after deposition of new pectins in a discrete and stable zone of the tip. In fact, these new pectins are quickly de-esterified, leading to competition for the cross-link stabilizer Ca^{++}, between new and old pectins causing an overall softening of the structure and expansion. This is supported by observations that extracellular de-esterified pectins lead to growth rate increase in *Chara corallina* (Proseus and Boyer, 2006). They posited a negative feedback loop between expansion and new deposition to maintain an equilibrium (Figure 2.16). With this model, they could explain both oscillating and stable growth

in lily pollen tubes: tubes that grow with a mild velocity and have a balance between deposition and growth, while tubes that grow too quickly,

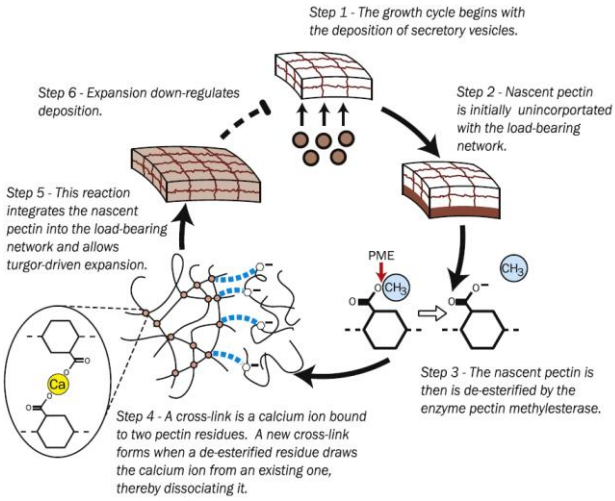

Figure 2.16. Chemo-rheological mechanism of tip growth in pollen tubes, based on pectin esterification and Ca^{++} stabilized cross-links (Rojas et al., 2011).

exhaust wall material deposition, leading to arrest until new material is deposited. Therefore, in this model the limiting factor for growth is new wall deposition. This model can also reproduce the variation in radius that is characteristic of oscillatory growth (Rojas et al., 2011). However, the pectin esterification model is specific to pollen tubes, while there is not direct evidence of similar chemical effects in other tip growing cell types.

In other works, the wall was modeled as a viscoplastic material, where the new wall being deposited at the tip of the cell "fluidizes" the structure, and only after deformation or modification (e. g. cross-links) undergoes a phase transition from a fluid to a gel-like elastic structure, allows for local growth. In these theoretical models, the authors included the effect of the size of the region of assembly that I will call polarity domain. They suggested a simple scaling law that links the radius of curvature of the tip (R_A) and the radius of the tubular part (R), with the size of the polarity domain (a):

$$\frac{R_A}{R} \sim \frac{a^2}{R^2}$$

By measuring simple geometrical parameters in phylogenetically distant organisms, they showed that many tip-growing organisms follow this scaling. In particular, in pollen tubes and filamentous

fungi *R* and R_A are very similar, leading to an almost perfect scaling between *a* and R (Figure 2.17) (Campàs and Mahadevan, 2009; Campas et al., 2012).

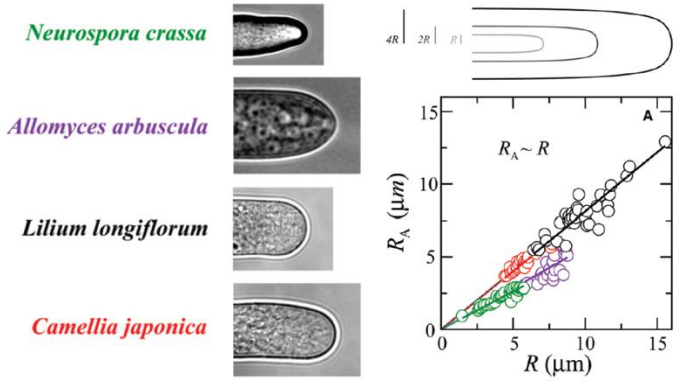

Figure 2.17. Tip scaling in various tip growing organisms. (Left) Typical images of fungal hypae from *Neurospora crassa* and *Allomyces arbuscula*, and pollen tubes from *Lilium longiflorum* and *Camelia japonica*. (Right) A schematic of shape scaling and plot of the measured parameters for the species on the left. Adapted from (Campas et al., 2012).

Direct measurements of polar domains in most of the tip growing cells are still missing.

Fission yeast is probably the best described tip-growing cell, and many experimental work probing the scaling between polar domain and cell radius have been performed in these cells. One can ask which marker is the best to follow wall deposition. In fact, the polar domain is comprised of proteins directly linked to wall assembly such as synthases, but also their regulators, then upstream machinery of secretion, and even more upstream RhoGTPAses involved in polarity establishment. The first works, in fission yeast, focused on the polar domain set by the active form of Cdc42, a small RhoGTPase considered as the master regulator of polarity (Chang and Martin, 2009), visualized by CRIB-GFP, where CRIB is a protein domain that selectively binds to Cdc42-GTP (Tatebe et al., 2008). The authors showed a good scaling between the width of CRIB-GFP and the diameter of wt cells, and having screened several mutants with defective Cdc42 activation and localization, coupled to diameter aberrations, where the scaling with CRIB domain was maintained (Das et al., 2012; Das et al., 2015; Kelly and Nurse, 2011b). More recently, in another work, by coupling the mechanical model described above to the size of polar domains defined by different components of the cap, the authors found that neither Cdc42 or its regulators, nor the wall synthases domains are reliable predictors of diameter establishment during growth. Experimentally they found that Cdc42 does not scale with the diameter of previously untested mutants, and that in one mutant (*pal1Δ*) Bgs4, the main glucan synthase in *S. pombe*, is completely delocalized. They

observed that this does not affect rod shape, but, in another work, the same mutation has been reported to cause morphogenetic defects (Ge et al., 2005). Instead, they report that the polar

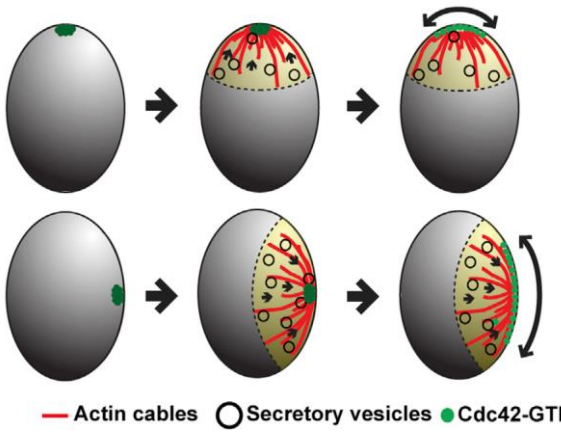

Figure 2.18. Model for the generation of a Cdc42-GTP polar cap, adapted to cell geometry, in fission yeast spores: An initial pool of Cdc42-GTP assemble for reaction diffusion. This lead to actin cables polymerization following the geometry of the spore. Polarized delivery of secretory vesicles enlarge the polar cap by a dilution mechanism (Bonazzi et al., 2015).

domains defined by the exocyst components Sec6, and Exo70, and by the SNARE Syb1, best predict cell geometry. Re-directing exocytosis to larger areas induces a proportional diameter change. Therefore, they propose that the size of the secretion zone defines cell diameter and suggest that this might be due to delivery of wall remodelers, which modify the wall structure after synthesis of linear chains (Abenza et al., 2015).

These last works described, suggest that the establishment of growth domain and of cell diameter are univocally due to the effect of polarized wall synthesis/secretion. However, other studies show that cell shape can affect the size of the polarity domain. In one work, carried out in *S. pombe*, cells have been confined in smaller diameters in microfluidic chambers and in this condition the active Cdc42 polar domain adapt to the new cell curvature. This has been more thoroughly investigated in germinating spores, where the polar domain assembles and disassembles several times before symmetry breaking and outgrowth, always adapting to the local curvature of the surface, in an actin dependent manner, suggesting an influence of cell shape on the size of polarity domain (Figure 2.18) (Bonazzi et al., 2015). Similarly, in plant tissues, cortical microtubule orientation directly influences the deposition of cellulose affecting morphogenesis, but in the same time, the final shape of the tissue creates stress patterns that influence microtubule orientation (Landrein and Hamant, 2013).

If both polarity domain and cell shape are affecting one another, this mutual influence entails a putative positive feedback between diameter and polarity that can lead to instability. Drake and coworkers proposed a theoretical model that considers mutual regulation between polar domain and cell shape in tip growing fission yeast. In this work, the authors first show, that a stable polarity cap can define a stable diameter. Then, they show that a small feedback from shape to cap size is needed, to promote corrections in the polarity domain, after perturbations or simple oscillations of polar components (Das et al., 2012). Through this mutual feedback, they could explain the maintenance of a stable diameter within generations. Interestingly, they show that if this positive feedback is too strong the cell will grow with smaller and smaller, or larger and larger, diameters if a perturbation causes a tiny diameter change in one or the other direction (Drake and Vavylonis, 2013). However, the mechanism maintaining feedback strength compatible with diameter homeostasis has not been described yet. Moreover, feedbacks between polarity domain and shape should pass through modifications of wall mechanical properties, to promote shape change and eventual elongation. However, so far, there are not direct measurements of wall mechanic changes related to these events.

Another important aspect is the balance between growth rate and wall assembly. In fact, as discussed before, the process of growth can be dangerous if these two aspects are not tightly regulated. Only very recently some works suggested the existence of coordination between rate of growth and wall mechanics/assembly. One study that shows how wall mechanics can regulate growth has been described in *S. pombe* spores, where the outer spore wall, a specialized structure probably conferring resistance to the spore envelope, hinders growth and destabilizes polarity, until the outer envelope ruptures allowing outgrowth (Bonazzi et al., 2014). More recently, in Banavar *et al.*, the authors developed a classical model of wall mechanics describing the generation of mating protrusions in *S. cerevisiae*, based on a shell with a constant thickness and variable viscosity (lower at the growing tip), inflated by turgor pressure that drives the rate of growth. To this end, they implemented the dynamics of cell wall assembly and observed that their model was unstable, leading to growth arrest or cell lysis, if growth and assembly were acting independently. They could solve this instability by including a negative feedback mechanism that senses cell wall strain rate and signals to wall assembly, modifying its elastic modulus. To test their model, they assayed deletion mutants of putative trans-wall mechanosensor, Wsc1. In this experimental setup they observed cell lysis, especially after hypo-osmotic treatment, and increasing turgor pressure, leading

to an increase of cell growth rate, thereby demonstrating the importance of the feedback. Interestingly, this feedback was found to be independent of cell shape, suggesting that shape determination and growth rate, are both dependent on wall mechanics, but do not seem to be regulated by the same mechanisms (Banavar et al., 2018).

Here, I summarized some of the most relevant works, comprising theoretical and experimental approaches carried to understand how cell wall mechanics influences growth and shape determination. They propose diverse and sometimes contrasting aspects of wall mechanics. Many works suggest a gradient in wall properties, with softer growing tips (Campàs and Mahadevan, 2009; Campas et al., 2012; Drake and Vavylonis, 2013; Rojas et al., 2011). Some works can explain rod shape and tip growth by focusing purely on mechanical wall parameters, showing the importance of wall mechanics in shape determination (Atilgan et al., 2015; Boudaoud, 2003). Other works implement the notion of molecular assembly, through the regulation of a polarity domain, to explain growth and radius establishment (Campas et al., 2012; Das et al., 2012; Das et al., 2015; Kelly and Nurse, 2011b). On the other side, cell shape is also influencing the size of the polarity domain, suggesting positive feedbacks between these cellular properties (Bonazzi et al., 2015; Drake and Vavylonis, 2013). Finally, other works suggest that only an interdependence between cell growth and wall assembly seems to stabilize cell growth (Banavar et al., 2018; Bonazzi et al., 2014; Rojas et al., 2011).

This reveals a picture of wall mechanics dynamically regulated at several levels, which at the same time is controlled by and controls shape establishment and growth rate. In this scenario, one cannot dismiss the effect of each element regulating the dynamics of tip elongation, from change in cell shape, to the dynamic of the molecular machinery assembling the wall, and the variation of wall mechanics itself. However, while some of these parameters have been observed dynamically (e. i. polar domain assembly), wall mechanics is often analyzed at single time points and considered as an almost static structure. One of the biggest limit in the reported models is that they neglect temporal variations of cell mechanical properties; moreover, they rely on parameters averaged at population scales which can mask the dynamic interplays between molecular players, cell mechanics and geometrical changes.

Chapter 3 – *Schizosaccharomyces pombe*, morphogenesis and growth

In this chapter, I introduce the model organism *Schizosaccharomyces pombe*, a precious tool for the study of complex cellular mechanisms, such as growth or shape generation in walled cells. I start with a quick historical overview of its use as a model organism, underlining the advantages of exploiting it to study tip growth. Then, I describe the different phases of fission yeast life cycle, characterized by relevant differences in morphology. Thereafter, I introduce the composition of the core polarity machinery assembled during polarized growth, and the general properties of *S. pombe* cell wall, including its composition, the synthesis machinery and its regulation. Finally, I provide a brief overview on the recently reported mean measurements of cell mechanical parameters.

Table of Contents

Chapter 3 – *Schizosaccharomyces pombe*, morphogenesis and growth 61
3.1 Different stages of fission yeast life cycle 64
3.2 Polarity machinery during tip elongation 68
3.3 Turgor regulation 73
3.4 Cell wall properties 74
3.1.1 Cell wall composition 74
3.1.2 Wall integrity pathway 77
3.5 Cell mechanics 79

Fission yeast *Schizosaccharomyces pombe* is an ascomycete, first isolated at the end of the XIX century from East African millet beer. It took its name from the Swahili term for beer.

S. pombe has been first used as a model organism in the 50s for genetic studies undertaken by Urs Leupold. Shortly after, Murdoch Mitchison decided to exploit it for physiological studies, in particular to study cell growth, for its simplicity. In fact, pombe is relatively easy to culture, with a rapid generation time (2-3 h). It is big enough for low resolution imaging and being a rod shape, that grows only by length until reaching an established size, makes geometrical calculations simple (Figure 3.1) (Mitchison, 1990). Since then, *S. pombe* has been widely used as a model to study cell biology and to address basic biological questions. Starting from the 70s, *S. pombe* has been largely used to study cell cycle regulation, and this work led to a Nobel Prize in Physiology or Medicine, awarded to Sir Paul M. Nurse, shared in 2001 with Tim Hunt and Leland H. Hartwell, "*for their discoveries in key regulators of the cell cycle*". Moreover, the genome of *S. pombe* has been fully sequenced in 2002 and it has been found to share several sequences with higher eukaryotes. It has 5123 genes on three chromosomes, and favors the haploid state in its cell cycle (Wood et al., 2002). Considering its wide use, several tools are available to study its cell biology, genetics, molecular biology and so on, making it a very suitable model organism to study diverse cellular processes (http://www-bcf.usc.edu/_forsburg/).

S. pombe is a rod shaped organism, with a stable diameter of 4 μm and a length between 8-14 μm. It grows by tip extension, targeting polarity components at the growing tips, where new wall material is synthetized. The polarity machinery is well characterized, together with the regulation of the cytoskeleton. Moreover, the stereotypical shape of fission yeast cells, eased the observation of morphogenetic mutants, from which many genes involved in shape

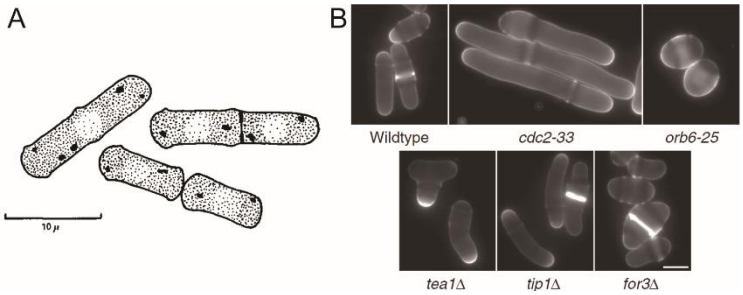

Figure 3.1. A. First drawing of *S. pombe* cells, from Mitchison, showing rod shape, septum (initially named "cell plate"), birth scars, lipid granules and nuclei (initially thought to be big vacuoles) (Mitchison, 1957, 1990). B. Calcofluor staining of wt and morphogenetic mutants of *S. pombe*, showing aberrant long, round, bent, T-shaped and dumpy shapes. Adapted from (Chang and Martin, 2009).

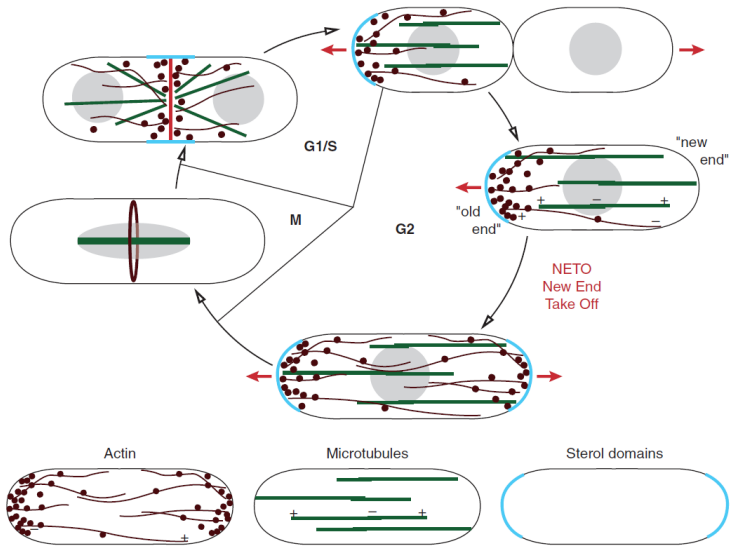

Figure 3.2. Typical cell cycle of S. pombe and distribution of cytoskeleton and lipid domains in each phase. Red arrows show sites of active growth. Below the distribution of cytoskeleton elements and specialized lipid domains adapted from (Chang and Martin, 2009)

establishment, but also wall synthesis, cytoskeleton regulation, growth, etc., have been described (Figure 3.1B).

S. pombe, is, so far, the best described tip growing cell. Thanks to its stereotypical shape and mode of growth, as well as its well described growth machinery, and to the availability of tools to perform imaging and genetics, fission yeast is an extremely powerful organism to study the link between cell wall mechanics, assembly, and its role in the regulation of morphogenesis and growth.

In the next part of this chapter, I first explore the different stages of *S. pombe* life cycle; after I describe in details the polarity machinery, involved in polarized growth; I then focus on the mechanisms controlling turgor pressure, then I will further describe more specific properties of *S. pombe* cell wall, from its composition to its synthesis and regulation. Finally, I report on recent progress for the estimation of cell mechanical properties, which have been used to develop predictions on how cell mechanics translates into shape and growth.

3.1 Different stages of fission yeast life cycle

Fission yeast has been described by Richard Egel as "eukaryotic life in a nutshell - simple enough to propagate as free-living, non-motile cells, yet able to differentiate to resting stages and/or sexual reproduction" (Egel, 2004). In fact, as discussed for other walled cells, during its life cycle, fission

yeast can differentiate in specialized structures, morphologically diverse, according to external stimuli.

During vegetative growth, haploid *S. pombe* cells grow by tip elongation and divide medially by fission (Figure 3.1A and Figure 3.2). Immediately after division, the cell starts to grow from the old end, the extremity inherited by the mother cell. Once the cell has reached a certain length it starts to grow simultaneously from the extremity generated during the last division, in a process named "New End Take Off" (NETO), finishing growth in a bipolar fashion. During active tip growth, polarity domains, cytoskeleton components and specialized lipid domains, are directed to the growing pole (or poles after NETO). In mitosis, growth is arrested at a final length of about 14 μm, and at the end of mitosis the growth machinery moves to cell center, to direct cell division and septation. Once septation is accomplished the polarity machinery moves to the old end, restarting the cycle (Figure 3.2) (Chang and Martin, 2009).

Upon nitrogen starvation, haploid cells enter in stationary phase and if cells of the opposite mating type are present, h^+ and h^- in *S. pombe*, they can sense their mating partners through release of pheromones and corresponding receptor. Mating partners grow towards each other until they fuse, after the activation of a signaling pathway that will be described in the next paragraph. After karyogamy, that is nuclear fusion, the diploid cell often undergoes meiosis and produces 4 round haploid spores (also called ascospores) encapsulated in a bean-shaped ascus (Figure 3.3). While the external ascus structure is inherited from previous wall of the two fusing cells, the surface of the spores is de novo synthesized. Spores can be dormant for a long time and resist harsh environmental conditions. Under favorable nutrient conditions spores can germinate, and by breaking the symmetry of the spherical spore, they generate new rod shaped vegetative cells.

However, the diploid can grow in a vegetative cycle if nutrient conditions are quickly restored after cell fusion. These cells are normally larger than haploids, 20/25 μm long at cell division with a diameter up to 5μm. Upon starvation, the diploid rapidly enters meiosis and sporulates.

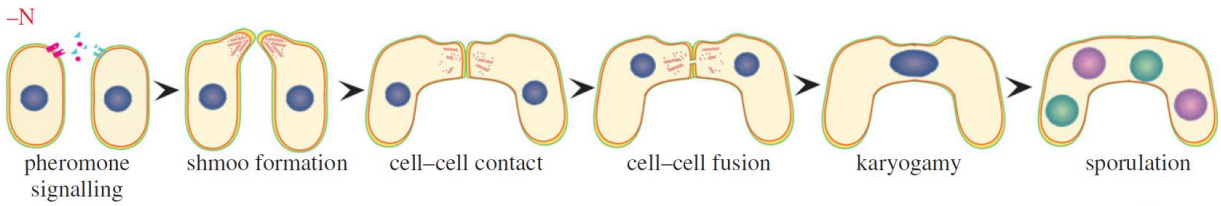

Figure 3.3. Sequential steps during mating in S. pombe. Cells undergo dramatic rearrangements of their surface, first growing towards each other, then fusing. Finally spores are generated, whom surface is totally de novo generated (Merlini et al., 2013).

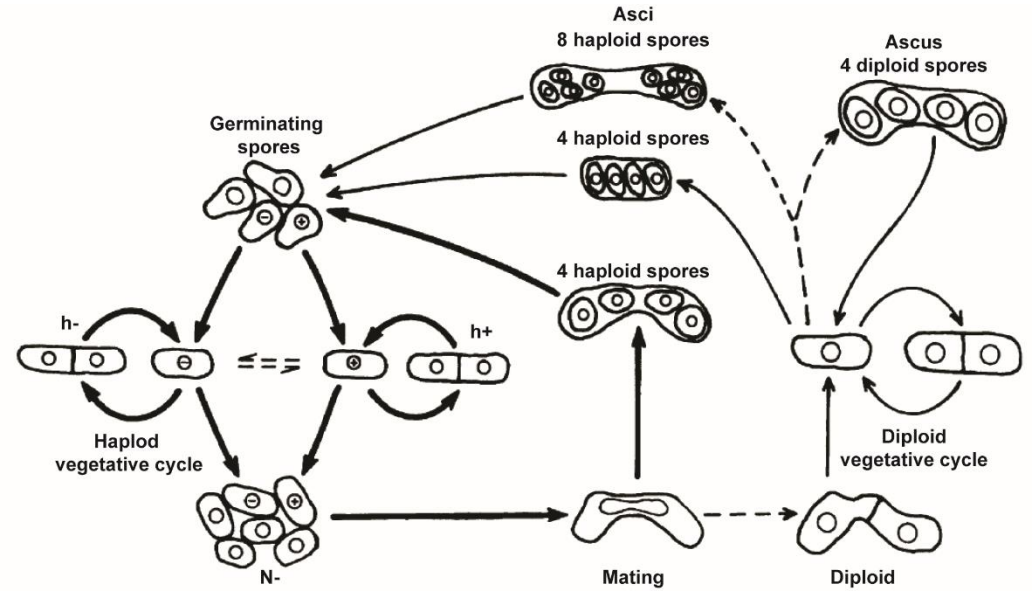

Figure 3.4. The life cycle of fission yeast. Vegetative cells can undergo cycles of cell division until, after nitrogen starvation, if the two mating types coexist, they mate, fuse and create diploid cells. Those can generate spores, which will germinate under favorable conditions, generating new vegetative cells. Otherwise, the diploid can undergo vegetative cycles, sporulating as soon as it withstands starvation. More rarely diploid cells can mate, generating large asci with either 4 diploid spores or eventually 8 haploid spores if karyogamy does not occur. Heavy arrows indicate events that are more common, while dashed lines delineate more rare events. Adapted from (Egel, 2004).

Depending on mating types, diploids can mate again, creating a tetraploid cell, which can generate an ascus of 4 diploid spores, or, if karyogamy does not happen, 8 haploid spores (Figure 3.4) (Egel, 2004).

If cells undergo nutrient starvation, and are not in the presence of mating partners, they stop proliferating and enter into a quiescent state. In this state, cells undergo several rounds of cell division, without relevant elongation, resulting in very short cells, almost rounded, that can resist harmful external conditions. After nutrient supply, these small cells can restart to elongate as normal vegetative cells. Interestingly, despite the almost non polar shape acquired, these cells elongate from the tips originated by previous cell divisions (Figure 3.5) (Laporte et al., 2015; Sajiki et al., 2009).

Although not exactly physiological, another interesting morphological change in fission yeast is the recovery of protoplasts after wall removal by enzymatic treatment. Protoplasts are isotropic spherical cells only surrounded by their plasma membrane. To balance turgor pressure, they can be kept alive under osmotic support (e.i. in media containing high solution of osmolytes). In this

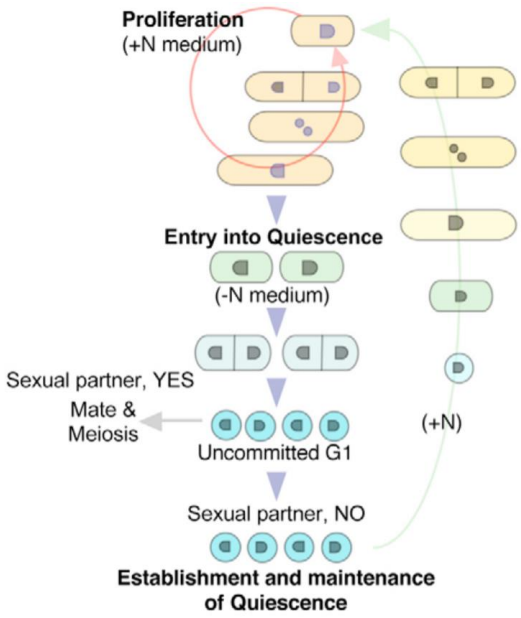

Figure 3.5. Entry into quiescent state after nitrogen starvation. Upon starvation, cells can undergo mating if mating partners are present, but they enter in quiescence otherwise. Supply of nitrogen restore elongation end cells enter again in vegetative state (Sajiki et al., 2009).

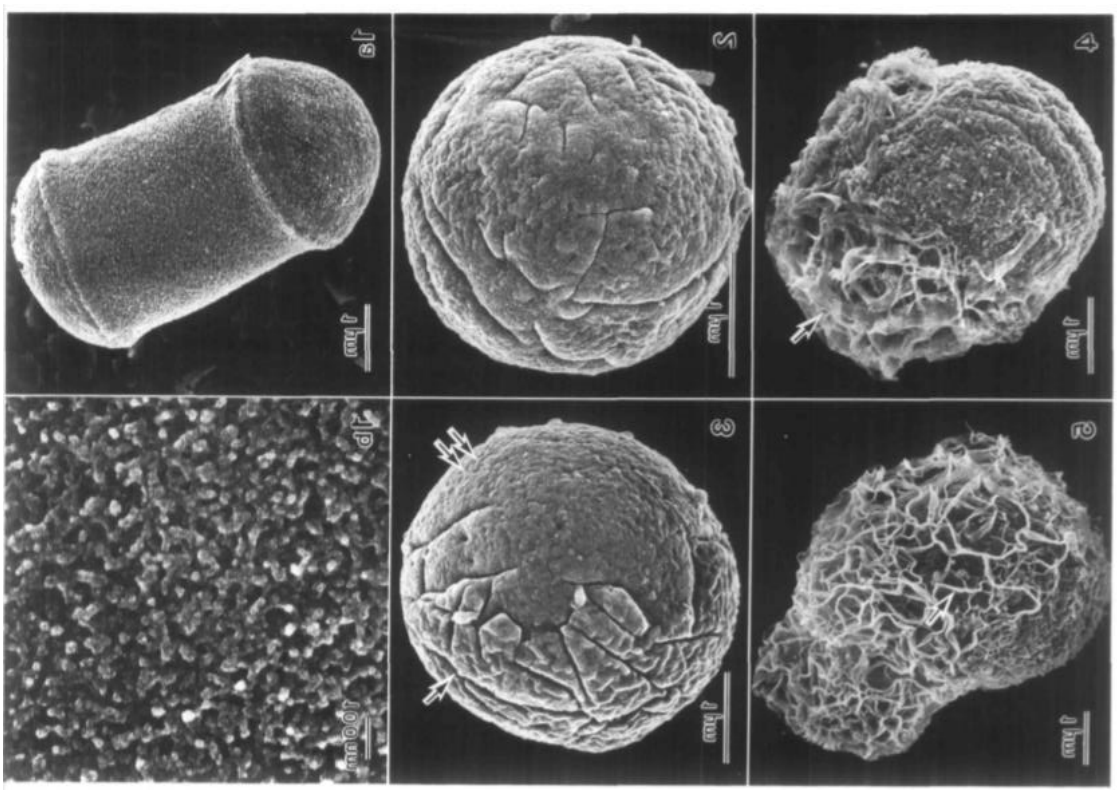

Figure 3.6. Protoplast regeneration. Scanning electron micrographs of S. pombe of (top left) a full cell and (bottom left) a detail of its surface. (Center top) A naked protoplast, and after 10 min (center bottom), 1.5 h (right top) and 3h (right bottom) in recovery (Osumi et al., 1989).

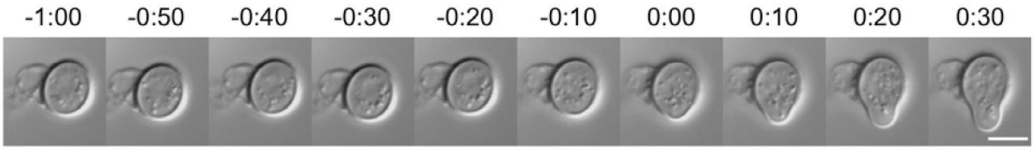

Figure 3.7. Recovery of protoplast Time-lapse images of a single recovering spheroplast forming a growth zone. From this polarized zonea new vegetative cell will be originated.. Time is in hours:minutes from spheroplast polarization. All scale bars represent 5 μm (Kelly and Nurse, 2011a).

condition, they can generate cell wall *de novo* that first covers the full cell surface and after originate a polarized protrusion, as in spores, from which new vegetative cells are generated (Figure 3.6, Figure 3.7) (Kelly and Nurse, 2011a; Osumi et al., 1989)

3.2 Polarity machinery during tip elongation

Here I discuss the molecular machineries involved in polar growth of *S. pombe*, focusing on two processes of polarized elongation in this organism: tip elongation during the vegetative cycle and growth of projections directed toward partner cells during mating.

During polarized growth, actin is organized in two main structures, actin cables and actin patches. Cables are long bundles of actin filaments, whose elongation is promoted by nucleators, such as formins. During growth they are polymerized from growing tips and elongate inward. They act as tracks for MyoV-based delivery of cargos. Actin patches are dendritic networks of branched actin filaments, nucleated by the Arp2/3 complex, involved in clathrin mediated endocytosis. During tip elongation actin patches are localized to growing tips (Figure 3.2) (Mishra et al., 2014).

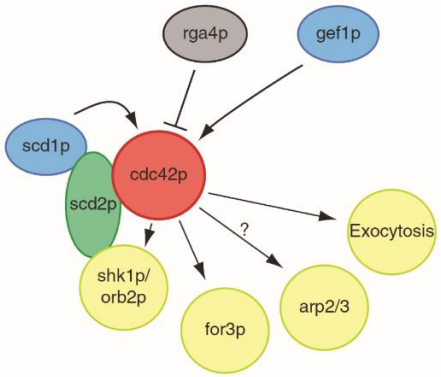

Figure 3.8. Cdc42 module, with its regulators and some effectors. Adapted from (Chang and Martin, 2009; Mishra et al., 2014).

The small RhoGTPase Cdc42 is considered as the master regulator of polarity in *S. pombe.* In this organism, Cdc42 is essential for viability, and defects in its expression or activation cause major defects in polarity, causing isotropic growth and loss of polar shape. Two GEFs of Cdc42, Scd1 (associating through its scaffold Sdc2) and Gef1 are involved in Cdc42 activation, and 3 GAPs, Rga4, Rga3 and Rga6 are involved in its inhibition (Chang and Martin, 2009; Gallo Castro and Martin, 2018; Perez and Rincón, 2010).

During vegetative growth, localization of Cdc42 regulators affects the localization of its active form, and deletions of some of the regulators, such as Scd1/2 and Rga4, cause defects in cell diameter, together with defects in Cdc42-GTP localization. This suggests a link between Cdc42 active domain and morphogenesis, and some works have shown a direct correlation between the size of active Cdc42 polar domain and cell diameter (Das et al., 2012; Das et al., 2015; Kelly and Nurse, 2011b). However, other mutants with defective diameter may not show the same correlation (Abenza et al., 2015). Therefore, despite its unmistakable importance in establishing polar domains and polarized shape, Cdc42 is probably not the only direct link between polarity and cell diameter establishment. Once activated, Cdc42 can interact with CRIB domain containing proteins, such as PAK proteins, and activate a series of effectors. One is the formin For3, an actin nucleator responsible for actin filament polymerization during vegetative growth, which is constitutively auto-inhibited. Cdc42-GTP, together with Bud6, another formin-binding protein, promotes For3 auto-inhibition release. Activated For3 localizes at cell tips, where it can nucleate actin filaments, promoting polarized delivery of secretory vesicles (Martin et al., 2007). Cdc42 is suggested to also activate endocytosis, by the Arp2/3 complex, although there is no direct evidence of mediators of this interaction. Cdc42 can also regulate polarized exocytosis, through its direct effectors Sec3 and Exo70, promoting further delivery of vesicles. Importantly, vesicle delivery can be independent of actin/MyoV mediated transport (Bendezu and Martin, 2010; Bendezu et al., 2012). We must note that secretion and exocytosis are directly linked to wall remodeling, since they are involved in the delivery and recycling of wall synthases and remodeling enzymes. Other effectors of Cdc42 are kinases, such as the NDR kinase Orb6, involved in Cdc42 spatial localization and membrane anchoring, and the PAK-related kinase Shk1/Orb2 that creates a complex with Cdc42 and Scd1 through the scaffold Scd2, a mechanism that enhances Cdc42 activation (Figure 3.8, Paragraph **1.2.2**) (Das et al., 2009; Martin, 2015).

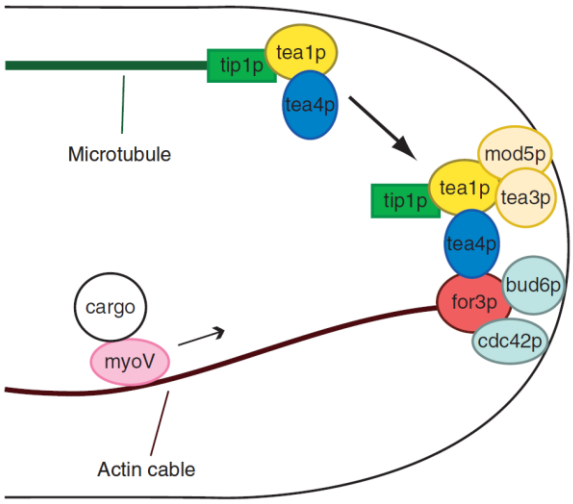

Figure 3.9. Model for microtubule mediated Tea1 complex delivery to cell tip and recruitments of For3, promoting actin nucleation and polarized cargos delivery. Adapted from (Chang and Martin, 2009)

Cdc42 is thought to polarize through positive feedbacks, where Cdc42 initially accumulates in small membrane areas by reaction diffusion. There, it can activate actin cable assembly, vesicle delivery and endocytosis, all processes that promote further delivery and recycling of Cdc42 and its regulators (paragraph **1.2.2**) (Martin, 2015).

As described in the previous chapter (***2.4***), the final size of a polar domain scales with the geometry of the cell (Bonazzi et al., 2015). This last observation, together with those previously mentioned (Das et al., 2012; Das et al., 2015; Kelly and Nurse, 2011b), shows that there is a positive feedback between polarity domain distribution and cell geometry, that has been suggested to stabilize diameter size over generations (Drake and Vavylonis, 2013).

During tip growth, microtubules are not essential to create polarity domains, but they do regulate polarity by promoting the delivery of important markers acting as spatial cues for polarity establishment. They are organized in bundles, oriented along the long axis of the cell, attached to the nuclear envelope. They scan continuously the tip of the growing cell, where they deliver a complex composed of Tip1 (CLIP170), bound to Tea1 that binds Tea4, and Tea1 is linked to cell cortex through at least Mod5 and Tea3. Tea4 binds to the actin nucleator For3 promoting its Myo5 dependent cargos delivery of growth machinery (Figure 3.9). The TEA complex is suggested to control NETO, as mutants in the complex often exhibit monopolar growth. Defects in microtubules also lead to defects in the orientation of the polarity domain, generating bent or T-shaped cells. Interestingly, microtubules rearrange quickly in cells forced into bent shape inside microwells,

showing once more cross-talks between polarity components and cell shape (Chang and Martin, 2009; Martin and Arkowitz, 2014; Martin et al., 2005; Minc et al., 2009b).

As previously mentioned, during growth arrest in mitosis the polarity machinery is detached from growing tips and many of the components are recruited to the cell center, where they direct cell division and septation (Figure 3.2).

During mating, polarized growth shares some of the polarity components with vegetative elongation, but with some profound differences, one of the most important is that polarity establishment is directed by an external cue, and mediated by a dedicated signaling pathway. As a response to nitrogen starvation, cells activate the transcription factor Sty11, which activates the production of both pheromone and pheromone receptors (Otsubo and Yamamoto, 2012). The two pheromones, P-factor (*h*+ cells) and M-factor (*h*- cells), bind to their respective receptors, Mam2 and Map3, expressed in cells of the opposing mating type. Both receptors activate Gpa1, the α-subunit of a G-protein, whom β and γ partners are still unknown (Obara et al., 1991). Gpa1 activates the Byr2-Byr1-Spk1 MAP kinase cascade, a signaling pathway specific for mating, probably through activation of Ste4, a protein binding Byr2 essential for mating. Interestingly Spk1 activates Sty11 promoting a positive feedback loop that is proposed to reinforce the mating response (Merlini et al., 2013). Byr2 activation is also promoted by Ras1 and Ras1 GEF Ste6. Since both Ras1 and Ste4 are essential for sexual differentiation they may cooperate for Byr2 activation. Another activator of Byr2 is the PAK protein Shk1, a substrate of Cdc42 that is, therefore, suggested to be involved in the activation of this cascade (Figure 3.10) (Tu et al., 1997).

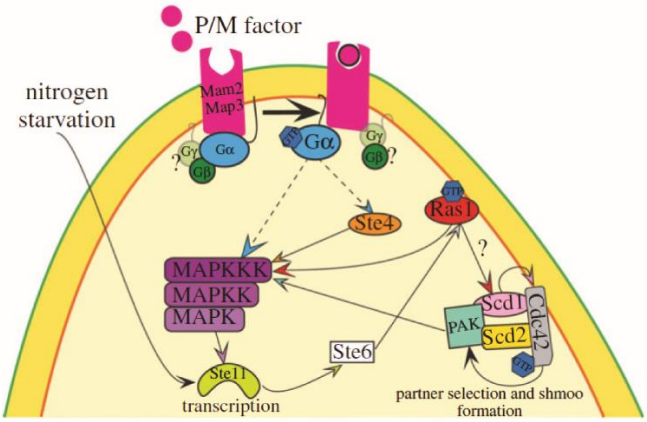

Figure 3.10. Mating signaling cascade activated by nitrogen starvation. MAPKKK is Byr2, MAPKK is Byr1, MAPK is Spk1. Adapted from (Merlini et al., 2013).

After the activation of the mating response, an active Cdc42 domain scans the cell surface, until it stably localizes at the new protruding tip. During random exploration, Cdc42 moves in concert with Scd1 and Scd2, while wall synthases, required for elongation, are retained in the endomembranes until the growth domain is stabilized. Cdc42 exploration is important for partner selection, constitutively active pheromone signaling induces a default choice for growth at cell poles, increasing events of mating between sister cells (Bendezu and Martin, 2013).

After partner cells contact, they undergo fusion, a process particular to mating in fission yeast. Cell fusion goes through erosion of tip cell walls, but the surrounding wall must be protected to prevent cell lysis. Actin is required for this process, as its de-polymerization through LatrunculinA highly decreases fusion efficiency. Fus1, a fusion specific formin, nucleates a very focalized actin structure called actin aster, which is made of short actin filaments. Type V myosin transport several wall hydrolases through this aster, in order to create a focus point of wall digestion. Wall synthases do not localize to this focus (Figure 3.11). Deletion in Fus1, MyoV and hydrolases causes defects in fusion efficiency, including cell lysis, showing the importance of the controlled and extremely polarized wall digestion (Dudin et al., 2015). Moreover, Ras1 activation is down regulated during fusion by recruitment of its GAP, Gap1. Constitutive activation of Ras1 leads to fusion focus stabilization independent of partners pairing, resulting in cell lysis. This suggests that a negative feedback controls the coupling between cell pairing and fusion (Merlini et al., 2018).

To conclude, here I summarized an overview of the polarity machineries involved in tip elongation in fission yeast. These machineries are highly controlled to allow the correct balance between wall

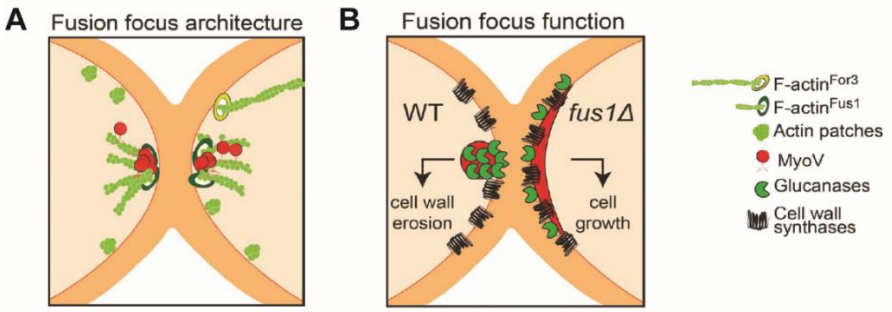

Figure 3.11. Fusion focus structure and function. (A) Fus1 elongates short filaments that form fusion focus, for MyoV delivery. (B) Correct focus architecture allow right distribution of synthases and hydrolases (glucanases), to accomplish wall erosion. Deletion of fus1 causes a different distribution of remodeling enzymes that reminds the distribution in cell growth, with consequent inability in fusion commitment. Adapted from (Dudin et al., 2015)

synthesis, remodeling and growth. Any mistake in this regulation can be deleterious for the cell, leading to aberrant shapes, inability to perform sexual differentiation, or more dramatically, cell lysis.

3.3 Turgor regulation

As discussed for other walled cells (***2.2***), in fission yeast, turgor pressure is regulated via dedicated pathways, described mainly as stress response after hyper or hypo osmotic treatments. The response to hyper-osmotic stress is regulated by the Sty1 MAP Kinase cascade, where Sty1 is the homologue of the budding yeast Hog1. This cascade is coordinated by Mcs4, which forms a complex with the two MAPKKK Wis4 and Win1. The complex binds constitutively the MAPKK Wis1. Under hyper-osmotic stress Wis1 is phosphorylated, unbinds from the complex and activates Sty1. This protein moves to the nucleus to activate the transcription factor Atf1, which regulates the transcription of several responsive genes. Among them, *gpd1* and *gpd2*, coding for glycerol-3-phosphate dehydrogenases, which promotes glycerol synthesis, and the repression of genes involved in the degradation and translocation of sugars to compensate osmotic imbalance and

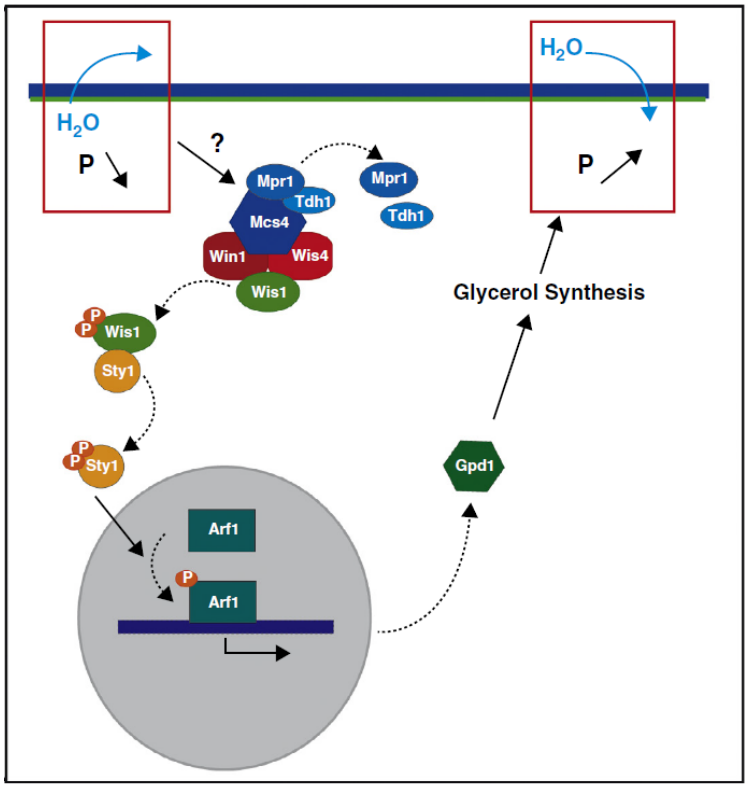

Figure 3.12. Signaling cascade involved in hyper osmotic stress response in fission yeast (Davì and Minc, 2015).

restore turgor and adaptation to the new osmotic condition. Despite this signaling cascade being well described, upstream sensors that function as triggers for this response are still unknown in fission yeast (Figure 3.12) (Davì and Minc, 2015).

Hypo osmotic response is admittedly less understood. However, as in other fungi, hypo-osmotic stress activates the cell wall integrity pathway, while ER localized putative sensors seem to mediate cytosolic calcium increase (Nakayama et al., 2014; Nakayama and Iida, 2014).

3.4 Cell wall properties

3.4.1 Cell wall composition

As for other fungi, the main component of the fission yeast cell wall is β-glucan, which constitutes 48-54% of the total polysaccharides. This fraction is composed of (1-3) β-D-Glucan, with 2-4% of (1-6) β-branches, linear (1-6) β-D-glucans and (1-6) β-D-glucans with (1-3) β-branches (Humbel et al., 2001). 7% of the wall is composed of α-glucans, composed of linear (1-3) α-D-Glucan, with 2-4% of (1-4) α-bonds. Those are the structural components of the wall in vegetative cells and they form a dense framework. Chitin is not present in vegetative cells. Many non-structural glycoproteins are embedded in the polysaccharide mesh, normally bound to α-galactomannan, a non-structural polymer that constitutes 9-14% of the wall (Perez and Ribas, 2004).

Transmission electron microscopy reveals a three layered structure, with a non-electron dense layer, surrounded by two electron dense layers. The central layer is the structural one, mainly composed of glucans. The electron dense layers are rich in α-galactomannan and glycoproteins (Horisberger and Rouvet-Vauthey, 1985; Perez and Ribas, 2004).

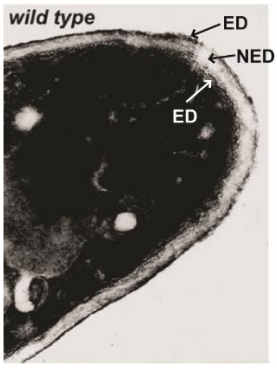

Figure 3.13 Transmission Electron Microscopy of *S. pombe* wild type cells, showing the two electron dense (ED) and the structural non electron dense (NED) layers of the cell wall. Adapted from (Perez and Ribas, 2004)

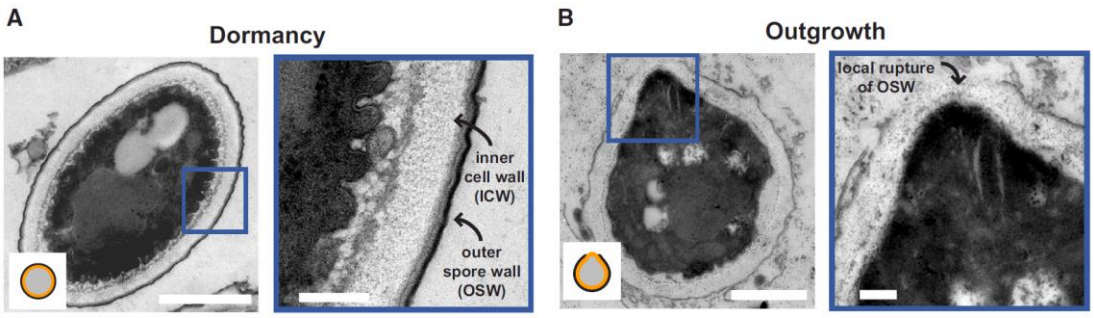

Figure 3.14. Transmission electron micrograph of fission yeast ascospores. (A) Spore in dormancy covered by inner and outer cell wall. (B) spore outgrowth occurs with a local rupture of the outer cell wall (Bonazzi et al., 2014).

Wall composition can be different in other stages of the cell cycle. During cell division, for instance, the septum is assembled at cell center, in order to physically divide the two sister cells. It is composed of a primary septum flanked by two secondary septa. The secondary septa will become the surfaces of the new tips in the nascent cells, while the primary septum must be digested to allow for cell separation. While secondary septa have a composition similar to the rest of the vegetative wall, the primary septum presents a high abundance of linear (1-3)-β-D-Glucan (not branched), a polymer not detected by immunogold labeling in other parts of the wall (Humbel et al., 2001).

A putative unique wall composition is that of ascospores. These are positive to wheat germ agglutinin staining, a lectin that binds to N-acetylglucosamine, a subunit of chitin and chitosan, suggesting that their surface may be reinforced by one of these polymers. The existence of a dedicated set of enzymes (as discussed in the next paragraph), most of which are expressed only during ascospore wall formation (Davì and Minc, 2015), suggest a diverse composition of wall material, although this has not been analyzed and quantified, so far. In support of this, transmission electron microscopy has revealed the presence of an outer electron dense layer, covering the wall structure (Figure 3.14). This outer spore wall features extreme mechanical properties, and has been suggested to have a Young's elastic modulus 30 times higher than the vegetative cell wall (Bonazzi et al., 2014).

At any stage of fission yeast life cycle, defects in wall composition, most likely translated in defects in wall mechanical properties, are associated with defects in morphology and can be lethal, as described in the following paragraph (Figure 3.15).

3.4.2 Cell wall synthesis

During polarized growth, several proteins involved in wall synthesis localize to the growing pole (or poles). *S.pombe* contains four different β-(1,3)glucan synthase (Bgs) proteins, Bgs1-4. Bgs2 is

expressed only during the sexual cycle and is essential for sporulation (Martin et al., 2000). The other three are essential and expressed during vegetative growth. They are all involved in septum formation, therefore defects in their synthesis or expressions are often linked to abnormal cell separation or cell lysis during cell division. However, they also localize to the tips of growing cells, showing their involvement in cell elongation. Bgs4 is the best described β-(1,3) glucan synthase during interphase, at the tip of the cell, where it can be activated by Rho1, producing linear chains of (1-3) β-D-Glucan, backbone for further branching and elongation activity. Decreased expression of these proteins, obtained with shut-off alleles, causes wall thinning at cell tips with consequent cell lysis in interphase (Figure 3.15 left) (Cortes, 2002; Cortés et al., 2005; Martin et al., 2003; Muñoz et al., 2013).

There are five genes coding for α-glucan synthases, *mok1/ags1* and *mok11-14*. *mok11* is not yet characterized. The last three are involved in sporulation (Garcia et al., 2006). Mok1/Ags1 is expressed during vegetative growth, localizes to growing tips, and is an essential protein. Decreased expression, obtained with shut-off alleles, causes huge defects in morphogenesis, leading to rounded or pear shaped cells, whose walls appear thicker. These cells also lyse, but this phenotype can be partially rescued by adding an osmotic stabilizer, suggesting that, despite the increase in thickness, the wall has lost its ability to maintain cell integrity (Figure 3.15 right). α-glucan synthesis seems to be controlled by Rho2, through the kinase Pck2 (Calonge et al., 2000; Garcia et al., 2006; Hochstenbach et al., 1998; Katayama et al., 1999).

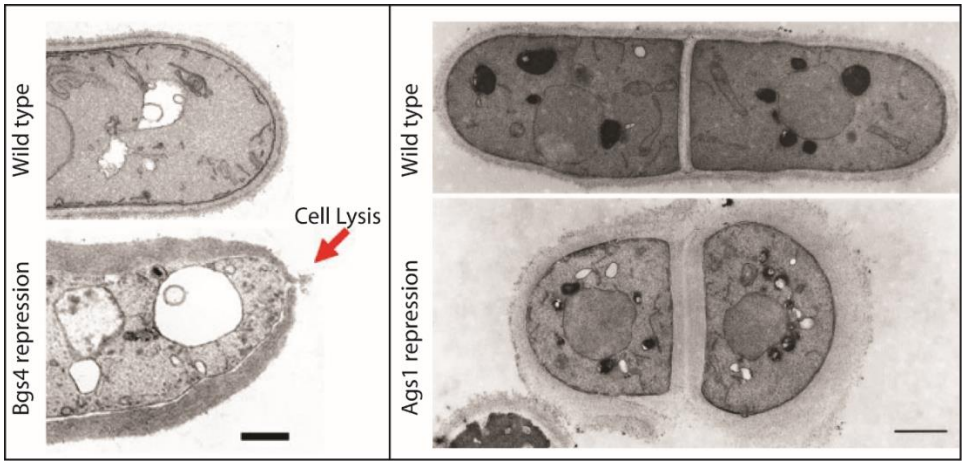

Figure 3.15. Cell wall defects after essential glucan synthases repression. Transmission Electron Microscopy of: (left) wall at old end in wild type cells or after 8 hours of repression of Bgs4. (right) full cell wall in wild type or after 10h repression of Ags1/Mok1. Adapted from (Hochstenbach et al., 1998; Muñoz et al., 2013).

S. pombe possesses four genes encoding for β-(1,3)glucanosyl-transferases: *gas1*, *gas2*, *gas4* and *gas5*, part of the GH72 family. Gas4 is expressed only in sporulation and is essential for ascospore wall maturation (de Medina-Redondo et al., 2008). The other three are expressed during vegetative growth. Gas1 and Gas2 localize to the cell periphery, with some accumulation at tips, and at cell center during septation. The localization of Gas5 is unclear. They have specific β-(1,3)glucanosyl-transferases activities, each one has a higher specificity for epitopes of different size. Only the deletion of Gas1 is lethal and can be rescued by osmotic stabilization. Cells released in normal media acquire a swollen shape, and undergo lysis, showing that β-(1,3)glucanosyl-transferase activity is essential for cell morphogenesis, wall integrity and cell viability (de Medina-Redondo et al., 2010).

Only one glycosil-hydrolase, Exg2, has been reported to be localized at cell tips during cell elongation. However, its activity was not clear in *in-vitro* assays, moreover its deletion does not cause visible phenotype and its overexpression causes wall thickening, even without the putative catalytic subunit (Duenas-Santero et al., 2010). Several other hydrolases are involved in other processes. The primary septum is digested by the endoglucanases Eng1, Exg1 and Agn1 to complete cell separation. Lack of those proteins causes incomplete cell division and generation of multiseptated cells (Dekker, 2004; Duenas-Santero et al., 2010; Martin-Cuadrado, 2003). A large set of exo and endoglucanases are recruited to the fusion focus and required for fusion (Dudin et al., 2015). Endoglucanases, like Eng2 and Agn1, are required for ascus wall digestion and spore release, to allow for ascospore dispersal (Dekker et al., 2007; Encinar del Dedo et al., 2009). Wall hydrolases are supposed to also modulate spore germination, in order to loosen the extremely resistant wall structure of the spore, but this aspect has not yet been investigated.

3.4.3 Wall integrity pathway

Disentangling the cell wall integrity pathway in fission yeast is complicated, since many components have more than one homologue and often exhibit promiscuous activity, activating more than one downstream partner. Here I report on the current understanding of the cascade (Figure 3.16).

At the core of the pathway are the two RhoGTPases, Rho1 and Rho2. Rho1, which has been characterized to a greater extent, is essential. It can directly activate β-(1,3) glucan synthases, or

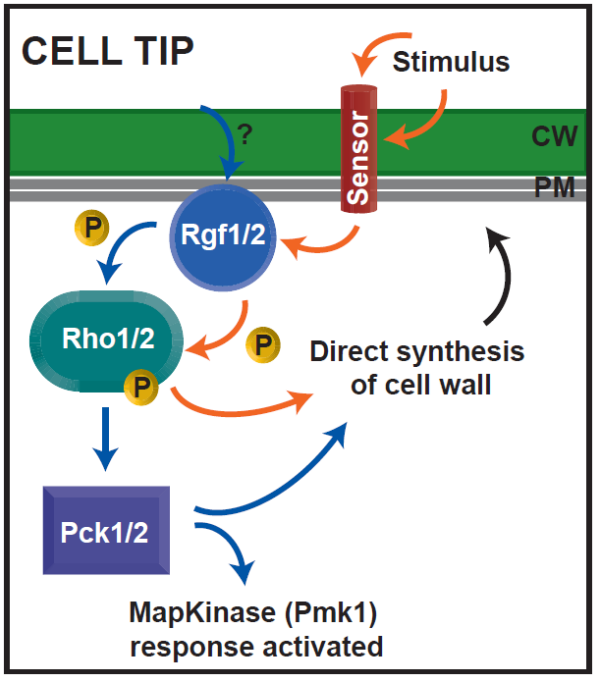

Figure 3.16. Schematic of cell wall integrity pathway. Sensors as Wsc1 or Mtl2 can activate the GEFs Rgf1 and Rgf2, that promote activation of Rho1 (Rho2 activation is not demonstrated). Rho1 can directly promote β-glucan synthases. Both Rho1 and Rho2 can promote glucan synthesis through Pck2. Only Rho1 seem to promote glucan synthesis through Pck1. Pck1 and Pck2 can activate the Mkh1/Pek1/Pmk1 MAP kinase cascade. However, signaling through Wsc1 and Mtl2 does not activate Pmk1 cascade, suggesting that maybe other sensors can activate this pathway, while those two are involved only in direct Rho1 wall synthesis activation. Adapted from (Perez and Rincón, 2010)

activate the phosphokinase C, Pck1 and Pck2. Rho2 on the other hand, is not essential, but can bind both Pck1 and Pck2, promoting α-glucan synthesis through Pck2. Regulators of Rho1 are the GEFs, Rgf1, Rgf2 and Rgf3.The last one is expressed only in septation. Rgf1 is the most important; in fact, its deletion can lead to partial cell lysis. Rgf2 most probably plays a secondary role to Rgf1 during tip elongation, but the double mutation is lethal, suggesting a compensatory role for Rgf2 in the absence of Rgf1. GAPs for Rho1 are Rga1, Rga4 and Rga8. There are no GEFs described for the activation of Rho2, but only one GAP, Rga2, which is shared with Cdc42. Rho1 and Rho2 bind both Pck1 and Pck2. Pck2 has been suggested to directly activate both α and β glucan synthases, while both Pck1 and Pck2 can activate the MAPKKK Mkh1, triggering the Mkh1/Pek1/Pmk1 MAP kinase cascade, promoting activation of the transcription factor Atf1 that modulates the integrity response. Neither *pck1*, nor *pck2* deletion is lethal, but may bring about wall aberration and morphogenesis defects; the double mutant, however, is not viable. Two putative trans-wall sensors have been described in *S. pombe*, Wsc1, homologue of WSC proteins in budding yeast, and Mtl2, homologue of Mid2. Wsc1, localizes mostly at cell tips, and has been shown to directly interact with Rgf2. Mtl2 is localized along the whole plasma membrane and might interact

with Rgf1. Mtl2 deletion causes high sensitivity to stress conditions. Deletion of one of the putative sensor induces an increased lysis phenotype, while the double mutant is not viable, suggesting that they may have redundant activities. Despite suggested to be upstream of the cell wall integrity pathway cascade, sensors activation does not lead to the activation of Pmk1, but only of Rho1, suggesting that they can promote Rho1 activity for the direct regulation of glucan synthesis (Cruz et al., 2013; Garcia, 2006; Madrid et al., 2014; Munoz et al., 2014; Perez and Rincón, 2010).
To conclude, many proteins involved in the cell wall integrity pathway in fission yeast have been described, but still the full picture of wall integrity control has yet to be elucidated, since we still lack pieces of the puzzle, such as activators of Rho2, or the upstream mechanisms involved in Pmk1 activation.

In sum, wall composition, synthesis and its regulation must be carefully regulated by the cell, as any miss-regulation can cause defects in shape, cell integrity and in viability during tip elongation. Most of these aspects are suggested to modulate local or global cell wall mechanics, with putative implications in shape establishment and growth.

3.5 Cell mechanics

As discussed in the previous chapter, the cell wall of *S. pombe* has a prominent elastic behavior (***2.1***) (Minc et al., 2009a; Minc et al., 2009b).
Wall thickness has been measured by Transmission Electron Microscopy and has values in the range of 100-200 nm (Osumi, 2012).
Elastic moduli have been estimated in different ways, as introduced in chapter 2. One method was based on the use of microchambers made of elastomers of controlled elastic properties. Cells were grown in these chambers until they grew so long to cause buckling. From the deformation a surface modulus of 6.5 N/m have been estimated, which corresponds to an elastic modulus of about 30 MPa (Minc et al., 2009a). Other methods used the geometrical deformation of the wall after plasmolysis or laser ablation. By using these parameters, coupled to mathematical models of deformations the authors could estimate elastic moduli of similar order (50-65 MPa) (Abenza et al., 2015; Atilgan et al., 2015).
Turgor pressure has been estimated with the same method of utilizing microchambers, as described before, and estimated to be on the order of 1MPa (Minc et al., 2009a). Alternatively sequential

osmotic shocks were compared to laser ablation, to estimate the external solute concentration that lead to total relaxation of the wall, from which turgor was estimated to be about 1.5 MPa (Atilgan et al., 2015).

These mean values have been precious to support quantitative description and modeling of cell growth, morphogenesis, but, also for other mechanically driven processes such as endocytosis or cytokinesis (Basu et al., 2014; Proctor et al., 2012). However, these mean values are not sufficient to understand the local behavior of wall mechanics, and how this may influence local processes such as polarized tip elongation. Moreover, the approaches used are often complex to perform, or lead to cell disruption, hindering any information related to the dynamics of cell wall mechanics. Therefore, most of the models proposed consider the wall as an almost static structure, while one expects to have a highly dynamic behavior, to coordinate dynamic processes such as growth.

Novel methods to monitor the dynamical behavior of cell wall mechanics are needed, to decipher the interplay between growth, morphogenesis and wall mechanics.

RESULTS

1- Mechanosensation Dynamically Coordinates Polar Growth and Cell Wall Assembly to Promote Cell Survival

Cell growth can be a very dangerous process in walled cells, where synthesis of new cell wall is a hazardous situation that the cell needs to carefully control: since the cell wall sustains the high internal turgor pressure, uncontrolled cell wall expansion can lead to cell wall piercing and cell lysis. Therefore, in these cells growth must come with an intricate interplay between local delivery of material, wall synthesis, remodeling and deformation. However, how cells dynamically regulate this process is still poorly understood.

In this work, we developed a novel method to measure cell wall thickness with sub-cellular scale resolution in live fission yeast cells: this method relies on the use of fluorescent markers to label the inner and the outer part of the cell wall. By using a semi-automated image analysis pipeline, the distance between the two fluorophores can be measured, along the full boundary of the cell.

The application of this method allowed, for the very first time to our knowledge, the observation of wall thickness dynamics over the polarized growth of a tip growing cell. This showed that the cell wall is polarized, being thinner and softer at elongating sites.

With the support of a simple theoretical model, we could observe that thickness at growing poles and growth rate are negatively influencing each other, which may cause catastrophic events: for instance, if a cell wall is thin, the cell will grow faster, leading to further thinning of the wall, with a high risk of cell lysis.

In order to investigate how cells preserve their integrity, we focused on the regulation of wall thickness at growing poles, and by monitoring local wall thickness evolution over time in single cells, we observed that thickness is highly dynamic, presenting continuous phases of thinning and thickening.

Those fluctuations were found to be regulated by a mechanosensing mechanism, that senses wall strain, and dynamically modulate wall synthesis in order to maintain cell integrity. This mechanosensation relies on highly conserved components of the cell wall integrity pathway and mutants failing in mechanosensing undergo cell lysis, as a consequence of uncontrolled wall thinning.

In conclusion, this work, while providing the very first method to measure cell wall thickness dynamics in fission yeast, showed that the cell wall is a dynamic structure, which needs to be finely regulated to maintain cell integrity, while ensuring correct elongation.

Article

Developmental Cell

Mechanosensation Dynamically Coordinates Polar Growth and Cell Wall Assembly to Promote Cell Survival

Graphical Abstract

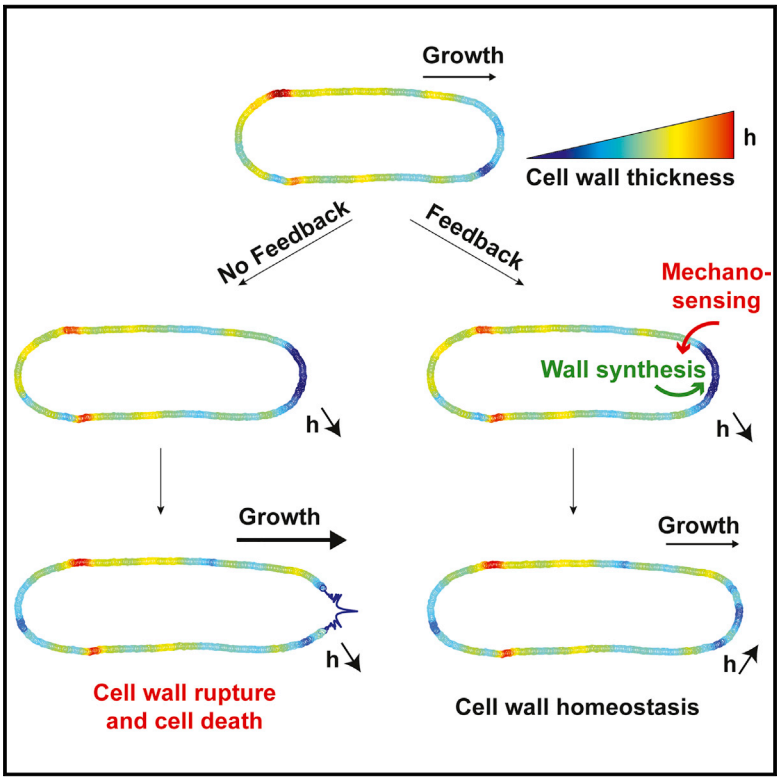

Highlights

- A new microscopy approach enables monitoring of cell wall (CW) thickness dynamics
- Cell wall mechanics are polarized, with growing domains being thinner and softer
- Cell growth and wall thickness negatively influence each other
- A feedback based on mechanosensing promotes cell wall homeostasis and cell survival

Authors

Valeria Davì, Hirokazu Tanimoto, Dmitry Ershov, ..., Etienne Couturier, Arezki Boudaoud, Nicolas Minc

Correspondence

arezki.boudaoud@ens-lyon.fr (A.B.), nicolas.minc@ijm.fr (N.M.)

In Brief

Davì et al. develop a sub-resolution microscopy method to monitor the dynamics of cell wall thickness and assembly in live fission yeast cells. They report thickness fluctuations with feedback, indicative of a mechanism for cell wall mechanical homeostasis important for cell integrity during normal growth.

Davì et al., 2018, Developmental Cell *45*, 170–182
April 23, 2018
https://doi.org/10.1016/j.devcel.2018.03.022

CellPress

CellPress

Developmental Cell
Article

Mechanosensation Dynamically Coordinates Polar Growth and Cell Wall Assembly to Promote Cell Survival

Valeria Davì,[1] Hirokazu Tanimoto,[1] Dmitry Ershov,[1] Armin Haupt,[1] Henry De Belly,[1,4] Rémi Le Borgne,[1] Etienne Couturier,[2] Arezki Boudaoud,[3,*] and Nicolas Minc[1,5,*]

[1]Institut Jacques Monod, CNRS UMR7592 and Université Paris Diderot, 15 rue Hélène Brion, 75205 Paris, France
[2]Laboratoire Matière et Systèmes Complexes, UMR7057, CNRS and Université Paris Diderot, 75205 Paris, France
[3]Reproduction et Développement des Plantes, Université de Lyon, ENS de Lyon, UCB Lyon I, INRA, CNRS, 46 Allée d'Italie, 69364 Lyon, France
[4]Present address: MRC-LMCB, University College London, WC1E 6BT London, UK
[5]Lead Contact
*Correspondence: arezki.boudaoud@ens-lyon.fr (A.B.), nicolas.minc@ijm.fr (N.M.)
https://doi.org/10.1016/j.devcel.2018.03.022

SUMMARY

How growing cells cope with size expansion while ensuring mechanical integrity is not known. In walled cells, such as those of microbes and plants, growth and viability are both supported by a thin and rigid encasing cell wall (CW). We deciphered the dynamic mechanisms controlling wall surface assembly during cell growth, using a sub-resolution microscopy approach to monitor CW thickness in live rod-shaped fission yeast cells. We found that polar cell growth yielded wall thinning and that thickness negatively influenced growth. Thickness at growing tips exhibited a fluctuating behavior with thickening phases followed by thinning phases, indicative of a delayed feedback promoting thickness homeostasis. This feedback was mediated by mechanosensing through the CW integrity pathway, which probes strain in the wall to adjust synthase localization and activity to surface growth. Mutants defective in thickness homeostasis lysed by rupturing the wall, demonstrating its pivotal role for walled cell survival.

INTRODUCTION

Growth control is of fundamental importance in biology, from the regulation of macromolecular assembly, cell physiology, up to organ development (Holley, 1975; Hong et al., 2016; Lander, 2011; Mahadevan and Mitchison, 2005). The growth of individual cells, for instance, has crucial implications for cell size determination, tissue homeostasis, or cancer progression (DeBerardinis et al., 2008a; Deberardinis et al., 2008b; Fantes and Nurse, 1977; Marshall et al., 2012; Thompson, 2010). To date, however, the mechanisms that control cellular growth remain poorly understood. This is because growth is an integrated output of multiple intertwined biochemical and biomechanical elements that dynamically probe and alter the cell surface to accommodate surface expansion. Those may include surface material synthesis mediated by processes such as exocytosis and endocytosis (Hepler et al., 2001; Novick and Schekman, 1979), as well as osmotic forces and mechanical elements that set the elasticity of the cell surface, such as the actin cortex, the glycocalyx, or the cell wall (CW) (Davi and Minc, 2015; Huang and Ingber, 1999; Salbreux et al., 2012). How those modules, which act at various time and length scales, may dynamically feed back onto each other to control the rate of cell surface expansion remains an outstanding open question.

Cell growth has been admittedly best documented in single walled cells, such as bacteria, fungi, or pollen tubes (Harris and Theriot, 2016; Mitchison and Nurse, 1985; Qin and Yang, 2011; Rojas et al., 2014). Those are among the fastest growing cells, with some fungal cells elongating at rates up to several tens of micrometers per minute (Lew, 2011; Qin and Yang, 2011). Size expansion in those cells is irreversible and limited by the synthesis of a thin and rigid sugar-made CW around the plasma membrane. The growth of the CW is thought to involve a complex balance between sugar synthesis, which builds the wall, and mechanical expansion driven by large internal turgor pressure, which puts the wall under tension to deform it (Cosgrove, 2005; Davi and Minc, 2015; Harold, 2002; McKenna et al., 2009). Because the CW bears large turgor-derived stress, it also provides mechanical integrity to those cells: removal or weakening of the CW yields near-immediate cell lysis and death. Given those considerations, cell growth may be seen as a dangerous process, as uncontrolled expansion and consequent thinning of the CW could compromise cell survival. To date, however, our understanding of how CW assembly and thickness may be dynamically controlled during cell growth has been limited, as historically it has been mostly studied with electron microscopy, which has biased our appreciation of the CW toward a static structure.

The biochemistry and genetics that support CW growth and composition have been well studied in model yeast cells (Lipke and Ovalle, 1998; Perez and Ribas, 2004). The rod-shaped fission yeast *Schizosaccharomyces pombe*, for instance, serves as a prime model for walled cell tip growth, stereotypical of many bacteria, fungi, and plant cells (Chang and Huang, 2014;

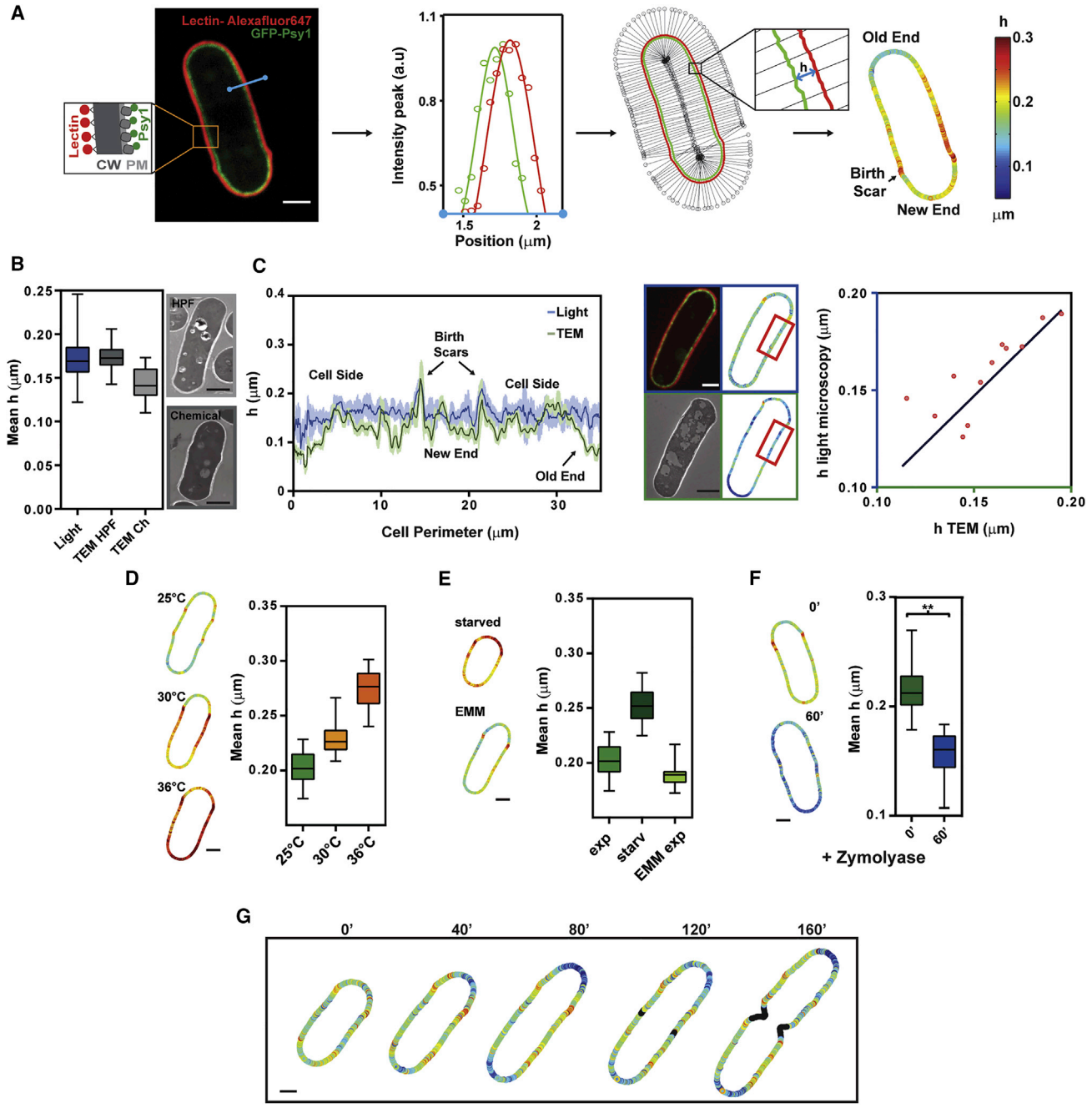

Figure 1. A Method to Image Cell Wall Thickness around Living Cells

(A) Mid-slice confocal image of a fission yeast cell expressing GFP-Psy1 (plasma membrane [PM]) and labeled with lectin-Alexafluor647 (CW outer surface). Contours are determined from the centers of Gaussian fits of each signal across the cell surface (blue line). After chromatic shift registration, the distance between the two contours yields local CW thickness measurements (h). (Right) Thickness color map around a cell.

(B) Measurement of CW thickness using photonic microscopy (n = 41) and TEM performed by high-pressure freezing (HPF) (*n=23*) or chemical fixation (Ch) (*n=22*). Representative TEM images in these conditions.

(C) (Left) Running average (on 10 pixels) and SD of thickness measurement of the same single cell, shown in the middle, measured by TEM or light microscopy using CLEM. (Right) Light versus TEM thickness measurement averaged over regions of ~2 μm (red rectangle) (n = 13 regions, from nine cells). The line is a linear fit. Light microscopy measurements for CLEM are corrected to compensate for the high internal fluorescent background caused by chemical fixation (see STAR Methods).

(D) Mean wall thickness of cells grown at different temperatures, and representative thickness color maps in the same conditions (n > 25 for each condition).

(E) Mean wall thickness of cells measured in exponential phase (exp) or after ~16 hr of starvation (starv), and in cells grown in Edinburgh minimal medium (EMM) (n > 25 for each condition).

(legend continued on next page)

Chang and Martin, 2009; Davi and Minc, 2015). The fission yeast CW behaves as a thin elastic shell with an elastic modulus estimated to be around 30–50 MPa, which resists an internal turgor pressure of 1–1.5 MPa (Abenza et al., 2015; Atilgan et al., 2015; Minc et al., 2009). In those cells, CW synthesis is first restricted to the old cell tip after division, and is redistributed to both growing tips after NETO (New End Take Off), and to the cell middle for septation (Cortes et al., 2005). At cell tips, wall synthesis is catalyzed by one α-glucan (Ags1) and three β-glucan (Bgs1, Bgs3, and Bgs4) synthases, which elongate glucan fibers, as well as glucanosyl-transferases enzymes (Gas1 and Gas2) and one putative exo-glucanase, Exg2, which may remodel and/or crosslink glucan fibers at cell tips (Davi and Minc, 2015; Perez and Ribas, 2004). Those enzymes are under the control of the activity of the highly conserved Rho-GTPases, Rho1 and Rho2, which are activated by the GEFs Rgf1 and Rgf2 (Arellano et al., 1999; Garcia et al., 2006). Damage to the CW, such as that caused by antifungal agents, is monitored by the CW integrity (CWI) pathway, which may be activated by Rgf1, Rho1, or Rho2, and triggers the expression of a set of CW repair genes through the Pmk1 MAPK (Garcia et al., 2009b; Perez and Cansado, 2010).

To understand how those different biochemical layers dynamically influence and probe the mechanics of the CW, we here introduce a microscopy method to directly measure CW thickness all around live growing fission yeast cells. We find that CW thickness at growing cell tips is highly dynamic in time, with phases of thickening followed by thinning phases, and vice versa. We demonstrate a homeostatic system that accounts for thickness fluctuations and stable values at the cell population. Homeostasis is supported by mechanosensing activities of the CWI that probe cellular growth as a mechanical stress and dynamically adjust synthesis to growth rates. Mutants defective in homeostatic thickness lyse by over-thinning the CW. This work provides evidence for mechanochemical feedbacks promoting growth control and cell survival.

RESULTS

A Sub-resolution Method to Monitor CW Thickness Dynamics in Living Cells

The fission yeast CW is a thin layer of typically 100–200 nm, below the resolution of light microscopy. Given large internal turgor pressure, the plasma membrane is plastered against the internal face of the CW (Osumi, 2012). In addition, glycosylated galactomannan proteins are secreted in the CW and can be selectively detected on the most outer surface of the wall with specific lectins (Horiseberger and Rosset, 1977). We exploited those properties to develop a sub-resolution method to compute CW thickness all around single live growing fission yeast cells. We labeled the inner and outer faces of the CW respectively using an integral membrane SNARE protein tagged with a GFP at its intracellular tail (GFP-psy1) (Nakamura et al., 2001) and by adding lectins from *Griffonia simplicifolia* that specifically bind the most outer face of the fission yeast CW, labeled with a different emitting fluorophore. Following image registration and cell contour segmentation, we computed the distance between the centers of the two fluorescent signals along lines bisecting the cell surface, which provided a local measurement of CW thickness (Chugh et al., 2017; Clark et al., 2013). Thickness measured by those means could be calculated with a precision around ~30 nm and a lateral resolution of ~500 nm, and was represented as colored cellular maps (Figures 1A and S1A–S1E) (see STAR Methods). Measurements were slightly sensitive to growth environment and media but robust to variations in lectin-bound fluorophores or membrane associated GFP signals (Figures S2A–S2C).

To validate our approach, we first compared it with transmission electron microscopy (TEM) measurements, which serve as the current standard to image the CW (Osumi, 2012). The mean CW thickness in a wild-type (WT) population measured by our method was 170 ± 23 nm. This was comparable with values obtained from high-pressure freezing TEM (172 ± 14 nm) and ~16% higher than values obtained in chemical fixation TEM (143 ± 19 nm), plausibly because chemical fixation may not fully protect the CW against subsequent resin embedding (Osumi, 2012) (Figure 1B). Next, we used correlative light electron microscopy (CLEM) to image and compute CW thickness in the same cell with TEM and our method. Although the use of high-pressure freezing did not allow the retention of fluorophores needed for CLEM, we could directly compare thickness values in individual chemically fixed cells. This CLEM analysis yielded nearly similar patterns of thickness along the cell boundary, supporting the reliability of our method as a local measurement of CW thickness (Figures 1C and S2D–S2G).

To assess the accuracy, precision, and range of this live imaging method, we next tested it against conditions thought to affect CW thickness. As previously suggested, we detected a dose-dependent increase in CW thickness with temperature or as a result of prolonged starvation (Figures 1D and 1E) (Cassone et al., 1979). Cells treated with zymolyase, a CW digesting enzyme, exhibited significant CW thinning (Figure 1F). Finally, thickness could be imaged in the same cell over several hours with no major cellular damage and no impact of bleaching on the measurement (Figures 1G, S3A, and S3B and Videos S1 and S2). Thus, it was possible to quantify the dynamics of CW thickness and assembly with unprecedented accuracy in populations of live growing cells.

Polar Growth Sites Are Associated with Thinner and Softer CWs

Given that wall assembly in fission yeast is restricted to growing cell tips during interphase and to the cell middle during septation, we computed CW thickness patterns in cell populations (Chang and Martin, 2009; Davi and Minc, 2015). Birth scars that are inherited from previous cell division were associated with a significantly thicker CW, with a thickness of h_{scar} = 224 ± 20nm. Interestingly, we observed that the CW was consistently thinner at the old end, the end that grows most during

(F) Thickness before (n = 35 cells) or after 60′ of zymolyase treatment (n = 19); **p < 0.0001.
(G) Time lapse of CW thickness maps of a growing cell. Black points correspond to positions in which thickness cannot be measured accurately. Scale bars, 2 μm; whisker plots show the median and full dataset range.
See also Figures S1–S3 and Videos S1 and S2.

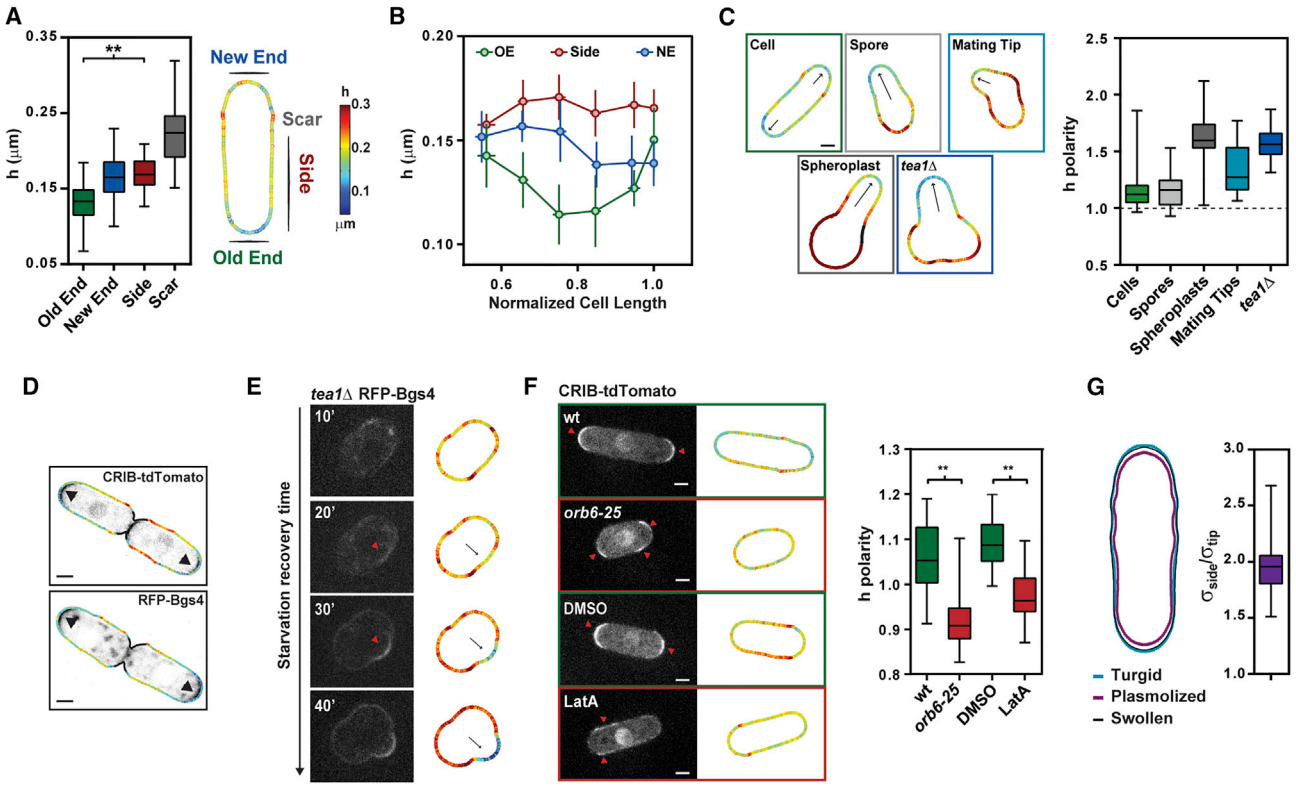

Figure 2. Cell Polarity and Cell Wall Thickness Patterns

(A) Thickness color map of a typical interphase cell, and thickness values at the old end (n = 50), new end (n = 41), cell sides (n = 51), and birth scars (n = 47).

(B) Evolution of cell wall thickness as a function of cell length (used as a proxy for cell cycle progression), in WT cells at the old end (OE; n = 12 cells), the new end (NE; n = 8 cells), and cell sides (n = 12 cells). Cell length is normalized by the length at septation.

(C) Representative thickness color maps and thickness polarity in WT interphase cells (n = 41), outgrowing spores (n = 24), recovering spheroplasts (n = 22), mating tips (n = 18), and *tea1Δ* cells recovering from starvation (n = 29). Arrows indicate growth directions. h polarity is defined as the side/tip ratio in WT interphase cells using an average of both tips values, and back/tip ratio in the other cases.

(D) Superimposition of h map and polar growth markers (arrowheads).

(E) Mid-slice confocal time-lapse and h maps of a *tea1Δ* cell recovering from starvation. Arrows indicate growth direction and arrowheads point at RFP-Bgs4 polar cap.

(F) (Left) Mid-slice confocal image and h maps in the indicated conditions. Red arrowheads point at CRIB-td-Tomato polar caps. (Right) h polarity in WT (*n=30*) and *orb6-25* (*n=29*) grown for 2 hr at restrictive temperature and in cells treated for 30′ with DMSO (*n=21*) or 100 μM LatA (*n=26*).

(G) (Left) Symmetrized cell boundary in turgid, plasmolyzed, and computationally swollen state, used to compute local elastic moduli, Y, at cell tips and sides. (Right) Ratio of surface modulus, σ = hY, between tips and sides (n = 21 cells). Scale bars, 2 μm; whiskers plots show median and full dataset range. Error bars represent SD. **p < 0.0001. Black points in thickness maps correspond to positions in which thickness cannot be measured accurately.

See also Figure S3 and Video S3.

interphase, h_{oe} = 130 ± 26 nm, compared with cell sides, h_{side} = 170 ± 20 nm. Thickness at the new end, which only initiates growth after NETO was in contrast only slightly thinner than cell sides, with a mean value of h_{ne} = 167 ± 14 nm (Figure 2A). To quantify how those values may evolve during the cell cycle, we performed long time lapses following full ~3 hr cell cycles in populations of cells, with a temporal resolution of 20'. In a WT population, this revealed a global decrease of thickness at the old end in the first part of the cell cycle, followed by a steady increase in the following phase, eventually yielding similar values to the beginning of the cycle. Tip thinning was also observed at the new end but delayed by the time needed for the new end to start growing at NETO. Thickness at cell sides exhibited much less variations than at cell tips (Figure 2B).

We also found that monopolar tips of outgrowing spores, spheroplasts, mating projections, and of *tea1Δ* mutants branching from cell sides were also markedly thinner at the front growing site than on the non-growing back (Bonazzi et al., 2014; Kelly and Nurse, 2011; Mata and Nurse, 1997; Petersen et al., 1998) (Figure 2C). These thin wall regions at sites of polar growth co-localized with the downstream polarity regulator GTP-Cdc42 (visualized with a CRIB domain fused to td-Tomato) and with the β-glucan synthase Bgs4, which mark sites of CW assembly and remodeling (Cortes et al., 2005; Tatebe et al., 2008) (Figure 2D). Furthermore, time lapse of polarized regrowth in *tea1Δ* cells recovering from starvation showed the stabilization of a Bgs4 polar domain, concomitant with local CW thinning and followed by the emergence of a new growing tip (Figure 2E and Video S3). Importantly, full depolymerization of actin with 100 μM Latrunculin A or the use of an *orb6-25* thermo-sensitive allele affecting Cdc42-based polarity both yielded the detachment of GTP-Cdc42 polar domains from cell tips and

consequent alteration of CW thickness patterns within tens of minutes (Bendezu and Martin, 2011; Das et al., 2009) (Figure 2F).

The CW was also softer at growing cell tips. This was shown by computing CW elastic moduli, Y, which characterizes the bulk mechanical properties of the CW. To this aim, we plasmolyzed cells by rapidly adding 1.5 M sorbitol to the medium in microfluidic flow channels, which causes a rapid drop in turgor pressure, and consequent cell shrinkage (Abenza et al., 2015; Atilgan et al., 2015; Bonazzi et al., 2014). Using the changes in cell shapes between inflated and plasmolyzed states and local thickness values, we could extract values of CW elastic moduli at cell tips and at cell sides, to be Y_{tip} = 45.3 ± 0.7 MPa, and Y_{side} = 72.5 ± 1.15 MPa, yielding a ratio in surface moduli ($\sigma = hY$) of $\sigma_{side}/\sigma_{tip}$ = 1.96 ± 0.27 (Figures 2G, S3C, and S3D). Together, those results suggest that internal polarity, which directs growth and CW synthesis, causes sites of polar growth to have thinner and softer CWs.

Contribution of Synthesis and Growth to CW Thickness at Cell Tips

Those findings prompted us to assess how CW thickness and assembly may be regulated at sites of polar growth. We first considered a minimal theoretical model for thickness dynamics at cell tips (Figure 3A). We posited that the CW thickens through synthesis and thins through cell elongation, which, given mass conservation, yields a dynamic evolution of h_{tip}:

$$\frac{dh_{tip}}{dt} = S - \gamma\, h_{tip}, \qquad \text{(Equation 1)}$$

where S is a rate of wall synthesis per unit surface and γ the strain rate of the CW. Accordingly, CW thickness is determined by the balance between synthesis and wall expansion, which explains the observation that thickness may not be directly positively correlated with Bgs4 signal (Figure 2D). The strain rate γ is related to the cell elongation rate, Gr, by the curvature radius at the tip, R_c:

$$Gr = dL/dt = qR_c\,\gamma, \qquad \text{(Equation 2)}$$

with L the length of the cell and q a numerical geometrical prefactor.

To assay the contribution of synthesis, we performed experiments to manipulate synthase activity. In cells overexpressing Pck2, a positive regulator of glucan synthesis, one major component of the fission yeast CW, we could detect significant thickening, up to ~900 nm in some cells (Arellano et al., 1999). Thickening was also observed by overexpressing a constitutively active Rho1 allele, *rho1-G15V* (Arellano et al., 1996) (Figure 3B). Conversely, a *cwg1-1* thermo-sensitive allele of the glucan synthase Bgs4 exhibited significant thinning at growing cell tips, consistent with previous TEM observations (Muñoz et al., 2013) (Figure 3C). As a more direct assay, we also reduced CW synthesis with low doses of caspofungin, a drug that specifically impairs β-glucan synthase activity (Martins et al., 2011). This treatment led to a net thickness decrease at growing ends over tens of minutes, eventually causing aberrant cell bulging at longer times (Figure 3D and Video S4).

Using those caspofungin treated cells, in which synthesis is partially impaired, we also computed the contribution of growth to thickness variation. We measured the relative changes in thickness, $\Delta h_{oe}/h_{oe}$, which, given Equations 1 and 2, is predicted to linearly scale with $-\Delta L_{oe}/R_c$. This analysis yielded a negative linear correlation with a slope of −0.81 (correlation coefficient, r = −0.57), and a positive y-intersect, which could correspond to remaining CW α-glucan synthesis in the presence of this drug (Figure 3E). Together, those data support a simple model for CW thickness evolution positively regulated by synthesis and negatively by growth.

Influence of CW Thickness on Cell Growth Rates

As the balance between turgor and CW mechanics has been proposed to set growth rates in fission yeast (Bonazzi et al., 2014; Minc et al., 2009), we sought to investigate the influence of thickness on strain and growth rates. Using a simple model for wall rheology (Minc et al., 2009; Rojas et al., 2011), we posited that the strain rate could be written as:

$$\gamma = r\frac{PR_c}{Yh_{tip}}, \qquad \text{(Equation 3)}$$

with r a wall remodeling rate, Y the elastic modulus of the wall, and P the turgor pressure (we here neglect a possible threshold in turgor for growth to occur). Given Equation 2, this assumption implies that the elongation rate Gr scales with R_c^2/h_{tip}. This scaling was confirmed using three-dimensional numerical simulations of a mechanical model of fission yeast growth (Abenza et al., 2015) (Figure 3F).

Experimentally, we first tested this model prediction by comparing the mean growth rate and thickness at the population level at different moments in the cell cycle. This showed that growth rates were indeed anti-correlated with thickness values (Figure S4A). We then used time-lapse videos to compute and plot single cell elongation rates, as a function of initial tip curvature radii and CW thickness. To vary R_c, we used WT cells and mutants with larger (*rga4Δ*) and smaller diameters (*rga2Δ*), as well as microfabricated channels to physically diminish the diameter of *rga4Δ* cells (Das et al., 2007; Villar-Tajadura et al., 2008; Zegman et al., 2015). This analysis yielded, as predicted, a robust linear dependency between Gr and R_c^2/h_{tip}, indicating that CW thickness could serve as a major determinant influencing elongation rates (Figures 3G–3I).

Homeostasis in CW Thickness through Strain Mechanosensing

The above findings suggest that, without regulatory layers, growth and thickness may negatively regulate each other, which could potentially lead to catastrophic situations of cell lysis through CW thinning or growth arrest through thickening. We thus computed tip thickness evolution in single cells over several hours, with a high temporal resolution of 6 min, focusing on the old end. Strikingly, this revealed a thickness fluctuating behavior with feedback, consisting of multiple phases of CW thickening, followed by thinning phases, and so on. Thickness on cell sides was, in contrast, almost completely stable (Figures 4A, 4B, and S4B–S4E). Fourier spectrum analyses allowed to clearly discern those fluctuations from the global trend at the cell cycle level, and yielded an estimate of the timescale for the feedback around 50–60 min (Figures S4F and S4G). Those

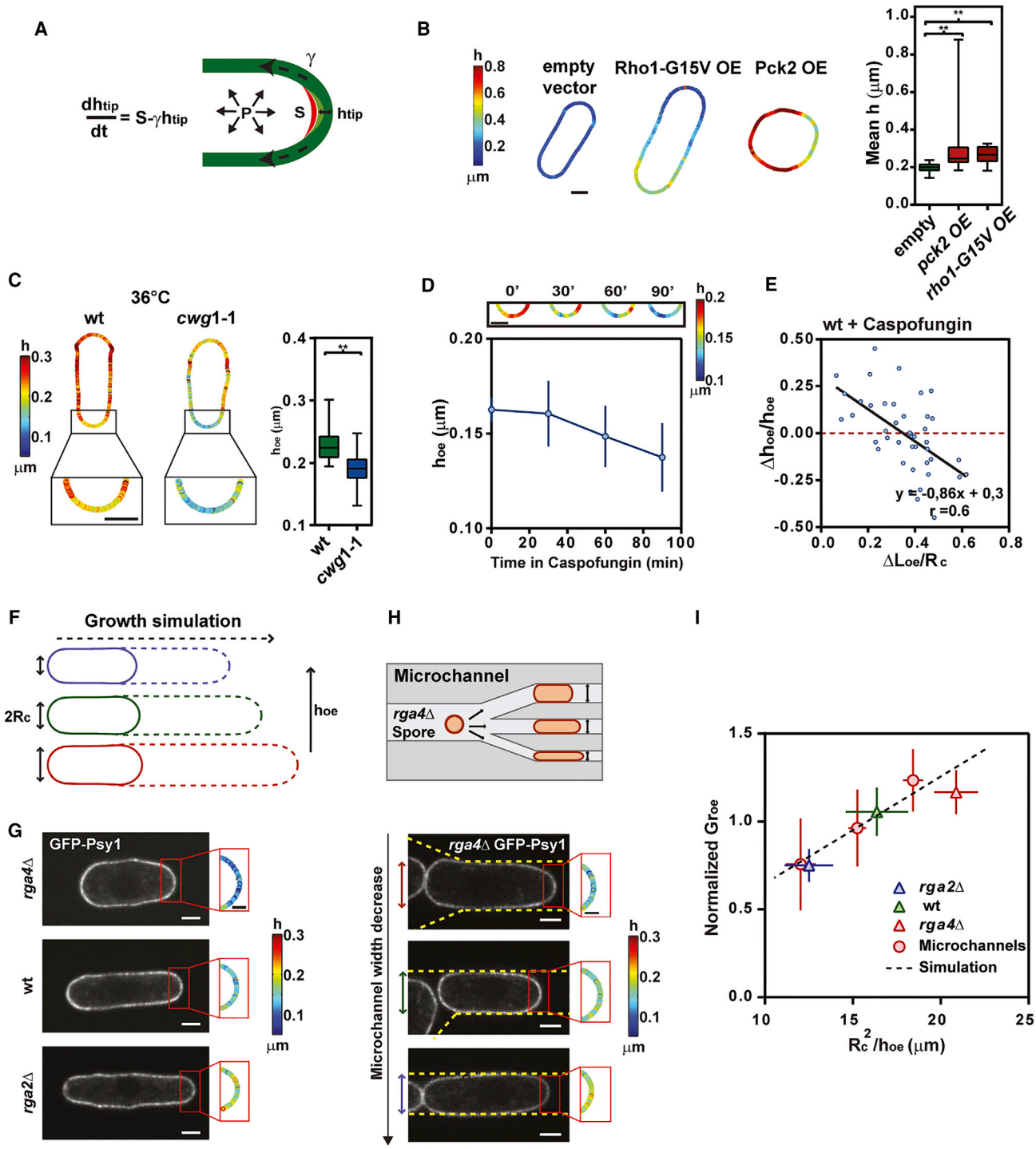

Figure 3. Dynamics of Cell Wall Assembly at Polar Growth Sites

(A) Simple model for tip thickness (h_{tip}) dynamics. S is a rate of wall synthesis per unit surface, γ the strain rate, and P the turgor pressure.

(B) Representative color maps and mean h measurement of cells overexpressing a control empty plasmid (n = 59 cells), a constitutively active Rho1-G15V allele (n = 27), and Pck2 (n = 59).

(C) Representative color maps and thickness values at the old end (h_{oe}) in WT (n = 27) and *cwg1-1* (n = 29) grown at restrictive temperature.

(D) (Top) Representative h_{oe} maps following caspofungin treatment, and evolution of h_{oe} in time (bottom, n = 11 cells).

(E) $\Delta h_{oe}/h_{oe}$, measured in caspofungin treated WT cells and plotted as a function of $\Delta L_{oe}/R_c$ (n = 12 cells). The black line is a linear fit.

(F) Growth simulations: plain and dashed lines mark cell shapes at the beginning and the end of the simulation.

(G) Mid-slice confocal images of typical *rga4Δ*, WT, and *rga2Δ* cells expressing the membrane marker GFP-Psy1 and close-up local h color maps at the old end.

(legend continued on next page)

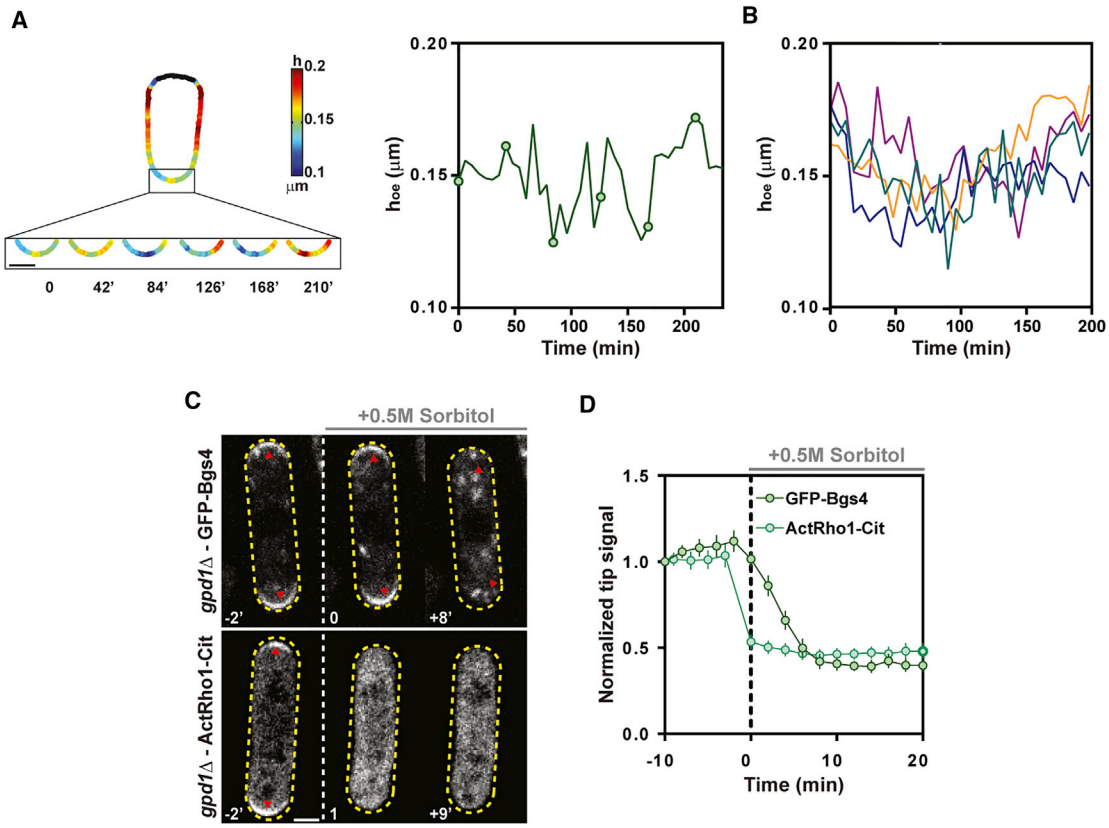

Figure 4. Cell Wall Thickness Fluctuations and Strain Rate-Dependent Cell Wall Synthase Activation and Localization

(A) Close-up views on thickness maps (smoothed on 10 pixels) at the old end of a growing WT cell, and corresponding plots of thickness evolution at the old end within a full cell cycle. Black points correspond to positions in which thickness cannot be measured accurately. Dots correspond to time points shown in color plots.

(B) Evolution of thickness at the old end h_{oe} imaged at 6 min interval for one cell cycle in four representative WT cells.

(C) GFP-Bgs4 and Active-Rho1-Citrin polar domains (arrowheads) detachment in *gpd1Δ* cells following turgor reduction caused by the addition of 0.5 M sorbitol in the medium.

(D) Evolution of normalized tip signal of GFP-Bgs4 (n = 14) and Active-Rho1-Citrine (n = 18) in cells rinsed with sorbitol at t = 0. Scale bars, 2 µm; error bars represent SD. Scale bars, 2 µm.

See also Figure S5.

fluctuations at cell tips suggested the presence of a delayed feedback dynamically regulating CW thickness and assembly at growing tips.

Based on reported observations in fission yeast and other cell types (Bonazzi et al., 2014; Nakayama et al., 2012), we assayed a potential positive feedback between growth, or equivalently strain rate, and polarized synthesis. To reduce strain rate, we rapidly decreased turgor by rinsing cells with medium containing 0.5 M sorbitol using a *gpd1Δ* background to prevent turgor adaptation (Minc et al., 2009). This caused an immediate growth arrest and the rapid detachment of active-Rho1 polar domains (Davidson et al., 2015) followed by the detachment of Bgs4 domains over the subsequent minutes (Figures 4C, 4D, and S4H). Those data suggest that CW synthase activity and localization may be actively sensitive to growth or strain rates.

To incorporate mechanical sensing in our model, we used a general delayed dependence, between strain rate and synthesis, of the form: $S(t) = S_0 + \lambda\gamma(t-T)$, with S_0 a basal synthesis rate, λ a positive parameter characterizing the strength of the sensing, and T a delay in the response between strain and synthesis, so that:

$$\frac{dh_{tip}}{dt}(t) = \left(S_0 - \frac{rPR_C}{Y}\right) + \lambda\frac{rPR_C}{Y}\frac{1}{h_{tip}(t-T)}. \quad \text{(Equation 4)}$$

Using the evolution of old end thickness in single cells, we thus evaluated experimentally the dependence of the thickness rate,

(H) Schematic for diameter manipulation in microchannels, and mid-slice confocal images of *rga4Δ* cells grown in microchannels with different diameters and close-up local h color maps at the old end. The yellow dashed lines mark the border of the microchannels.

(I) Normalized growth rate at the old end plotted as a function of R_c^2/h_{oe}, for WT (n = 36), *rga2Δ* (n = 26), *rga4Δ* (n = 37), and *rga4Δ* cells grown in microchannels (n = 33, binned on 11, 10, 13 cells). The dotted line is a fit of the growth simulation results. Whiskers plots show median and full dataset range. r is a Pearson correlation coefficient. Error bars correspond to SD. **p < 0.0001. Scale bars represent 2 µm in confocal images and full cell color maps, and 1 µm in insets.

See also Figure S4 and Video S4.

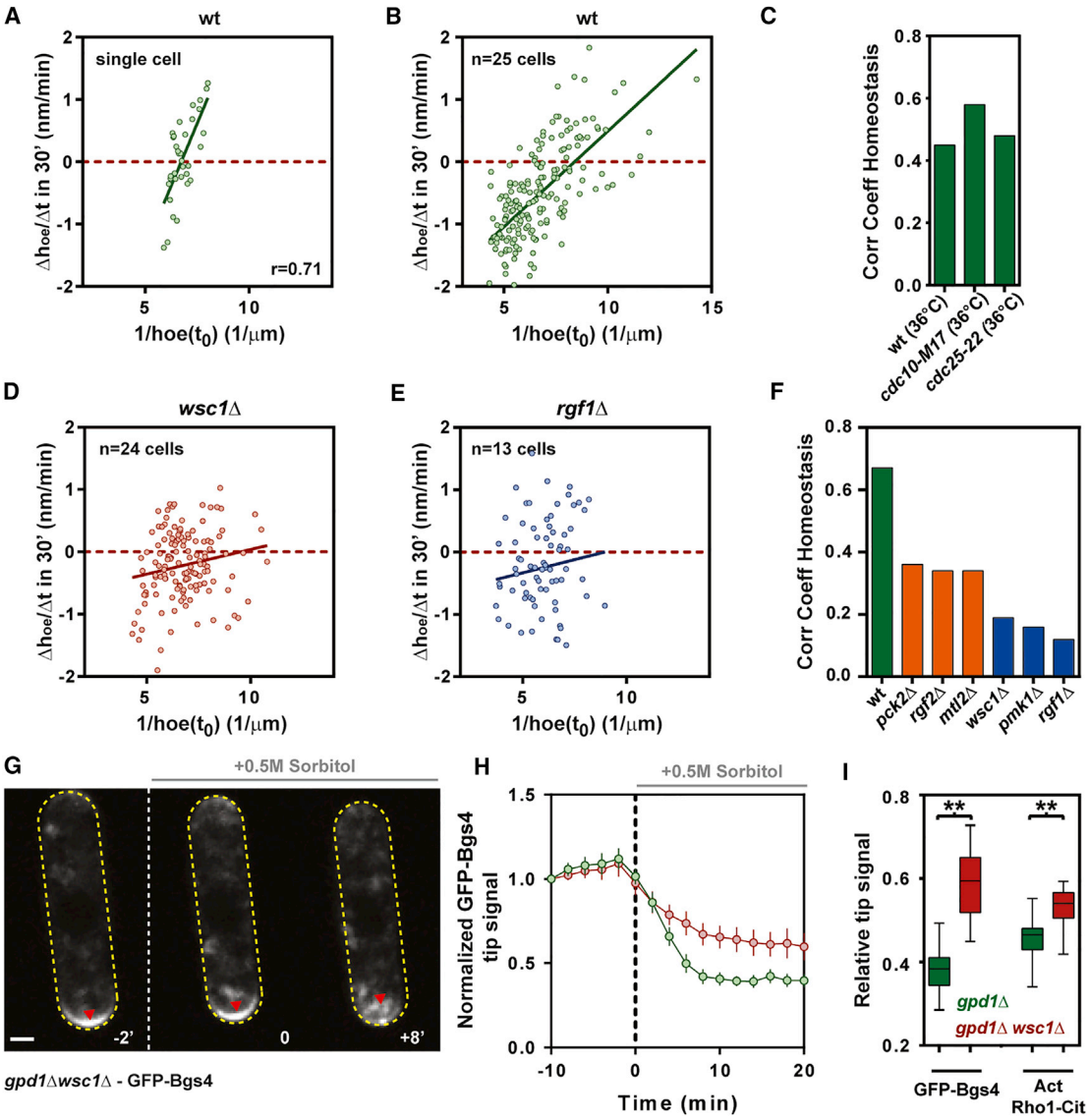

Figure 5. The Cell Wall Integrity Pathway Mediates Cell Wall Thickness Homeostasis

(A and B) (A) Thickness homeostasis plot in a single WT cell imaged during a full cell cycle at 6′ interval. $\Delta h_{oe}/\Delta t$ is computed as $(h_{oe}(t_0+30')-h_{oe}(t_0))/30$, for various t_0 and plotted as a function of $1/h_{oe}(t_0)$ (B) Thickness homeostasis plot in a population of WT cells (n = 25 time lapses of individual cells). The plain line is a linear fit.

(C) Pearson correlation coefficient of thickness homeostasis for WT (35 cells), *cdc10-M17* (13 cells), and *cdc25-22* (19 cells) grown at restrictive temperature (36°C).

(D and E) (D) Thickness homeostasis plot for a *wsc1Δ* mutant (24 cells). (E) Thickness homeostasis plot for a *rgf1Δ* mutant (13 cells). Plain lines are linear fits.

(F) Pearson correlation coefficient for thickness homeostasis of WT (25 cells), *mtl2Δ* (24 cells), *pck2Δ* (27 cells), *rgf2Δ* (22 cells), *wsc1Δ* (24 cells), *rgf1Δ* (13 cells), and *pmk1Δ* (25 cells).

(G) Defect in GFP-Bgs4 detachment in response to turgor reduction in a *gpd1Δwsc1Δ* double mutant. Note the remaining signal compared with a *gpd1Δ* single mutant shown in Figure 4C. Arrowheads point to a GFP-bgs4 polar domain.

(H) Evolution of normalized tip signal of GFP-Bgs4 (n = 19) in *gpd1Δ* and *gpd1Δwsc1Δ* cells rinsed with sorbitol at t = 0.

(I) Ratio between tip signals of the indicated markers after and before sorbitol treatment in *gpd1Δ* and *gpd1Δwsc1Δ* cells (n = 14, 19, 18, 18). The excess of negative points in homeostasis plots is caused by an oversampling in the first part of the cell cycle. r is the Pearson correlation coefficient. Whiskers plots show median and full dataset range. Error bars represent SD. **p < 0.0001. Scale bars, 2 μm.

See also Figures S5 and S6.

$dh_{oe}/dt(t_0 + T)$, computed at different delays, on the inverse of initial thickness $1/h_{oe}(t_0)$, measured at various t_0 in time lapses. We found a positive correlation at delays starting around 12 min (r = 0.4), which improved for longer delays, yielding highest correlations at delays around 30–40 min (r = 0.7), in agreement with Fourier spectrum analyses (Figures 5A, 5B, and S5A–S5E). In this plot, the x-intercept corresponded to a homeostatic thickness of $h_{oe}^* = 119$ nm, close to the mean thickness of the old end at the population level. Importantly, this homeostatic behavior was not influenced by cell cycle driven thickness variations and was still

observed in *Cdc10-M17* and *Cdc25-22* mutants respectively blocked in G1 or in G2 phase, ruling out putative contribution of cell cycle variations to this behavior (Figures 5C and S5F–S5I). Solving the delayed differential Equation 4 for h(t) yielded, in a range of parameter values, fluctuating behavior, reminiscent of experimental observations (Figures S5J–S5L and Supplemental Information). Together those findings support the existence of a homeostatic mechanism, in which an overshoot (or an undershoot) in thickness is corrected by thinning (respectively thickening) the wall over the subsequent tens of minutes to maintain it around a narrow range of values.

The CWI Pathway Mediates Strain Mechanosensing for Thickness Homeostasis

A prime candidate system that may sense CW properties and influence synthesis is the CWI, a signaling cascade involved in general CW stress response (Perez and Cansado, 2010). In fission yeast, this pathway is thought to be activated at the cell surface by the putative trans-membrane stress sensors Wsc1 and Mtl2, which interact with the CW, plausibly through long serine/threonine rich domains extending in the CW matrix (Cruz et al., 2013). Those factors signal downstream to Rho-GEFs Rgf1 and Rgf2, which may directly regulate the Rho-GTPases Rho1 and Rho2 for glucan synthase activation (Garcia et al., 2006, 2009a; Mutoh et al., 2005). The CWI also triggers the activation of gene transcription for CW repair, through the Pmk1 MAPK cascade (Garcia et al., 2009b; Perez and Cansado, 2010). By performing a candidate screen on single mutants of the CWI, we found that *wsc1Δ*, *rgf1Δ*, and *pmk1Δ* were severely defective in thickness homeostasis, with changes in thickness being mostly independent on previous thickness values (Figures 5D–5F, S6A, and S6B). Importantly, those mutants still exhibited global thinning and thickening phases during the cell cycle, suggesting those large-scale variations are independent of the CWI (Figure S6C). In addition, we found that the detachment of Bgs4 and active-Rho1 polar domains as a response to pressure and strain reduction in a *gpd1Δ wsc1Δ* mutant was significantly less pronounced than in a *gpd1Δ* alone, suggesting that Wsc1 may directly probe CW strain rate to tune synthesis through the CWI (Figures 5G–5I and S6D).

Finally, we assayed whether the implication of the CWI pathway in thickness homeostasis could account for the lysis phenotype of some CWI mutants during normal growth (Cruz et al., 2013; Garcia et al., 2006). By imaging thickness evolution in *rgf1Δ*, we observed in ~30% of cases cells that started with a relatively thick wall and little growth, which switched incidentally to a phase of unusually rapid growth concomitant with rapid CW thinning eventually causing tip lysis and cell death (Figures 6A and 6B). We noted, however, that the thickness at which lysis occurred in some of those cells could have values similar to WT tips. As the failure strain of the CW yielding to lysis may depend on the surface modulus, $\sigma = Yh$, which has contributions from both thickness and elastic modulus, we suspect that those cells also have lower bulk modulus, arising from misregulated CW composition. This was supported by the similar growth rate values that individual *rgf1Δ* cells reached before lysis, which is predicted to inversely depend on the surface modulus (Figure 6B). Similar lysis phenotype was also observed in *wsc1Δ*, but to a much lesser extent, which precluded a careful analysis of thickness dynamics. Together those findings demonstrate that the CWI may directly probe CW strain rates to adjust synthesis, thereby coordinating growth and CW assembly needed for cell survival (Figure 6C).

DISCUSSION

The mechanical properties of the CW and turgor values underlie walled cells' growth and shapes, and have been redundantly used as tunable cellular properties to survive, colonize, infect, or reproduce (Bastmeyer et al., 2002; Dagdas et al., 2012; Dudin et al., 2015; Harold, 2002; Keegstra, 2010; Lew, 2011; Silhavy et al., 2010). This importance contrasts with the limited knowledge we have on the dynamic regulation of those mechanical parameters in growing and dividing cells. By developing and validating here the very first approach to monitor CW thickness in live cells, we provide evidence of key contributions of the polarized dynamics of the CW for growth and viability. Our approach overcomes numerous limitations of EM studies, such as alterations in cell shape and CW caused by fixation (Osumi, 2012), and brings the possibility to visualize the CW in a planar section in large populations of living cells. We foresee that this approach could serve as a standard for studying CW function in processes such as growth, reproduction, or infection in bacteria, fungi, or plants, with potential therapeutic values for antifungal and antibiotic chemical screens.

Spatiotemporal CW Dynamics

One important output of our study is to find that CW thickness and mechanics are polarized, with growing poles being typically twice as soft and thin as the rest of the cell. Those mechanical anisotropies, which here derive from internal polarity, have long been speculated to be required for tip elongation and rod-shape morphogenesis (Boudaoud, 2003; Drake and Vavylonis, 2013; Rojas et al., 2011). Patterns of wall elasticity may also influence the morphogenesis of other tip growing cells (Ma et al., 2005; Yanagisawa et al., 2015), as well as that of multicellular plant tissues (Kierzkowski et al., 2012; Milani et al., 2014; Peaucelle et al., 2011). Given the large variety of shapes found in fungal species and mutants, it will be interesting to systematically compare spatial patterns of CW mechanics and thickness with cell shape parameters, to identify generic biomechanical principles guiding the morphogenesis of walled cells. Animal cells also exhibit anisotropic mechanical properties needed for shape changes, cell migration, or tissue morphogenesis, which rest on the organization of internal polarity and cytoskeleton (Levayer and Lecuit, 2012; Mogilner and Keren, 2009). Thus, our data reinforce a concept that morphogenesis may primarily emerge from spatial surface mechanical properties patterned from intracellular biochemical organization.

We also discovered that the CW is highly dynamic at sites of polar growth, with variations in thickness amplitude reaching up to 30% of the mean, on a timescale of tens of minutes. Thickness on cell sides appeared more stable, although we did note some patterns of thickness translating away from cell tip (Videos S1 and S2), plausibly reflecting CW material flowing during cell growth (Abenza et al., 2015). We suggest that thickness fluctuations are indicative of a homeostatic system correcting thickness changes over time, needed to maintain CW

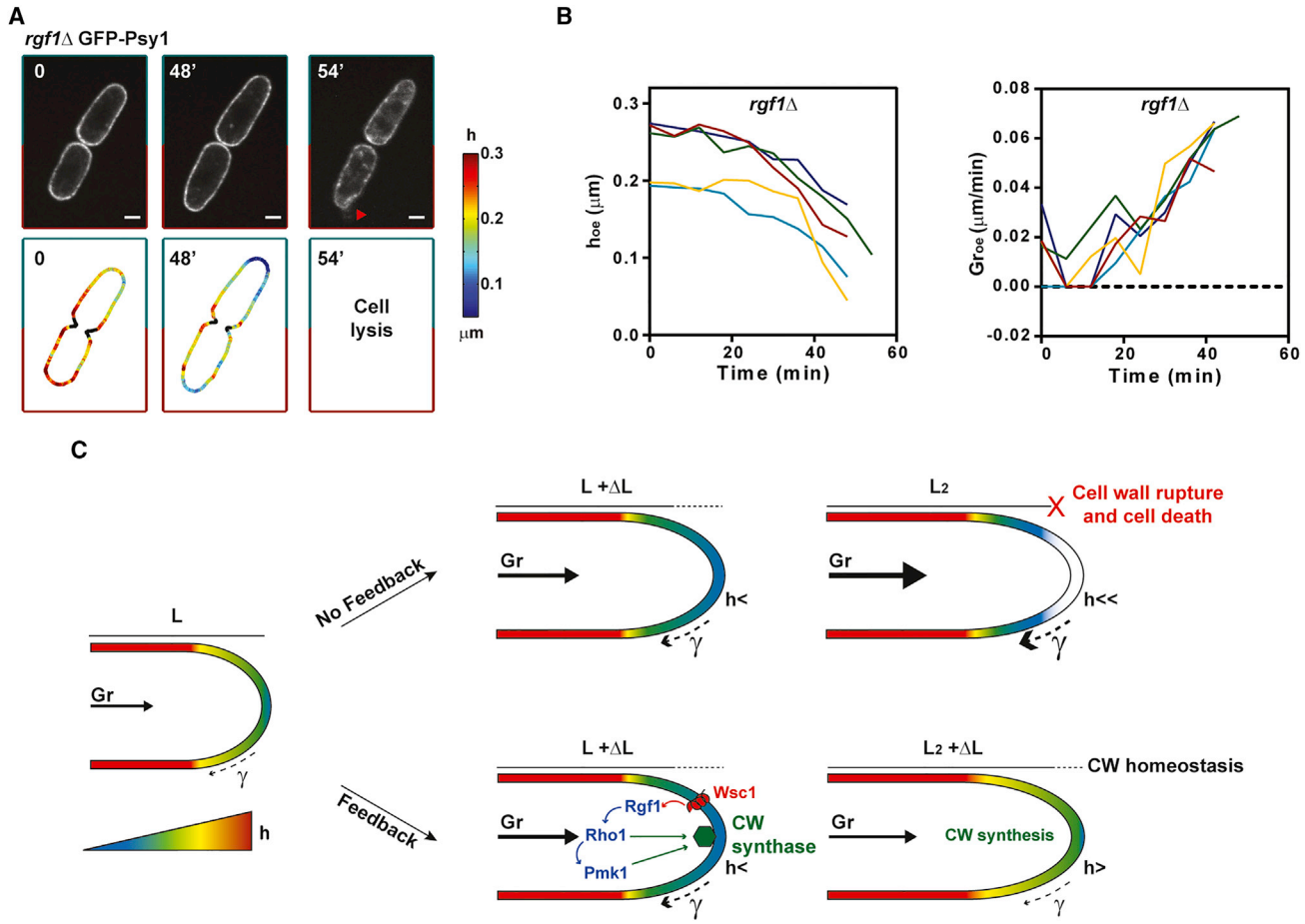

Figure 6. Implication of Thickness Homeostasis for Cell Survival during Normal Growth

(A) Time lapse of GFP-Psy1 and thickness maps for a representative lysing *rgf1Δ* cell. The arrowhead points to membrane leaking at cell tips after lysis.

(B) Evolution of old end thickness (h_{oe}) and growth rates (Gr_{oe}) in lysing *rgf1Δ* cells. The last point is recorded before lysis.

(C) Mechanosensing-based feedback for CW thickness homeostasis during cell growth. In absence of feedback, growth causes CW thinning, which promotes faster growth and further CW thinning, and so on, until the CW ruptures and cells lyse. The CWI pathway probes strain rate (or equivalently growth rates) through the surface protein Wsc1, which promotes the activation (directly or indirectly) of the Rho1-GEF Rgf1 to activate Rho1 and CW synthase. Rgf1 and Rho1 may directly act on synthesis or through the Pmk1 MAPK cascade. As a result, thickness increases, thereby reducing strain rate, yielding to a dynamic homeostatic system for CW mechanical properties and cell integrity. Scale bars, 2 μm.

See also Video S5.

mechanical parameters in an optimal range for growth and viability.

Although the current state of the art precludes dynamically computing changes in elastic moduli in growing cells, we suspect that similar homeostatic systems could also influence composition and bulk elasticity in addition to thickness. CW mechanical oscillations have been speculated to exist in rapidly growing cells such as pollen tubes and fungi, and to be related to cycles of Rho-GTPase activation or calcium signaling and variations in growth rates (Qin and Yang, 2011; Rojas et al., 2011). Fission yeast cells also exhibit oscillations in the abundance of active Cdc42 at cell tips (Das et al., 2012). However, the timescale of those oscillations is typically ten times shorter than that of the CW thickness fluctuations reported here, suggesting those behaviors may not be directly connected in a linear manner in this system. Mechanical fluctuations may thus represent a general readout for negative feedbacks acting at the biochemical or biomechanical level, instrumental to confer robustness to growth and viability (Howell et al., 2012).

Mechanical Homeostasis of the CW by the CWI

By screening through mutants, we uncovered a primary role for specific components of the CWI in probing CW strain and cell growth. Although the role of the CWI in general CW stress response and as a regulator of cell integrity during polar growth had been previously recognized in yeast, fungi, and plants (Banavar et al., 2018; Boisson-Dernier et al., 2013; Levin, 2005; Perez and Cansado, 2010), to our knowledge, those are the very first evidence of its direct role in dynamically controlling CW properties. The implication of Wsc1 in thickness homeostasis and in probing CW mechanical strain to regulate synthase polar domain localization and activity provides significant support that this protein may act as a direct CW mechanical sensor. Wsc1 localizes in patches at cell tips and has a predicted

serine/threonine rich domain spanning the CW (Cruz et al., 2013). It remains a puzzle to understand how such a configuration could directly probe lateral strain in the CW. Studies of *Saccharomyces cerevisiae* orthologs have proposed that WSC clustering may underlie mechanosensory activities (Heinisch et al., 2010). Further work will be needed to understand how those domains may probe the dynamic mechanical properties of the CW. Mutants in the second known fission yeast stress sensor, Mtl2, did not exhibit strong defects in homeostasis, suggesting a dominant function of Wsc1 here. This may be in agreement with the more diffuse localization of Mtl2 all around the cell surface (Cruz et al., 2013). Surprisingly, we found that loss of Rgf2, which has been suggested to physically interact with Wsc1 (Cruz et al., 2013), only had a mild effect on wall thickness homeostasis. *rgf1Δ* mutants exhibited the most pronounced effect, which may account for its severe lysis phenotype. This suggests a potential link between Wsc1 sensing and Rgf1 activation in wall homeostasis and a dominant role for Rgf1p in activating Rho1 in this response (Garcia et al., 2009a). However, we note that 70% of *rgf1Δ* mutant cells still survived, suggesting that a secondary system, likely based on Rgf2, may maintain some form of mechanical homeostasis. Finally, we also found that Pmk1 was required for homeostasis. This suggests that proper homeostasis involves at least partially the expression of a set of regulatory genes for CW construction. This would imply that the Pmk1 cascade acts at short time scales of several minutes, similar to turgor pressure-regulating Sty1/Hog1 MAPK (Miermont et al., 2011). Thus, the dynamic regulation of walled cells' mechanical properties, through rapid adaptation systems, appears as a central element to support viability not only in response to stress but also during normal growth and division (Rojas et al., 2017).

In addition to this homeostatic system protecting single cell thickness dynamics against erratic variations, we also observed thickness variations at the population level on the timescale of 3–4 hr. Although those variations could potentially account for some of the asymmetry in the number of points in certain homeostatic plots, they did not appear to contribute to their global trend (Figure S5). Those two effects were also largely independent: mutants delayed in specific cell cycle phases still exhibited fluctuations and homeostasis, and mutants in CWI components defective in short-term homeostasis displayed similar cell cycle thickness evolution at the population scale as WT (Figures S5H, S5I, and S6C). Further work will be needed to identify the mechanisms driving those large-scale variations, and their potential function.

Growth Control through Mechanochemical Systems

The notion that surface mechanics can alter the core spatiotemporal organization of cells through mechanosensing systems is becoming increasingly important in biology (DuFort et al., 2011). Examples range from the regulation of cell polarity, migration, and cell division up to tissue homeostasis (Bonazzi et al., 2014; Fink et al., 2011; Houk et al., 2012). Here, we uncovered a core function of mechanosensing in growth control. In this view, growth is directly perceived as a mechanical signal straining the CW, without any requirement for interactions with neighboring cells or the cell environment. When a cell begins to elongate rapidly, the strain rate increases, which turns on synthase activation by the CWI to assemble more wall, and vice versa. This homeostatic system thus compensates surface material dilution associated with growth to maintain its thickness around values compatible with survival. As thickness influences elongation rates, this system may also work toward controlling growth rate values around a defined range. Those findings thus have important implications for cell cycle control, as well as size homeostasis, which are both influenced by growth rate values. We speculate that cells may have evolved built-in mechanical properties and sensing elements that allow them to control expansion speeds adapted to their lifestyles. Future work studying similar problems of surface expansion control will inform on how those elements have been modified to guide the growth of rapidly expanding cells such as those in fungi and plants, or slowly growing cells such as those of animals.

STAR★METHODS

Detailed methods are provided in the online version of this paper and include the following:

- KEY RESOURCES TABLE
- CONTACT FOR REAGENT AND RESOURCE SHARING
- EXPERIMENTAL MODEL AND SUBJECT DETAILS
  - Yeast Strains, Media and Genetics
  - Drug Treatments
- METHOD DETAILS
  - Microscopy
  - Transmission Electron Microscopy
  - Microfabricated Channels
  - Turgor Pressure Manipulation by Sorbitol Addition
- QUANTIFICATION AND STATISTICAL ANALYSIS
  - Image Analysis
  - Strain-Stress Assay Simulation
  - Spectrum Analysis of Thickness Fluctuations
  - Analytical Models for Tip Thickness Fluctuations
  - 3D Cell Growth Model
- DATA AND SOFTWARE AVAILABILITY

SUPPLEMENTAL INFORMATION

Supplemental Information includes six figures and five videos and can be found with this article online at https://doi.org/10.1016/j.devcel.2018.03.022.

ACKNOWLEDGMENTS

The authors acknowledge P. Perez, Y. Sanchez, H. Valdivieso, T. Toda, T. Nakamura (YGRC/NBRP Japan), and J.Q. Wu for sharing material. We acknowledge the ImagoSeine core facility of the Institut Jacques Monod, member of IBiSA and France-BioImaging (ANR-10-INBS-04) infrastructures. A.B. is supported by Institut Universitaire de France. The Minc laboratory is supported by the CNRS and grants from the FP7 CIG program (no. 303821), ITN "FungiBrain" (no. 607963), and the European Research Council (CoG Forcaster no. 647073).

AUTHOR CONTRIBUTIONS

V.D., A.H., H.D.B., R.L.B., and N.M. performed experiments. V.D., H.T., D.E., and N.M. developed image analysis scripts. E.C. and A.B. performed modeling. V.D., A.B., and N.M. designed the research and wrote the manuscript.

DECLARATION OF INTERESTS

A patent on this method was deposited under the number FR1657801 on August 17, 2016.

Received: October 11, 2017
Revised: February 5, 2018
Accepted: March 26, 2018
Published: April 23, 2018

REFERENCES

Abenza, J.F., Couturier, E., Dodgson, J., Dickmann, J., Chessel, A., Dumais, J., and Carazo Salas, R.E. (2015). Wall mechanics and exocytosis define the shape of growth domains in fission yeast. Nat. Commun. *6*, 8400.

Arellano, M., Durán, A., and Pérez, P. (1996). Rho 1 GTPase activates the (1-3) beta-D-glucan synthase and is involved in *Schizosaccharomyces pombe* morphogenesis. EMBO J. *15*, 4584–4591.

Arellano, M., Valdivieso, M.H., Calonge, T.M., Coll, P.M., Duran, A., and Perez, P. (1999). *Schizosaccharomyces pombe* protein kinase C homologues, pck1p and pck2p, are targets of rho1p and rho2p and differentially regulate cell integrity. J. Cell Sci. *112* (Pt 20), 3569–3578.

Atilgan, E., Magidson, V., Khodjakov, A., and Chang, F. (2015). Morphogenesis of the fission yeast cell through cell wall expansion. Curr. Biol. *25*, 2150–2157.

Banavar, S.P., Gomez, C., Trogdon, M., Petzold, L.R., Yi, T.M., and Campas, O. (2018). Mechanical feedback coordinates cell wall expansion and assembly in yeast mating morphogenesis. PLoS Comput. Biol. *14*, e1005940.

Bastmeyer, M., Deising, H.B., and Bechinger, C. (2002). Force exertion in fungal infection. Annu. Rev. Biophys. Biomol. Struct. *31*, 321–341.

Bendezu, F.O., and Martin, S.G. (2011). Actin cables and the exocyst form two independent morphogenesis pathways in the fission yeast. Mol. Biol. Cell *22*, 44–53.

Boisson-Dernier, A., Lituiev, D.S., Nestorova, A., Franck, C.M., Thirugnanarajah, S., and Grossniklaus, U. (2013). ANXUR receptor-like kinases coordinate cell wall integrity with growth at the pollen tube tip via NADPH oxidases. PLoS Biol. *11*, e1001719.

Bonazzi, D., Haupt, A., Tanimoto, H., Delacour, D., Salort, D., and Minc, N. (2015). Actin-based transport adapts polarity domain size to local cellular curvature. Curr. Biol. *25*, 2677–2683.

Bonazzi, D., Julien, J.D., Romao, M., Seddiki, R., Piel, M., Boudaoud, A., and Minc, N. (2014). Symmetry breaking in spore germination relies on an interplay between polar cap stability and spore wall mechanics. Dev. Cell *28*, 534–546.

Boudaoud, A. (2003). Growth of walled cells: from shells to vesicles. Phys. Rev. Lett. *91*, 018104.

Cassone, A., Kerridge, D., and Gale, E.F. (1979). Ultrastructural changes in the cell wall of *Candida albicans* following cessation of growth and their possible relationship to the development of polyene resistance. J. Gen. Microbiol. *110*, 339–349.

Chang, F., and Huang, K.C. (2014). How and why cells grow as rods. BMC Biol. *12*, 54.

Chang, F., and Martin, S.G. (2009). Shaping fission yeast with microtubules. Cold Spring Harb. Perspect. Biol. *1*, a001347.

Charvin, G., Cross, F.R., and Siggia, E.D. (2008). A microfluidic device for temporally controlled gene expression and long-term fluorescent imaging in unperturbed dividing yeast cells. PLoS One *3*, e1468.

Chugh, P., Clark, A.G., Smith, M.B., Cassani, D.A.D., Dierkes, K., Ragab, A., Roux, P.P., Charras, G., Salbreux, G., and Paluch, E.K. (2017). Actin cortex architecture regulates cell surface tension. Nat. Cell Biol. *19*, 689–697.

Clark, A.G., Dierkes, K., and Paluch, E.K. (2013). Monitoring actin cortex thickness in live cells. Biophys. J. *105*, 570–580.

Cortes, J.C., Carnero, E., Ishiguro, J., Sanchez, Y., Duran, A., and Ribas, J.C. (2005). The novel fission yeast (1,3)beta-D-glucan synthase catalytic subunit Bgs4p is essential during both cytokinesis and polarized growth. J. Cell Sci. *118*, 157–174.

Cosgrove, D.J. (2005). Growth of the plant cell wall. Nat. Rev. Mol. Cell Biol. *6*, 850–861.

Cruz, S., Muñoz, S., Manjón, E., García, P., and Sanchez, Y. (2013). The fission yeast cell wall stress sensor-like proteins Mtl2 and Wsc1 act by turning on the GTPase Rho1p but act independently of the cell wall integrity pathway. Microbiologyopen *2*, 778–794.

Dagdas, Y.F., Yoshino, K., Dagdas, G., Ryder, L.S., Bielska, E., Steinberg, G., and Talbot, N.J. (2012). Septin-mediated plant cell invasion by the rice blast fungus, *Magnaporthe oryzae*. Science *336*, 1590–1595.

Das, M., Drake, T., Wiley, D.J., Buchwald, P., Vavylonis, D., and Verde, F. (2012). Oscillatory dynamics of Cdc42 GTPase in the control of polarized growth. Science *337*, 239–243.

Das, M., Wiley, D.J., Chen, X., Shah, K., and Verde, F. (2009). The conserved NDR kinase Orb6 controls polarized cell growth by spatial regulation of the small GTPase Cdc42. Curr. Biol. *19*, 1314–1319.

Das, M., Wiley, D.J., Medina, S., Vincent, H.A., Larrea, M., Oriolo, A., and Verde, F. (2007). Regulation of cell diameter, For3p localization, and cell symmetry by fission yeast Rho-GAP Rga4p. Mol. Biol. Cell *18*, 2090–2101.

Davi, V., and Minc, N. (2015). Mechanics and morphogenesis of fission yeast cells. Curr. Opin. Microbiol. *28*, 36–45.

Davidson, R., Laporte, D., and Wu, J.Q. (2015). Regulation of Rho-GEF Rgf3 by the arrestin Art1 in fission yeast cytokinesis. Mol. Biol. Cell *26*, 453–466.

DeBerardinis, R.J., Lum, J.J., Hatzivassiliou, G., and Thompson, C.B. (2008a). The biology of cancer: metabolic reprogramming fuels cell growth and proliferation. Cell Metab. *7*, 11–20.

Deberardinis, R.J., Sayed, N., Ditsworth, D., and Thompson, C.B. (2008b). Brick by brick: metabolism and tumor cell growth. Curr. Opin. Genet. Dev. *18*, 54–61.

Drake, T., and Vavylonis, D. (2013). Model of fission yeast cell shape driven by membrane-bound growth factors and the cytoskeleton. PLoS Comput. Biol. *9*, e1003287.

Dudin, O., Bendezu, F.O., Groux, R., Laroche, T., Seitz, A., and Martin, S.G. (2015). A formin-nucleated actin aster concentrates cell wall hydrolases for cell fusion in fission yeast. J. Cell Biol. *208*, 897–911.

DuFort, C.C., Paszek, M.J., and Weaver, V.M. (2011). Balancing forces: architectural control of mechanotransduction. Nat. Rev. Mol. Cell Biol. *12*, 308–319.

Fantes, P., and Nurse, P. (1977). Control of cell size at division in fission yeast by a growth-modulated size control over nuclear division. Exp. Cell Res. *107*, 377–386.

Fink, J., Carpi, N., Betz, T., Betard, A., Chebah, M., Azioune, A., Bornens, M., Sykes, C., Fetler, L., Cuvelier, D., et al. (2011). External forces control mitotic spindle positioning. Nat. Cell Biol. *13*, 771–778.

Flor-Parra, I., Zhurinsky, J., Bernal, M., Gallardo, P., and Daga, R.R. (2014). A Lallzyme MMX-based rapid method for fission yeast protoplast preparation. Yeast *31*, 61–66.

Garcia, P., Garcia, I., Marcos, F., de Garibay, G.R., and Sanchez, Y. (2009a). Fission yeast rgf2p is a rho1p guanine nucleotide exchange factor required for spore wall maturation and for the maintenance of cell integrity in the absence of rgf1p. Genetics *181*, 1321–1334.

Garcia, P., Tajadura, V., Garcia, I., and Sanchez, Y. (2006). Rgf1p is a specific Rho1-GEF that coordinates cell polarization with cell wall biogenesis in fission yeast. Mol. Biol. Cell *17*, 1620–1631.

Garcia, P., Tajadura, V., and Sanchez, Y. (2009b). The Rho1p exchange factor Rgf1p signals upstream from the Pmk1 mitogen-activated protein kinase pathway in fission yeast. Mol. Biol. Cell *20*, 721–731.

Harold, F.M. (2002). Force and compliance: rethinking morphogenesis in walled cells. Fungal Genet. Biol. *37*, 271–282.

Harris, L.K., and Theriot, J.A. (2016). Relative rates of surface and volume synthesis set bacterial cell size. Cell *165*, 1479–1492.

Heinisch, J.J., Dupres, V., Wilk, S., Jendretzki, A., and Dufrene, Y.F. (2010). Single-molecule atomic force microscopy reveals clustering of the yeast plasma-membrane sensor Wsc1. PLoS One *5*, e11104.

Hepler, P.K., Vidali, L., and Cheung, A.Y. (2001). Polarized cell growth in higher plants. Annu. Rev. Cell Dev. Biol. *17*, 159–187.

Holley, R.W. (1975). Control of growth of mammalian cells in cell culture. Nature *258*, 487–490.

Hong, L., Dumond, M., Tsugawa, S., Sapala, A., Routier-Kierzkowska, A.L., Zhou, Y., Chen, C., Kiss, A., Zhu, M., Hamant, O., et al. (2016). Variable cell growth yields reproducible organ development through spatiotemporal averaging. Dev. Cell *38*, 15–32.

Horiseberger, M., and Rosset, J. (1977). Localization of alpha-Galactomannan on the surface of *Schizosaccharomyces pombe* cells by scanning electron microscopy. Arch. Microbiol. *112*, 123–126.

Houk, A.R., Jilkine, A., Mejean, C.O., Boltyanskiy, R., Dufresne, E.R., Angenent, S.B., Altschuler, S.J., Wu, L.F., and Weiner, O.D. (2012). Membrane tension maintains cell polarity by confining signals to the leading edge during neutrophil migration. Cell *148*, 175–188.

Howell, A.S., Jin, M., Wu, C.F., Zyla, T.R., Elston, T.C., and Lew, D.J. (2012). Negative feedback enhances robustness in the yeast polarity establishment circuit. Cell *149*, 322–333.

Huang, S., and Ingber, D.E. (1999). The structural and mechanical complexity of cell-growth control. Nat. Cell Biol. *1*, E131–E138.

Keegstra, K. (2010). Plant cell walls. Plant Physiol. *154*, 483–486.

Kelly, F.D., and Nurse, P. (2011). De novo growth zone formation from fission yeast spheroplasts. PLoS One *6*, e27977.

Kierzkowski, D., Nakayama, N., Routier-Kierzkowska, A.L., Weber, A., Bayer, E., Schorderet, M., Reinhardt, D., Kuhlemeier, C., and Smith, R.S. (2012). Elastic domains regulate growth and organogenesis in the plant shoot apical meristem. Science *335*, 1096–1099.

Lander, A.D. (2011). Pattern, growth, and control. Cell *144*, 955–969.

Levayer, R., and Lecuit, T. (2012). Biomechanical regulation of contractility: spatial control and dynamics. Trends Cell Biol. *22*, 61–81.

Levin, D.E. (2005). Cell wall integrity signaling in *Saccharomyces cerevisiae*. Microbiol. Mol. Biol. Rev. *69*, 262–291.

Lew, R.R. (2011). How does a hypha grow? The biophysics of pressurized growth in fungi. Nat. Rev. Microbiol. *9*, 509–518.

Lipke, P.N., and Ovalle, R. (1998). Cell wall architecture in yeast: new structure and new challenges. J. Bacteriol. *180*, 3735–3740.

Ma, H., Snook, L.A., Kaminskyj, S.G., and Dahms, T.E. (2005). Surface ultrastructure and elasticity in growing tips and mature regions of *Aspergillus* hyphae describe wall maturation. Microbiology *151*, 3679–3688.

Mahadevan, L., and Mitchison, T.J. (2005). Cell biology: powerful curves. Nature *435*, 895–897.

Marshall, W.F., Young, K.D., Swaffer, M., Wood, E., Nurse, P., Kimura, A., Frankel, J., Wallingford, J., Walbot, V., Qu, X., et al. (2012). What determines cell size? BMC Biol. *10*, 101.

Martins, I.M., Cortes, J.C., Munoz, J., Moreno, M.B., Ramos, M., Clemente-Ramos, J.A., Duran, A., and Ribas, J.C. (2011). Differential activities of three families of specific beta(1,3)glucan synthase inhibitors in wild-type and resistant strains of fission yeast. J. Biol. Chem. *286*, 3484–3496.

Mata, J., and Nurse, P. (1997). tea1 and the microtubular cytoskeleton are important for generating global spatial order within the fission yeast cell. Cell *89*, 939–949.

McKenna, S.T., Kunkel, J.G., Bosch, M., Rounds, C.M., Vidali, L., Winship, L.J., and Hepler, P.K. (2009). Exocytosis precedes and predicts the increase in growth in oscillating pollen tubes. Plant Cell *21*, 3026–3040.

Miermont, A., Uhlendorf, J., McClean, M., and Hersen, P. (2011). The dynamical systems properties of the HOG signaling cascade. J. Signal Transduct. *2011*, 930940.

Milani, P., Mirabet, V., Cellier, C., Rozier, F., Hamant, O., Das, P., and Boudaoud, A. (2014). Matching patterns of gene expression to mechanical stiffness at cell resolution through quantitative tandem epifluorescence and nanoindentation. Plant Physiol. *165*, 1399–1408.

Minc, N., Boudaoud, A., and Chang, F. (2009). Mechanical forces of fission yeast growth. Curr. Biol. *19*, 1096–1101.

Mitchison, J.M., and Nurse, P. (1985). Growth in cell length in the fission yeast *Schizosaccharomyces pombe*. J. Cell Sci. *75*, 357–376.

Mogilner, A., and Keren, K. (2009). The shape of motile cells. Curr. Biol. *19*, R762–R771.

Muñoz, J., Cortés, J.C., Sipiczki, M., Ramos, M., Clemente-Ramos, J.A., Moreno, M.B., Martins, I.M., Peréz, P., and Ribas, J.C. (2013). Extracellular cell wall beta(1,3)glucan is required to couple septation to actomyosin ring contraction. J. Cell Biol. *203*, 265–282.

Murray, S. (2008). High pressure freezing and freeze substitution of *Schizosaccharomyces pombe* and *Saccharomyces cerevisiae* for TEM. Methods Cell Biol. *88*, 3–17.

Mutoh, T., Nakano, K., and Mabuchi, I. (2005). Rho1-GEFs Rgf1 and Rgf2 are involved in formation of cell wall and septum, while Rgf3 is involved in cytokinesis in fission yeast. Genes Cells *10*, 1189–1202.

Nakamura, T., Nakamura-Kubo, M., Hirata, A., and Shimoda, C. (2001). The *Schizosaccharomyces pombe* spo3+ gene is required for assembly of the forespore membrane and genetically interacts with psy1(+)-encoding syntaxin-like protein. Mol. Biol. Cell *12*, 3955–3972.

Nakayama, N., Smith, R.S., Mandel, T., Robinson, S., Kimura, S., Boudaoud, A., and Kuhlemeier, C. (2012). Mechanical regulation of auxin-mediated growth. Curr. Biol. *22*, 1468–1476.

Novick, P., and Schekman, R. (1979). Secretion and cell-surface growth are blocked in a temperature-sensitive mutant of *Saccharomyces cerevisiae*. Proc. Natl. Acad. Sci. USA *76*, 1858–1862.

Osumi, M. (2012). Visualization of yeast cells by electron microscopy. J. Electron Microsc. (Tokyo) *61*, 343–365.

Peaucelle, A., Braybrook, S.A., Le Guillou, L., Bron, E., Kuhlemeier, C., and Hofte, H. (2011). Pectin-induced changes in cell wall mechanics underlie organ initiation in *Arabidopsis*. Curr. Biol. *21*, 1720–1726.

Perez, P., and Cansado, J. (2010). Cell integrity signaling and response to stress in fission yeast. Curr. Protein Pept. Sci. *11*, 680–692.

Perez, P., and Ribas, J.C. (2004). Cell wall analysis. Methods *33*, 245–251.

Petersen, J., Heitz, M.J., and Hagan, I.M. (1998). Conjugation in *S. pombe*: identification of a microtubule-organising centre, a requirement for microtubules and a role for Mad2. Curr. Biol. *8*, 963–966.

Qin, Y., and Yang, Z. (2011). Rapid tip growth: insights from pollen tubes. Semin. Cell Dev. Biol. *22*, 816–824.

Rojas, E., Theriot, J.A., and Huang, K.C. (2014). Response of *Escherichia coli* growth rate to osmotic shock. Proc. Natl. Acad. Sci. USA *111*, 7807–7812.

Rojas, E.R., Hotton, S., and Dumais, J. (2011). Chemically mediated mechanical expansion of the pollen tube cell wall. Biophys. J. *101*, 1844–1853.

Rojas, E.R., Huang, K.C., and Theriot, J.A. (2017). Homeostatic cell growth is accomplished mechanically through membrane tension inhibition of cell-wall synthesis. Cell Syst. *5*, 578–590.e6.

Salbreux, G., Charras, G., and Paluch, E. (2012). Actin cortex mechanics and cellular morphogenesis. Trends Cell Biol. *22*, 536–545.

Silhavy, T.J., Kahne, D., and Walker, S. (2010). The bacterial cell envelope. Cold Spring Harb. Perspect. Biol. *2*, a000414.

Tatebe, H., Nakano, K., Maximo, R., and Shiozaki, K. (2008). Pom1 DYRK regulates localization of the Rga4 GAP to ensure bipolar activation of Cdc42 in fission yeast. Curr. Biol. *18*, 322–330.

Thompson, B.J. (2010). Developmental control of cell growth and division in *Drosophila*. Curr. Opin. Cell Biol. *22*, 788–794.

Villar-Tajadura, M.A., Coll, P.M., Madrid, M., Cansado, J., Santos, B., and Perez, P. (2008). Rga2 is a Rho2 GAP that regulates morphogenesis and cell integrity in *S. pombe*. Mol. Microbiol. *70*, 867–881.

Yanagisawa, M., Desyatova, A.S., Belteton, S.A., Mallery, E.L., Turner, J.A., and Szymanski, D.B. (2015). Patterning mechanisms of cytoskeletal and cell wall systems during leaf trichome morphogenesis. Nat. Plants *1*, 15014.

Zegman, Y., Bonazzi, D., and Minc, N. (2015). Measurement and manipulation of cell size parameters in fission yeast. Methods Cell Biol. *125*, 423–436.

STAR★METHODS

KEY RESOURCES TABLE

REAGENT or RESOURCE	SOURCE	IDENTIFIER
Experimental Models: Organisms/Strains		
h- *cut11-RFP:HygR GFP-psy1:leu* (*leu1-32 ura4-D18*)	This study	VD11
h- *CRIB-tdTomato:ura GFP-psy1:leu* (*leu1-32 ura4-D18*)	This study	VD20
h- *tea1::NatMX CRIB-tdTomato:ura GFP-psy1:leu* (*leu1-32 ura4-D18)*	This study	VD31
h+*CRIB-tdTomato:ura GFP-psy1:leu* (*leu1-32 ura4-D18*)	This study	VD39
h- *CRIB-tdTomato:ura GFP-psy1:leu orb6-25* (*leu1-32 ura4-D18*)	This study	VD50
h+ *GFP-psy1:ade bgs4::ura4 RFP-bgs4-Leu* (*leu1-32 ura4-D18 ade6*)	This study	VD57
h- *GFP-psy1:ade bgs4::ura4 RFP-bgs4-Leu Leu* (*leu1-32 ura4-D18 ade6*)	This study	VD58
h- *rga2::KanMX bgs4::ura4 RFP-bgs4-Leu GFP-psy1:ade* (*leu1-32 ura4-D18*)	This study	VD72
h- *rga4::KanMX bgs4::ura4 RFP-bgs4-Leu GFP-psy1:ade* (*leu1-32 ura4-D18*)	This study	VD81
h- *GFP-psy1:ade pREP3X-pck2* (*leu1-32 ade6*)	This study	VD93
h- *GFP-psy1:ade pRep3X empty vector* (*leu1-32 ade6*)	This study	VD105
h+ *GFP-psy1:ade pRep3X-rho1G15V*	This study	VD69
h- *tea1::NatMX GFP-psy1:ade bgs4::ura4 RFP-bgs4:leu* (*leu1-32 ura4-D18 ade6*)	This study	VD110
h- cwg1-1 GFP-psy1:leu CRIB-tdTomato:ura (*leu1-32 ura4-D18*)	This study	VD115
h+ wsc1::KanMX GFP-psy1:ade bgs4::ura4 RFP-bgs4:leu (*leu1-32 ura4-D18 ade6*)	This study	VD158
h- mtl2::KanMX GFP-psy1:ade bgs4::ura4 RFP-bgs4:leu (*leu1-32 ura4-D18 ade6*)	This study	VD160
h^{90} *rga4::KanMX GFP-psy1:ade bgs4::ura4 RFP-bgs4:leu* (*leu1-32 ura4-D18 ade6*)	This study	VD162
h- *pck2 :leu GFP-psy1:ade*	This study	VD109
h+ rgf2::ura GFP-psy1:ade (*leu1-32 ura4-D18 ade6*)	This study	VD164
h+ *rgf1::KanMX GFP-psy1:ade* (*leu1-32 ura4-D18 ade6*)	This study	VD167
h+ pmk1:ura GFP-psy1:leu (*leu1-32 ura4-D18*)	This study	VD173
h+ *pRep3X-Phluorin-ritc* (*leu1-32*)	This study	NM164
h+ *Leu:GFP-psy1* (*leu1-32 ura4-D18*)	This study	NM468
h- *Leu:GFP-psy1* (*leu1-32 ura4-D18*)	This study	NM469
h+ *shk1:GFP-LactC2:leu*	This study	AH159
h+ *shk1:GFP-8+:leu (ura4-D18 ade6*)	This study	AH208
h+ gpd1::NatMX GFP-bgs4:leu bgs4::ura (*leu1-32 ura4-D18 ade6*)	This study	NM266
h- gpd1::NatMX wsc1::KanMX GFP-bgs4:leu bgs4::ura (*ade6*)	This study	AH330
h- *gpd1::NatMX P3nmt1-pkc1(HR1-C2)-ECitrine* (*ura4-D18*)	This study	AH385
h- gpd1::NatMX wsc1::KanMX P3nmt1-pkc1(HR1-C2)-ECitrine (*leu1-32 ura4-D18 ade6*)	This study	AH401
h+ *cdc10-M17 GFP-psy1:ade bgs4::ura4 RFP-bgs4-Leu (ade6)*	This study	VD122
h- *cdc25-22 GFP-psy1:ade bgs4::ura4 RFP-bgs4-Leu* (*leu1-32 ura4-D18 ade6*)	This study	VD123
Chemicals, Peptides, and Recombinant Proteins		
Zymolyase	ZymoResearch	E1004
LatrunculinA	Sigma-Aldrich	L5163
Caspofungin	Sigma-Aldrich	SML0425
Gs-IB_4 -Alexafluor647	ThermoFisher	I32450
Bs-IB4-TRIC	Sigma-Aldrich	N/A

CONTACT FOR REAGENT AND RESOURCE SHARING

Further information and requests for resources and reagents should be directed to and will be fulfilled by the Lead Contact, Nicolas Minc (nicolas.minc@ijm.fr).

EXPERIMENTAL MODEL AND SUBJECT DETAILS

Yeast Strains, Media and Genetics

Standard methods for *Schizosaccharomyces pombe* media and genetic manipulations were used (http://www-bcf.usc.edu/~forsburg/). Strains used in this study are listed in Key Resource Table below. Cells were grown at 25°C in yeast extract plus 5 supplements (YE5S) media unless otherwise indicated. Over-expression driven from plasmids, was induced by growing cells at 25°C in Edinburgh minimal medium (EMM) + supplements without thiamine for 24-36 h for Pck2, Rho1-G15V, and 48h for the membrane probe GFP-RITC and for ActRho1-Cit. Starvation of wild-type (wt) cells was induced by over-growing cells in liquid YE5S for an additional 16 h after they had reached stationary phase (OD_{600}>1). Recovery from starvation in *tea1Δ* cells was induced by growing cells on YE5S plates for > 3 days, and subsequently transferring them in YE5S liquid media for 2-3h before observation or directly on 2% YE5S agar pads for time lapse. Temperature sensitive alleles, *cwg1-1*, *orb6-25, cdc25-22* and *cdc10-M17* were grown in liquid culture at permissive temperature (25°C) and switched to restrictive temperature (36°C) for 6h, 2h, 1h and 3h respectively, before observation. Spores were obtained from homothallic h90 strains, or from heterothallic crosses. Freshly growing cells were placed on malt extract (ME) solid media for 3 days. Mating mixtures were then digested for 1h at room temperature in a 1/200 glusulase solution in water to kill vegetative cells, washed three times in water, and incubated for >7h in YE5S before observation (Bonazzi et al., 2014). Spheroplasts were generated from exponentially growing cells in YE5S, which were washed twice in digestion buffer (0.1M Citric Acid 0.1 M NaCitrate pH = 5.8; 1.2 M Sorbitol) and subsequently treated with Lallzyme (0.1 g/ml) during 1h at room temperature. Newly formed spheroplasts, were washed twice in YE5S+1.2 M Sorbitol, and let to regenerate at 25°C for >16h, until outgrowing protrusions appeared (Flor-Parra et al., 2014). To image mating protrusions, homothallic cells growing exponentially in liquid YE5S were placed on solid ME until mating protrusion appeared (>5h). Cells were then harvested, labeled and imaged directly.

Drug Treatments

Cell wall digestion was achieved by incubating cells with 5000U/ml Zymolyase (ZymoResearch) at room temperature, and imaged immediately after treatment and 1h after. LatrunculinA (Sigma) was used at a final concentration of 100 μM from a 100X stock in DMSO. Cells were incubated for 30' at room temperature before imaging. For Caspofungin experiments, cells were plated on 2% agar pads made with YE5S+10 mg/ml *Gs*-IB_4 -Alexafluor647 and a final concentration of 5μM Caspofungin.

METHOD DETAILS

Microscopy

Live-cell imaging was performed on two different inverted spinning-disk confocal microscopes equipped with motorized stages, automatic focus and controlled with MetaMorph® (Microscopy Automation & Image Analysis Software). The first one (Nikon Ti-Eclipse), is equipped with a Yokogawa CSU-X1FW spinning head, and an EM-CCD camera (Hamamatsu), a 100× oil-immersion objective (Nikon CFI Plan Apo DM 100×/1.4 NA) and a 2.5× magnifying lens, yielding a pixel size of 43 nm. The second one (Leica DMI8), is equipped with a Yokogawa CSU-W1 spinning head, and a sCMOS Orca-Flash 4 V2+ (Hamamatsu) a 100× oil-immersion objective (Leica Plan Apo DM 100×oil/1.4 NA), yielding a pixel size of 70 nm.

Image registration was performed by imaging a slide containing a solution of 0.2 μm TetraSpeck™ microspheres (Thermofisher). A field containing one bead, was moved sequentially using the Metamorph function "ScanStage" coupled with a home built plugin to allow multi-dimensional acquisition. This generated an array of fluorescent spots imaged at multiple wavelength, for image registration (Figure S1A, see below). Alternatively, single images of a dense field of non-aggregated beads, could be used to generate the vectorial map.

For cell wall thickness measurements, cells were pre-labeled in growth media containing 5 μg/ml of labelled lectin from *Griffonia simplicifolia* (alias *Bandeiraea simplicifolia*) *Gs*-IB_4-Alexafluor647 or *Bs*-IB_4-TRIC (Horiseberger and Rosset, 1977). For single-time imaging, cells were placed between a glass slide and a coverslip and imaged within 20 min. For time-lapse imaging, cells were placed on 2% agar-pads made of YE5S containing 10 μg/ml *Gs*-IB_4-Alexafluor647 and covered with a coverslip. We detected small differences in thickness between experiments performed in glass slides (202±19 nm, n=169) and in agar pads (177±28 nm, n=66), with glass slides generally yielding thicker values, which could be attributed to small cell deformation or starvation. For this reason, all experiments done in mutants, drugs or by modifying protocols are associated with a control measured in the same manner. Comparison with electron microscopy was performed on agar pads. Imaging was generally performed at room temperature (22-26°C), with controlled humidity (>30%). For temperature-sensitive mutants, the temperature of the sample was kept at 36°C by using either a temperature controlled cage or an objective heater (Bioptechs).

Transmission Electron Microscopy

For high pressure freezing (Figure 1B), cells were grown in liquid and harvested on a vacuum filter. The pellets were transferred to 100μm deep flat carriers (Leica Microsystems). Samples were then cryo-immobilized by HPF (EM-Pact2, Leica microsystems). Freeze substitution was performed with an AFS2 (Leica Microsystems) in 2% Osmium, 0,1% Uranyl acetate in pure acetone following protocols described in (Murray, 2008). Samples were rinsed three times with acetone and infiltrated with gradually increasing

concentrations of an Epon resin mix (Agar scientific) and polymerized for 24h at 60°C. Ultrathin (70 nm) sections were generated with an ultramicrotome (UC6, Leica Microsystems) and collected on formvar/carbon-coated grids. Sections were post-stained by aqueous 2% uranyl acetate and lead citrate before imaging.

For chemical fixation (Figure 1B), samples were fixed with 2% glutaraldehyde in Phosphate Buffer 0.2M buffer, for 1h at room temperature followed by overnight fixation at 4°C and post-fixed with 2% osmium tetroxide in water. Samples were dehydrated through a graded series of ethanol and propylene oxide and embedded in epoxy resin. Ultrathin (70 nm) sections were generated with an ultramicrotome (UC6, Leica Microsystems) and collected on formvar/carbon-coated copper grids. Sections were then post-stained by aqueous 4% uranyl acetate and lead citrate.

For Correlative Light Electron Microscopy (CLEM), cells were immobilized on specialized bottom glass petri-dish with micro-grids for image position registrations (MatTek) (Figure S2D). Dishes were pre-treated with 1 mg/ml poly-lysine, followed by 0.1 mg/ml *Bs*-IB_4-lectin and rinsed with water and YE5S. Cells, pre-labeled with *Gs*-IB_4-Alexafluor647, were placed on the dish, let to sediment and stick for ~15 min, and were subsequently rinsed vigorously with YE5S to detach non-sticking cells. Cells were then fixed with 2% glutaraldehyde in YE5S media for 2h at 4°C. Cells were then imaged in light microscopy and their positions were recorded using marks on the micro-grid. The samples were post-fixed with 2% osmium tetroxide in water and dehydrated through a graded series of ethanol and embedded in epoxy resin, which tends to stick to the micro-grid. Ultrathin (70 nm) sections of selected regions of the micro-grid, were generated with an ultramicrotome (Ultracut UC6, Leica) and collected on formvar/carbon-coated copper grids. Sections were then post-stained by aqueous 4% uranyl acetate and lead citrate. We observed often a partial cell deformation recorded in TEM, plausibly due to resin embedding. In spite of this, the cell wall remained intact in most cases. All samples were observed in a Tecnai12 (FEI, The Netherlands) transmission electron microscope at 80 kV equipped with a 1K×1K Keen View camera.

Microfabricated Channels

Microchannels used to manipulate cell diameter, were fabricated in PDMS from a silicon wafer using classical soft-lithography procedures, as described in (Zegman et al., 2015) (Figure 3H). Homothallic *rga4Δ* spores were inserted into the PDMS microchannels, let to germinate for >20h at 25°C, and subsequently rinsed with YE5S + *Gs*-IB_4 -Alexafluor647 for 2h before imaging.

Turgor Pressure Manipulation by Sorbitol Addition

For sorbitol treatments cells were pre-labeled in growth media containing 5 μg/ml of labelled lectin *Gs*-IB_4 -Alexafluor647, then placed in PDMS microfluidic chambers between a dialysis membrane and a coverslip, which allowed live fluid exchange (Charvin et al., 2008). Cells were left in the chamber 40 minutes for adaptation before starting the assay. For Young modulus estimations cells were imaged, then immediately rinsed in the same media containing 1.5 M sorbitol and imaged again within the next 4 minutes. For growth rate manipulation, cells were imaged every 2 minutes for 10 minutes in YE5S + *Gs*-IB_4-Alexafluor647, then washed in the same media containing 0.5M Sorbitol and imaged for 30-60 minutes. In this context, we noted that the induced ActRho1-Cit strain exhibited higher growth rate than unlabeled controls, suggesting some putative levels of non-functionality of the probe (Figure S4H).

QUANTIFICATION AND STATISTICAL ANALYSIS

Image Analysis

Cell Wall Thickness Measurement

The analysis pipeline to compute CW thickness was fully automated with a manual check option at each step. All the analyses were performed using custom scripts written in MATLAB (Mathworks, R2013a equipped with Image Processing and Statistics toolboxes). Initial cell segmentation was performed using either fluorescent membrane or lectin signals. The signal was first binarized using a threshold determined with the graythresh function. The cell contour was defined as the most outer set of pixels of the binarized signal. The coordinates corresponding to the points along the cell contour were then equally spaced with an interval of 1 pixel using a spline function. Typically, a single cell contour was represented by ~ 600-800 points for a pixel size of 43 nm. At each point of the contour, a 40 pixels long line perpendicular to the cell contour was defined as the normal to the tangent of the curve determined using 11 neighboring points (Figure 1A first panel, blue line). The membrane and lectin signals were scanned along these lines, leading to one dimensional intensity profiles for each signal at each position around the cell contour (Figure 1A second panel). The center of each intensity profile was identified by fitting a Gaussian function on 11 points around the point with maximum intensity. Each of these centers defined the XY coordinates of membrane and lectin along the contour of the cell. To correct for chromatic shifts, the coordinates of the wall were changed using the position-dependent chromatic shift vectorial map (Figure S1A, see next section). This first set of analyses defines the precise in-plane coordinates of both outlines of cell membrane and lectin signals (Figure 1A, third panel). Subsequently, novel lines perpendicular to the lectin boundary spaced by 1pixel were defined, following the same procedure as above (In Figure 1A second panel, only 1 out 10 of those lines are drawn, for clarity). The position of the cell membrane along the normal lines was defined as the intersection point between the normal line and the cell membrane. Finally, the local cell wall thickness h was computed as the distance between lectin and membrane coordinates along the normal line (Figure 1A third panel insert). Lateral resolution was estimated based on the lateral precision with which we could detect birth scars (~500 nm) (Figure 1A fourth panel, Figures 1C and S2E–S2G).

Chromatic Shift Correction

To correct for chromatic positional XY shifts between the channels used for the lectin and membrane signals across the field of view we used a ''point-by-point correction'' approach. In contrast to standard ''whole image'' alignment approaches (Clark et al., 2013), this produces a continuous vector field containing shifts for all pixels in the field of view, and can thus account for non-uniformity in the positional drift. Starting from arrays of 200 nm beads imaged at different wavelengths (see above), we first detect the particles positions with a sub-pixel precision (~20-25 nm) using a modified Matlab script available from M. Kilfoil lab (http://people.umass.edu/kilfoil/). The positions of the particles in the two channels (X1, Y1) and (X2, Y2) were then used to compute a sparse map of point-by-point shift vectors, defined as: V = (Vx, Vy) = (X2 – X1, Y2 – Y1) (with one channel used as the reference and features in the second one being aligned) (Figure S1A right panel). This sparse array was then used to generate a continuous point-by-point shift map. For this, each of the two 3-dimentional sets of data: (X1, Y1, Vx) and (X1, Y1, Vy) were fitted with a plane, which allows for computing a point-to-point shift vector Vi at any position (Xi, Yi) with a sub-pixel resolution close to the particle center detection limit (~20-25 nm) (Figure S1A). This map was finally used as an input in the cell wall thickness measurement scripts described above (Figure S1C).

To assess chromatic shifts in Z, we imaged a 3 μm deep Z stack with 10 nm spacing between slices of the same 200 nm beads in 5 different positions in the field of view in two wavelengths channels. To reproduce the distance of the cell center from the cover glass (about 2 μm), beads were embedded in 2% agar pad, and only beads at about 2 μm from the glass surface were imaged. For each stack the fluorescent peaks were detected using a Gaussian fit, and the shifts computed from the distance between the peaks. We found that this shift ranged typically from 0.1 to 0.4 μm, which corresponds to a maximum projected shift in thickness smaller than 30 nm that we neglected for the measurement (Figure S1B).

Generation and Analysis of Simulated Images

Simulated images were generated as described in (Clark et al., 2013), using custom scripts written in MATLAB. The simulation starts with two dimensional data, corresponding to a simple spherical cell shape of 3 μm diameter, drawn with a 5 nm resolution. The simulated cell has a cell membrane thickness of 15 nm and a cell wall thickness of 200 nm. To best represent the experimental imaging conditions, the cell membrane was assumed to be uniformly stained, and only 5 nm of the most outer part of the cell wall was uniformly stained in another color. To account for the experimental noise and finite background signals inside and outside of the cell, two different Gaussian noises were added. The mean and standard deviation of the noise was determined so that the noise in the final image matches typical experimental signals. The original image was then convoluted with a Gaussian function with a standard deviation of 200 nm corresponding to the point spread function. The smoothed data were sampled at 40 nm to generate the final pixelized image. To systematically test for the effects of finite signals in the cytoplasm, we kept the standard deviation of the noise and changed only its mean values. The generated images were analyzed using the same scripts as for the experimental data described above.

The simulation results suggest that the inside-outside difference in the background signal could potentially influence cell wall thickness measurement (Figure S1D). By running a systematic modification of background difference between inside and outside, and signal/noise ratio in simulations, we thus computed the influence of those parameters on the error in thickness measurement (Figure S1E). Those results defined a region in which the predicted error is below 30 nm, which is less than 20 % of the typical experimental thickness. We thus used this simulation result as a criterion for image quality, and discarded images or regions of images where the predicted error is out of this accepted region (Figure S1E). For CLEM analysis, however, we systematically observed a much higher intracellular background due to chemical fixation. In that context we thus implemented a correction script to extract the true signal peak by using an analytical expression of the convoluted intensity profile (Clark et al., 2013).

TEM and CLEM Images

The full cell wall in electron microscopy images was detected using custom scripts written in MATLAB, by using a threshold value for the signal intensity. In some images with inhomogeneous contrast, the results were manually updated. The edge of the binarized signal were traced to define the inside and outside boundaries of the cell wall. The normal direction was defined based on the inside cell wall boundary, and the cell wall thickness was defined as the distance between inside and outside boundaries along the normal direction. To compare EM and light microscopy images in CLEM analyses (Figure 1B first panel and S2E-G), we defined four morphologically distinguishable points (two tips and two scars), and used these points to overlay the two images by matching the distance between them. Comparison on larger regions, was done by measuring thickness in EM pictures manually within 2 μm regions at 8 individual positions, and compared with an average value computed from light-microscopy measurement in the Matlab script (Figure 1B third panel).

Cell Shape, Growth and Polarity Factor Concentration Measurements

Cell length was generally measured using lectin signals in ImageJ. To compute old end elongation rates visible birth scars were used as fiducial reference landmarks. Tip curvature was computed from the lectin contour defined for cell wall measurements, by fitting a local circle in Matlab (Bonazzi et al., 2015).

To analyze changes in cell shape, growth rates and localization of polar factors following turgor reduction by sorbitol addition, we developed dedicated Matlab scripts. We first segmented cells using the signal from the lectin-labelled cell wall. To this aim, we first smoothed the image with median and Gaussian filters and detected cell edges using the Laplacian of the Gaussian filter. The resultant binary image was then filtered to remove small segments. Given that the signal of the labelled cell wall has a finite thickness, we detected the inner and the outer border of this signal. All spaces in this image are then filled in white except for the spaces between the inner and outer border of the wall, yielding a black band representing the cell wall. Using the watershed algorithm, we finally

extracted the whole-cell contour defined as the middle of this band. To compute cell length, we fitted the long axis of the segmented cell with a polynomial of degree 3. This fit was then used to define a ''cell spine'' and its length was calculated, and used as a measure for cell length.

The whole-cell contour could then be manipulated using morphological and logical operations to obtain a set of arbitrary regions (tips, cytoplasm, etc.). The tip regions are for instance shaped as a cut off from the whole-cell mask perpendicular to the cell spine at specific distances along the spine. A segment outside of the cell can be shaped to compute the background.

Fluorescent signals of interest are then extracted from fluorescent images by using a mask based on corresponding sub-regions. The signal from the tips is corrected for the background signal and for bleaching. This is done by normalizing the background corrected tip signal with the background corrected cytoplasm signal:

$$I_{tip} = \frac{I_{tip\ raw} - I_{bg}}{I_{cytoplasm} - I_{bg}}$$

Strain-Stress Assay Simulation

The estimation procedure of cell mechanical parameters was similar to the one described in the paragraph ''Measurement of material properties'' in (Abenza et al., 2015) with the exception that, here, the cell wall thickness is measured all around the cell contour. For each cell, we followed steps described here:

1. Symmetrization of both the plasmolyzed contour and the turgid contour of each cell; the same symmetrization was kept for the thickness profile.
2. The plasmolyzed contour was swelled at different pressure steps (pressure is normalized by the Young modulus at the equator) assuming a distribution of thickness, and mechanical parameters away from the equator. Two different distributions of thickness were tested: (i) averaged plasmolyzed thickness and (ii) measured plasmolyzed thickness. Three distributions of Young modulus were tested: (i) a zero-parameter (i.e. constant Young modulus) and (ii and iii) two two-parameters distributions ("cos" and "sigmoid"), with one parameter describing the tip width and the other parameter accounting for the ratio between the Young modulus at the tip and the equator. As two recent articles (Abenza et al., 2015; Atilgan et al., 2015) consistently reported a zero-value for the in-plane Poisson ratio, this ratio was set to 0.01 for all the simulations.
3. Among the pressure steps and tested parameters, the ones for which the swelled plasmolyzed contour best fitted the turgid contour were retained to estimate mechanical parameters. Independently of the distribution of Young moduli, the selected normalized pressure step provided a ratio between the Young modulus at the equator and the internal turgor. The turgor pressure inside fission yeast cells has been estimated to be 1.5 MPa in (Atilgan et al., 2015) providing an absolute estimate of the Young moduli.

Variation in local Young moduli were simulated using:

a) A "sigmoid" distribution on the form: $Y(s)=Y_{tip}+(Y_{side}-Y_{tip})(sigmf(s,[5\ d])-sigmf(s,[5\ arc-d]))$, with s, the curvilinear coordinate, d the width along cell tip, and arc the total arclength. The "sigmoid" distribution (sigmf in Matlab) is flat at the equator, decreases sharply at a distance d from the tips, then is flat again at the tips.

Deviation from the computationally swollen cell and the original cell before turgor reduction was calculated as a distance from the best-fit. For tip sizes of 2.5 μm; 3 μm and 3.5 μm we obtained respective values for Y_{side}/P of 48.1±0.7; 49.0±0.8 and 48.9±0.8 ; for Y_{tip}/Y_{side} of 0.59±0.02; 0.63±0.02 and 0.68±0.02 with distances to best fits of 0.048±0.001; 0.050±0.001; 0.053±0.001.

Those values suggested that the lowest distance from the best fit are obtained for a small enough tip-width d. The value of E_{cyl}/P were not very sensitive to d whereas E_{tip}/E_{cyl} increased with d. The correlation between E_{tip} and E_{cyl} was not significant for d below 3 (p-value>0.5 for both the Pearson and Spearman tests) whereas it became significant for d=3.5 μm (p-value 0.02 Pearson, 0.11 Spearman).

b) A "cos" distribution: $Y(s)=Y_{tip}+(Y_{cyl}-Y_{tip})(0.5(1-\cos(2\pi s/arc)))^{d}$. The "cos" distribution is narrower around the equator than the sigmoid one especially for d>1 μm. Similarly to the sigmoid distribution, the best fit were obtained when the Young modulus decreased in the slowest manner from the equator (d=0.5, d=1). The estimations of Y_{cyl}/P were very sensitive to d as the decrease from the equator became very sharp when d=2. They were also higher than with the "sigmoid" fit in order to compensate for the quicker decrease at the equator. For the best fit (d=0.5, d=1), the estimated ratio of Y_{tip}/Y_{side} are slightly lower than for "sigmoid" ones. Obtained values are for exponent d of 0.5, 1 and 2 respectively: Y_{side}/P : 48.6±0.5, 54.9±0.5 and 73.6±0; Y_{tip}/Y_{cyl}: 0.46±0.02, 0.49±0.07 and 0.39 with distances from best-fit of 0.045; 0.048 and 0.065.

Spectrum Analysis of Thickness Fluctuations

Fourier-transform analyses were performed on two independent data sets on signals from time-lapses at 6' intervals, using custom-made Matlab scripts. The first data set consisted of 60' long videos of n=25 individual cells taken at random position in the cell cycle (Figure S4F). The second data set consisted of 210' long videos of n=8 individual cells taken from the beginning to the end of one cell

cycle (Figure S4G). For the first data set, we subtracted the mean thickness for each cell, and computed the amplitude of the discrete Fourier transform on the frequency domain. In the second data set we performed a short-time Fourier transform analysis, by subtracting for each cell trace a smoothed signal generated with a rectangular window. The spectrum was robust to changes in window width from 7 up to 17 time-points (42' to 102'). Both analyses yielded peaks corresponding to a full period of 50 to 60 min, supporting the consistency of this analysis.

Analytical Models for Tip Thickness Fluctuations

Equation 4 of the main text can be written in the form:

$$\frac{dh_{tip}}{dt}(t) = -a + b\frac{1}{h_{tip}(t-T)}, \qquad \text{(Equation S1)}$$

with $a = \frac{rPR_c}{Y} - S_0$, and $b = \lambda\frac{rPR_c}{Y}$.

Using T as a unit of time and the homeostatic thickness value b/a as a unit of thickness, this equation can be rewritten as:

$$\frac{d\bar{h}_{tip}}{d\bar{t}}(\bar{t}) = A\left(-1 + \frac{1}{\bar{h}_{tip}(\bar{t}-1)}\right) \qquad \text{(Equation S2)}$$

with $\bar{h}_{tip} = \frac{a}{b}h_{tip}$, $\bar{t} = t/T$, and $A = a^2T/b$. Numerical solutions of this ordinary differential equation were obtained using the NDSolve function of Mathematica (Wolfram Research Inc.). Equation S2 has damped solutions with no oscillations for $A < A_1$, oscillating damped solutions for $A < A < A_2$, and sustained oscillations for $A > A_2$. The values of A_1 and A_2 increase when $\bar{h}_{tip}(0)$ departs from 1. Analytical calculations show that when $\bar{h}_{tip}(0)$ is close to 1, $A_1 = exp(1)$ and $A_2 = \pi/2$. Optimal homeostasis corresponds to maximal damping, which occurs for, $A = A_1$. Coming back to initial model parameters, $A = \left(S_0 - \frac{rPR}{Y}\right)^2 T \Big/ \left(\lambda\frac{rPR}{Y}\right)$. Therefore, a decrease in λ yields an increase in A, and hence to fluctuations with higher amplitude.

3D Cell Growth Model

The growth model developed in (Abenza et al., 2015) was modified to include varying thickness and varying young modulus. The parameters h (thickness) and Y (Young modulus) (Formula 36-38 in the supplemental material of (Abenza et al., 2015)) are no more constant.

The thickness distribution profile has been selected by the following procedure: all the symmetrized thickness profiles were linearly re-parametrized from new end to old end so that the new end lays at curvilinear abscissa 0 and the old end at a curvilinear abscissa of 13.9. After this operation all the thickness profiles were averaged, the average was very well fitted by a three-parameters linear combination of sigmoids. The three parameters h_{ne}, h_{oe} and h_{side} are the cell wall thickness at the new end, at the old end, and at the equator.

Only the modification to the original algorithm are detailed here (Supplemental material of Abenza-Martinez *et al* (Abenza et al., 2015)):

- At step *n* (iii), once the new curvilinear abscissa s_n has been calculated using formula 46, arc_n, the total arclength is updated and the thickness profile can also be updated using the shape family

$$h_n(s_n) = h_{ne} + \frac{h_{side} - h_{ne}}{1 + e^{-2.20(s_n - 2.36)}} - \frac{h_{side} - h_{oe}}{1 + e^{-73.3(s_n - arc_n + 2.36)/arc_n}} \qquad \text{(Equation S3)}$$

as well as the Young modulus distribution:

$$Y_n(s_n) = 62 + \frac{38}{1 + e^{-2.20(s_n - 2.36)}} - \frac{30}{1 + e^{-73.3(s_n - arc_n + 2.36)/arc_n}} \qquad \text{(Equation S4)}$$

- The amplitude of each step of growth in formula (47-48) is: $\delta = 1.2$
- The model for the fluorescence profile K of the polarity marker is:

$$K(s) = 1.037\exp\left(-0.4165\left|\frac{s}{D}\right|^{1.745}\right) \qquad \text{(Equation S5)}$$

where D=1.17, 1.06 and 0.93 depending on which strain is modeled *rga4Δ*, wt and *rga2Δ*. Each of the D constants have been chosen such that the asymptotic radius of convergence of the cell corresponds to a value close to the experimental tip radii 1.76 μm (*rga4Δ*), 1.62 μm (wt) and 1.46 μm (*rga2Δ*). The cell wall tip thicknesses of *rga4Δ*, wt and *rga2Δ* are 0.149 μm, 0.166 μm and 0.179 μm.

DATA AND SOFTWARE AVAILABILITY

The software for live cell wall thickness measurement is available at: http://www.minclab.fr/research/.

All the other image analysis scripts developed in the context of this study can be made available upon request.

Developmental Cell, Volume *45*

Supplemental Information

Mechanosensation Dynamically Coordinates Polar Growth and Cell Wall Assembly to Promote Cell Survival

Valeria Davì, Hirokazu Tanimoto, Dmitry Ershov, Armin Haupt, Henry De Belly, Rémi Le Borgne, Etienne Couturier, Arezki Boudaoud, and Nicolas Minc

SUPPLEMENTAL INFORMATION

This supplemental Information file contains:

Figures S1 to S6 and Figure legends

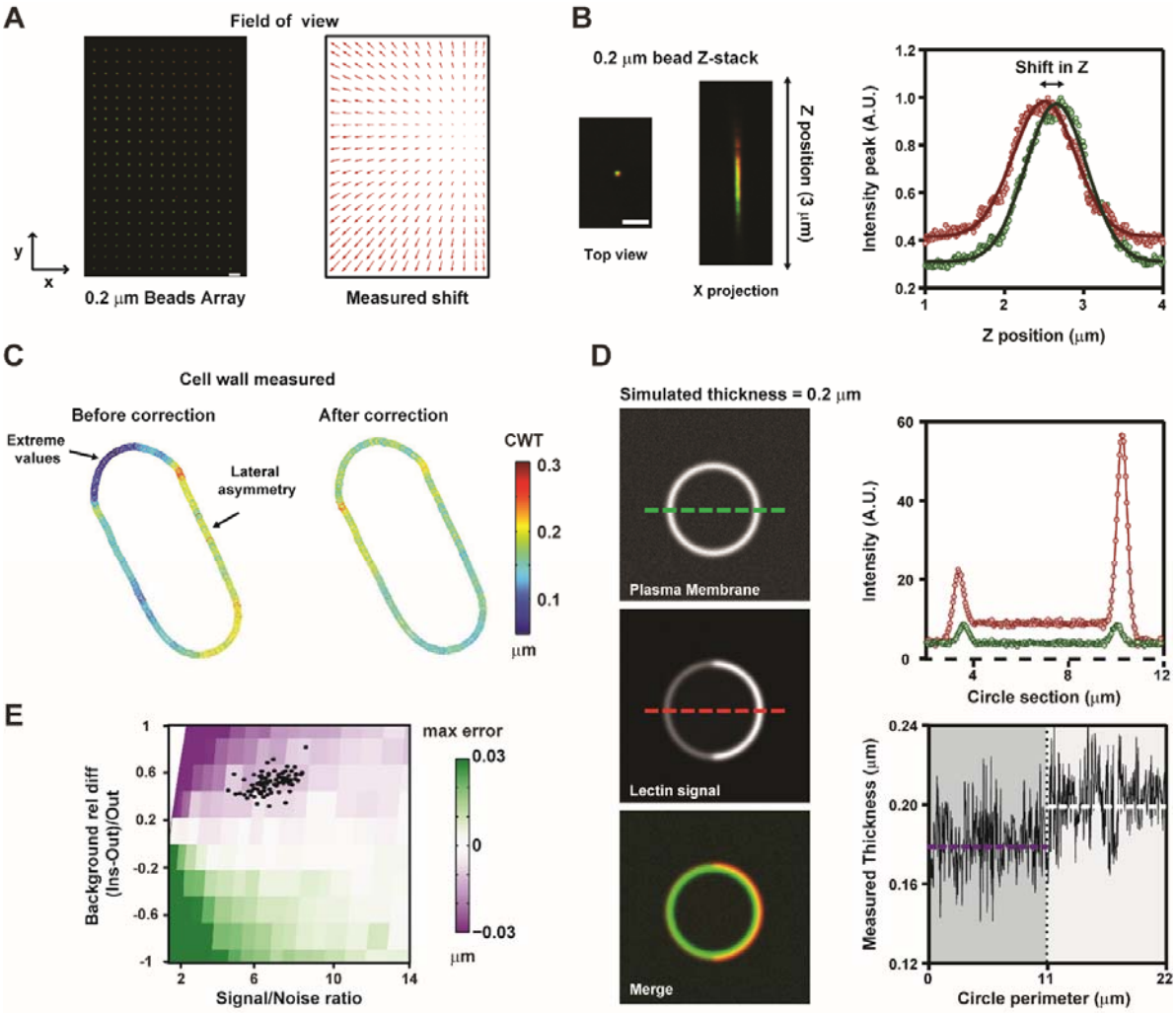

Figure S1

Figure S1 (related to Figure 1). Image analysis and registration for cell wall thickness measurement. **(A)** Merged confocal images of a TetraSpeck^{TM} microsphere moved and imaged in the green and far red channels at several positions in the field of view. Corresponding X and Y shifts used for image registration and measurement corrections. Arrows are magnified 15X. **(B)** Calibration of chromatic Z-shift: a stack of TetraSpeck^{TM} microspheres is taken in the green and far red channels. Fluorescent peaks in Z are fitted with Gaussians (Right). The distance between the peaks corresponds to the chromatic Z-shift. **(C)** Thickness color maps before and after correction. **(D)** Left: Simulated images of two shells, separated by a distance of h=0.2 μm (corresponding to typical CW thickness). Signals and background noise correspond to typical experimental images. (Top plot) Signal distribution along the dashed line. (Bottom plot) Measurement of simulated h (the dark gray zone corresponds to the left part of the simulated cell). **(E)** Estimation of the maximum error as a function of the background relative difference, and signal/noise ratio for the lectin signal. Black scattered points correspond to typical experimental images. Experimental points in which the error is estimated to be above ±0.03 μm are discarded in the analysis script. Scale bars, 2 μm.

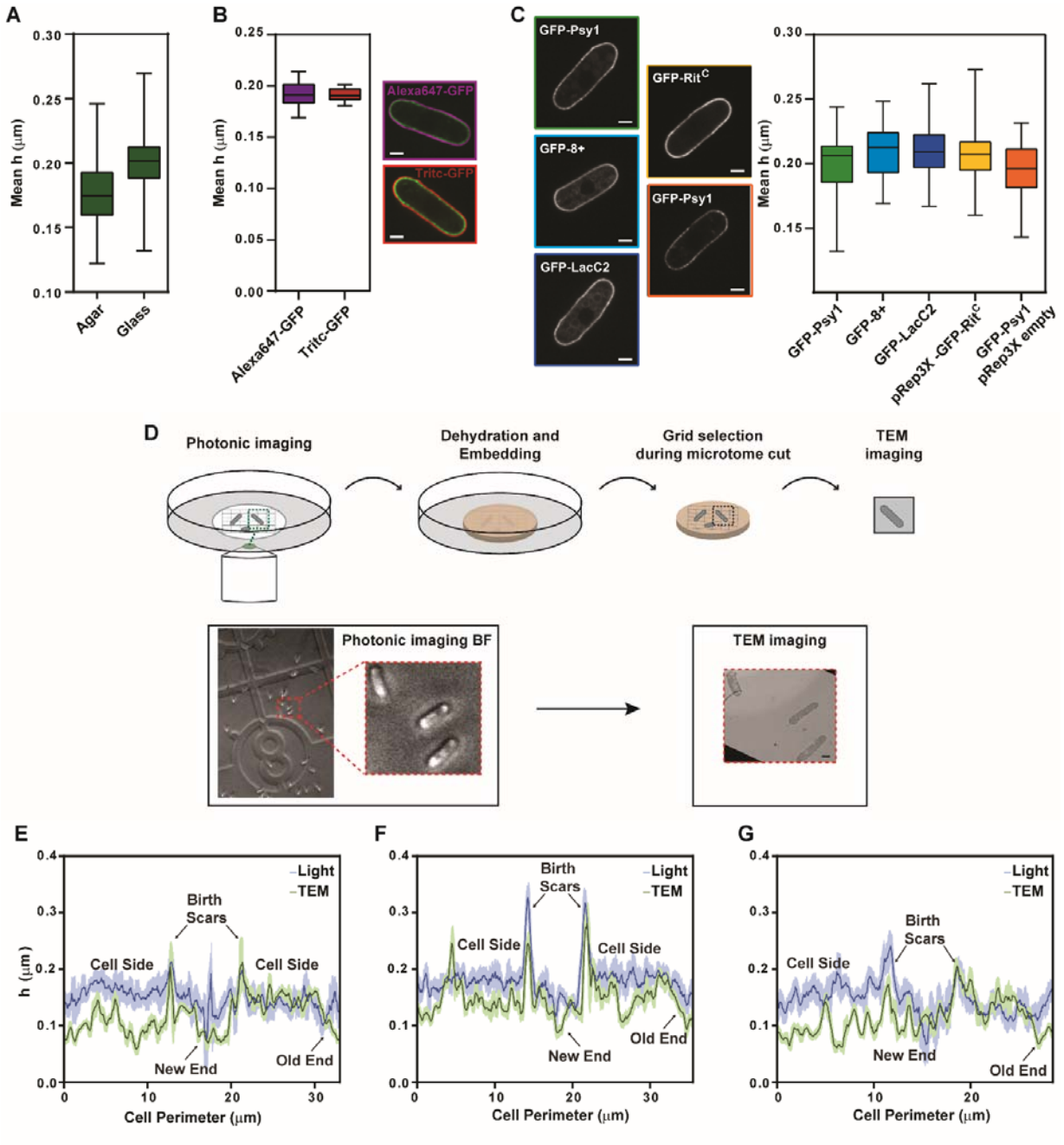
A
Mean h (μm)
Agar
Glass
B
Mean h (μm)
Alexa647-GFP
Tritc-GFP
C
GFP-Psy1
GFP-8+
GFP-LacC2
GFP-Rit^C
GFP-Psy1
Mean h (μm)
GFP-Psy1
GFP-8+
GFP-LacC2
pRep3X -GFP-Rit^C
GFP-Psy1
pRep3X empty
D
Photonic imaging
Dehydration and Embedding
Grid selection during microtome cut
TEM imaging
Photonic imaging BF
TEM imaging
E
F
G
h (μm)
Light
TEM
Birth Scars
Cell Side
Cell Side
New End
Old End
Cell Perimeter (μm)

Figure S2

Figure S2 (Related to Figure 1). Tests for the accuracy and robustness of the live cell wall thickness measurement method. **(A)** Influence of growth conditions on CW thickness measurement (n=66, 169). **(B)** Mean thickness, h, measured using GFP-Psy1 and *Gs*-IB_4-Alexafluor647 (Alexa647-GFP) (*n=30*) or GFP-Psy1 and *Bs*-IB_4- TRITC (Tritc-GFP) (*n=24*) and representative mid-plane confocal images. **(C)** Mid-plane confocal images of different GFP-tagged membrane proteins or membrane associated domains, and quantifications of mean h measured using a *Gs*-IB_4- Alexafluor647 lectin. Cells transformed with pREP3x-Phluorin-Ritc and pREP3x-empty were grown in minimal media in the absence of thiamine for 48h. (n>25 cells for all conditions). **(D)** (Top) Schematic representing the methodology used to perform Correlative Light Electron Microscopy (CLEM). Cells are stuck down on a dedicated bottom glass coverdish with a grid, fixed, and imaged for CW thickness measurement. Cells are then embedded in resin, which is sliced with a microtome for subsequent TEM imaging. (Bottom) Typical bright field image of cells in the coverdish and close-up view of bright field and TEM images of the same cells. The partial cell deformation (shrinkage) visible in TEM was frequently observed and likely caused by resin embedding. The cell wall, however, appeared to remain intact in most cases. **(E-G)** CLEM analyses of 3 individual cells. Running average on 10 pixels and standard deviation of thickness measurements around individual cells. Light microscopy measurements for CLEM are corrected to compensate for the high internal background caused by chemical fixation (see STAR Methods). Scale bars 2 μm. Whiskers plots represent median and full data set range.

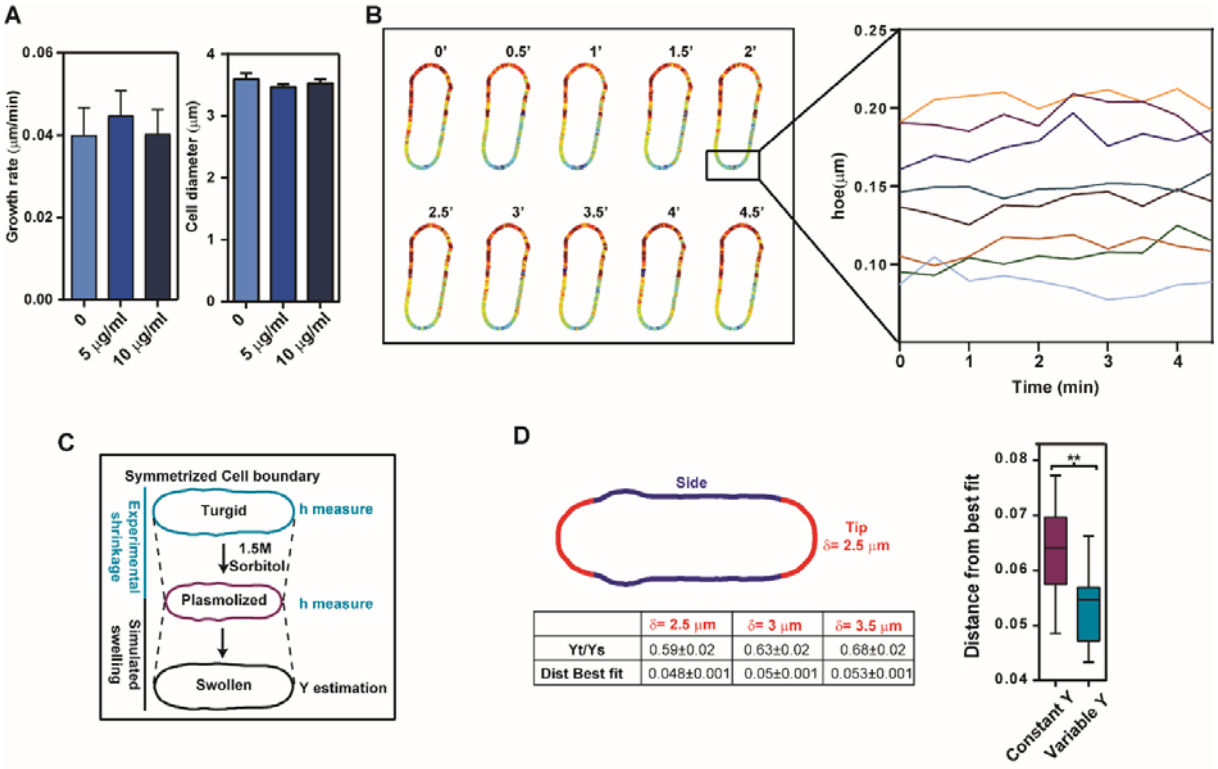
A
Growth rate (μm/min)
0.06
0.04
0.02
0.00
0
5 μg/ml
10 μg/ml
Cell diameter (μm)
4
3
2
1
0
0
5 μg/ml
10 μg/ml
B
0'
0.5'
1'
1.5'
2'
2.5'
3'
3.5'
4'
4.5'
hoe(μm)
0.25
0.20
0.15
0.10
0
1
2
3
4
Time (min)
C
Symmetrized Cell boundary
Experimental shrinkage
Turgid
h measure
1.5M Sorbitol
Plasmolized
h measure
Simulated swelling
Swollen
Y estimation
D
Side
Tip
δ= 2.5 μm
δ= 2.5 μm
δ= 3 μm
δ= 3.5 μm
Yt/Ys
0.59±0.02
0.63±0.02
0.68±0.02
Dist Best fit
0.048±0.001
0.05±0.001
0.053±0.001
Distance from best fit
0.08
0.07
0.06
0.05
0.04
**
Constant Y
Variable Y

Figure S3

Figure S3 (Related to Figure 1 and 2). **Influence of time-lapse imaging on growth rate, and tests for stress-strain assays used to compute local cell wall elastic moduli. (A)** Growth rate and mean diameter of cells grown in different concentrations of *Gs*-IB_4-Alexafluor647 and imaged every 15', during 90' (n>10 for each condition). The growth rate is measured in bipolar cells. **(B)** Color maps of a cell imaged every 30" during 5', and time evolution of thickness measurements at cell tips for 7 individual cells measured in this manner. Note that variations within each cell trace are significantly smaller than variations between different cells. **(C)** Principle of experiments and simulations used to compute the CW elastic modulus, Y. Cell wall thickness is measured prior to rinsing cells in 1.5M sorbitol. Cell swelling is then simulated using various values of pressure and local elastic moduli. **(D)** (Left) Influence of the size used to define cell tips on the ratio of young moduli between cell tips and sides. (Right) Distance from best fit when using constant or variable young moduli between tips and sides. Error bars correspond to SD. Whiskers plots represent median and full data range.

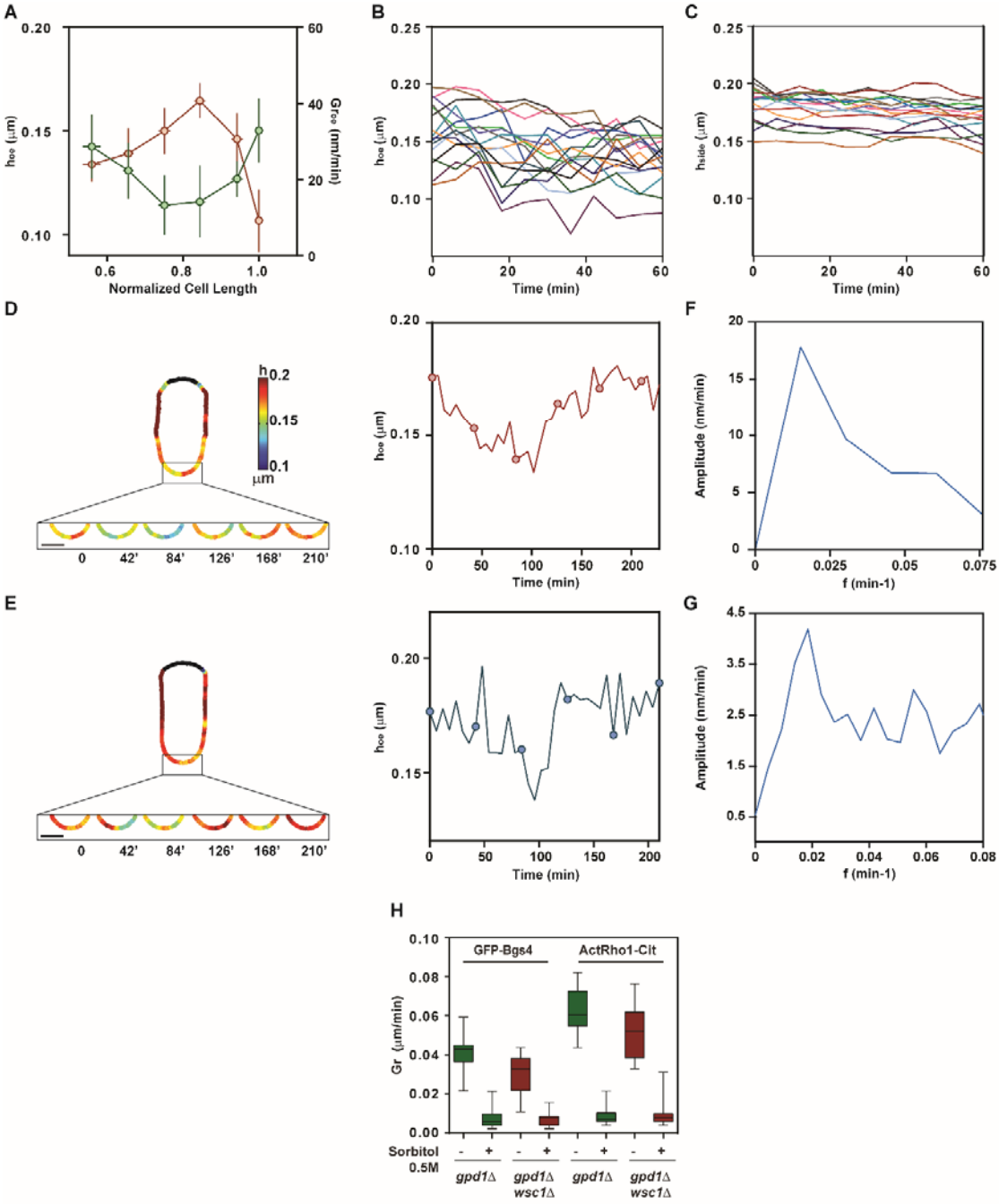
A
B
C
D
E
F
G
H
Normalized Cell Length
Time (min)
Amplitude (nm/min)
f (min-1)
Gr (μm/min)
GFP-Bgs4
ActRho1-Clt
Sorbitol 0.5M
gpd1Δ
gpd1Δ wsc1Δ

Figure S4

Figure S4 (Related to Figure 3 and Figure 4). Mean thickness and growth rate changes on the cell cycle, oscillations in tip thickness, and influence of turgor reduction on growth rates. **(A)** Plot of the evolution of old end thickness (green) and old end growth rates (red) as a function of cell length (used as a proxy for cell-cycle progression) in wt cells (n=12 cells). Cell length is normalized by the length at septation. **(B)** Evolution of thickness at the old end, $h_{oe,}$ imaged at 6 min intervals in 16 wt cells. **(C)** Evolution of thickness on cell sides in the same cells as in (B) (line colors correspond to the same cell in both plots). **(D-E)** Close up views on thickness maps (smoothed on 10 pixels) at the old end of a growing wt cell, and corresponding plots of thickness at the old end for 2 typical cells. Black points in thickness maps correspond to positions in which thickness cannot be measured accurately. Dots correspond to time points shown in the tip insets of thickness maps. **(F)** Amplitude spectrum based on a discrete Fourier analysis of 60' long movies of n=25 individual wt cells. **(G)** Amplitude spectrum based on a short-time Fourier analysis of 210' long movies of n=8 individual cells, achieved using a rectangular window on 11 points (66'). **(H)** Growth rates measured before (10 min prior, '-') and after (20min past, '+') 0.5M sorbitol treatments in the indicated mutants expressing the indicated probes. Whiskers plots represent median and full data range. Error bars represent SD. Scale bars, 2μm.

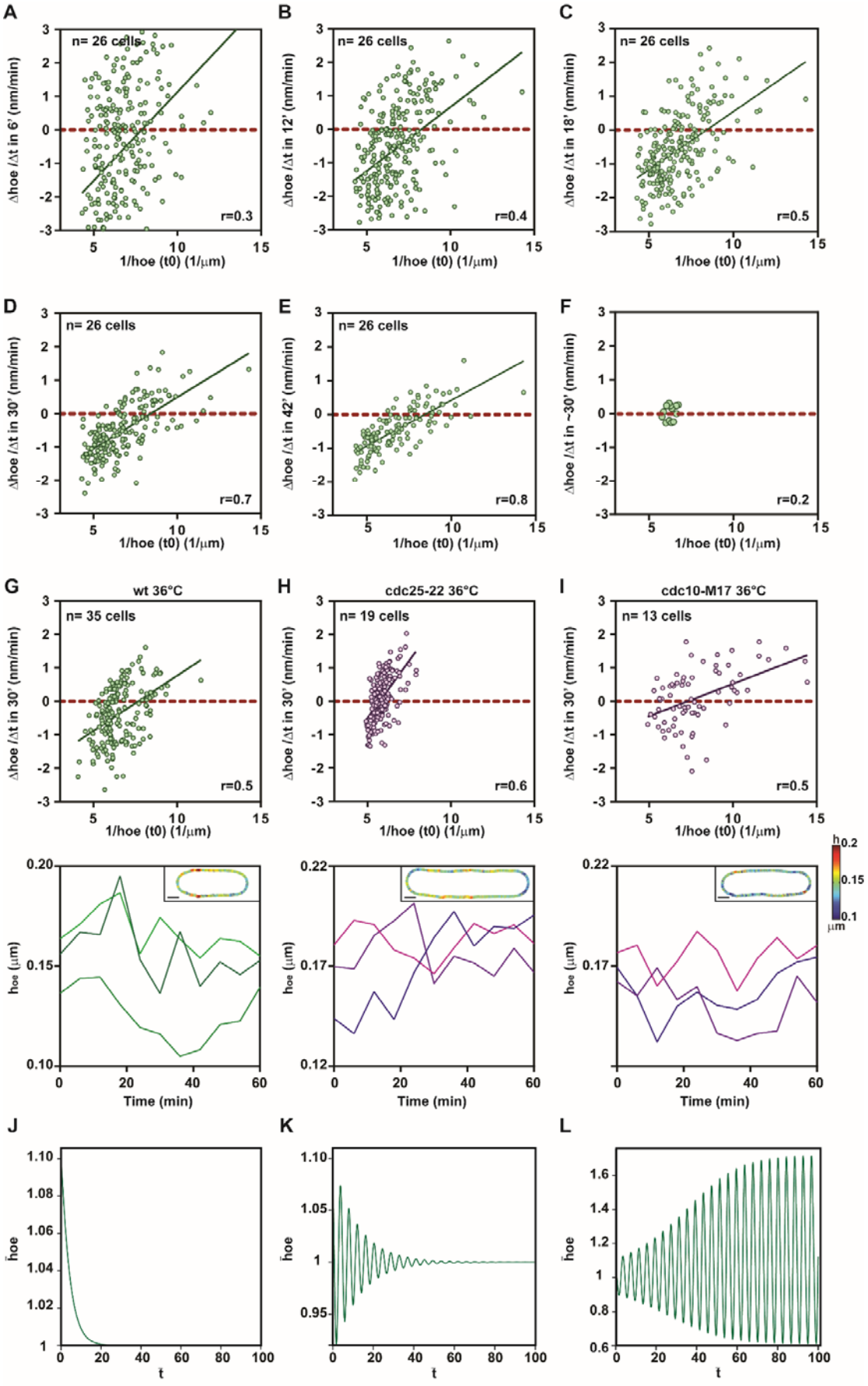
A
n= 26 cells
r=0.3
Δhoe /Δt in 6' (nm/min)
1/hoe (t0) (1/μm)
B
n= 26 cells
r=0.4
Δhoe /Δt in 12' (nm/min)
1/hoe (t0) (1/μm)
C
n= 26 cells
r=0.5
Δhoe /Δt in 18' (nm/min)
1/hoe (t0) (1/μm)
D
n= 26 cells
r=0.7
Δhoe /Δt in 30' (nm/min)
1/hoe (t0) (1/μm)
E
n= 26 cells
r=0.8
Δhoe /Δt in 42' (nm/min)
1/hoe (t0) (1/μm)
F
r=0.2
Δhoe /Δt in -30' (nm/min)
1/hoe (t0) (1/μm)
G
wt 36°C
n= 35 cells
r=0.5
Δhoe /Δt in 30' (nm/min)
1/hoe (t0) (1/μm)
H
cdc25-22 36°C
n= 19 cells
r=0.6
Δhoe /Δt in 30' (nm/min)
1/hoe (t0) (1/μm)
I
cdc10-M17 36°C
n= 13 cells
r=0.5
Δhoe /Δt in 30' (nm/min)
1/hoe (t0) (1/μm)
h
0.2
0.15
0.1
μm
hoe (μm)
Time (min)
J
K
L
t

Figure S5

Figure S5 (Related to Figure 4) Estimation of the delay for thickness homeostatic feedback, influence of the cell cycle on homeostasis, and oscillating behavior of tip thickness from a minimal model with delayed feedback. **(A-E)** $\Delta h_{oe}/\Delta t$ is computed as $(h_{oe}(t_0+T) - h_{oe}(t_0))/T$ and plotted as a function of $1/ h_{oe}(t_0)$, for different delays T (6', 12', 18', 30' and 42'), in wt cells (n=25 cells). Pearson correlation coefficients, r, are indicated at the bottom-right of the graphs. The lines are linear fits. **(F)** Homeostatic plots at 30'delays computed from the global mean cell cycle variation of tip thickness in a population of WT cells. **(G-I)** (Top) Homeostatic plots at 30'delays for wt (35 cells), *cdc10-M17* (13 cells) and *cdc25-22* (19 cells) imaged at 36°C. (Bottom) Evolution of thickness at the old end, h_{oe}, imaged at 6 min intervals in 3 representative cells for each indicated strain. A representative thickness map is shown in the insets. The excess of negative or positive points in homeostasis plots (A-I) may be associated with a slight unbalanced sampling along the cell cycle. **(J-L)** Minimal model: Each graph corresponds to the evolution of simulated tip thickness as a function of time, which corresponds to different solutions of Eq. S2 (non-dimensional version of Eq. 4). **(J)** Damped solutions with no fluctuations for $A < A_1$ **(K)** Fluctuating damped solutions for $A_1 < A < A_2$ **(L)** Sustained fluctuations reached after a transient increase in amplitude.

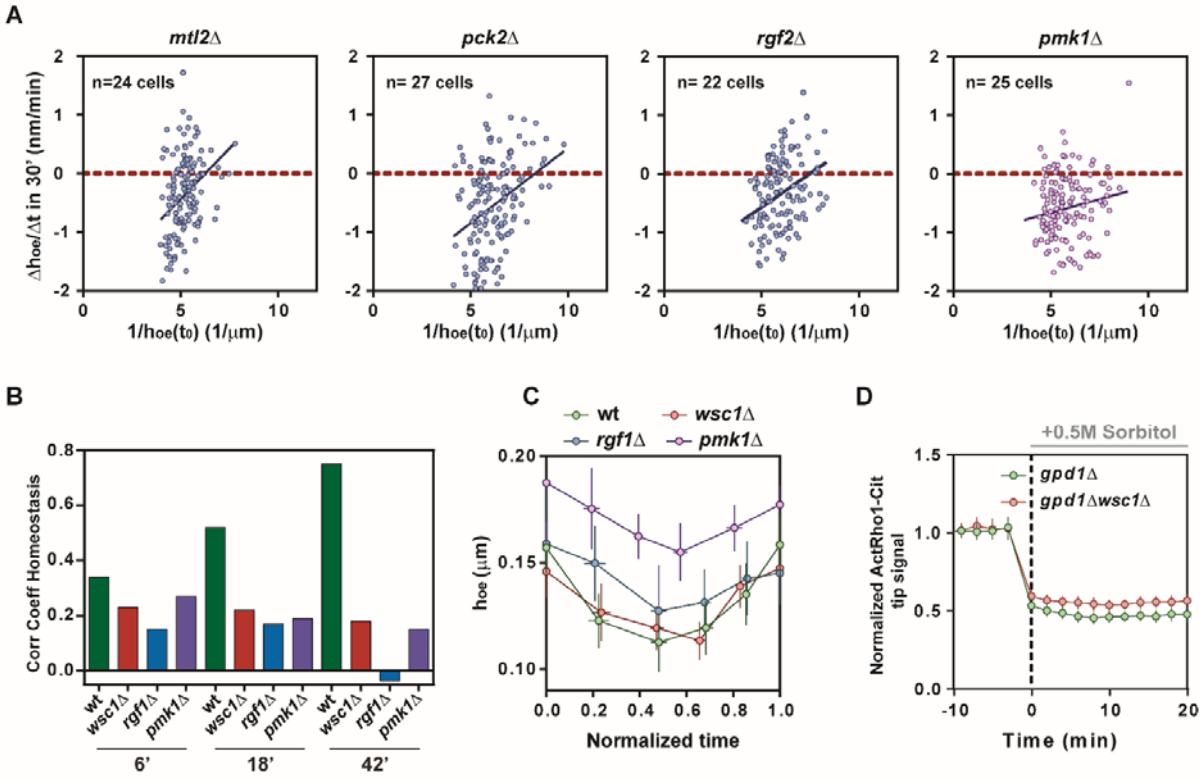
A
mtl2Δ
pck2Δ
rgf2Δ
pmk1Δ
n=24 cells
n= 27 cells
n= 22 cells
n= 25 cells
Δhoe/Δt in 30' (nm/min)
1/hoe(t0) (1/μm)
B
Corr Coeff Homeostasis
wt
wsc1Δ
rgf1Δ
pmk1Δ
6'
18'
42'
C
wt
wsc1Δ
rgf1Δ
pmk1Δ
hoe (μm)
Normalized time
D
+0.5M Sorbitol
gpd1Δ
gpd1Δwsc1Δ
Normalized ActRho1-Cit tip signal
Time (min)

Figure S6

Figure S6 (Related to Figure 5). Influence of components of the CWI pathway on cell wall thickness homeostasis (A) $\Delta h_{oe}/\Delta t$ computed as $(h_{oe}(t_0+30') - h_{oe}(t_0))/30'$ and plotted as a function of $1/ h_{oe}(t_0)$, in *mtl2Δ* (n=24 cells), *pck2Δ* (n=27), *rgf2Δ* (22 cells), and *pmk1Δ* (25 cells). The excess of negative points in homeostasis plots is caused by an oversampling in the first part of the cell cycle, as dividing cells are discarded. Lines are linear fits **(B)** Correlation coefficients between $\Delta h_{oe}/\Delta t$ and $1/h_{oe}$ for the indicated mutants computed at various delays. **(C)** Evolution of old end wall thickness as a function of time, in wt cells (n=12 cells), *wsc1Δ* (n=13), *rgf1Δ* (7 cells), and *pmk1Δ* (21 cells). Time is normalized by the time of the cell cycle, with 0 being the end of septation and 1 the end of the next septation. **(D)** Evolution of ActRho1-Cit tip signal following turgor reduction in *gpd1Δ* (n=14) and *gpd1Δ wsc1Δ* (n=19) mutant cells. Error bars correspond to SD.

2- Mechanical Control of Cell Shape and Size in Fission Yeast

The determination of a cell's shape ultimately relies on the properties of its surface. The surface of walled cells is composed of a layer of polysaccharides, necessary to balance high internal turgor pressure typical of these cells. Many experimental and theoretical works have explored how wall mechanics can influence cell morphogenesis, however a systematic assessment of wall mechanical properties and their influence on single cell morphology is still missing.

In this work, we expanded the wall thickness measurements method described in the first set of results, in order to estimate other mechanical parameters of the cell. To this aim, we implemented a laser ablation set up, through which growing fission yeast cells can be pierced, provoking lysis and consequent cell wall relaxation. By exploiting simple geometrical rules (Atilgan et al., 2015), comparing turgid and relaxed wall shape, and coupling this to local values of wall thickness in the turgid state, we are able to estimate local values of wall bulk modulus divided by turgor pressure.

This analysis confirmed that growing walls are softer than stable ones, but showed that wall bulk modulus is stable within the cell cycle in growing poles and sides, while it significantly varies at new poles, probably in conjunction with growth initiation.

We then focused on how the mechanics of the cell wall can influence cell shape determination, and in particular diameter regulation.

We observed that the surface modulus (product of bulk modulus and thickness) at cell sides scales firmly with local diameter in different wild type conditions, and in several mutants, which have defects in diameter establishment or maintenance, as well as in mutants known to miss-regulate wall synthesis and remodeling.

Ectopic perturbation of wall synthesis causes modifications in wall mechanical properties and simultaneous alteration in diameter.

Our quantitative analysis reveals that in all the conditions tested, cell walls deform similarly between relaxed and turgid state, suggesting a conservation in elastic strain, which appear to be a key parameter to determine cell shape from wall properties in these cells.

These results enlarge our understanding on how wall mechanical parameters are involved in cell shape determination, and can be the basis for further analysis aimed to the understanding of how this process is dynamically regulated, in fission yeasts as well as in other walled cells.

MECHANICAL CONTROL OF CELL SHAPE AND SIZE IN FISSION YEAST

Valeria Davì[1], Haotian Guo[1,$], Hirokazu Tanimoto[1,&], Arezki Boudaoud[2] and Nicolas Minc[1]

Affiliations:

[1] Institut Jacques Monod, CNRS UMR7592 and Université Paris Diderot, 15 rue Hélène Brion, 75205 Paris Cedex 13, France

[2] Reproduction et Développement des Plantes, Univ. Lyon, INRA, CNRS, ENS de Lyon, UCB Lyon I, 46 Allée d'Italie, 69364 Lyon Cedex 07, France

[$] Current affiliation: Institut National de la Santé et de la Recherche Médicale, U1001; Faculty of Medicine, Paris Descartes University, 75014, Paris, France.

[&] Current affiliation: Department of Materials Science, Yokohama City University, Japan

SUMMARY

The mechanical properties of the cell surface ultimately determine cellular morphogenesis. In walled cells, such as those of plants and microbes, cell wall mechanical parameters including thickness and bulk elastic modulus, have been proposed to influence shape and size, but a systematic assessment of how their local and/or global values affects single cell morphogenesis is still lacking. Here, using fission yeast as the most established walled cell to study cell shape determination, we mapped subcellular values of wall thickness (h) and bulk elasticity (Y) in large populations of mutants and conditions affecting cell diameter. We find that while thickness and elastic moduli are only weakly correlated with diameters, the wall surface modulus defined as $\sigma=hY$ is robustly scaled with diameter in tens of mutants in genes regulating various cellular functions, within a population of a given strain, and even within a single misshaped cell. Dynamic modulations of wall synthesis localization, and/or alteration of wall mechanical properties, directly alter wall surface modulus and consequent diameter. Those quantitative data suggest that the shape of the cell wall may be constrained by a conservation of elastic strains, and impact our current understanding of the mechanisms defining morphogenesis in fission yeast.

KEYWORDS

Cell shape; Cell Wall; Cell surface Mechanics; Fission Yeast

RESULTS AND DISCUSSIONS

A medium-throughput method to map subcellular mechanical properties of the cell wall

The fission yeast, *Schizosaccaromyces pombe*, is a well-established model to understand the emergence of cell morphogenesis. Those are rod-shaped cells which grow by tip extension with a near-constant diameter of ~4 microns, which shape is strictly defined by their cell wall (CW) encasing the plasma membrane and bearing the turgor-pressure derived stresses [1-3]. Building on previous methodologies to map CW thickness and compute its bulk elastic modulus around single cells [4-7]; we sought to develop a systematic approach to map with a medium-throughput those key mechanical parameters in large populations of cycling cells and mutants. To this aim, we used strains expressing GFP-psy1 which label the plasma membrane at the inner side of the wall, and added lectin from *Griffonia Simplicifolia* labeled with a far-red fluorophores to mark the outer face of the wall. As previously reported, this combined with a dedicated image analysis pipeline, allows to map CW thickness around a given cell, as well as to delineate cell shape with precision [4] (Figure1 B). After imaging a given cell to compute wall thickness, we deflated it using laser ablation at a small diffraction-limited point on the surface [5]. Cell shape analysis before and less than 2 min after ablation allowed to compute local values of the ratio of the bulk elastic modulus of the CW to turgor pressure Y/P (Figure1 C). This method yielded near similar values of wall anisotropic extension as in other assays, and also near similar mean values of bulk elastic moduli of ~ 50 MPa using previous estimates of internal turgor value of 1.5MPa [4, 6-8] (Figure S1A-S1B).

The local values of the CW bulk modulus, revealed interesting mechanical anisotropies around the cell. As previously reported, the growing ends (old end or new end after NETO) were the softer parts of the cell, likely accounting for growth and wall remodeling there [4]. The birth scars were in contrast typically ~3X stiffer than growing ends, and the sides and non-growing new ends ~2X stiffer than growing ends (Figure1 D). Sorting cells by length, showed that the old end and cell sides kept near-constant wall bulk and surface elastic moduli, through the cell cycle. In contrast, the new end underwent a reduction of nearly 2X in bulk elastic modulus at a length of around 10-12 μm, likely corresponding to grows resumption there after NETO (Figure1E and Figure S1C).

Using WT populations, we next asked if local cell shape parameters, such as the tube diameter defined as the mean of diameter along the cylinder (see material and methods), and local radii

of curvature at cell tips were correlated with CW mechanical parameters around the cell. Because normal WT cells have a narrow range of diameters, we used starved cells and cells grown at 36°C, conditions which affect cell shape and CW properties [4]. This analysis showed that the local radius of curvature at the growing old end, is mildly correlated with CW thickness, elastic and surface moduli, defined as the product of thickness with the bulk modulus, $\sigma = hY$. In contrast, radii at non growing new ends and sides, exhibited a strong correlation with their local counterpart values of elastic moduli and surface moduli, and almost no correlation with thickness (Figure S1D-S1J). Especially, the radius along the cylinder, exhibited the highest positive correlation with values of side surface modulus, suggesting, that this mechanical parameter could encode for diameter regulation (Figure1 F-I).

Surface modulus of the cell wall accounts for diameter variations

Building on those observations, we asked if mechanical properties of the CW would vary in populations of mutants with defective diameter regulation. To that aim, we examined 62 mutants knocked out for a single Open Reading Frame, which have been reported as defective in cell diameter from previous visual screens of the fission yeast KO library [9, 10]. After careful validation and diameter quantification (see material and methods), we refocused our analysis, on a specific set of 18 mutants, which solely exhibited diameter mis-regulation, discarding more complex misshaped mutants with other bent or branched features, for instance [9, 10]. Importantly, those mutants covered several physiological processes, including cell polarity, chromosome segregation, signaling, metabolism and wall synthesis (Table 1, Figure 2A-C and Figure S2A). Defects in diameter regulation in those strains, could be split into 3 sub-categories. One category of mutants had a mean diameter significantly different (higher or lower) than WT cells. A second category had a similar mean value as WT diameters, but a much larger variability (computed as a standard deviation), reflecting defects in diameter maintenance through successive divisions (Figure 2A-B). A last category was made of mutants with defects in cell diameter along a single cell, thereby adopting skittle-like shapes. Finally, we added to this screen 8 mutants involved in cell wall regulation, which do not have major defects in diameter, but are expected to exhibit severe problems in regulating wall mechanics. To compute wall mechanical properties, thickness and elastic moduli, those mutant strains were crossed or transformed to stably express GFP-Psy1, and grown and assayed as controls following a rigorous standardized procedure (see material and methods).

Using this set of mutant strains, we computed mean thickness and bulk elastic moduli focusing on cell sides. For each strain, we typically analyzed ~ 20-30 cells, discarding dividing cells. In addition, although we kept mutants with skittle-like shapes, we first analyzed a sub-population in those strains with near intact rod-shapes. Overall, this large scale analysis, revealed a relatively narrow distribution of side CW thickness around 200nm, with one particular mutant, *kin1Δ* [11], strongly departing from the rest, and exhibiting a much higher thickness of more than 300nm (Fig 2D). Correlation between diameter and thickness, was positive, but relatively low, with a Pearson's coefficient of r=0.39 (Figure 2D). Elastic moduli divided by pressure, Y/P, also increased with cell diameter, and displayed a higher correlation (r=0.73) (Figure 2E). Those data confirmed the behavior in WT conditions, suggesting that bulk properties of the CW on cell sides, may account for diameter regulation, rather than thickness. Furthermore, the surface modulus, hY/P exhibited the highest correlation coefficient with the cell radius (r=0.82) (Figure 2F). As such, mutants which departed from the main trend in thickness or bulk elastic modulus appeared to be compensated so that the surface modulus remained in the mean trend. For instance, *kin1Δ*, exhibited a much larger thickness of ~300nm, as compared to mutants with similar mean diameter, but also featured a reduced Y/P yielding a near similar surface modulus. Importantly, we also found a good correlation between the surface modulus at the old end, and the surface modulus at side, which suggests that mechanical properties of the lateral CW may be defined during the initial synthesis of the CW at cell tips In contrast, the mechanical properties at the new end were not much correlated with that of the lateral CW, likely as a consequence of the effect of prior septum synthesis there [7] (Figure S2B-S2H). Together, those data suggest a clear link between cell diameter and the surface modulus of the CW, which best represents the stiffness of this structure.

Next, we focused on diameter variations within a given mutant strain. For this, we re-examined a mutant strain, *plc1Δ*, deleted for a gene which encodes for a phospholipase C enzyme, and exhibits the highest standard deviation in diameter (Figure 2A-B) [12]. When analyzed at the level of a population of single mutant cells, we found a net positive correlation (r=0.57) between CW surface modulus and cell diameter (Figure 2G). Next, we re-analyzed skittle-like mutants, now focusing on skittle-shaped cells. We selected 2 representative mutants with a high penetrance of skittle like defects, but pertaining to distinct genotypic classes (*myo1Δ* and *ubr1Δ*), and used the *plc1Δ* rod-like cells, as controls. We analyzed local diameters along the cell long axis in one representative cell from each mutants, and computed

diameter as a function of local surface modulus. While *plc1Δ* points clustered around a single value for R and σ, those parameters varied and were strongly correlated within single skittle cells of *myo1Δ* and *ubr1Δ* mutants (Figure 2H). Importantly, changes in local diameter, were not specifically regular with respect to the distance to cell tip, ruling out putative gradients from cell tips, and arguing in favor for a local regulation of mechanical wall properties and diameter. We conclude that the surface elastic modulus (elastic stiffness) of the CW, provides a strong mechanical predictor for local as well as global diameter values in fission yeast.

Using data from this screen, we then computed which conceptual mechanical element may be constrained for cell diameter definition. Strikingly, the elastic strain in the CW, defined as PR/Yh, appeared to be mostly constant across strains assayed with a value around ~28%, with no dependence on cell diameter. We note however, that two mutants exhibited smaller elastic strains, *kin1Δ* and *myo1Δ,* with values around 20% (Figure S3A). The stress in the CW reads, PR/h, and was estimated by assuming that values of turgor pressure were equal to 1.5 MPa for all the strains and conditions tested. We found that CW stress increases with diameter, showing that the CW of fatter cells, likely bear higher stresses than in smaller cells, and suggesting that stress limitation is not a strategy to define cell shapes in those walled cells [13] (Figure S3B). The bending energy of the CW normalized by that of pressure, computed as PR^3/Yh^3, also increased with diameter suggesting that CW bending may not constrain diameter definition [14] (Figure S3C). We also analyzed the relaxed cell radius, R_0, defined as the cell radius after laser ablation, when turgor is brought to 0. We found that this radius, strongly correlated with the pressurized radius R_1 (r=0.99), in a linear manner, so that $R_1 \sim 1.3R_0$, in agreement with near-constant elastic strains (Figure S3D). Together, those analysis suggest a simple picture for the regulation of CW mechanics and cell diameter: each portion of the CW is built with a relaxed length, and comes with a surface modulus which increases with relaxed length (Figure S3E). Both parameters may depend on global and/or dynamic alteration in wall synthesis machinery or other elements during growth. Each portion of the CW is being stretched with a fixed strain of ~30% to define cell diameter along a single mis-shaped cell, at a population level, or in different mutant backgrounds and conditions.

Dynamic modulations of cell diameter is associated with changes in CW surface moduli. We next asked if mechanical properties of the CW could be modulated dynamically in conjunction with cell diameter changes. For this, we treated cells with a low dose (10 µM) of the actin-depolymerizing drug LatruncunlinA. This intermediate dose, likely leaves some

remnant of actin patches, and has been shown to weaken polar domains of the active-GTP-bound Cdc42, and create fatter cells [15]. By performing a time-course after addition of this drug, we noted, that cells enlarged their diameters in times as short as 60-90 min, without the requirement to build a whole new CW through growth and division (Figure S4A). Rather, by observing the localization of the glucan synthase Bgs4, we noticed a gradual expansion around the whole cortex, over ~1h which probably yielded some ectopic CW synthesis and diffuse growth all around the cell, thereby enlarging diameter (Figure 3A-3C). By computing thickness and bulk elastic moduli in controls treated with DMSO for 90 min, and comparing with cells treated with LatA, we found, that cell diameter increase, was associated with a net reduction of side thickness, concomitant with an increase in Y/P (Figure 3D-G). One possible explanation for this result, is that the re-localization of CW remodeling enzymes to cell sides, makes the lateral CW more compliant at short time scales. This CW can thus deform (grow) and thereby thins as a result of mass conservation, much like what normally happens at cell tips [4]. This thinning may concentrate sugar strands, or other elastic elements in the wall and create at the end a net increase in bulk elastic modulus. Importantly, those changes resulted in a net increase of the surface modulus on cell sides, yielding again a conservation of elastic strain during this dynamic changes in diameter (23% in LatA, as compared to 26% in DMSO).

We next sought to alter local cell diameters along the cell, and test if local values in CW mechanics would dynamically correlate with shape changes. For this we used low doses of Caspofungin, a drug which affects glucan synthase activity, and can yield to bulging tips [4]. A 4h treatment with a relatively low dose of 5 µg/ml of Caspofungin yielded cell enlargement at growing cell ends. Locally, this expansion in diameter, was not associated with any notable pattern of thickness changes, but was concomitant with an increase in bulk and surface modulus, with comparable values of local elastic strain in different parts of those cells (22% on the sides, as compared to 19% at the bulging tip) (Figure 3H-I and Figure S4B). Together those findings, suggest that dynamic variations in local and/or global cell diameter are directly associated with changes in CW surface mechanics, and demonstrate that diameter definition through the mechanics of the CW may be regulated on short time scales much smaller than one or several cell cycles.

Overall, our data provide the very first assessment at the single cell level of a correlation between cell shape, size and local values of CW mechanical properties, including, rest length,

thickness, bulk and surface modulus. We find that both the surface modulus and rest length of the CW are tightly linked to local as well as global diameters in fission yeast cells. Importantly, those scaling remain valid for mutants with pleiotropic phenotypes affecting processes as wide as polarity, signaling and metabolism. This suggests that an imbalance in the biochemistry /dynamics of CW assembly could result from multiple complex pathways, not solely as the result of an alteration in the spatial regulation of the activity of polarity platforms like Cdc42, as previously suggested [6, 15-17]. In light of those findings, we suggest a simple model for the regulation of cell diameter. At cell tips the CW is built with a relaxed length and surface elastic modulus which may both depend on polarity as well as other CW related biochemical elements. Those two parameters define the final pressurized state of the CW as it is being moved along the cylinder of the cell, with a major constrain of a fixed elastic strain (deformation). The scaling between surface elasticity and relaxed diameter, suggest that CW portions which are built into a larger rest length, are also stiffer. Although, we do not yet understand the nature of this coupling, we foresee that it may constitute a built-in active or passive property which limits CW strain and overall diameter expansion in those cells. Indeed, the failure strain of the CW (at which the CW layer would break open) has been estimated to be around 45% in *S. Cerevisiae* [18]. Although the composition of the CW in *S. pombe* is different, our findings of a conserved strain of 25-30% well below this failure strain, suggest that the CW will remain mostly intact even when the cell is grown into a larger size. Further systematic investigations of CW mechanical properties in other walled cells with much larger size, may help to uncover conserved design mechanical principles of the CW supporting both cell shape and integrity.

AUTHOR CONTRIBUTION

V.D and H.G. performed experiments. H.T. developed image analysis scripts. V.D., A.B. and N.M designed the research and wrote the manuscript.

ACKNOWLEDGEMENTS

The authors acknowledge Y. Sanchez, T. Toda, P. Perez for sharing material. We acknowledge the ImagoSeine facility, a member of France BioImaging (ANR-10-INSB-04). This project was supported by the CNRS and grants from the FP7 CIG program, ITN ‘‘FungiBrain’’, the ANR (“CellSize”) and the European Research Council (CoG Forcaster no. 647073).

REFERENCES

1. Chiou, J.G., Balasubramanian, M.K., and Lew, D.J. (2017). Cell Polarity in Yeast. Annu Rev Cell Dev Biol *33*, 77-101.

2. Davi, V., and Minc, N. (2015). Mechanics and morphogenesis of fission yeast cells. Curr Opin Microbiol *28*, 36-45.

3. Martin, S.G., and Arkowitz, R.A. (2014). Cell polarization in budding and fission yeasts. FEMS Microbiol Rev *38*, 228-253.

4. Davì, V., Tanimoto, H., Ershov, D., Haupt, A., De Belly, H., Le Borgne, R., Couturier, E., Boudaoud, A., and Minc, N. (2018). Mechanosensation Dynamically Coordinates Polar Growth and Cell Wall Assembly to Promote Cell Survival. Developmental Cell *45*, 170-182.e177.

5. Bonazzi, D., Julien, J.D., Romao, M., Seddiki, R., Piel, M., Boudaoud, A., and Minc, N. (2014). Symmetry Breaking in Spore Germination Relies on an Interplay between Polar Cap Stability and Spore Wall Mechanics. Dev Cell *28*, 534-546.

6. Abenza, J.F., Couturier, E., Dodgson, J., Dickmann, J., Chessel, A., Dumais, J., and Carazo Salas, R.E. (2015). Wall mechanics and exocytosis define the shape of growth domains in fission yeast. Nat Commun *6*, 8400.

7. Atilgan, E., Magidson, V., Khodjakov, A., and Chang, F. (2015). Morphogenesis of the Fission Yeast Cell through Cell Wall Expansion. Curr Biol *25*, 2150-2157.

8. Minc, N., Boudaoud, A., and Chang, F. (2009). Mechanical forces of fission yeast growth. Curr Biol *19*, 1096-1101.

9. Graml, V., Studera, X., Lawson, J.L.D., Chessel, A., Geymonat, M., Bortfeld-Miller, M., Walter, T., Wagstaff, L., Piddini, E., and Carazo Salas, R.E. (2014). A genomic Multiprocess survey of machineries that control and link cell shape, microtubule organization, and cell-cycle progression. Dev Cell *31*, 227-239.

10. Hayles, J., Wood, V., Jeffery, L., Hoe, K.L., Kim, D.U., Park, H.O., Salas-Pino, S., Heichinger, C., and Nurse, P. (2013). A genome-wide resource of cell cycle and cell shape genes of fission yeast. Open Biol *3*, 130053.

11. Cadou, A., Couturier, A., Le Goff, C., Soto, T., Miklos, I., Sipiczki, M., Xie, L., Paulson, J.R., Cansado, J., and Le Goff, X. (2010). Kin1 is a plasma membrane-

associated kinase that regulates the cell surface in fission yeast. Mol Microbiol *77*, 1186-1202.

12. Andoh, T., Yoko, T., Matsui, Y., and Toh, A. (1995). Molecular cloning of the plc1+ gene of Schizosaccharomyces pombe, which encodes a putative phosphoinositide-specific phospholipase C. Yeast *11*, 179-185.

13. Sapala, A., Runions, A., Routier-Kierzkowska, A.L., Das Gupta, M., Hong, L., Hofhuis, H., Verger, S., Mosca, G., Li, C.B., Hay, A., et al. (2018). Why plants make puzzle cells, and how their shape emerges. Elife *7*.

14. Boudaoud, A. (2003). Growth of walled cells: from shells to vesicles. Phys Rev Lett *91*, 018104.

15. Kelly, F.D., and Nurse, P. (2011). Spatial control of Cdc42 activation determines cell width in fission yeast. Mol Biol Cell *22*, 3801-3811.

16. Kelly, F.D., and Nurse, P. (2011). De novo growth zone formation from fission yeast spheroplasts. PLoS One *6*, e27977.

17. Drake, T., and Vavylonis, D. (2013). Model of fission yeast cell shape driven by membrane-bound growth factors and the cytoskeleton. PLoS Comput Biol *9*, e1003287.

18. Stenson, J.D., Hartley, P., Wang, C., and Thomas, C.R. (2011). Determining the mechanical properties of yeast cell walls. Biotechnol Prog *27*, 505-512.

19. Horiseberger, M., and Rosset, J. (1977). Localization of alpha-Galactomannan on the surface of Schizosaccharomyces pombe cells by scanning electron microscopy. Arch Microbiol *112*, 123-126.

20. Clark, A.G., Dierkes, K., and Paluch, E.K. (2013). Monitoring actin cortex thickness in live cells. Biophys J *105*, 570-580.

Materials and Methods

Yeast strains, media and genetics:

Standard methods for *Schizosaccharomyces pombe* media and genetic manipulations were used (http://www-bcf.usc.edu/~forsburg/). Strains used in this study are listed in supplementary Table 1. Strains indicated with a '*' were derived from the commercially available '*S. pombe* Haploid Deletion Mutant Set version 2.0' strains collection (Bioneer Corporation; http://pombe.bioneer.com). Cells were grown at 25°C in yeast extract plus 5 supplements (YE5S) media.

Selection of diameter mutants from the KO library.

A selection of 62 misshapen mutants was first made by intersecting results from the two reports of visual screens of the KO library [9, 10]. Mutants were then transformed with the plasmid pTN509 obtained from the Yeast National Bioresearch Project (Japan), to generate mutant strains expressing GFP-Psy1. Alternatively, mutants were crossed with wt strains carrying GFP-Psy1, and selected following standard procedures. Strains were visually inspected to confirm the phenotype. To facilitate diameter investigations, only mutants with cylindrical or quasi-cylindrical shape were selected, excluding more complex phenotypes, through a pure qualitative screen. When present, skittle shape phenotype was not totally penetrant, allowing imaging of a subset of cylindrical cells in the population. A final quantification was done, selecting mutants with a larger averaged diameter, or a greater variation (i.e. standard deviation), than the wt. From this screen 18 strains were selected.

Drug treatments:

LatrunculinA (Sigma) was used at a final concentration of 10 μM from a 1000X stock in DMSO. The same amount of DMSO was used for the control. Cells were incubated for 1.5h at room temperature before imaging for population analysis. For time lapse LatrunculinA (Sigma) treatment, cells were placed on 2% agar pads made with YE5S+10 mg/ml *Gs*-IB_4 -Alexafluor647 and a final concentration of 10 μM LatrunculinA from a 1000X stock in DMSO. For Caspofungin experiments, cells were placed on 2% agar pads made with YE5S+10 mg/ml *Gs*-IB_4 -Alexafluor647 and a final concentration of 5 mg/ml Caspofungin.

Microscopy:

Live-cell imaging was performed on two different inverted spinning-disk confocal microscopes equipped with motorized stages, automatic focus and controlled with MetaMorph® (Microscopy Automation & Image Analysis Software). The first one (Nikon Ti-Eclipse), is equipped with a Yokogawa CSU-X1FW spinning head, and an EM-CCD camera (Hamamatsu), a 100× oil-immersion objective (Nikon CFI Plan Apo DM 100×/1.4 NA) and a 2.5× magnifying lens, yielding a pixel size of 43 nm. The second one (Leica DMI8), is equipped with a Yokogawa CSU-W1 spinning head, and a sCMOS Orca-Flash 4 V2+ (Hamamatsu) a 100× oil-immersion objective (Leica Plan Apo DM 100×oil/1.4 NA), yielding a pixel size of 70nm.

In all experiments, cells were pre-labeled in growth media containing 5 μg/ml of labelled lectin from *Griffonia simplicifolia* (alias *Bandeiraea simplicifolia*) *Gs*-IB_4-Alexafluor647 [19]. For single-time imaging and laser ablation, cells were usually placed between a glass slide and a coverslip and imaged within 20 min. For time-lapse imaging and for Caspofungin treatment, cells were placed on 2% agar-pads made of YE5S containing 10 μg/ml *Gs*-IB_4 -Alexafluor647 and covered with a coverslip. Imaging was performed at room temperature (22-26 °C), with controlled humidity (>30%).

Laser ablation assay: The laser ablation set up uses a pulsed 355 nm ultraviolet laser interfaced with an iLas system (Roper Scientific) in the ‘‘Mosquito’’ mode. This allows irradiating at multiple positions in the field with laser spots. This system was mounted on the Nikon confocal spinning disk described above, using a 60× oil-immersion objective (CFI Apochromat 60× Oil λS, 1.4 NA, Nikon) in combination with a 2.5× magnifying lens. The irradiation was performed with a low laser power, in order to minimize bleaching of the lectin labeling, used for shape parameters determination. The irradiation was repeated 3-5 times, until the cell visibly deflated with a clear ejection of cytosolic material observable in bright field, to ensure complete wall relaxation. Cells were imaged before and immediately after ablation, switching to a 100× oil-immersion objective (Nikon CFI Plan Apo DM 100×/1.4 NA) and a 2.5× magnifying lens, yielding a pixel size of 43 nm. The full process, including the first image acquisition, laser ablation and the second image after ablation, was typically performed in less than 2 minutes.
Imaging for chromatic registration was performed as in [4], by imaging a slide containing a solution of 0.2 μm TetraSpeck™ microspheres (Thermofisher), and generating images of the same bead at different positions in the field of view to create an ordered array.

Image analysis:

Cell Wall thickness computation: Wall thickness measurement was performed as in [4], including chromatic shift registration and correction. Images of cells labeled for the plasma membrane (GFP-Psy1) and cell wall surface (*Gs*-IB_4-Alexafluor647), were analyzed. A first binarization defined the most external cell boundary, on which perpendicular lines were defined at each pixel. The membrane and lectin signals were scanned along these lines, and a Gaussian fit determined the center for each signal, leading to the definition of membrane and wall contour. After chromatic shift correction, the distance between the two contours where measured, to compute local CW thickness. Because some of the mutants showed a variable intracellular background, plausibly due to partial defects in Psy1 delivery to plasma membrane or increased auto-fluorescence, we systematically implemented a correction script to extract the true signal peak by using an analytical expression of the convoluted intensity profile [4, 20].

Cell Shape and local Wall thickness measurements: For each cell, wall boundaries were obtained by binarization of mid-slice confocal fluorescent images of lectin-Alexafluor647 label, before and after laser ablation. For some cells, the results were manually updated, to correct for local signal bleaching after laser ablation. The long axis of the cell was automatically detected and defined as cell length. Old and new ends were defined by the user, and local radii of curvature ($R_{c1\text{-}0}$) were measured by fitting local tips with a circle using a portion of cell surface of 3.44 μm around the center of the tip; the same section was used to measure tip wall thickness. The two scar bulges localization was defined by the user, scar radius was automatically measured as the distance between them, and thickness computed as a mean of values on a distance of 0.430 μm around the selected center. Cell sides limits were defined by the user, and the radius of the cell ($R_{1\text{-}0}$) was measured as the mean of all diameters on the selected region, as well as side thickness. Birth scars were sometimes superimposed on the selected side region, as in multi-scarred cells. In such case, the scar region (0.430 μm around the selected center) was automatically excluded to compute side parameters.

Subcellular estimation of Y/P: Values of bulk modulus divided by turgor pressure were estimated by the force balance equation, as described in [7], using the variations in cell shape

before and after laser ablation. To this, we implemented local measurements of wall thickness, measured in the inflated state (before ablation), obtaining local values of wall thickness in each cell analyzed. For cell side the force balances on the CW yields:

$$\frac{Y_{side}}{\Delta P} = \frac{R_1}{{R_1}^* h_{side}}$$

where ${R_1}^* = \frac{R_1 - R_0}{R_0}$, while for the tips:

$$\frac{Y_{tip}}{\Delta P} = \frac{Rc}{2Rc^* h_{tip}}$$

where $Rc^* = \frac{Rc - Rc_0}{Rc_0}$.

Old and new tips were analyzed separately.

GFP-Bgs4 concentration measurements: To analyze the localization of polar factors we used the same approach as in [4]. Cells expressing GFP-Bgs4 were labeled with *Gs*-IB$_4$ - Alexafluor647. The cell was first segmented by using the signal from the lectin-labelled cell wall, in order to extract the whole-cell contour. Fluorescent signals of interest were then extracted from fluorescent images by using a mask based on corresponding sub-regions. Signals were corrected for the background signal:

$$I_{tip} = I_{tip\,raw} - I_{bg}$$

$$I_{cell\ contour} = I_{cell\ contour\ raw} - I_{bg}$$

Normalized tip signal is the ratio between the averaged intensity at the two tips divided by the intensity along the full membrane.

$$Norm - Bgs4\ Tip\ Signal = \frac{I_{tip}}{I_{cell\ contour}}$$

Gene ID	GO biological processes					
scd2	signaling	establishment or maintenance of cell polarity	conjugation with cellular fusion			
myo52	mitotic cytokinesis	actin cytoskeleton organization	establishment or maintenance of cell polarity			
coq10	cofactor metabolic process					
kin1	mitotic cytokinesis	membrane organization	actin cytoskeleton organization	establishment or maintenance of cell polarity		
pub1	protein catabolic process	transmembrane transport	protein modification by small protein conjugation or removal			
mae2	generation of precursor metabolites and energy					
vps1	peroxisome organization	membrane organization	vesicle-mediated transport			
dad1	meiotic nuclear division	mitotic sister chromatid segregation				
yaf9	DNA repair	regulation of transcription, DNA-templated	chromatin organization	transcription, DNA-templated		
plc1	signaling	lipid metabolic process				
gpa1	ascospore formation	signaling	conjugation with cellular fusion			
myo1	membrane organization	protein-containing complex assembly	actin cytoskeleton organization	vesicle-mediated transport	establishment or maintenance of cell polarity	
efc25	signaling	establishment or maintenance of cell polarity				
ubr1	signaling	protein catabolic process	regulation of transcription, DNA-templated	protein modification by small protein conjugation or removal	transcription, DNA-templated	
rdp1	regulation of transcription, DNA-templated	meiotic nuclear division	chromatin organization	transcription, DNA-templated		
rga2	signaling					
rga4	signaling	actin cytoskeleton organization	establishment or maintenance of cell polarity			
mtq2	cytoplasmic translation					
wsc1	signaling					
mtl2	signaling					
rgf2	cell wall organization or biogenesis	signaling				
rgf1	signaling	carbohydrate metabolic process	cell wall organization or biogenesis			
pmk1	metal ion homeostasis	signaling	transmembrane transport	regulation of transcription, DNA-templated	transcription, DNA-templated	cell wall organization or biogenesis
pck2	signaling	carbohydrate metabolic process	establishment or maintenance of cell polarity	cell wall organization or biogenesis		
agn1	carbohydrate metabolic process	conjugation with cellular fusion	cell wall organization or biogenesis			
omg1	carbohydrate metabolic process	conjugation with cellular fusion	cell wall organization or biogenesis			

Table 1: Gene functions for our set of mutants assigned from the Gene Ontology classification (https://www.pombase.org/)

Experimental Models: *S. pombe* Strains	SOURCE	IDENTIFIER
h+ *GFP-psy1:ade bgs4::ura4 RFP-bgs4-Leu* (*leu1-32 ura4-D18 ade6*)	This study	VD57
h- *GFP-psy1:ade bgs4::ura4 RFP-bgs4-Leu* (*leu1-32 ura4-D18 ade6*)	This study	VD58
h+ *bgs4::ura4 RFP-bgs4-Leu* (*leu1-32 ura4-D18 ade6-M216*)	This study	NM387
h- *rga2::KanMX bgs4::ura4 RFP-bgs4-Leu GFP-psy1:ade* (*leu1-32 ura4-D18*)	This study	VD72
h- *rga4::KanMX bgs4::ura4 RFP-bgs4-Leu GFP-psy1:ade* (*leu1-32 ura4-D18*)	This study	VD81
h+ wsc1::KanMX GFP-psy1:ade bgs4::ura4 RFP-bgs4:leu (*leu1-32 ura4-D18 ade6*)	This study	VD158
h- *mtl2::KanMX GFP-psy1:ade bgs4::ura4 RFP-bgs4:leu* (*leu1-32 ura4-D18 ade6*)	This study	VD160
h- *pck2::leu GFP-psy1:ade*	This study	VD109
h+ *rgf2::ura GFP-psy1:ade* (*leu1-32 ura4-D18 ade6*)	This study	VD164
h+ *rgf1::KanMX GFP-psy1:ade* (*leu1-32 ura4-D18 ade6*)	This study	VD167
h+ *pmk1:ura GFP-psy1:leu* (*leu1-32 ura4-D18*)	This study	VD173
h+ *scd2::KanMX CRIB-tdTomato:ura Leu:GFP-psy1 (ura4-D18 leu1-32)*	This study	VD97
h+ *myo52::ura CRIB-tdTomato:ura Leu:GFP-psy1 (ura4-D18 leu1-32)*	This study	VD127
h+ *coq10::KanMX GFP-psy1:ade (ade6-M216 ura4-D18 leu1-32)*	This study*	HG77
h+ *kin1::KanMX GFP-psy1:ade (ade6-M216 ura4-D18 leu1-32)*	This study*	HG101
h+ *pub1::KanMX GFP-psy1:ade (ade6-M216 ura4-D18 leu1-32)*	This study*	HG72
h+ *mae2::KanMX GFP-psy1:ade (ade6-M216 ura4-D18 leu1-32)*	This study*	HG74
h+ *vps1::KanMX GFP-psy1:ade (ade6-M216 ura4-D18 leu1-32)*	This study*	HG31
h+ *dad1::KanMX GFP-psy1:ade (ade6-M216 ura4-D18 leu1-32)*	This study*	HG76
h+ *yaf9::KanMX GFP-psy1:ade (ade6-M216 ura4-D18 leu1-32)*	This study*	HG103
h+ *plc1::KanMX GFP-psy1:ade (ade6-M216 ura4-D18 leu1-32)*	This study*	HG104
h+ *gpa1::KanMX GFP-psy1:ade (ade6-M216 ura4-D18 leu1-32)*	This study*	HG106
h+ *myo1::KanMX: GFP-psy1:ade (ade6-M216 ura4-D18 leu1-32)*	This study*	HG27
h+ *efc25::KanMX GFP-psy1:ade (ade6-M216 ura4-D18 leu1-32)*	This study*	HG29
h+ *ubr1::KanMX GFP-psy1:ade (ade6-M216 ura4-D18 leu1-32)*	This study*	HG33
h+ *rdp1::KanMX GFP-psy1:ade (ade6-M216 ura4-D18 leu1-32)*	This study*	HG35
h+ *mtq2::KanMX GFP-psy1:ade (ade6-M216 ura4-D18 leu1-32)*	This study*	HG116
h+ *agn1:KanMX GFP-psy1:ade (ade6-M216 ura4-D18 leu1-32)*	This study*	HG75
h+ *omg1:KanMX GFP-psy1:ade (ade6-M216 ura4-D18 leu1-32)*	This study*	HG121

Table S1. Strain list. * indicates strains derived from '*S. pombe* Haploid Deletion Mutant Set version 2.0' strains collection (Bioneer Corporation; http://pombe.bioneer.com).

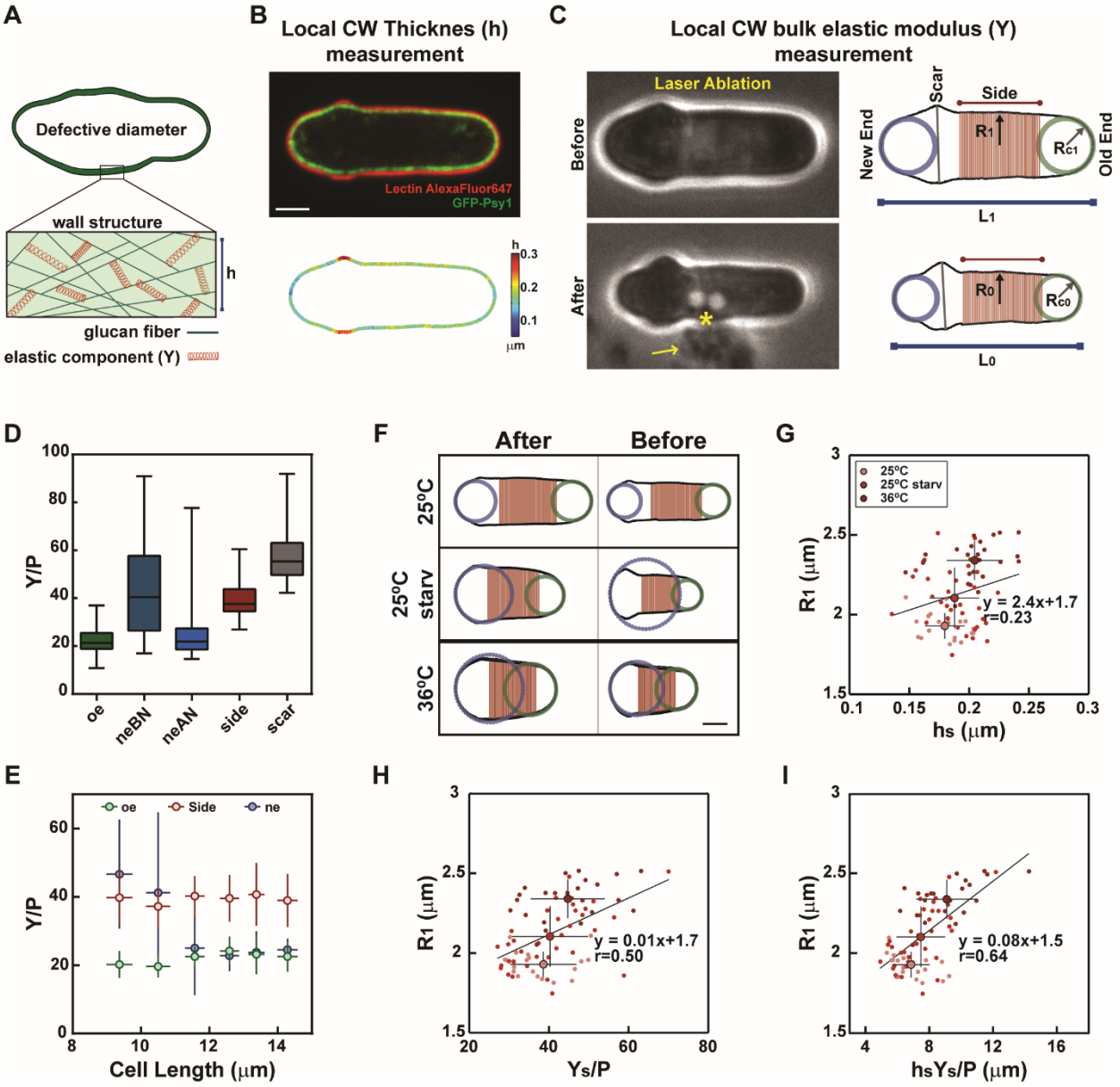
A
Defective diameter
wall structure
h
glucan fiber
elastic component (Y)
B
Local CW Thicknes (h) measurement
Lectin AlexaFluor647
GFP-Psy1
h
0.3
0.2
0.1
μm
C
Local CW bulk elastic modulus (Y) measurement
Laser Ablation
Before
After
Scar
Side
New End
Old End
R1
Rc1
L1
R0
Rc0
L0
D
Y/P
oe
neBN
neAN
side
scar
E
oe
Side
ne
Y/P
Cell Length (μm)
F
After
Before
25°C
25°C starv
36°C
G
25°C
25°C starv
36°C
R1 (μm)
y = 2.4x+1.7
r=0.23
hs (μm)
H
R1 (μm)
y = 0.01x+1.7
r=0.50
Ys/P
I
R1 (μm)
y = 0.08x+1.5
r=0.64
hsYs/P (μm)

Figure 1. A method to measure local wall mechanical properties in *S. pombe* cells

(A) Schematic representation of a cell with varying diameters, and zoom on cell wall bulk organization, defining thickness (h) and bulk elastic modulus (Y). **(B)** Mid-slice confocal fluorescent image of a cell expressing GFP-psy1 and labelled with lectin-Alexafluor647, and corresponding CW thickness map obtained as in [4]. **(C).** (Left) Method to estimate local wall bulk modulus (Y) divided by turgor pressure (P). Bright-field images of the same cell depicted in B before (top) and after (bottom) laser ablation. The star indicates the location of laser ablation, the arrow point at a cloud of cytosolic material ejected from the cell. (Rigth) Cell wall boundaries of the same cell, obtained by binarization of the lectin-Alexafluor647 signal, before and after ablation, are used to compute local radii of curvature at cell tips, and the radius along the cell side, defined as a mean on the red region. **(D)** Y/P values computed at old end (oe, n=99), new end before (neBN, n=20) and after (neAN, n=64)) NETO, sides (n=99) and scars (n=99), in a WT population of cells. **(E)** Evolution of Y/P as a function of cell length. Individual cells have been imaged and binned by length, (between 8 and 20 cells for each point). **(F)** Cell wall boundaries and local features, before and after ablation, of typical wt cells grown at 25^0C in exponential phase (25^0C), after 16 hs of starvation (25^0C starv), and at 36^0C in exponential phase (36^0C). **(G-I)** Cell radius (R_1), as a function of side wall thickness (h_s), side Y/P (Y_s/P) or surface modulus divided by P ($Y_s h_s$/P), in the same conditions as in F (for 25^0C n=21, 25^0C starv n=34, 36^0C n=24). Small dots correspond to single cells measurements, and larger dots represent the average values. The line is a linear fit on single cell measurements. r values correspond to Pearson correlation coefficients. Whisker plots represent median and full data set range. Error bars are standard deviations, scale bars 2μm.

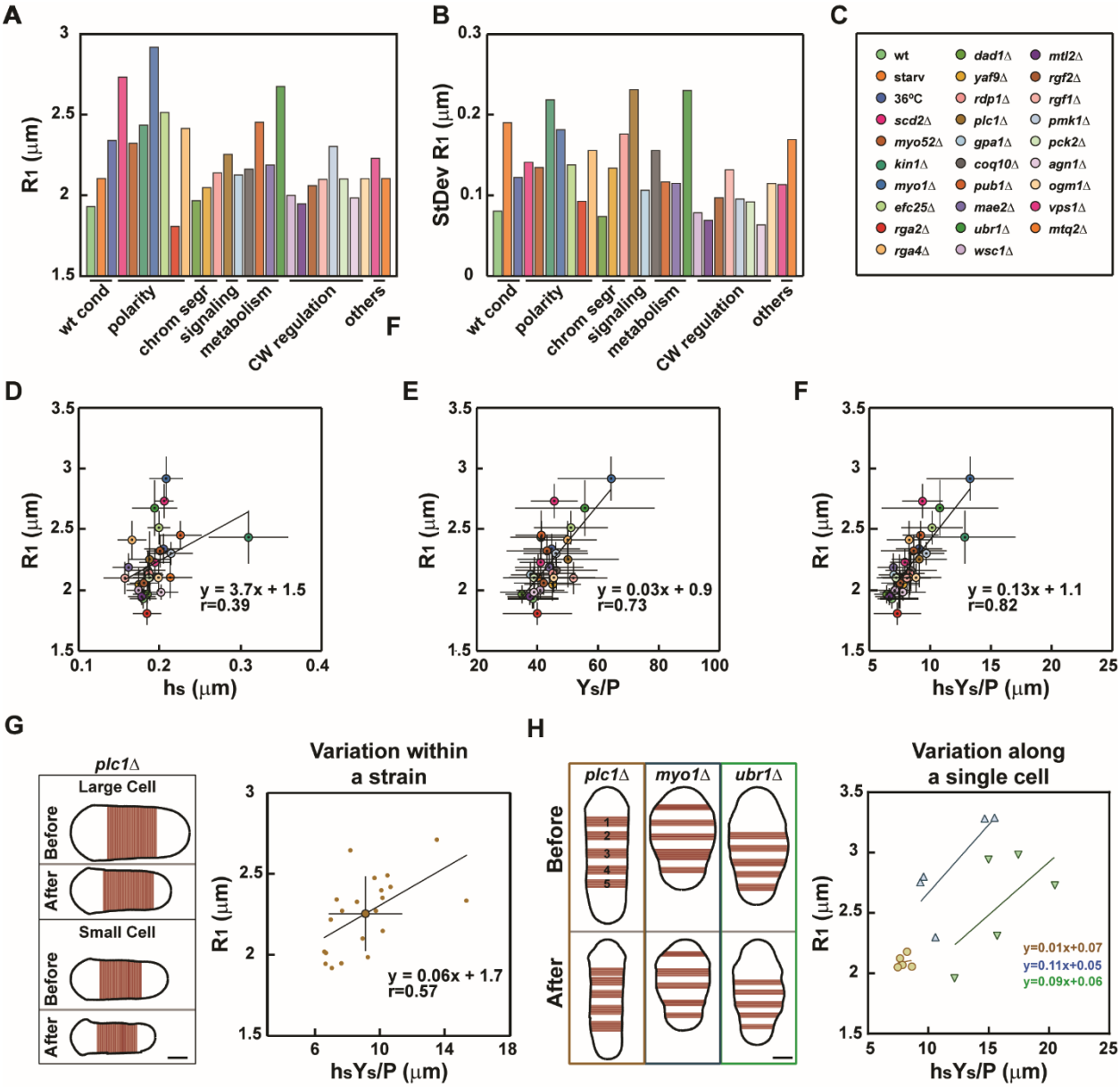
A
R1 (μm)
wt cond
polarity
chrom segr
signaling
metabolism
CW regulation
others
B
StDev R1 (μm)
C
wt
starv
36ºC
scd2Δ
myo52Δ
kin1Δ
myo1Δ
efc25Δ
rga2Δ
rga4Δ
dad1Δ
yaf9Δ
rdp1Δ
plc1Δ
gpa1Δ
coq10Δ
pub1Δ
mae2Δ
ubr1Δ
wsc1Δ
mtl2Δ
rgf2Δ
rgf1Δ
pmk1Δ
pck2Δ
agn1Δ
ogm1Δ
vps1Δ
mtq2Δ
D
y = 3.7x + 1.5
r=0.39
hs (μm)
E
y = 0.03x + 0.9
r=0.73
Ys/P
F
y = 0.13x + 1.1
r=0.82
hsYs/P (μm)
G
plc1Δ
Large Cell
Before
After
Small Cell
Variation within a strain
y = 0.06x + 1.7
r=0.57
H
plc1Δ
myo1Δ
ubr1Δ
Variation along a single cell
y=0.01x+0.07
y=0.11x+0.05
y=0.09x+0.06

Figure 2. Genetic screening of CW mechanical parameters on diameter defective mutants
(A-C) Mean cell radius on cell sides of different mutants and WT conditions **(A)** and standard deviations **(B)** as annotated in the legend in **C**. Mutants are sorted by a simplification of the Gene Ontology functions as annotated in Table 1. **(D-F)** Cell radius (R_1), plotted as a function of side wall thickness (h_s), side bulk modulus (Y_s/P) or side surface modulus divided by P ($Y_s h_s/P$), in the conditions and mutants listed in the legend in **C**. Each strain is represented by its average value. The line is a linear fit on averages. **(G)** (Left) Cell Wall boundaries, before and after ablation, of 2 extreme *plc1Δ* cell examples with large and small radii. (Right) Cell radius (R_1), as a function of surface modulus divided by P ($Y_s h_s/P$) within a population of *plc1Δ* (n=21). Small dots are single cells measurements, and the big dot is the average. The line is a linear fit of single cell measurements. **(H)** (Left) Cell wall boundaries and definition of 5 side regions, before and after ablation, for one rod shape cell (*plc1Δ*) and two skittles cells (*myo1Δ* and *ubr1Δ*). (Right) Local radius (R_1), plotted as a function of the corresponding surface modulus divided by P ($Y_s h_s/P$) in 5 different parts along the side of the same cell, for the same cells represented on the left (colors correspond). Small dots are single cells measurements, the line is a linear fit on of those measurements. r values correpond Pearson correlation coefficients. Error bars represent standard deviations, scale bars 2μm.

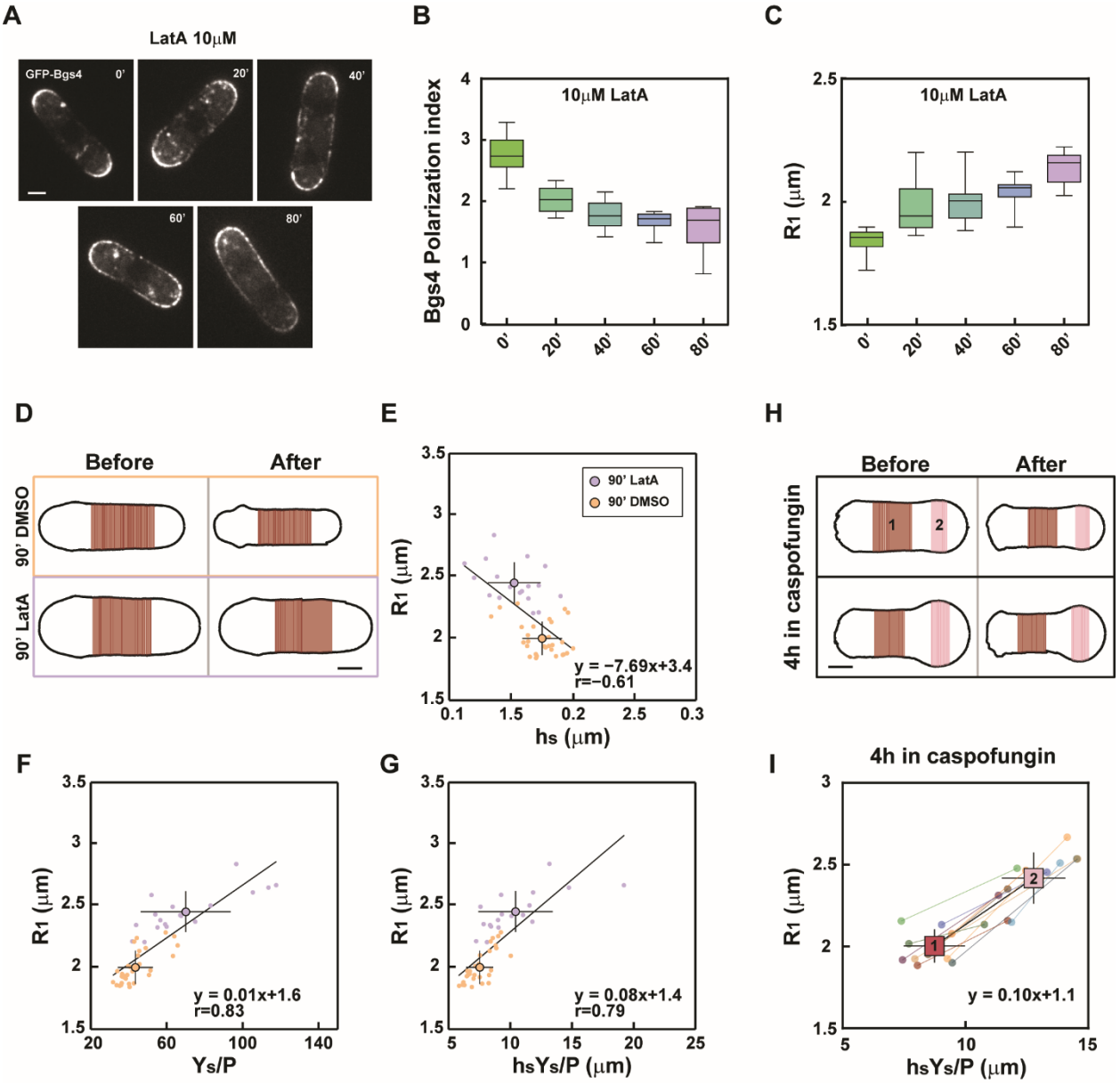
A
LatA 10μM
GFP-Bgs4
0'
20'
40'
60'
80'
B
10μM LatA
Bgs4 Polarization index
0'
20'
40'
60'
80'
C
10μM LatA
R1 (μm)
D
Before
After
90' DMSO
90' LatA
E
90' LatA
90' DMSO
y = −7.69x+3.4
r=−0.61
R1 (μm)
hs (μm)
H
Before
After
4h in caspofungin
1
2
F
y = 0.01x+1.6
r=0.83
R1 (μm)
Ys/P
G
y = 0.08x+1.4
r=0.79
R1 (μm)
hsYs/P (μm)
I
4h in caspofungin
y = 0.10x+1.1
R1 (μm)
hsYs/P (μm)

Figure 3. Dynamic modulation of CW mechanical parameters during local and global changes in cell radius

(A) GFP-Bgs4 localization in wt cells at different time points after treatment with 10μM Latrunculin A. **(B)** Quantification of GFP-Bgs4 polarity (tip signal divided by full cell contour signal), in cells treated as in **A**. **(C)** Mean cell radius (R_1), in cells treated as in **A. (D)** Cell wall boundaries and cell side definition, before and after ablation, of typical cells treated for 1.5 hr with DMSO or 10μM LatrunculinA **(E-G)** Cell radius (R_1), plotted as a function of side wall thickness (h_s), side bulk (Y_s/P) or surface modulus divided by P ($Y_s h_s/P$), in wt cells treated for 1.5 hr with DMSO (n=30) or 10μM LatrunculinA (n=18). Small dots are single cells measurements, and larger dots are averages. The line is a linear fit on single cell measurements. **(H)** Cell wall boundaries and definition of rod (red - 1) and swollen (pink - 2) radii, before and after ablation, in wt cells treated with Caspofungin (5μg/ml) for 4 hr. **(I)** Local radius (R_1), as a function of corresponding surface modulus divided by P ($Y_s h_s/P$), measured in the rod part (1) and in the swollen part (2) of single wt cells treated as in **H**. Small dots of the same color, linked by a line, are single cells measurements of rod (red - 1) or swollen (pink - 2) part. Big dots are the average of rod parts (1) and swollen parts (2) (n=11). r values correspond to Pearson correlation coefficients. Error bars are standard deviations, scale bars 2μm.

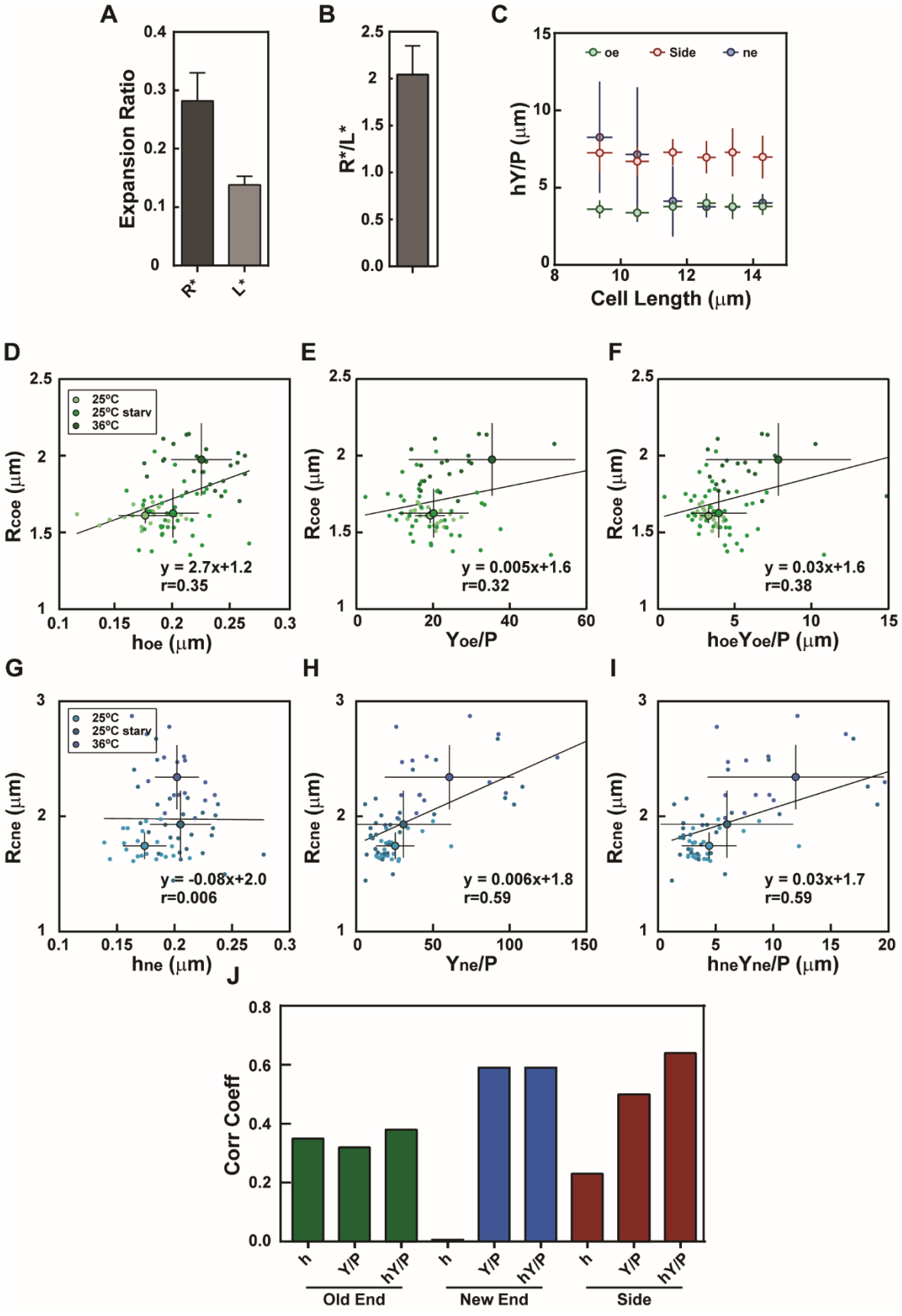
A
Expansion Ratio
R*
L*
B
R*/L*
C
oe
Side
ne
hY/P (μm)
Cell Length (μm)
D
25°C
25°C starv
36°C
Rcoe (μm)
hoe (μm)
y = 2.7x+1.2
r=0.35
E
Yoe/P
y = 0.005x+1.6
r=0.32
F
hoeYoe/P (μm)
y = 0.03x+1.6
r=0.38
G
Rcne (μm)
hne (μm)
y = -0.08x+2.0
r=0.006
H
Yne/P
y = 0.006x+1.8
r=0.59
I
hneYne/P (μm)
y = 0.03x+1.7
r=0.59
J
Corr Coeff
h
Y/P
hY/P
Old End
New End
Side

Figure S1. Anisotropy and tip behavior of cell wall in *S. pombe*

(A) Relative expansion radius (measured as (R1-R0)/R0) and relative expansion length (measured as (L1-L0)/L0) of wt cells after laser ablation (n=99). **(B)** Ratio between the two expansion ratios calculated for each cell in **A** (n=99). **(C)** Evolution of local values of hY/P as a function of cell length. Individual cells have been imaged and binned by length, (between 8 and 20 cells for each point). **(D-F)** Radius of curvature at the old end (R_{oe}), plotted as a function of old end wall thickness (h_{oe}), old end bulk modulus divided by P (Y_{oe}/P) or surface modulus divided by P ($Y_{oe}h_{oe}/P$), in the same conditions as in **Fig. 1G** (for 25^0C n=21, 25^0C starv n=39, 36^0C n=25). **(G-I)** Radius of curvature at the new end (R_{ne}), plotted as a function of new end wall thickness (h_{ne}), new end bulk modulus divided by P (Y_{ne}/P) or surface modulus divided by P ($Y_{oe}h_{oe}/P$), in the same conditions as in **Fig. 1G** (for 25^0C n=21, 25^0C starv n=29, 36^0C n=17). For **D-I** small dots correspond to single cells measurements, and the larger dot the average. The line is a linear fit of single cell measurements. Error bars are standard deviations. **(J)** Pearson correlation coefficients, between cell radius and wall thickness (h), bulk modulus divided by pressure Y/P or surface modulus divided by pressure (Yh/P), in different parts of the cell as indicated. Those values correspond to those presented in **Fig. 1 and S1.**

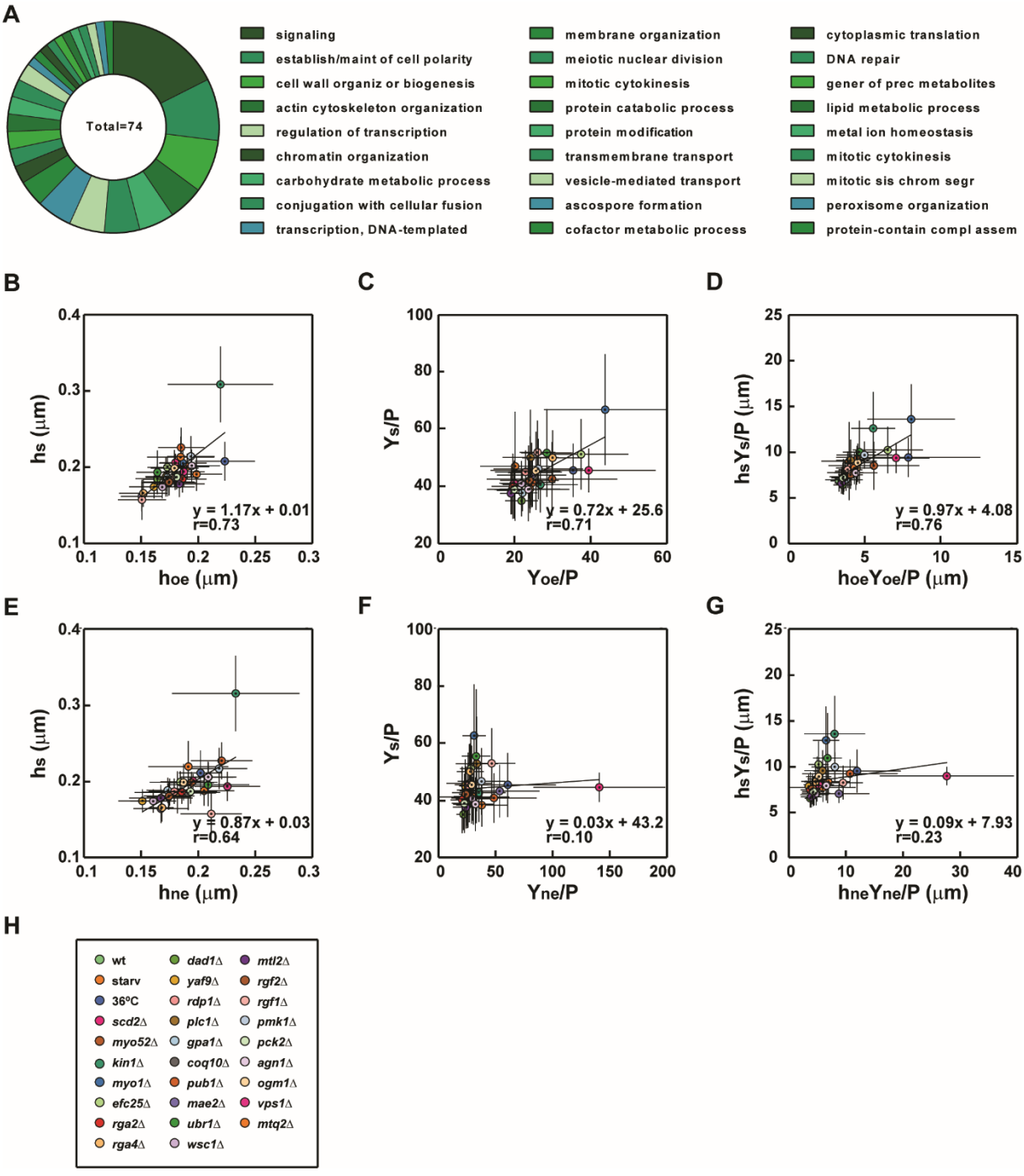
A
Total=74
signaling
establish/maint of cell polarity
cell wall organiz or biogenesis
actin cytoskeleton organization
regulation of transcription
chromatin organization
carbohydrate metabolic process
conjugation with cellular fusion
transcription, DNA-templated
membrane organization
meiotic nuclear division
mitotic cytokinesis
protein catabolic process
protein modification
transmembrane transport
vesicle-mediated transport
ascospore formation
cofactor metabolic process
cytoplasmic translation
DNA repair
gener of prec metabolites
lipid metabolic process
metal ion homeostasis
mitotic cytokinesis
mitotic sis chrom segr
peroxisome organization
protein-contain compl assem
B
hs (μm)
hoe (μm)
y = 1.17x + 0.01
r=0.73
C
Ys/P
Yoe/P
y = 0.72x + 25.6
r=0.71
D
hsYs/P (μm)
hoeYoe/P (μm)
y = 0.97x + 4.08
r=0.76
E
hs (μm)
hne (μm)
y = 0.87x + 0.03
r=0.64
F
Ys/P
Yne/P
y = 0.03x + 43.2
r=0.10
G
hsYs/P (μm)
hneYne/P (μm)
y = 0.09x + 7.93
r=0.23
H
wt
starv
36ºC
scd2Δ
myo52Δ
kin1Δ
myo1Δ
efc25Δ
rga2Δ
rga4Δ
dad1Δ
yaf9Δ
rdp1Δ
plc1Δ
gpa1Δ
coq10Δ
pub1Δ
mae2Δ
ubr1Δ
wsc1Δ
mtl2Δ
rgf2Δ
rgf1Δ
pmk1Δ
pck2Δ
agn1Δ
ogm1Δ
vps1Δ
mtq2Δ

Figure S2. Classification of wall or diameter defective mutants and influence of tips wall mechanics on cell shape

(A) Cake plot of Gene Ontology classification of the mutants used in the screening presented in **Fig. 2**. The list starts with the most abundant and follows in a clockwise direction. **(B-D)** CW thickness, bulk elastic modulus divided by pressure, and surface modulus divided by pressure on cell sides plotted as a function of those at old ends. **(E-G)** CW thickness, bulk elastic modulus divided by pressure, and surface modulus divided by pressure on cell sides plotted as a function of those at new ends. **(H)** Legend of conditions or mutants used in **B-G.** r values correspond to Pearson correlation coefficients. Error bars are standard deviations.

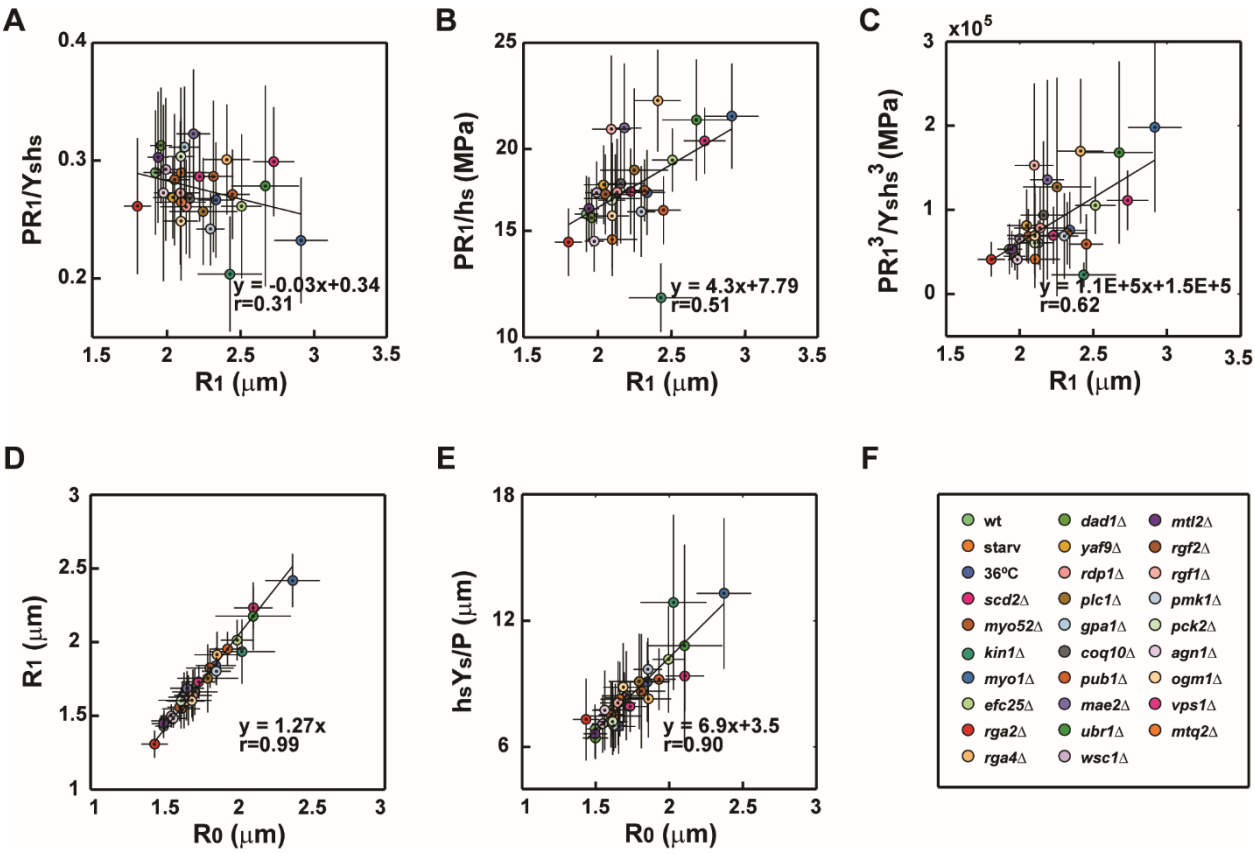
A
PR1/Yshs
R1 (μm)
y = -0.03x+0.34
r=0.31
B
PR1/hs (MPa)
R1 (μm)
y = 4.3x+7.79
r=0.51
C
x10^5
PR1^3/Yshs^3 (MPa)
R1 (μm)
y = 1.1E+5x+1.5E+5
r=0.62
D
R1 (μm)
R0 (μm)
y = 1.27x
r=0.99
E
hsYs/P (μm)
R0 (μm)
y = 6.9x+3.5
r=0.90
F
wt
starv
36ºC
scd2Δ
myo52Δ
kin1Δ
myo1Δ
efc25Δ
rga2Δ
rga4Δ
dad1Δ
yaf9Δ
rdp1Δ
plc1Δ
gpa1Δ
coq10Δ
pub1Δ
mae2Δ
ubr1Δ
wsc1Δ
mtl2Δ
rgf2Δ
rgf1Δ
pmk1Δ
pck2Δ
agn1Δ
ogm1Δ
vps1Δ
mtq2Δ

Figure S3. Evolution of key mechanical values in the CW as a function of cell radius

(A) Elastic strain in the cell wall plotted as a function of cell radius **(B)** Elastic stress in the cell wall plotted as a function of cell radius **(C)** Energy corresponding to pressure normalized to the energy of cell wall bending plotted as a function of cell radius **(D)** Turgid radius plotted as a function of rest radii, R_0 **(E)** Surface modulus plotted as a function of the rest radius **(F)** Legend of conditions or mutants used in **A-E.** Error bars are standard deviations.

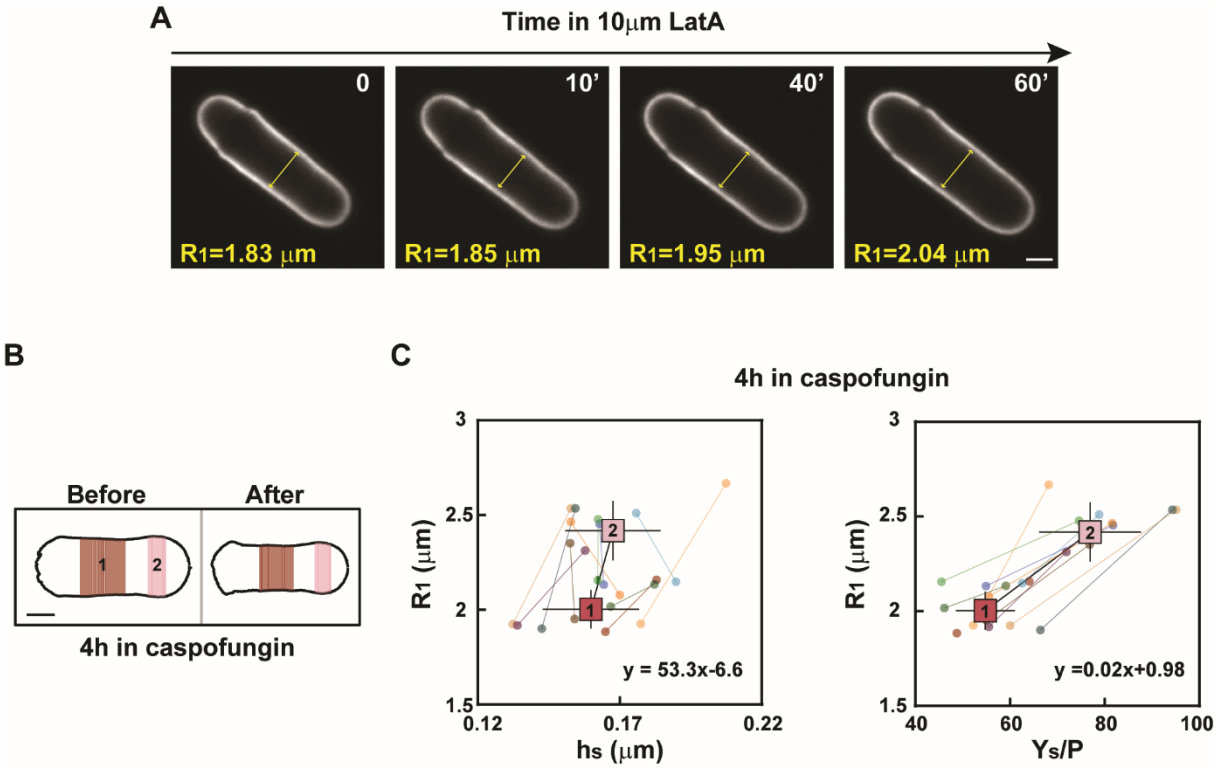
A
Time in 10μm LatA
0
10'
40'
60'
R1=1.83 μm
R1=1.85 μm
R1=1.95 μm
R1=2.04 μm
B
Before
After
1
2
4h in caspofungin
C
4h in caspofungin
R1 (μm)
hs (μm)
y = 53.3x-6.6
Ys/P
y =0.02x+0.98

Figure S4. Evolution of cell diameter and CW parameters upon perturbations

(A) Time lapse of diameter increase, in a cell treated with 10 μM LatA. The cell is labeled with lectin *Gs*-Alexafluor647. **(B)** Cell wall boundaries and definition of rod (red - 1) and swollen (pink - 2) radius, before and after ablation, in wt cells treated with Caspofungin (5μg/ml) for 4 hr. **(C)** Local radius (R_1), as a function of corresponding wall thickness or bulk modulus divided by P (Y_s/P), measured in the rod part and in the swollen part of single wt cells treated as in **B**. Small dots of the same color, linked by a line, are single cells measurements of rod (smaller radius) or swollen (larger radius) part. Squares are the average of rod parts (red - 1) and swollen parts (pink - 2) (n=11). Error bars are standard deviations, scale bars 2μm.

DISCUSSION

During my PhD studies, I investigated the influence of cell wall mechanics on growth and morphogenesis of the fission yeast *Schizosaccharomyces pombe*. To this aim, I developed diverse methods to directly monitor cell mechanical parameters *in vivo*. Through my results, I provided, for the first time, information on the dynamical changes of cell wall mechanics over growth and I could show that a very tight control of wall mechanical properties can ensure cell integrity and correct morphology.

In each single set of results, a specific discussion is already included. The aim of this chapter is to provide a more general overview on my work, and to propose some future directions that can arise from it.

In my results, I have shown that cell wall thickness is highly variable at growing ends and its variation is directly linked to patterns of growth. Although I could not measure bulk modulus variation with the same time resolution for reasons intrinsic to the experimental method exploited (laser ablation), I could observe that the bulk modulus is almost constant within the cell cycle. This is a peculiar result, which suggests that in wild type cells the wall deposited at cell tips has constant composition over growth, while the amount of the deposited material (that I assume here to be proportional to thickness) varies, influencing growth.

It would be interesting to assess the molecular regulation of tip thickness change, through simultaneous observations of thickness patterns and wall synthesis regulators (synthases, RhoGTPase and others). Unfortunately, with our current methodology we cannot image fluorescent tagged polarity proteins for extended periods of times. In fact, the main lectin used to stain the cell wall surface fluoresces normally in the far-red spectrum, but after sequential excitations it starts to bleed through in the red channel, making problematic any quantification of red fluorescent probes. We use the green spectrum for the membrane labeling. We have strived, in the past years, to construct CFP-labels but their signals resulted too feeble and difficult to detect in our microscopy set-up. Admittedly, the methodology involved has still room for improvement, for example by developing more stable labeling for the lectin, in far red or using other fluorophores.

However, in independent experiments performed within my team, my colleagues are monitoring patterns of polarized proteins within growth. After analysis of several candidates related to wall synthesis, including synthases, regulators of polarity and cytoskeleton related proteins, we could not find a candidate, which follows the observed wall thickness patterns. I believe that this might

be due to the fact that thickness is not the mere result of synthesis, but that is the more complex output of synthesis, remodeling and growth. Theoretical models, supported by further measurements and analysis, implementing the parallel observations of all the mentioned parameters, will be crucial to thoroughly understand this complex interplay.

The behavior of the new end is still partially unclear in the field. In fact, in wild type cells, this tip is not growing immediately after division, and the polarity machinery is assembled there only after the cell has reached a certain length, in a process named New End Take Off (NETO). This process depends on cell cycle progressions, as cells blocked in G1 do not undergo NETO. Microtubule related proteins, Tea1 and Tea4, are involved in this event, as their deletions mutants fail to develop a second polarity domain, but they are not sufficient to trigger take off, as they are localized at the new end also before polarity establishment (Das et al., 2007; Martin et al., 2005). Tea1 and Tea4 have been suggested to recruit For3 to promote actin filaments elongations, as *for3Δ* has defects in NETO and fusion of Tea1 to For3 is sufficient to trigger take off, even in G1 (Martin et al., 2005). However, no previous report has described eventual mechanical differences between a growing and a non-growing end, which are most likely necessary to explain how two tips under the same pressure behave differently. Here, I have shown that the mechanics of the wall at the new end changes dramatically before and after take-off, starting with characteristics typical of non-growing parts such as cell sides, becoming very similar to the other tip at the end of the first cell cycle, suggesting that the initial rigidity of the wall may hinder premature growth. However, more work should be carried to further this aspect, for example, to understand how wall remodeling is influencing growth. Mutants lacking For3 or the GAP Rga4 present a remarkable phenotype, where after division the two sister cells behave differently, with one cell growing bipolar from the very beginning and the other monopolar for the full cell cycle (Das et al., 2007). Since these cells are genotypically identical, this difference must be somehow encoded in non-genetic differences between the two cells (Chiou et al., 2017). Within the possibilities, it would be useful to test whether those mutants, and other mutants impaired in NETO, exhibit differences in the mechanical properties of the new end and how wall remodeling is regulated. This work will clarify how cell growth is mechanically hindered at the beginning, and how elongation initiates from these new sites. Further analysis on the interplay between polarity components and wall mechanics variation

may explain how competition between the two poles may influence surface mechanics variation and different elongation.

Another important result of my work is that the diameter of the cylinder is mostly defined by the properties of the wall at cell side. Both thickness and bulk modulus are stable over growth in *wt* cells, consistent with the highly stable value of the diameter. Moreover, as observed in other tip growing fungi (Goldenbogen et al., 2016; Ma, 2005), the bulk modulus have a net increase at cell side compared to the apex and this is accompanied by a further increase in thickness, corresponding to an almost two fold increase in the lateral surface modulus. In addition, in the mutants and conditions screened, the mechanical properties at old ends scale with those at cell sides. This is consistent with a model of wall maturation after the initial synthesis, and might be the result of the enzymatic activity of wall remodelers. Structural and chemical analysis on β-glucans extracted from different microorganisms including fungi, have revealed that the length of linear chains and their branching profoundly modify the physical and chemical properties of the molecules, such as solubility (Stone, 2006). Moreover, linear long chains tend to arrange mostly in single helices, while relatively small linear chains (<30 monomers) and branched (1-6) β-branched molecules can form triple helices (Saito et al., 1990). It is reasonable to think that these structural modifications are also translated in variation in mechanical properties of glucans, and therefore of the wall structure.

As mentioned in the *Introduction,* Gas1 is the only glucanosyl-transferase essential during vegetative growth described in *S. pombe,* whose lethal deletion phenotype can be attenuated by osmotic support, suggesting that its wall is not fully mature and stiff enough to restrain turgor pressure. Gas1 promotes the elongation of glucan chains up to more that 30 monomers *in vitro,* and although it has not been reported to have a branching activity, its deletion reduces (1-6) β-branches, which may be a consequence of the decrease of glucan chains length (de Medina-Redondo et al., 2010).

It would be interesting to further characterize how this enzyme, and other putative wall remodelers, are influencing the mechanisms of wall maturation, by characterizing better their deletion mutants and wall mechanics.

In addition, the parameter that best correlates with diameters is the ratio between side surface modulus and turgor pressure. By assuming homogeneous turgor pressure between mutants, this

analysis implies that the surface modulus of the wall increases with increasing diameter. This may happen because, mutants growing with larger diameters produces an excess of wall synthases and/or remodelers building an excess of material for each wall segment. More material can result in a larger relaxed radius, which I observed to be proportional to the inflated radius of the cell. This result is interesting because it suggests that a larger relaxed circular wall segment has a stiffer wall. By pure speculation, this can be due to molecular properties of glucans, where longer glucans can be more remodeled increasing the stiffness of the segment. Testing the genetic interactions between diameter defective mutants and remodeling enzymes may allow to elucidate those aspects.

Another important point is to understand whether diameter establishment is a mere output of synthesis and remodeling, purely regulated by the amount and quality of wall material produced, or if it is regulated by an active process of geometrical control. As already described in the *Introduction* and in the *Results*, proteins involved in wall control are the two putative sensors Mtl2 and Wsc1. As observed in the *Results*, the two deletion mutants do not show diameter or wall defects. This can suggest that the composition of the wall at cell sides is not regulated by those sensors, and the sole properties of the wall material converge to defined diameters. However, these two sensors have been shown to be redundant, as the double deletion is lethal. Moreover, *mtl2Δ* is hypersensitive to diverse perturbations, like caffeine, SDS, NaCl. Differently than Wsc1 that is polarized at cell tips, Mtl2 is localized along the full plasma membrane (Cruz et al., 2013), making it a good candidate for the surveillance of lateral wall composition. To confirm or rule out implications of wall sensors in this process, it would be interesting to test whether the double mutant (through shut-off alleles) shows transient defects in diameter before death and if *mtl2Δ* is hypersensitive to perturbation of diameter maintenance, through β-glucanase inhibition or mild actin de-polymerization.

To summarize, my second work demonstrated that cell diameter is tightly linked to cell mechanical properties. However, how wall mechanics is biochemically regulated is still unclear. I believe that cell diameter is the output of the complex synthesis and remodeling of the cell wall structure. Here I propose some further experiments that may be the direct evolution of my project, and will help to understand how the synthase and remodeling machineries can regulate wall composition. I also proposed some hypothesis on how different type of glucans can give specific mechanical composition to the wall. However, to understand the link between chemical structure, mechanical

properties and final shape of this complex shell, further works on wall composition and its ultrastructure will be necessary.

In some of the previous arguments, I assumed homogeneous turgor pressure between mutants, but this might be an oversimplification. A recent work described a method to estimate cell turgor pressure, by coupling relaxed wall geometry to wall shrinkage after osmotic treatment (Atilgan et al., 2015). A similar approach can be coupled to the laser ablation measurement, to estimate turgor pressure in the mutants screened and to clarify this point.

One important achievement of my work is the establishment of methods to measure cell mechanical properties *in vivo* at large population scale, in fission yeast. We are currently working on the extension of this method to other organisms, starting from other fungi. These methods rely on confocal imaging of internal and external boundary of the cell wall, labeled with diverse fluorophores. In fission yeasts, we exploited the established knowledge of its cell wall composition, through which we could easily identify a galactomannans specific lectin, binding the surface of the cell wall, whose fluorescent labeled versions are commercially available (Horisberger and Rouvet-Vauthey, 1985). For the internal surface, we took advantage of the profound knowledge of fission yeast cell biology, and we identify Psy1, as a rather homogeneous transmembrane SNARE protein, whose GFP fusion was already described, and found to be stable and functional (Maeda et al., 2009; Nakamura et al., 2001).
A similar approach can be taken in other well described organisms. For instance, in *Saccharomyces cerevisiae,* by carrying some preliminary experiments, we identified ConcanavalinA, a mannan

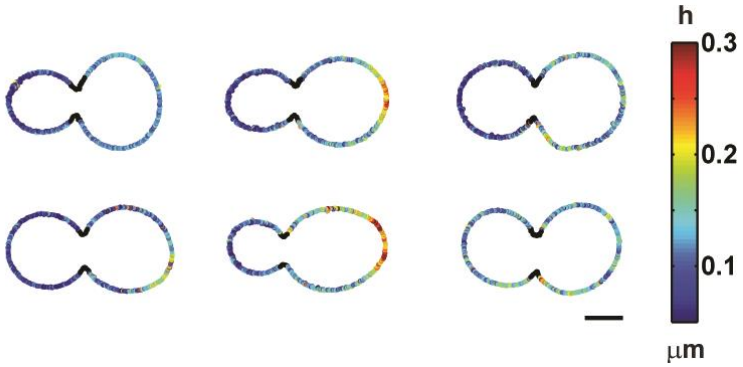

Figure D.1. Typical wall thickness maps in budding yeast. Cells expressing GFP-LacC2 as a membrane marker were stained with ConcanavalinA-Alexafluor647 to label the external surface of the cell wall (unpublished results from Zsuzsanna Gere).

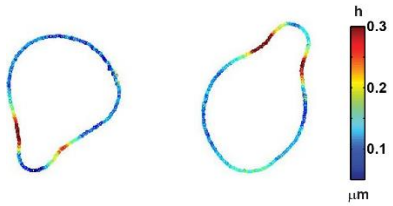

Figure D.2. Typical wall thickness maps of mating protrusions in budding yeast. Cells expressing GFP-LacC2 as a membrane marker, were incubated with α-pheromone for 2.5h, then stained with ConcanavalinA-Alexafluor647 to label the external surface of the cell wall (unpublished results from Zsuzsanna Gere).

binding lectin, as a good candidate for wall external surface labeling (Horisberger and Vonlanthen, 1977) , and GFP-LacC2, a phosphatidylserine probe, as plasma membrane tag. Through this work, we could measure local values of thickness comparable to previous transmission electron microscopy studies. We have also noticed a trend in thickness between mothers and daugthers, where mother cells have generally a thicker cell wall, which may be a consequence of wall maturation or aging, since the cell wall of the bud is synthetized *de novo* (Figure D.1). Moreover, by observing wall thickness in mating protrusions, we could observe a general trend, in which the wall at the protrusion side is visibly thicker than at the apex, consistent with our observation in fission yeast, where polarized growth is almost always accompanied by polarization in wall mechanics (Figure D.2).

However, this approach can be much less straightforward if used as a strategy to study poorly described organisms, where the composition of the cell wall is not clear, proteins are not characterized and there is little access to genetic manipulations. To overcome this issue, it is possible to screen for diverse commercially available fluorescent chemicals, which bind the inner or the outer part of the cell wall, in the less species-specific manner possible. We started to develop this approach, aimed to the study of diverse filamentous fungi, such as *Botrytis cinerea, Sordaria macrospora, Coprinus cinereus, Trametes versicolor*. For the external label, we screened diverse fluorescently labeled lectins, such as Concanavalin A, soybean agglutinin, peanut agglutinin and wheat germ agglutinin, which bind specifically to diverse glucans. Among them wheat germ agglutinin (WGA), specific for N-acetylglucosamine (present in chitin), resulted in the most homogeneous signal along the wall boundary, in the species tested. To label the inner part of the wall we initially tested some chemicals, classically used to mark the plasma membrane (Dibac$_3$4, Dibac$_4$5, Filmtracer), but unfortunately we could not set up any successful protocol. In contrast,

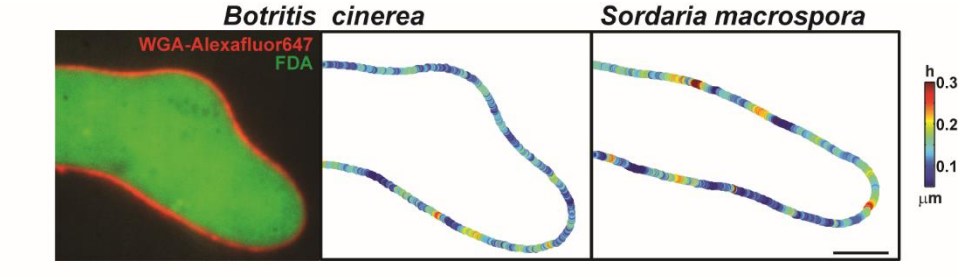

Figure D.3. Wall thickness maps in filamentous fungi. For image analysis cells were labeled with Fluorescein Diacetate (FDA) and wheat germ agglutinin (WGA) tagged with Alexafluor647 (unpublished results from Louis Chevalier).

we found that Fluorescein Diacetate (FDA), a cell permeant esterase substrate, labels the cytosol of the tested fungi in a highly reproducible way. The signal from this marker can be used to define the border of the cytosol, theoretically equivalent to the plasma membrane. To this aim, we modified the image analysis pipe line, in order to fit this signal with an error function instead of a Gaussian fit. The mean of the error function corresponds to the limit of the cytosol, therefore to the inner part of the cell wall surface. Some very preliminary results show that this approach might be used to map cell wall thickness in filamentous fungi. We are currently validating the method, by using similar labeling in fission yeasts and by correlative light electron microscopy (Figure D.3). The development of this method, which can be further extended to other walled cells, like pollen tubes and root hairs, can be used to provide large informations on wall properties in a broad range of walled organisms.

In conclusion, in this work, I developed the very first approaches to assess wall mechanical parameters in large populations of live fission yeast cells, at the single cell scale, with subcellular resolutions. These methods highlight how cell walls behave dynamically. Thanks to the resolution obtained, I revealed complex interplays between wall mechanics, growth and cell shape at the single cell level, as well as mechano-sensing mechanisms that control cell surface preserving cell integrity. These results show that surface mechanics regulation is essential for cells to develop and grow in the proper manner, and that systematic observation of these parameters is key to the complete understanding of these processes.

I believe that my PhD work lays the foundations for the understanding of general mechanical rules that regulate intricate processes such as growth or shape establishment in walled cells, and can be further expanded for the investigation of other biologically relevant events, such as tropism, host invasion, mycelial development or plant fertilization.

METHODS

In this chapter I include detailed instruction to perform the image analysis described in my results, by using the script packages available as described below.

The first script package described (WALLTRACKER), relative to my first set of results, is sufficient for cell wall thickness measurements and it is already available on the website of our laboratory (http://www.minclab.fr/research/).

The second package, WALLTRACKER 2.0 has been used for thickness measurements and bulk modulus estimations, and it implements a correction for eventual differences in background. This pipeline is available at the following link: https://drive.google.com/open?id=128Pnyi9bQd8C-MV38O_gDUw-9qJ37NP8

The third package described can be used to extract local shift maps, used for chromatic registration in both aforementioned packages. This package has been uploaded in the lab website as a subfolder of WALLTRACKER.

WALLTRACKER

Matlab script package to measure cell wall thickness in live cells

Developed by Hirokazu Tanimoto, Dmitry Ershov, Valeria Davì and Nicolas Minc (ver.1, 2018/04)

For questions: Contact: tanimotohr@gmail.com and/or Valeria.DAVI@ijm.fr

Note

This document introduces a Matlab script package for the measurement of cell wall thickness in cells imaged by confocal microscopy, originally developed for Davi et al., Dev Cell (2018). Refer to the article for complementary information. Please cite the original article when you publish results using these scripts.

Requirement

- Matlab software including CurveFitting and ImageProcessing toolboxes. The scripts can run on Matlab R2013b. Higher versions may not work.
- Confocal fluorescent images of internal and external sides of the cell wall.

For measurements in fission yeast we used a transmembrane protein GFP tagged for the inside, and a lectin (from *Griffonia simplicifolia)* marked with Alexafluor-647 for the outside.
Though not essential, we recommend to use simple name and numbering for images. Each sample to analyze need two images with the same name-root in the two channels, as:
cell_1_FarRed.tif
cell_1_Green.tif
As support, we provide a folder with examples of fission yeast cells, labeled as previously mentioned.

- A shift-map corresponding to the same microscopic setting used to images the samples (To make a shift-map download the package “shift-map” in the lab website and follow the user guide).

Analysis flow

1. Extract the script package
2. Prepare folders and place images.
3. Edit “CWTdetection_manuPartSep” script to define analysis folder and some parameters.
4. Execute it. Some of the step are manually controlled by the user.
5. Edit “CWTqualityCheck” script to define analysis folder and some parameters.
6. Execute it.
7. Edit “CWTanalysis” script to define analysis folder and some parameters.
8. Execute it. Some of the step are manually controlled by the user.

(1) Extract script package

Extract script package zip file somewhere in your PC. You will have a single folder named Cell-Wall-Thickness-Analysis-Software, and all scripts in the main folder, test images in the subfolder "data" and a test analysis in the subfolder "test".

(2) Prepare folders and place row images

Create a parent folder for analysis (called "path" in the script), and a folder named "data" under the analysis folder.
For example: Create `'C:\Users\Valeria\Documents\MATLAB\20180322_folder submission dev cell\'`.
Put row images into the "`data`" folder.
For each sample we need two images, one for each channel. The name of the image should follow this schematic: dataname_index_channel.tif
Index must be a number.
For example:
cell _1_FarRed.tif
cell_1_Green.tif

(3) Edit "CWTdetection_manuPartSep" script

Open the script
L6-8 Define path, analysis name and data folder

Ex.

```
path = 'C:\Users\Valeria\Documents\MATLAB\20180322_folder submission dev cell\';
analysisName = 'test';
folder_data = ('C:\Users\Valeria\Documents\MATLAB\20180322_folder submission dev cell\data\'
```

L11 Define pixel size in μm
L12 Decide one image between the two channels, to use for thresholding. Chose the one that normally has a better signal. 1 is inside, 2 is outside (more details is paragraph 3.3).
L13 CellN2 is the index of images that you want to analyze (cell_n_FarRed.tif). between brackets the number of images that you want to analyze.

```
Ex. cellN2=[1 2];
```

L14 If some of your cells are close to other cells in the images you can chose to manually crop them using non-rectangular cropping windows (as cell_1 in the example data). Put the number in brackets as before
L16 Maximum distance between two neighboring points accepted (in pixel). (see the rationale in paragraph 3.5)
L18-19 Minimum and maximum thickness accepted. Points out of this limit will be discarded and replaced with an average of the neighboring points.
L22 Define the folder and name of the shift-map that you want to use. (To make a shift-map download the package "shift-map" in the lab website).

Ex. `'C:\Users\Valeria\Documents\MATLAB\20180322_folder submission dev cell\map_shift.mat'`

L34 Set dataname.for, as the first part of your image name (cell_n_FarRed.tif)

L35-36 Set dataname.back, are the channel part of your image name. 1 is for the inside and 2 is for the outside. (cell_n_Green.tif or cell_n_FarRed.tif).

(3) Execute "CWTdetection_manuPartSep" script

The following steps will include:

1- Crop (Manual)
2- Manual Crop (Manual, Optional)
3- Thresholding (Semi Automated)
4- Initial Boundary Detection (Automated)
5- Remove extreme points 1st (Automated)
6- Manual Check (Manual)
7- Shift Correction (Automated)
8- Wall thickness measurement (Automated)
9- Remove extreme points 2nd (Automated)

1- Crop

Each sample defined in cellN2 **(L13**) will pop up and you can crop the desired cell, to remove signal coming from background or neighbors.

Draw a square (from top left to bottom right). Once drown, adjust the shape if necessary and double click to save and move to the next image.

2- Manual Crop

Images defined in L14 will pop up, you can re-crop them using a non-rectangular window as below.

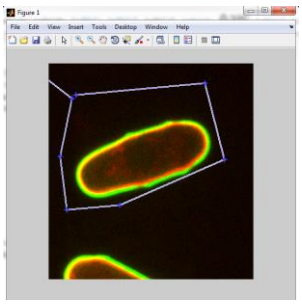

3- Thresholding

Based on minimum and maximum intensity the software automatically sets a threshold, to define the boundary of the cell in each color.
An image as the one below will pop up, showing the automatic result. A good binarization will show all the inside in white and the outside in black (as below left). If this is not the case (as on the right) you can modify the thresholding values from 1 (default) to other values.

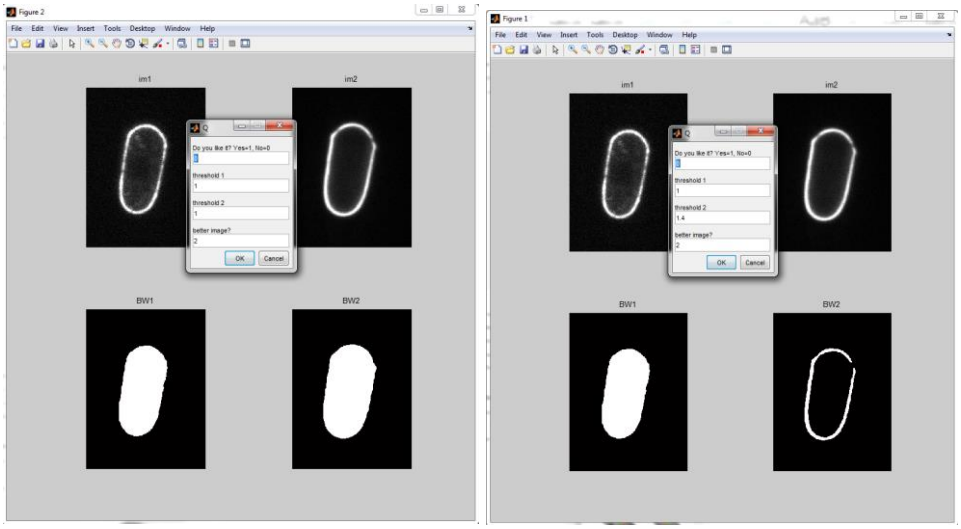

This boundary will be used as a first contour for the following analyses. Only one of the two boundary will be selected for this purpose (default decided in **L12**, can be modified in the last line of the inset for each image – better image?).
If you are satisfied with at least one of the two images, make sure that this is the same in the box “better image”, then select 1 in the first line of the inset to proceed with the next image.

4- Initial Boundary Detection

The software automatically draws lines perpendicular to the surface of the boundary selected in the previous step 3 (thresholding). In the image below the lines and the two boundaries before Gaussian fit.

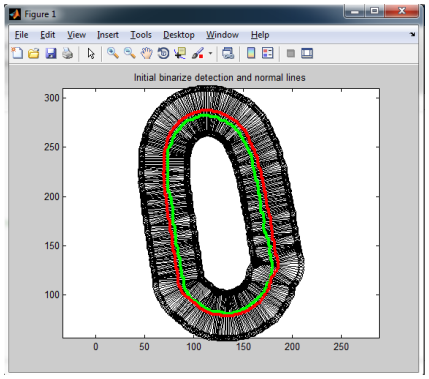

Then, on each line a Gaussian fit for each color is done, giving the corrected boundary (not shown at this step).

5- Remove extreme points 1st

In this automated step the software remove for each contour extremes points as defined in **L16**. Each point is compared to its neighbors, if its distance is above the threshold set in L16 and there are not neighboring points with similar shape this point is considered as a “Spike”, probably due to noise. The point is removed and substituted with an average of the neighbors.

6- Manual Check

A window as below will pop up. The top plot shows the contour in green of the cell below. In x the contour in pixels, in y the distance between one point and its neighbors.
You can scroll with the top bar to move to different position of the contour, as shown by the white line in the image below.

Press “Show fitting” to see the Gaussian fit in the two colors. You can change the values of fitting parameters, in the insets top right, on color at a time (the one shown in the plot). Press “Refit” to see the new fit, and accept or delete points if necessary.
Deleted points will be substituted with an average of the neighbors.

Once this check is finished, press “Done”, and Enter on the Matlab window. This will take you to the same window for the second color.

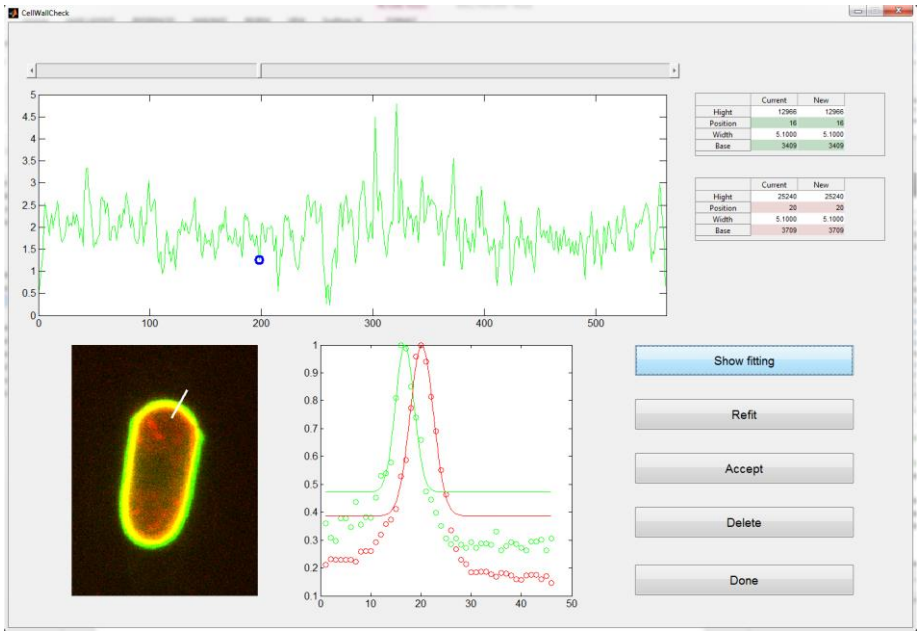

The two contours fitted automatically and manually corrected are then shown as below

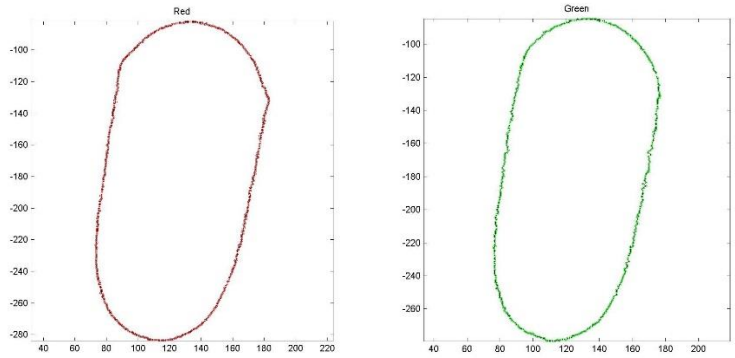

7- Shift Correction

The software move one of the contour, pixel by pixel, according to shift-map and shows an image with the vectors used for the shift (not very visible in this case, sometimes they are more).

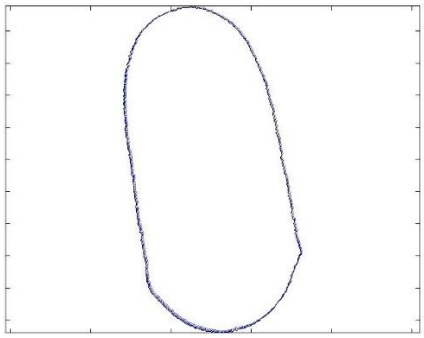

8- Wall thickness measurement

The software draws new perpendicular lines on the shifted contours.

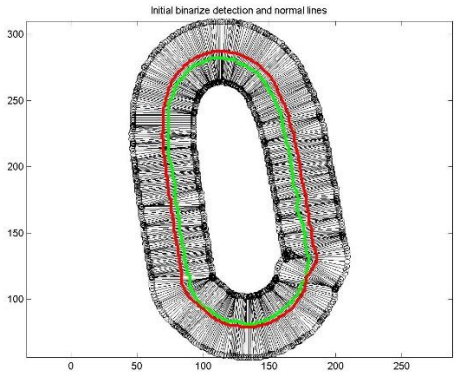

For each line the distance between the two contours is measured as cell wall thickness (below in the center x is cell contour (in pixels) and y is Thickness (in nm), on the right the hit-map in nm

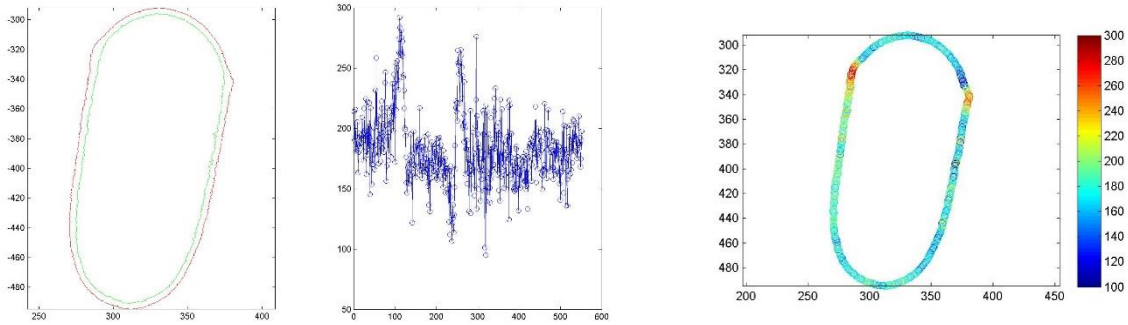

9- Remove extreme points 2nd

Eventual values above or below the limits set in L18-19 are removed and substituted with an average of the neighboring points

At this step thickness is measured and all the image of the analysis are saved in Path/analysisname/cell_n

(4) Edit "CWTqualityCheck"

Through this script we can discriminate cells where the background is too high or unbalanced, making the analysis imprecise.

Open the script
L14-16 update as in "CWTdetection_manuPartSep".
L18 Define the limit of acceptance in nm

(5) Execute "CWTqualityCheck"

For every line of the contour in each sample the software measures the inside and outside noise and shows the signal to noise ratio (left) and the (inside-outside)/outside noise (center). According to simulations (as described in Davi et al. Dev Cell 2018), the image on the panel on the right shows blue points where the error is below the limit set in L18, and in red those that are above.
Red regions shall be avoided during the manual thickness measurement in session **(7).**

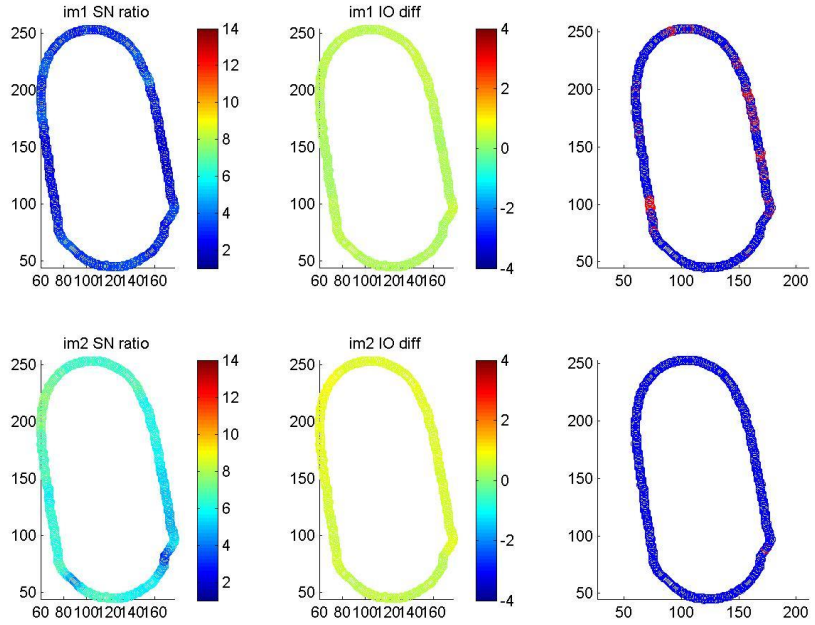

This image is saved in Path/analysisname/all

Finally, as below, two scatter plots, one for each color are shown.
They represent averages every 10 points of measured (inside-outside)/outside noise in y and signal/noise in x. Color map represent the averaged error for each group of points.
Below on the left scatter for image 1 (inside) and on the right image 2 (outside).

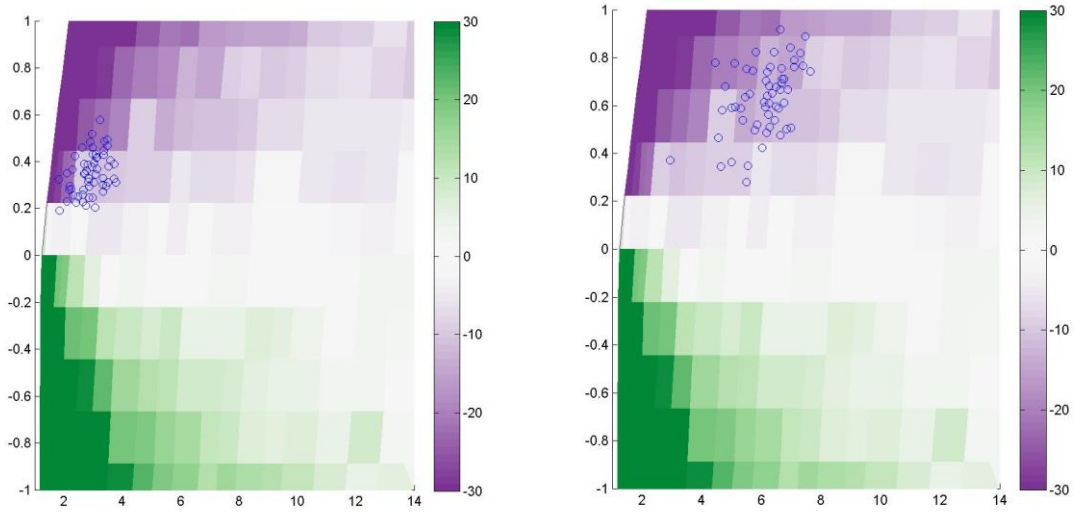

These images are saved in Path/analysisname/cell_n

(6) Edit "CWTanalysis" script

With this script we can manually measure wall thickness in regions of interest and geometrical parameter of the cell.

Open the script
L5-6 update as in "CWTdetection_manuPartSep **L6-7**".
L9 According to quality check and specific interest, decide which images you want to analyze. The index corresponds to the same used in "CWTdetection_manuPartSep".
L56-57 Define the minimum and maximum of the colorplot for the final cell wall thickness image saved.

(7) Execute "CWTanalysis" script

The following window will appear.

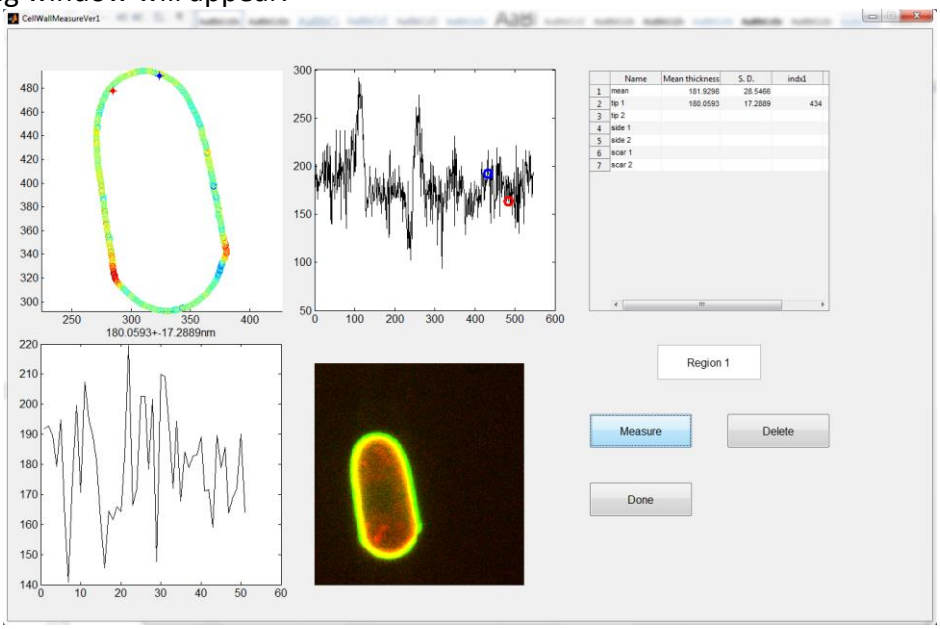

Top left is the color thickness map, at its tight thickness (y) as a function of the cell boundary (x). You can click your region of interest, first the blue dot will appear, second the red. Define the region in counterclockwise direction. Dots of the same colors will appear in the right plot, indicating the region chosen. Below on the left a zoom in on the region chosen and the original image of the sample, useful to avoid regions with anomalies.
Once defined the region of interest clock on "measure", then define another region and so on, until you are satisfied. Click on done to continue with the next image.
Regions names are set as default, the first measurement (mean) also appear as default and is the average around the whole contour.
You can, of course, measure other regions and also more than 6, but the string will not vary.
Remember to look in parallel the quality check image, to avoid imprecise regions.

Once you have done with all your measurements the software will save an excel file containing all the measurements in Path/analysisname/all.

Next, by using the outside contour the software measures length and diameter of the cell

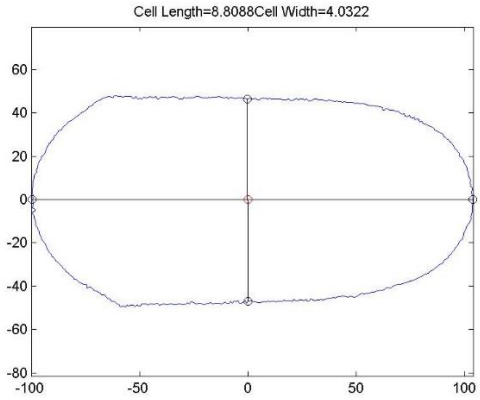

and finally shows the final thickness map, colormap is in nm.

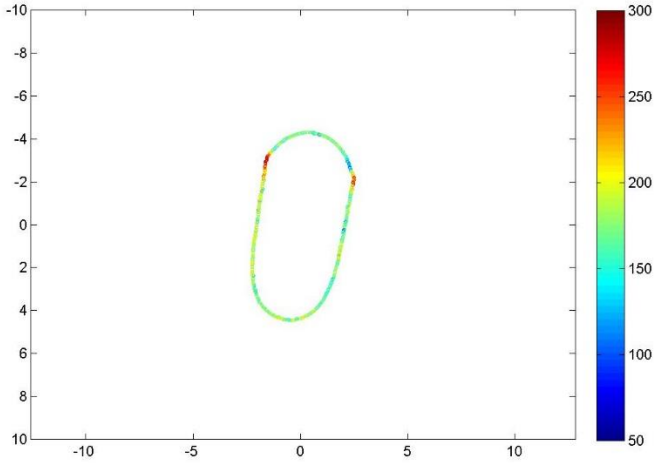

These two last images are saved in Path/analysisname/all.

The analysis is finished.

WALLTRACKER 2.0

Matlab script package to measure local cell wall thickness, geometrical parameters and estimate local bulk modulus in live cells

Developed by Hirokazu Tanimoto, Valeria Davì and Nicolas Minc (ver.2, 2018/06)

For questions: Contact: tanimotohr@gmail.com and/or Valeria.DAVI@ijm.fr

Note

This document introduces an update of the Matlab script package for the measurement of cell wall thickness in cells imaged by confocal microscopy, originally developed for Davì et al., Dev Cell (2018), further improved in Davì et al., in preparation (2018). Refer to those articles for complementary information. Please cite the original articles when you publish results using these scripts.

New in this update:
- Correction script to extract the true signal peak by using an analytical expression of the convoluted intensity profile, used to solve asymmetries in intracellular/extracellular background
- The quality check is removed, since the script above corrects for the same issue, with no need of data rejection
- Semi-automatic extraction of cell shape parameters and relative local thickness values
- Shape parameters comparison of two cells, originally developed to compare the same cell before and after laser ablation, for extraction of local mechanical parameters
- Manual correction of cell binarization, originally developed to correct for local signal bleaching after laser ablation

Requirement

- Matlab software including CurveFitting and ImageProcessing toolboxes. The scripts can run on Matlab R2013b. Higher versions may not work.
- Confocal fluorescent images of internal and external sides of the cell wall, of condition 1
- Confocal fluorescent images of internal and external sides of the cell wall, of condition 2 (in case of comparison assays).

For measurements in fission yeast we used a transmembrane protein GFP tagged for the inside, and a lectin (from *Griffonia simplicifolia)* marked with Alexafluor-647 for the outside.
Though not essential, we recommend to use simple name and numbering for images. Each sample to analyze need two images with the same name-root in the two channels, as:
cell_1_FarRed.tif
cell_1_Green.tif
As support, we provide a folder with examples of fission yeast cells, labeled as previously mentioned.

- A shift-map corresponding to the same microscopic setting used to images the samples (To make a shift-map download the package “shift-map” in the lab website and follow the user guide).

Analysis flow

9. Extract the script package
10. Prepare folders and place images.
11. Edit “F0_WallDetection” script to define analysis folder and some parameters.
12. Execute it. Some of the step are manually controlled by the user.
13. Edit “F1_CellShapeParams” script to define analysis folder and some parameters.
14. Execute it. Manually define regions of interest.
15. Edit “F2_GhostAnalysis” script to define analysis folder and some parameters.
16. Execute it.
17. (Optional) Edit “F3_WallThickness” script to define analysis folder and some parameters.
18. (Optional) Execute it. Manual wall thickness measurements

(1) Extract script package

Extract script package zip file somewhere in your PC. You will have a single folder named Cell-Wall-Thickness-Analysis-Software 2.0, and all scripts in the main folder, test images in the subfolder “data” and a test analysis in the subfolder “test”.

(2) Prepare folders and place row images

Create a parent folder for analysis (called “path” in the script), and a folder named “data” under the analysis folder.
For example: Create `C:\Users\Valeria\Documents\MATLAB\20180523_wall tracker 2.0\'`.
Put row images into the “`data`” folder.
For each sample you two images are required, one for each channel. The name of the image should follow this schematic: dataname_index_channel.tif
Index must be a number.
For example:
test_1_fr.tif
test_1_green.tif

In case of comparison assays, both images have to be analyzed in the same analysis, and should be named following the same schematic.

(3) Edit “F0_WallDetection” script

Open the script
L6-8 Define path, analysis name and data folder

Ex.

```
path = 'C:\Users\Valeria\Documents\MATLAB\20180523_wall tracker 2.0\';
analysisName = 'test';
folder_data = ('C:\Users\Valeria\Documents\MATLAB\20180523_wall tracker
2.0\data\');
```

L11 Define pixel size in μm
L12 Decide one image between the two channels, to use for thresholding. Chose the one that normally has a better signal. 1 is inside, 2 is outside (more details is paragraph 3.3).
L13 CellN2 is the index of images that you want to analyze (cell_n_FarRed.tif). between brackets the number of images that you want to analyze.

```
Ex. cellN2=[1 2];
```

L14 If some of your cells are close to other cells in the images you can chose to manually crop them using non-rectangular cropping windows. Put the number in brackets as before
L15 If some of your cells have signal interruption (e. g. caused by laser ablation) you can manually close their boundary to facilitate binarization (as cell_2 in the example data). Put the number in brackets as before. NB. regions manually updated cannot be used for thickness measurements!
L16 Maximum distance between two neighboring points accepted (in pixel). (see the rationale in paragraph 3.6)

L18-19 Minimum and maximum thickness accepted. Points out of this limit will be discarded and replaced with an average of the neighboring points.
L21 Decide whether to perform the manual contour check or not (1 yes, 0 not)

L24 Define the folder and name of the shift-map that you want to use. (To make a shift-map download the package "shift-map" in the lab website).

Ex. `'C:\Users\Valeria\Documents\MATLAB\20180523_wall tracker 2.0\map_shift.mat'`

L34 Set dataname.for, as the first part of your image name (cell_n_fr.tif)
L35-36 Set dataname.back, are the channel part of your image name. 1 is for the inside and 2 is for the outside. (cell_n_green.tif or cell_n_fr.tif).

(3) Execute "CWTdetection_manuPartSep" script

The following steps will include:

1. Crop (Manual)
2. Manual Crop (Manual, Optional)
3. Manual Close (Manual, Optional)
4. Thresholding (Semi Automated)
5. Initial Boundary Detection (Automated)
6. Remove extreme points 1st (Automated)
7. Manual Check (Manual, Optional)

8 Shift Correction (Automated)
9 Wall thickness measurement (Automated)
10 Remove extreme points 2nd (Automated)
11 Inside/Outside asymmetry correction (Automated)

1. Crop

Each sample defined in cellN2 **(L13**) will pop up and you can crop the desired cell, to remove signal coming from background or neighbors.
Draw a square (from top left to bottom right). Once drown, adjust the shape if necessary and double click to save and move to the next image.

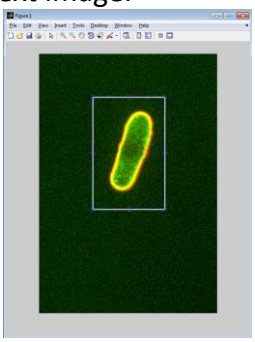

2. Manual Crop

Images defined in **L14** will pop up, you can re-crop them using a non-rectangular window as below.

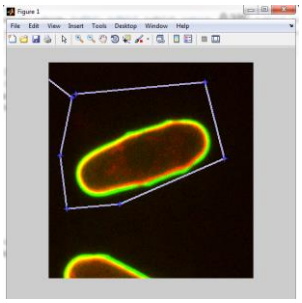

3. Manual Close

The image relative to the external surface of the wall, as defined in **L15,** will pop up, you can close the contour of partially bleached or inhomogeneous cells.

NB. Manual closure is not precise for thickness measurements. DO NOT consider thickness measurements in these regions. Manual closing tips regions affect radius of curvature determination as well. We accept this approximation only for cell diameter measurements, when we close lateral regions with simple straight lines. Only one region can be closed.

4. Thresholding

Based on minimum and maximum intensity the software automatically sets a threshold, to define the boundary of the cell in each color.
An image as the one below will pop up, showing the automatic result. A good binarization will show all the inside in white and the outside in black, with a smooth border (as below right – both images). If this is not the case (as on the left – left image) you can modify the thresholding values from 1 (default) to other values.

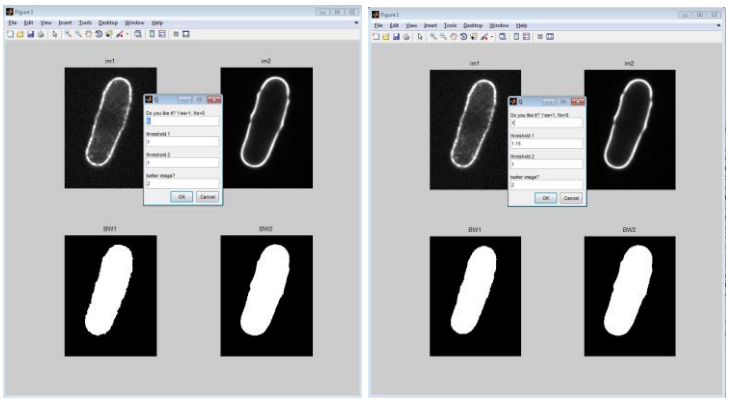

This boundary will be used as a first contour for the following analyses. Only one of the two boundary will be selected for this purpose (default decided in **L12**, can be modified in the last line of the inset for each image – better image?).
If you are satisfied with at least one of the two images, make sure that this is the same in the box “better image”, then select 1 in the first line of the inset to proceed with the next image.

5. Initial Boundary Detection

The software automatically draws lines perpendicular to the surface of the boundary selected in the previous step 3 (thresholding). In the image below the lines and the two boundaries before Gaussian fit.

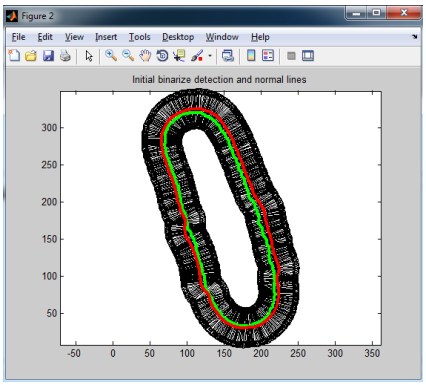

Then, on each line a Gaussian fit for each color is done, giving the corrected boundary (not shown at this step).

6. Remove extreme points 1st

In this automated step the software remove for each contour extremes points as defined in **L16**. Each point is compared to its neighbors, if its distance is above the threshold set in L16 and there are not neighboring points with similar shape this point is considered as a “Spike”, probably due to noise. The point is removed and substituted with an average of the neighbors.

7. Manual Check

If in line 21 you decided to perform the manual check (value 1), a window as below will pop up. This manual adjustment is done to check and eventually correct Gaussian fits where the automatic analysis has been imprecise. The top plot shows the contour in green of the cell below. In x the contour in pixels, in y the distance between one point and its neighbors.
You can scroll with the top bar to move to different position of the contour, as shown by the white line in the image below.

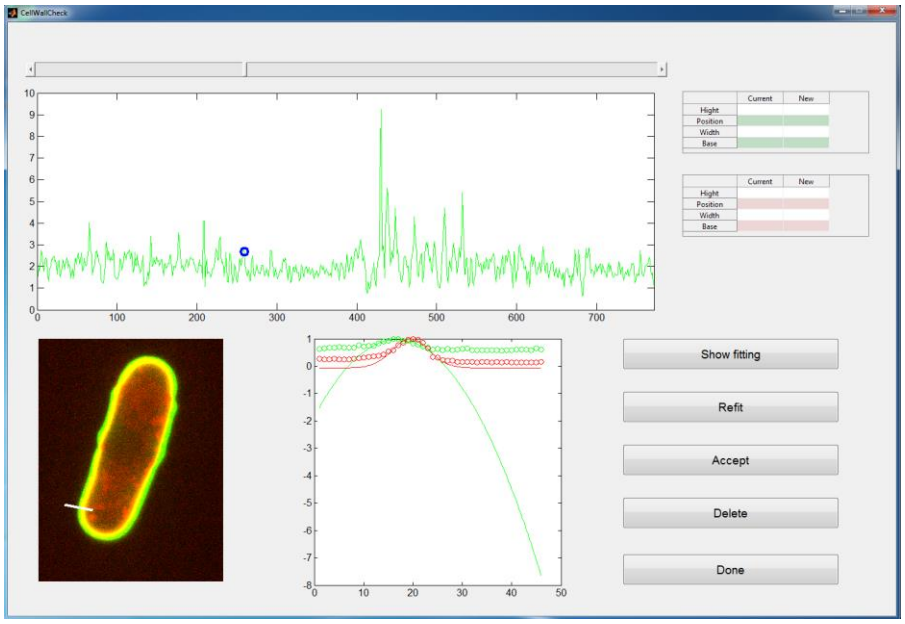

Press “Show fitting” to see the Gaussian fit in the two colors. You can change the values of fitting parameters, in the insets top right, on color at a time (the one shown in the plot). Press “Refit” to see the new fit, and accept or delete points if necessary.
Deleted points will be substituted with an average of the neighbors.

Once this check is finished, press “Done”, and Enter on the Matlab window. This will take you to the same window for the second color.

The two contours fitted automatically and manually corrected are then shown as below

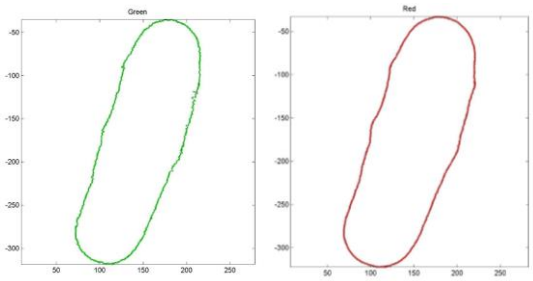

8. Shift Correction

The software move one of the contour, pixel by pixel, according to shift-map and shows an image with the vectors used for the shift (not very visible in this case, sometimes they are more).

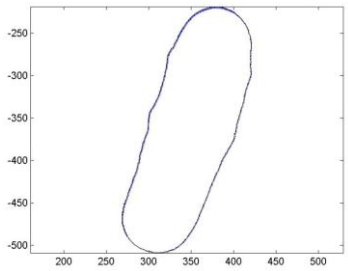

9. Wall thickness measurement

The software draws new perpendicular lines on the shifted contours.

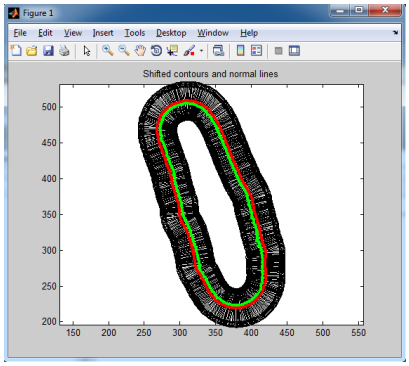

For each line the distance between the two contours is measured as cell wall thickness (below in the center x is cell contour (in pixels) and y is Thickness (in nm), on the right the hit-map in nm

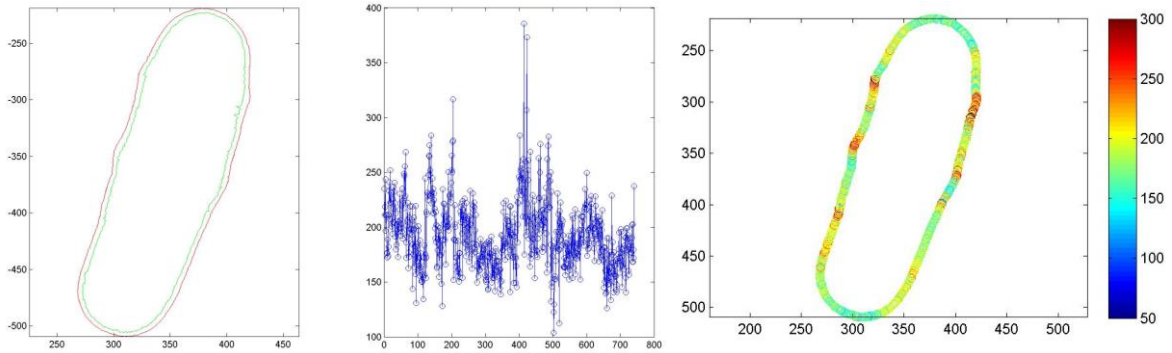

At this step thickness is measured

10. Remove extreme points 2nd

Eventual values above or below the limits set in **L18-19** are removed and substituted with an average of the neighboring points

11. Inside/Outside asymmetry correction

In this step, the software measures internal, external background and peak intensity along each line defined in **3.9**, both for membrane and wall signal. For each line it calculates the local shift, that it apply to correct to asymmetries in the background.

The following images pop up, first one by one and then in a subplot

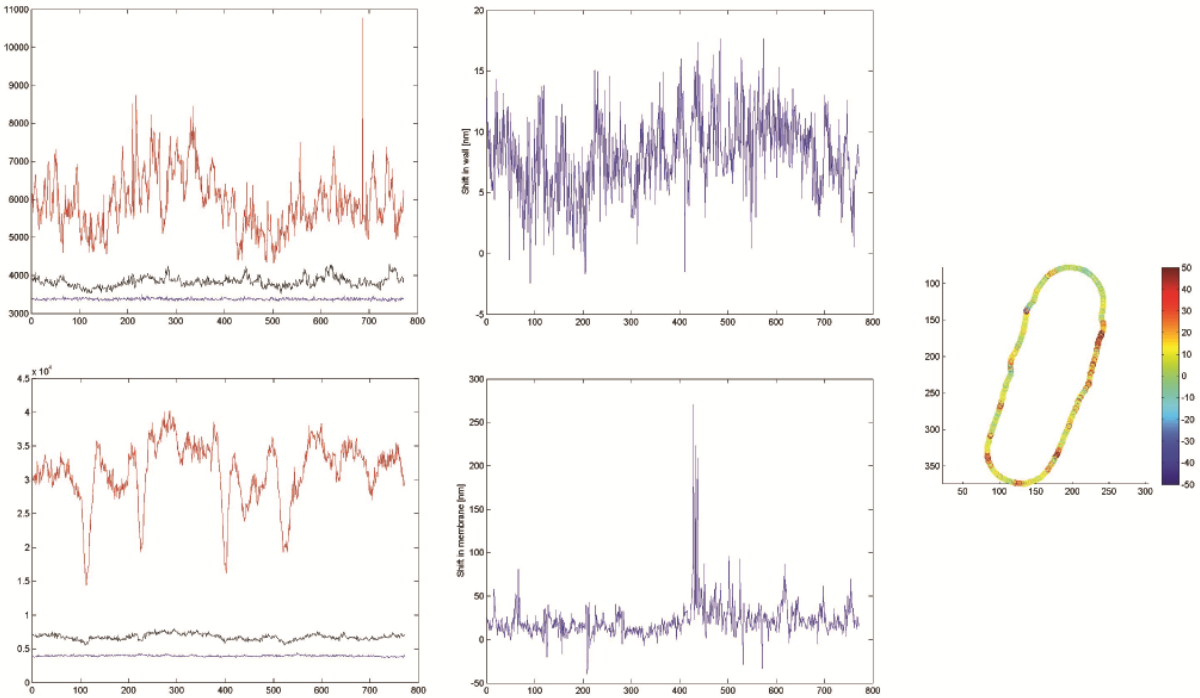

From the left to right: Inside (black), outside (blue) and peak (red) intensity for the membrane signal (top), or wall signal (bottom) along the whole contour. Contour is in pixel, intensity is in arbitrary units. Shift contribution for membrane (top), or wall (bottom), signal background

asymmetries, along the whole contour. Updated cell wall thickness, after inside/otside correction. Inside (black), outside (blue) and peak (red) intensity for the wall signal, along the whole contour. Contour is in pixel, intensity is in arbitrary units. On the right measurement of the local total shift (from membrane plus wal), to apply at wall thickness measurements.

After this step the measured shift is applied locally, the new map is displayed, and the wall values are updated.

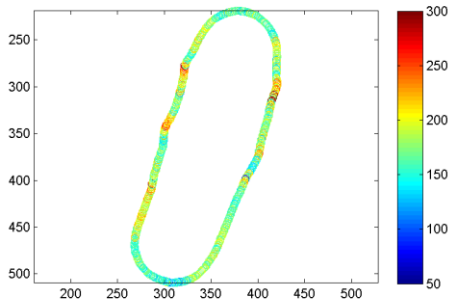

All the images of the analysis are saved in 'Path/analysisname/cell_n'. Final wall map is also saved in Path/analysisname/all as 'finalWallThickness_Cell1_n.tif'

(4) Edit "F1_CellShapeParams"

Through this script we can define local regions for each cell. This script is adapted to cell shape and features of *Schizosaccharomyces pombe* cells.
Open the script
L5-7 update as in "F0_WallDetection **L6-7**".
L9 Decide which images you want to analyze. The index corresponds to the same used in "F0_WallDetection".
L40 set how many points to use around each side of the tip center, to measure tip curvature.

(5) Execute "F1_CellShapeParams"

The software automatically define the long axis of the cell and orient it horizontally.
The image of cell boundary pop up. For correct analysis the new end must be oriented on the left, to achieve this, the user choses whether to flip or not the shape.

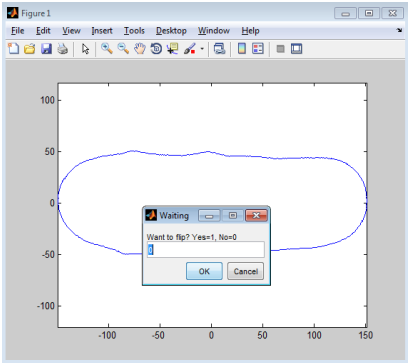

The user sets the number of scars and side sections that he wants to analyze. In the example below two scars and one side.

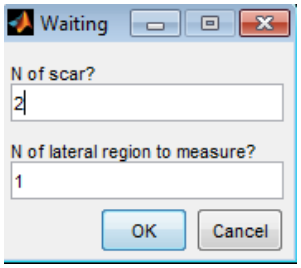

He marks the center of each scar (both sides)

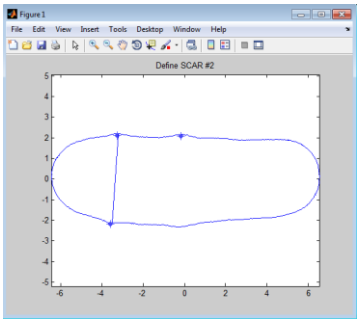

And then set the side region that he wants to analyze by clicking on the extremes left and right of this region

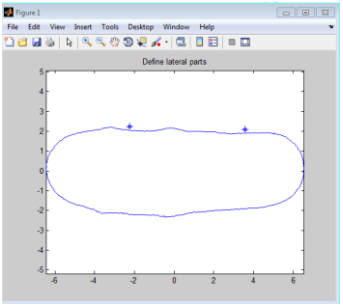

The software will use the regions defined by user to measure shape parameters:

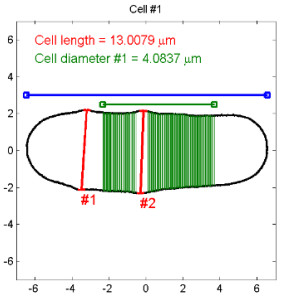

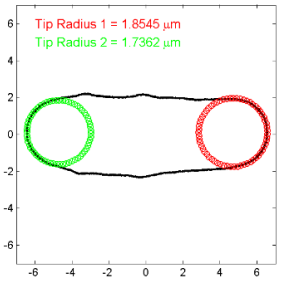

In multi-scarred cells the scar is excluded from side analysis.

In case of multiple side analysis, mark the two extremities of each region.

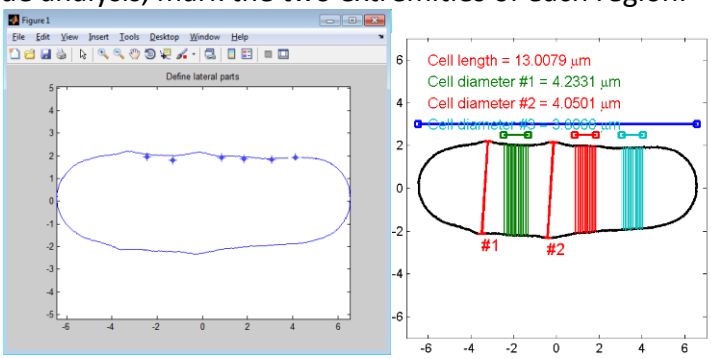

The image of cell shape parameters is saved in Path/analysisname/all.

(6) Edit "F2_GhostAnalysis" script

This script extract local values of wall thickness in the regions defined in "F1_CellShapeParams", and it can compare shape parameters of two conditions (before and after laser ablation in this case). From these data, it estimates local bulk modulus divided by turgor pressure (Y/ΔP) as:

$$\frac{Y_{side}}{\Delta P} = \frac{R_1}{R_1{}^{*} h_{side}}$$

where $R_1{}^* = \frac{R_1 - R_0}{R_0}$; for scars:

$$\frac{Y_{scar}}{\Delta P} = \frac{R_1}{R_1{}^* h_{scar}}$$

where $R_{scar}{}^* = \frac{R_{\text{scar}1} - Rscar_0}{R_{\text{scar}0}}$; while for the tips:

$$\frac{Y_{tip}}{\Delta P} = \frac{Rc}{2Rc^* h_{tip}}$$

where $Rc^* = \frac{Rc - Rc_0}{Rc_0}$.

Condition one is (1), condition 2 is (0). *h* is wall thickness measured in condition (1).

Open the script
L5-7 update as in "F0_WallDetection **L6-7**".
L9 Decide which images you want to analyze and compare. The index corresponds to the same used in "F0_WallDetection". Each couple of image in the same line as:

```
[1     2
 3     4
 5     6];
```

The first column is condition (1), the second is condition (0).

(7) Execute "F2_GhostAnalysis" script

The software displays updated wall thickness, the shape of the cell before and after ablation (in this example), some shape parameters measurements and their comparisons:

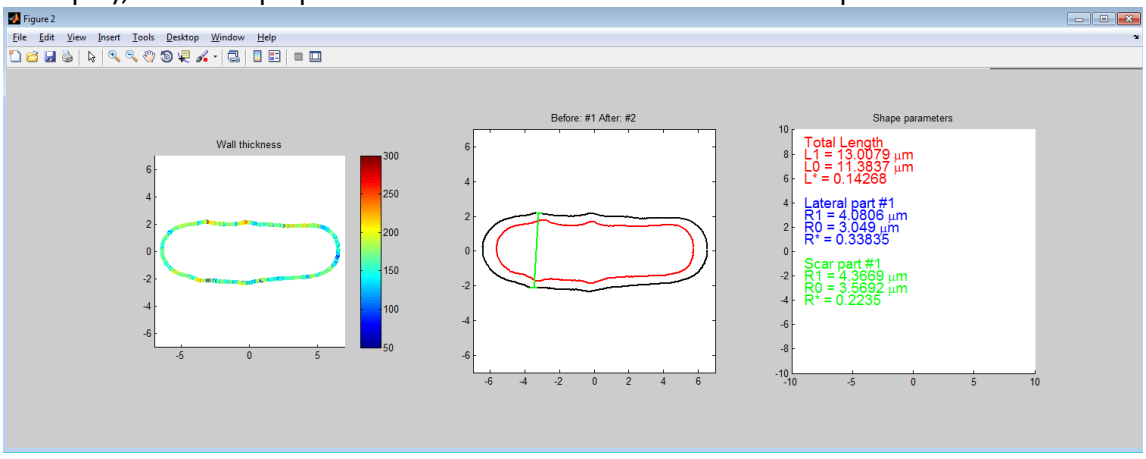

Thickness and wall parameters for each cell are saved in an excel file named "GhostAnalysis_Cell1=n1_Cell2=n2.xlsx", where n1 and n2 are the images before and after ablation respectively. In this document you can find all the values for each part, also multiple sides if analyzed.

	X1	X0	dX	X*	CWT 1	CWT 2	CWT Mean	Y/P
Total Length	13.00788	11.38367	1.624211	0.142679	170.1513	162.7855	166.468397	
Side1	2.0403	1.524487	0.515813	0.338352	175.3175	159.9557	167.636606	35.97133
Scar1	2.183447	1.784591	0.398856	0.2235	218.564	200.1856	209.374773	46.6596
Tip #1	1.854496	1.516845	0.337651	0.222601	146.4159	146.4159	146.415942	28.44987
Tip #2	1.73624	1.397753	0.338486	0.242165	159.8117	159.8117	159.811726	22.4316

Tip1 is the old end, Tip2 is the new end
X is the local measurement, 1 – before ablation, 0 – after ablation
dX is the is X1-X0. X* is calculated as above.
CWT1 and CWT2 are thickness measurements on the top and bottom part of the cell (in the horizontal orientation), relative only total length, scar and side. CWT mean is the average of these two. For tips the three values are equal.

Data from all the cells measured are summarized in another excel file named as the analysis: "test.xlsx" in the example. Each raw corresponds to one comparison
Here, for simplicity, only the first side measurement is reported.

NB. If in your analysis you don't need shape comparison (and you don't want to estimate Y/P) you can compare each cell with itself and automatically extract thickness and shape values. dX and X* will be 0.

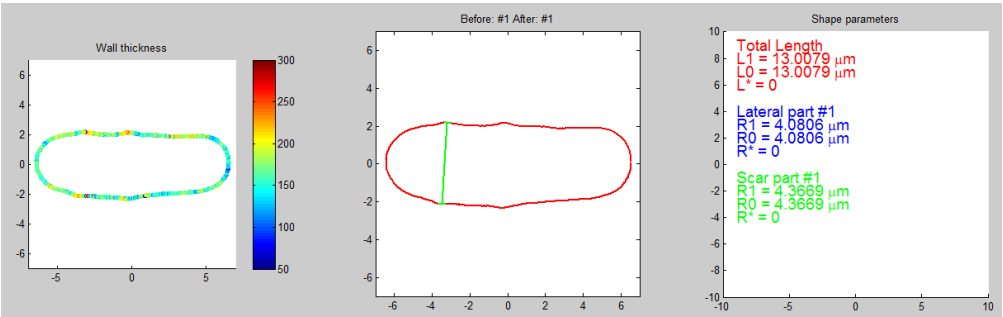

The analysis is finished here, unless you are not satisfied with the automatic measurements. In this case continue with (6) and (7).

(6) OPTIONAL Edit "F3_WallThickness" script

In case you are not satisfied with the automatic wall thickness measurements, with this script you can manually measure wall thickness in regions of interest.

You can skip F2 if you find F3 more suitable for your analysis, but remember that F3 does not, measure geometrical parameters.

Open the script
L5-6 update as in "F0_WallDetection **L6-7**".
L9 Decide which images you want to analyze. The index corresponds to the same used in "F0_WallDetection".

(7) OPTIONAL Execute "F3_WallThickness" script

The following window will appear.

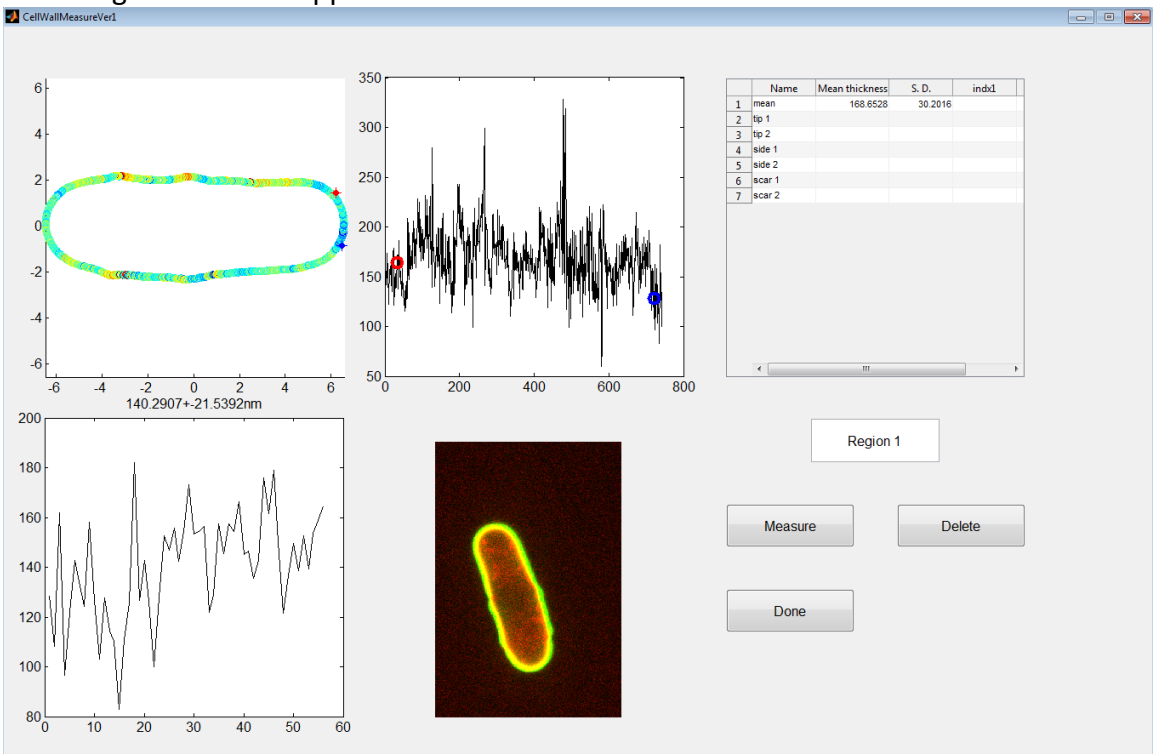

Top left is the color thickness map, at its tight thickness (y) as a function of the cell boundary (x).
You can click your region of interest, first the blue dot will appear, second the red. Define the region in counterclockwise direction. Dots of the same colors will appear in the right plot, indicating the region chosen. Below on the left a zoom in on the region chosen and the original image of the sample, useful to avoid regions with anomalies.
Once defined the region of interest clock on "measure", then define another region and so on, until you are satisfied. Click on done to continue with the next image.
Regions names are set as default, the first measurement (mean) also appear as default and is the average around the whole contour.
You can, of course, measure other regions and also more than 6, but the string will not vary.

Once all measurements are done the software will save an excel file containing all the measurements in Path/analysisname/all, named 'WallThickness.xlsx'.

Shift_Map

Matlab script package to create a map for the correction of shift in signal detection

Developed by Dmitry Ershov and Valeria Davi (ver.1, 2018/04).

For info and question contact: Dmitry Ershov : dimitracis@gmail.com

Note

This document introduces a Matlab scripts package for the generation of a shift map that can be used to correct for chromatic aberrations and shift in the detection of the signal, while performing co-localizations or distance measurements of two different fluorophores (or items fluorescently tagged).
It was originally developed for Davì et al., Dev Cell (2018), to correct the shift for thickness measurements.
Refer to the article for complementary information. Please cite the original article when you publish results using these scripts.

Requirement

- Matlab software including CurveFitting and ImageProcessing toolboxes. The scripts can run on Matlab R2013b and higher versions.
- Images of one microbeads with a broad emission spectrum in two channels, imaged in different part of the field of view, in an array.
  The condition of imaging must be the same as while imaging sample (wavelengths, filters, magnification).
  As support, we provide a folder with examples of a bead array imaged in green and far red.

Analysis flow

We detect the position of the bead in each channel and each portion of the array. Detection is done by using a modified Matlab script available from M. Kilfoil lab (http://people.umass.edu/kilfoil/); we utilize part of their Matlab code.
For each bead, we calculate the position shift vector from one channel to the other. After having calculated the shift vectors for all detected beads, we interpolate/extrapolate the resulting sparse shift map to the entire field of view (assuming linear change in both x and y directions) and get the continuous shift map.

To use the script:

19. Extract script package
20. Prepare folders and place images.
21. Edit “f1_get_spot_list” script to define analysis folder and some parameters.

22. Edit “sequence_to_val”.
23. Execute “sequence_to_val”.

(1) Extract script package

Extract script package zip file somewhere in your PC. You will have a single folder named Shift-Map, and all scripts in the main folder and test images in the subfolder “map_shift”.

(2) Prepare folder and place row images

Create a parent folder for analysis (called “path_in” in the script), and a subfolder of a chosen name, for example “map_shift” as in the example.
Ex. `C:\Users\Valeria\Documents\MATLAB\20180322_folder submission dev cell\shift_map\map_shift\'`.

Put bead array images into the “map_shift” folder.
Each position must be represented in the two channels. The name of the image should follow this schematic: channelstring_index.tif
channelstring can be alphanumeric, index must be a number.
For example:
642 _1.tif
491_1.tif

Note: The software does not accept empty positions in the array.

(3) Edit “f1_get_spot_list”

L17 decide whether to use a Gaussian or a circular fit. For small beads as those in the example use Gaussian. For big beads where you can distinguish the boundary use the circular.
L19 Define the number of columns in the array
L20 Define the number of rows in the array
L24 Define the string for the first channel ex. ‘642’
L25 Define the string for the second channel ex. ‘491’

Note: for cell wall thickness measurements, the first channel here corresponds to the wall signal outside, the second to the inside.

(4) Edit “sequence_to_val”.

L1 Define path_in with the name of the parent folder + subfolder generated in (2).
L2 Assign a name to the map. Ex. 'map_shift'
Note that this file will be saved in the running folder of Matlab, so displace it at the end if needed.

(5) Execute “sequence_to_val”.

The software makes a Gaussian fit for each position in each channel. It measures the discrete shift in each position in x and y, as below

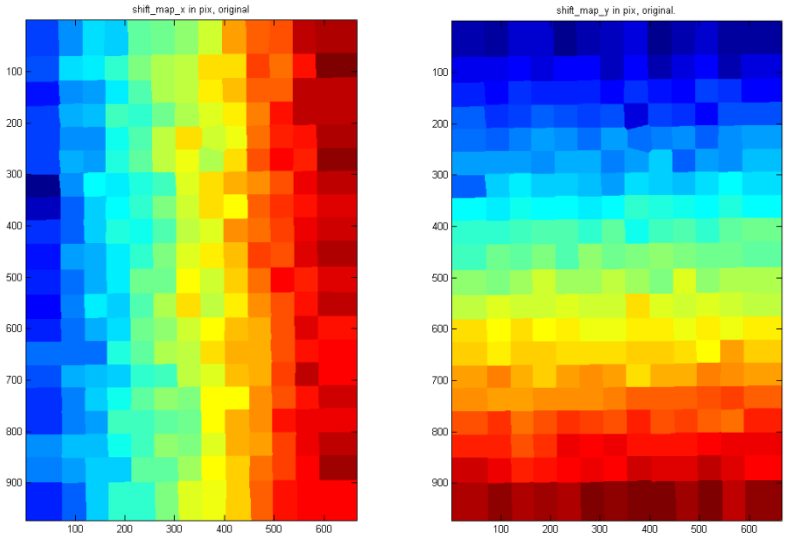

The discrete shift is then smoothed, this produces a continuous vector field containing shifts for all pixels in the field of view

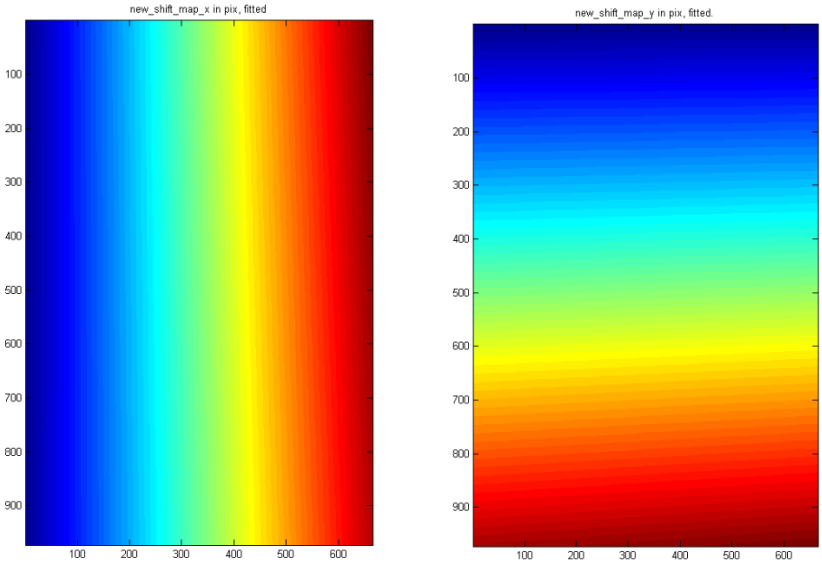

The analysis is finished: the xy shift_map is saved in path_in under the name previously assigned (**L2**), as a Matlab matrix.

ANNEX 1

Mechanics and morphogenesis of fission yeast cells

ANNEX 1

Available online at www.sciencedirect.com

ScienceDirect

Current Opinion in Microbiology

Mechanics and morphogenesis of fission yeast cells

Valeria Davì and Nicolas Minc

The integration of biochemical and biomechanical elements is at the heart of morphogenesis. While animal cells are relatively soft objects which shape and mechanics is mostly regulated by cytoskeletal networks, walled cells including those of plants, fungi and bacteria are encased in a rigid cell wall which resist high internal turgor pressure. How these particular mechanical properties may influence basic cellular processes, such as growth, shape and division remains poorly understood. Recent work using the model fungal cell fission yeast, *Schizosaccharomyces pombe*, highlights important contribution of cell mechanics to various morphogenesis processes. We envision this genetically tractable system to serve as a novel standard for the mechanobiology of walled cell.

Address
Institut Jacques Monod, 15 rue Hélène Brion, 75205 Paris cedex 13, France

Corresponding author: Minc, Nicolas (nicolas.minc@ijm.fr)

Current Opinion in Microbiology 2015, **28**:36–45

This review comes from a themed issue on **Growth and development: eukaryotes and prokaryotes**

Edited by **Sophie Martin (Eu)** and **Dan Kearns (Pro)**

http://dx.doi.org/10.1016/j.mib.2015.07.010

Introduction

Growth and form of biological matter ultimately relies on similar mechanical principles as for non-living matter. Cells and tissues grow and adopt defined shapes from the dynamic biochemical regulation of mechanical elements at multiple scales: from nanometric molecular motors, to millimetric tissue stress [1,2]. The shape of animal cells, for instance, is set by a balance between cortical tension and adhesion [3]. Cortical tension is mostly regulated by the actin cortex, a thin layer of branched actin filaments beneath the plasma membrane [4]. Opposite to animal cells, plants, bacteria and fungi, possess an extracellular case outside their plasma membrane called the cell wall, which has conceptual equivalence with the actin cortex and/or elements of the extracellular matrix. The cell wall is thin, typically hundreds of nm, and is made of heterogeneous polysaccharides and glycoproteins interwoven by hydrogen and covalent bonds. Walled cells are also characterized by high internal osmotic pressure, called turgor, typically 3–4 orders of magnitude higher than in animal cells [5–7,8•,9]. The balance between turgor and wall mechanics has long been recognized to influence the shape and growth properties of walled cells [10–12]. Recent advances in microscopy and biophysical approaches, have allowed to measure and manipulate relevant mechanical parameters of cell walls and turgor [6,8•,9,13••]. These technical progresses, combined with a growing appreciation of the importance of physical considerations in biology, may begin to challenge and refine some basic paradigms in the morphogenesis of walled cells.

Here we focus on recent progress in the mechanics and morphogenesis of fission yeast cells. These rod-shape cells exhibit stereotypical tip growth and elongate from 7 to 14 μm in length during interphase, with a near constant diameter of 4 μm [14,15]. Growth ceases at mitosis and cells divide in their exact middle [16]. For tip elongation, polarity machineries organized around active GTP-Cdc42 and actin, are targeted to cell tips to restrict membrane and cell wall addition there [14]. During cell division, similar modules are re-targeted to the cell middle to drive the assembly of a cytokinetic ring and septum needed for division [16]. To date, this system has been mostly used as a model to dissect the basics of cell-cycle regulation and cytoskeletal assembly which are conserved from yeast to humans, and their contribution to growth, size, polarized behavior and cell shape [17]. The influence of cell mechanics however, is only beginning to be appreciated. We will first introduce the physical parameters characterizing fission yeast mechanics, the molecular elements that control these mechanical properties, and then discuss how they may influence processes such as cell shape, growth, division and polarization.

Main text

Mechanical properties of fission yeast cells

The balance between mechanical stress in the cell wall and turgor pressure contributes to define fission yeast cell shape (Figure 1). If turgor is reduced by submitting cells to high osmolarity medium (by adding sorbitol), cells shrink in a dose-dependent manner, and cease growth temporarily until turgor has adapted (Figure 1a) [8•,13••]. Second, if the cell wall is digested, cells rapidly burst; and if wall digestion is done in high osmolarity medium, to reduce turgor, they form round protoplasts which, in certain conditions can leave behind cell wall remnants (sacculus) with near intact rod-shapes (Figure 1b) [18]. These extreme experimental evidences, which apply to most walled cell, suggest that the values of mechanical

Figure 1

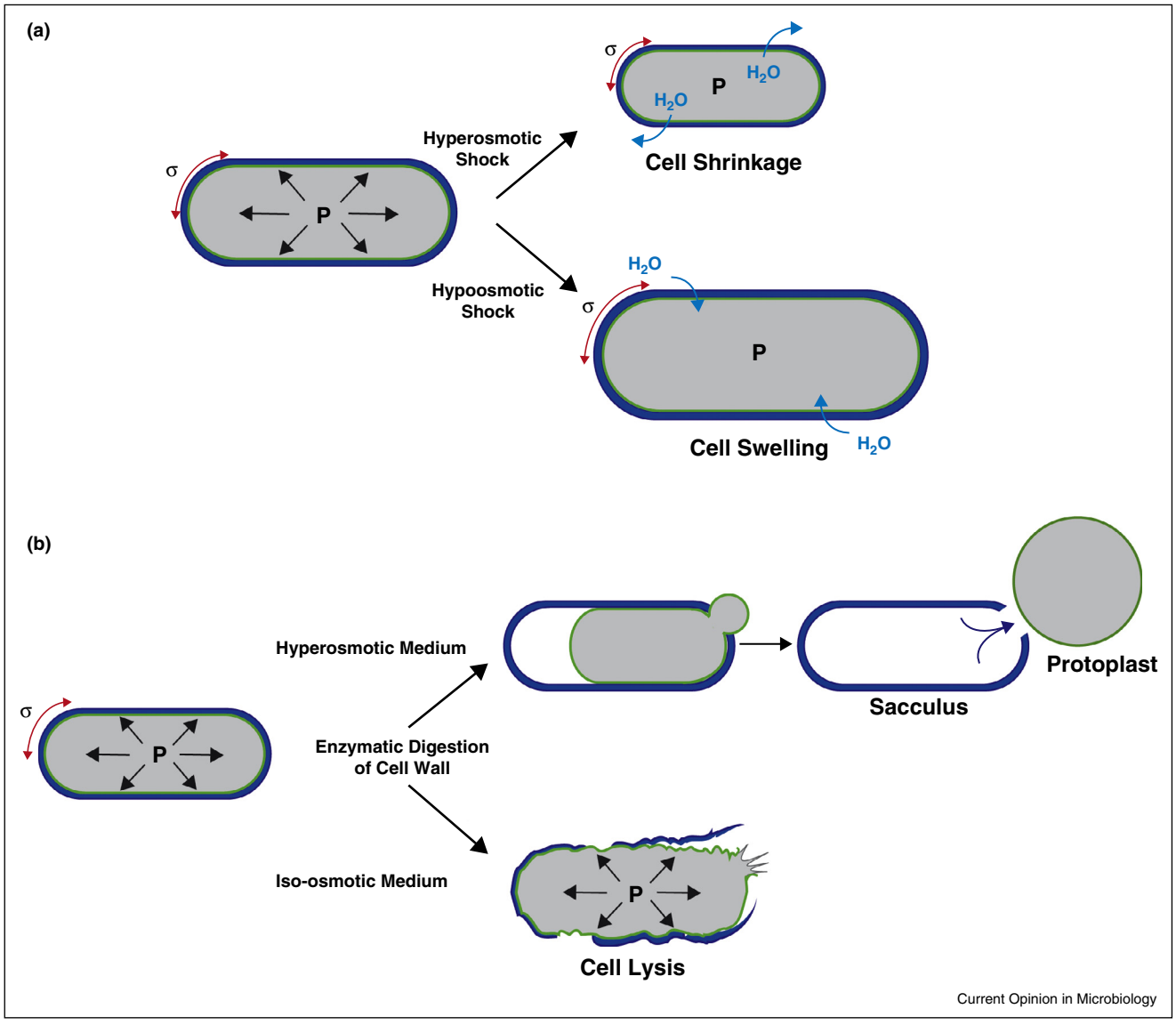

Cell mechanics and cell shape in fission yeast. **(a)** Cell shape changes upon hyper- (top panel) or hypo- (bottom panel) osmotic shock. Water permeates the cell, to balance the difference in osmolytes concentration, causing drastic changes in turgor pressure and cell wall stress. As a result, cells rapidly change shape, by shrinking (hyperosmosis) or swelling (hypoosmosis). **(b)** Cell shape changes after enzymatic digestion of the cell wall in hyperosmotic (top) or isoosmotic (bottom) media. In hyperosmotic medium, the cell wall opens, but turgor is low, which yields to the slow exit of the cell membrane and cytoplasm into a round protoplast leaving behind cell wall remnants, that may maintain near intact rod-shape in certain conditions. In isoosmotic medium, turgor is high and an opening in the cell wall yields immediate cell lysis since turgor is not balanced anymore by cell wall stress.

parameters characterizing turgor and cell wall are important elements for morphogenesis. How can they be measured?

On time scales on the order of few minutes, the fission yeast cell wall may behave as an elastic material ('a spring'). This has been evidenced in experiments in which cells were pushed into bent shapes into microfabricated wells [8•,19,20]. In this assay, cells occasionally popped out of microwells and restored their straight rod-shapes in seconds, suggesting the wall is elastic. On longer time-scales (tens of minutes to hours), however, the wall may also incorporate irreversible deformations and behave more as a plastic material; but relevant measurements are still lacking to document these aspects.

The bulk elastic modulus, or Young's modulus of an elastic material, has units of pressure, and characterizes

its intensive properties, independently of its geometry. For the cell wall, it can be seen as a physical measure of the composition and/or crosslinking of sugars chains. The surface modulus, which is the product of the bulk modulus with wall thickness, which has been estimated to be around 200 nm from transmission electron microscopy images [21,22], has units of tension, and provides the most relevant parameter to understand the contribution of wall mechanics to cell shape and growth [8•,23]. A method often used to compute surface mechanics in various cell types is atomic force microscopy (AFM) [24–26]. However, a complication of using this approach in walled cells, is to separate the contribution of wall mechanical properties and turgor pressure [9,27,28]. A rather simpler method, consists of using microfabricated wells made of elastomers with controlled elastic properties, as single cell force sensors. When fission yeast cells are pushed into these wells, they will buckle and deform the chamber at the same time. The balance between the buckling force and chamber deformation yields an estimate of the wall surface modulus of 6.5 N m^{-1}, typically 3–4 orders of magnitude higher than measured surface tension in animal cells [29], which corresponds to a bulk elastic modulus of about 30 MPa, similar to that of rubber [8•].

Estimating the values of internal turgor pressure in small cells such as yeast, can be challenging, as it involves impaling cells with pressure probes [6]. Here again cell-scale microchambers, have been used to estimate turgor values, by measuring how cells deform an elastic microchambers, to derive force–velocity relationships for single growing cells. Based on a minimal model for growth, these data yield estimates of the maximal force that yeast cells exert as they grow, to be on the order of 11 μN, which corresponds to a turgor pressure of approximately 0.85 MPa [8•].

These measurements, which fall within the same range as for other walled cell such as bacteria, plants and other fungi [6,9,26,30,31]; provide a basic mechanical picture of fission yeast cells, similar to an inflated tire of a racing bicycle. They are key to support quantitative descriptions and modeling, and to test basic concepts in other mechanically-driven processes like endocytosis and cytokinesis (see hereafter). These mean values are however not sufficient to explain the asymmetric morphology of fission yeast cells [12]. In rod-shaped bacteria, for instance, anisotropies in the elasticity of the cell wall plausibly created by a circumferential orientation of wall fibers, are thought to contribute to define a rod [31,32]. In other tip-growing cells, like plant pollen tubes, local variations in wall mechanical properties along the cell perimeter, associated with spatial pattern of wall composition have been proposed to guide tip growth [33]. Future work in fission yeast will reveal which spatial mechanical anisotropies may guide rod-shape establishment, and more importantly how these anisotropies relate to intracellular distribution of polarity machineries.

The fission yeast cell wall

The mechanical properties of the cell wall are regulated by its biochemical composition, but the links between mechanics and biochemistry remain poorly described. The fission yeast cell wall is a polymer network made of two major polysaccharides: β(1,3) glucan chains with β(1,6) branches and α(1,3) glucan chains attached to short chains of α(1,4)glucan; two minor polysaccharides: linear β(1,3) glucan chains and β(1,6) glucan chains with a high amount of β(1,3) branches; and glycoproteins (α-galactomannan). Glucan synthases promote the synthesis of sugar chains. Endoglucanases digest and remodel the cell wall by shortening the chains, and glucanosyl-transferases may promote chain elongations and control crosslinking [34].

The architecture, synthesis and mechanics of the cell wall vary in different life stages of *Schizosaccharomyces pombe*. In interphase, new cell wall is synthesized at growing cell tips through the localization and activation of the β(1,3) glucan synthase Bgs4 and the putative α-glucan synthase Ags1/Mok1 [35–37]. Bgs1 and Bgs3, two other putative β-glucan synthases, are also recruited to cell tips, but their function there remains to be clarified [38,39]. One glucanase, Exg2, and two β(1,3)-glucanosyltransferases Gas1 and Gas2 are also localized to cell tips and could potentially influence wall synthesis or crosslinking [40,41] (Figure 2a). For cytokinesis, the septum is assembled in a centripetal manner outside the ring in the cell middle, and is composed of a central primary septum, flanked by two secondary septa. Bgs1 may be predominantly involved in assembling the primary septum [42], while Bgs4 and Ags1 may function in the synthesis of both primary and secondary septa [35,43,44]. After septum has finished ingression, it is digested in its middle by the endoglucanases Eng1, Exg1 and Agn1 to complete cell separation [40,45,46] (Figure 2b). During mating, and cell–cell fusion, a local degradation and remodeling of the cell wall is necessary to allow the fusion of the two plasma membranes of mating partners. This event is mechanically challenging because an opening of the walls before fusion would yield cell lysis; and involves a specialized focused actin structure which ensures precise spatio-temporal patterning of endoglucanases and glucan synthases around mating tips [47••]. Ascospores, which are products of meiosis, possess a particular cell wall composed of an inner spore wall surrounded by a thin outer spore wall, that confers resistance to spores [13••,48]. Although the composition of the spore wall remain understudied, it may involve in addition to other aforementioned enzymes a specific set of factors, such as the β-glucan synthase Bgs2, the α-glucan synthase Mok12, Mok13 and Mok14, [48–50] and the glucanosyl-transferase Gas4 for elongation and crosslinks [51]. In addition, the chitin synthase Chs1 may promote chitin or

Figure 2

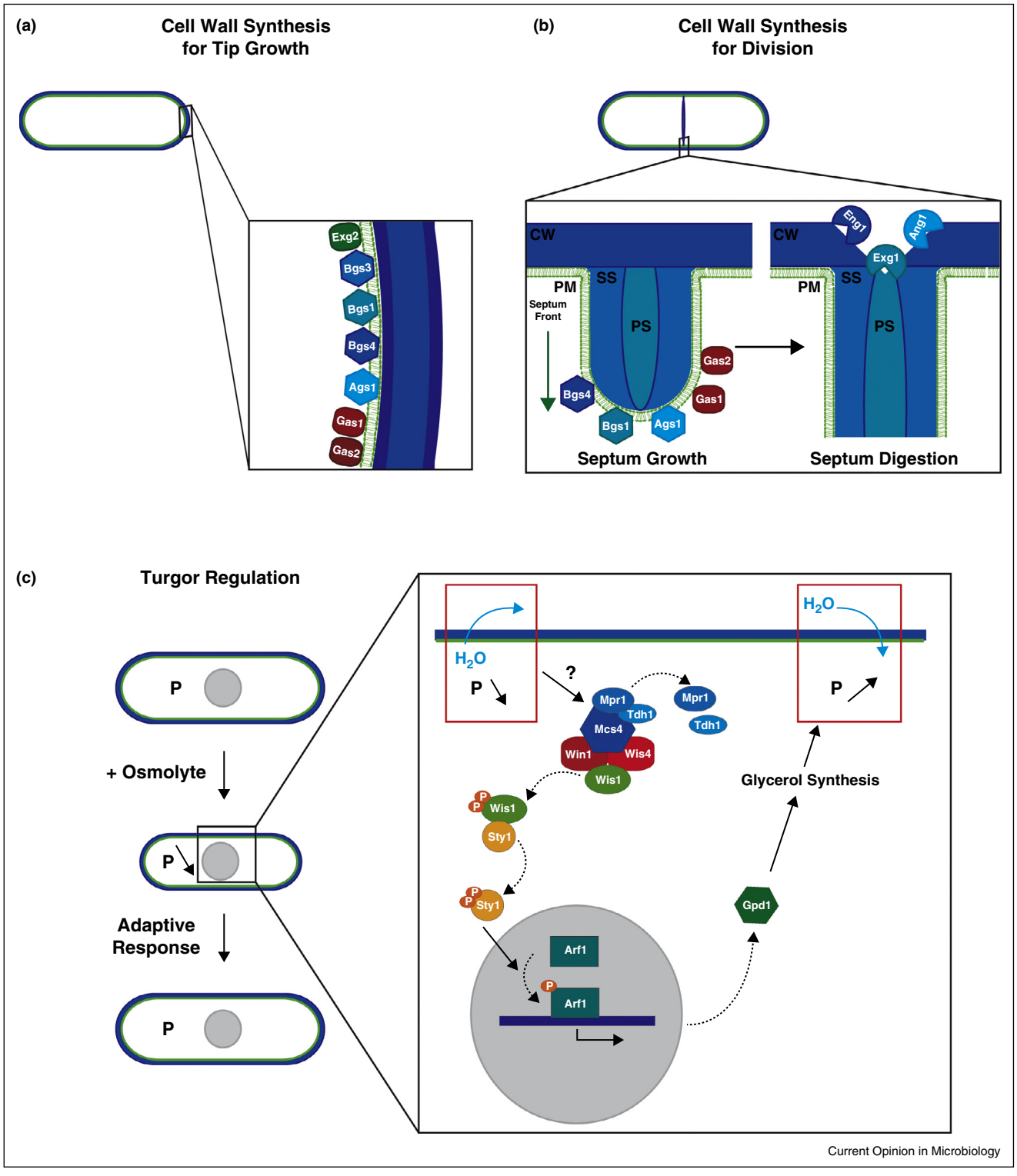

Molecular regulation of fission yeast mechanics. **(a)** Cell wall synthesis at cell tips during interphase. α and β glucan synthases (Ags1, Bgs4) at the plasma membrane catalyze the synthesis of sugar chains in the cell wall. Other putative β glucan synthases (Bgs1 and 3) are also rectruited there, but their role remains uncharacterized. Gas1,2 are glucanosyltransferases that may influence sugar chain elongation and crosslinks. Exg2 is a predicted glucanase that could remodel or digest the wall. The cell wall is a three layered structure with an inner and outer electron dense layers and a less dense middle layer. **(b)** Septum synthesis and degradation during cytokinesis and cell division. Bottom left panel: During cytokinesis α and β glucan synthases and glucanosyltransferases are recruited at the cell middle to synthesize the septum (PS: primary septum, SS: secondary

chitosan synthesis, a component absent from vegetative walls [52]. The outer spore wall features extreme mechanical properties, and has been suggested to have a Young's elastic modulus 30 times higher than the vegetative cell wall [13••].

Synthesis and remodeling of the cell wall is regulated in space and time by the Rho GTPases Rho1, Rho2 and Rho1-homologue Rho5 [53–58]. Rho1 regulates the activity of β-glucans synthases both directly and/or through the protein kinases C, Pck1 and Pck2, while Rho2, may regulate α-glucans synthases through Pck2 [57,58]. Damage in the cell wall stimulates the cell wall integrity pathway mediated by the MAPK cascade Mkh1/Pek1/Pmk1 [59], which results in the activation of Pck1 and Pck2 by Rho1 and Rho2, for cell wall repair [60,61]. Recent work in budding yeast suggests that cell wall damage may also be linked to polarity machineries to ensure the very local recruitment of repairing cell wall factories [62••].

Overall, the links between wall assembly/composition, mechanics and morphogenesis remain poorly established at a quantitative level. Many mutants in synthases and Rho GTPases activation display globally thinner or thicker walls, or dramatic changes in wall composition [36,42,63–67]; while others may have more localized defects, at cell tips or septum [40,43]. These defects have striking consequences on cell shapes and growth patterns; which support the broad concept that wall properties, and likely mechanics, is key to control cell shape. Integration of biochemical tools with mechanical measurements will be necessary to rigorously establish those links.

Turgor pressure regulation

Turgor pressure in walled cells is osmotically generated, and maintained through rapid and efficient homeostatic systems [68]. In fission yeast, a hyperosmotic stress leads to the intracellular accumulation of glycerol [69] (Figure 2c). This mechanism is regulated by the stress activated pathway through the MAPK Sty1, a homolog of Hog1 in budding yeast and p38 in mammalian cells [70–72]. This cascade is coordinated by Mcs4 which forms a complex with the two MAPKKK, Win1 and Wis4 [73–76]. In hyperosmotic conditions, the MAPKK Wis1 becomes phosphorylated and unbinds from this complex, to phosphorylate the MAPK Sty1, which enters the nucleus to activate the transcription factor Atf1 [71,77]. Atf1 then regulates the transcription of 13 core genes [78]. This includes an increase in the expression of Gpd1 and Gpd2, glycerol-3-phosphate dehydrogenases, which promote glycerol synthesis; and the repression of genes involved in the degradation and translocation of sugars to compensate osmotic imbalance and restore turgor [69,79]. To fine tune pressure adaptation, Atf1 also promotes a negative feedback loop, through the transcription of *psy1* and *psy2*, that encode for phosphatases that inhibit Sty1 [71,80]. In budding yeast, several trans-membrane proteins have been proposed as upstream 'osmosensors' to trigger Hog1-dependent adaptation [81–83], whether similar systems exist or function in *S. pombe* remains to be explored.

The response to hypoosmotic stress is markedly different, and admittedly less understood. It leads to cell swelling and intracellular Ca^{2+} increase [84]. Two homologues of the *E. coli* mechanosensitive channels MscS [85] have been recently proposed to influence this response: Msy1 and Msy2. Both are ER associated proteins, which become overexpressed in hypoosmotic conditions to support cell viability, but mechanistic details remain to be established [86,87]. Both hyper-osmotic and hypo-osmotic stress also promote the activation of Pmk1 and the cell wall integrity pathway, suggesting links between regulatory systems of cell mechanical properties [88,89].

Cell mechanics and cell growth

How do walled cell grow is not fully understood. Both material synthesis (membrane and cell wall) and turgor pressure are required for growth, yet, how these parameters contribute to define elongation rates is not known [8•]. Without turgor, deposition of new material, is predicted to yield a thicker wall with no growth, and turgor alone would only yield thinning of the wall [90]. Those important questions have long motivated theoretician, and several models for walled cell growth have been proposed over the years [90,91,23,8•,92,13••,106]. Experimental tests for these models are still sparse. A commonly used modeling framework, is to represent growth as a viscoplastic process. In that view the elastic cell wall freshly deposited at cell tips, is deformed by the stress exerted by internal turgor and this deformation becomes irreversible (plastic) passed a certain deformation threshold. The details for how cell wall remodeling may relate to viscoplasticity remain however poorly documented [91]. Conceptually, this amounts to an 'ageing' picture of the wall: as new wall is being incorporated at the tip it becomes irreversibly stretched with a certain time scale. Old cell wall may then flow along cell sides during cell elongation to maintain a constant wall thickness (Figure 3a).

(Figure 2 Legend Continued) septum, CW: cell wall, PM: plasma membrane). Bottom right panel, glucanases are then targeted to the sides of the septum to degrade the PS and cell wall edges for cell separations. **(c)** Osmoadaptation to hyperosmotic shocks. (Left) Upon hyperosmotic treatments cells first shrink and activate the stress pathway to increase internal turgor and recover their initial length and diameter. (Right) Details of signaling pathways involved in turgor maintenance upon hyperosmosis. Hyperosmotic stress causes an immediate loss of water from the cytosol, and consequent decrease in turgor pressure. This activates a MAPK cascade that leads to the expression of several genes, such as gpd1 which promotes glycerol synthesis to balance osmotic differences and restore turgor.

Figure 3

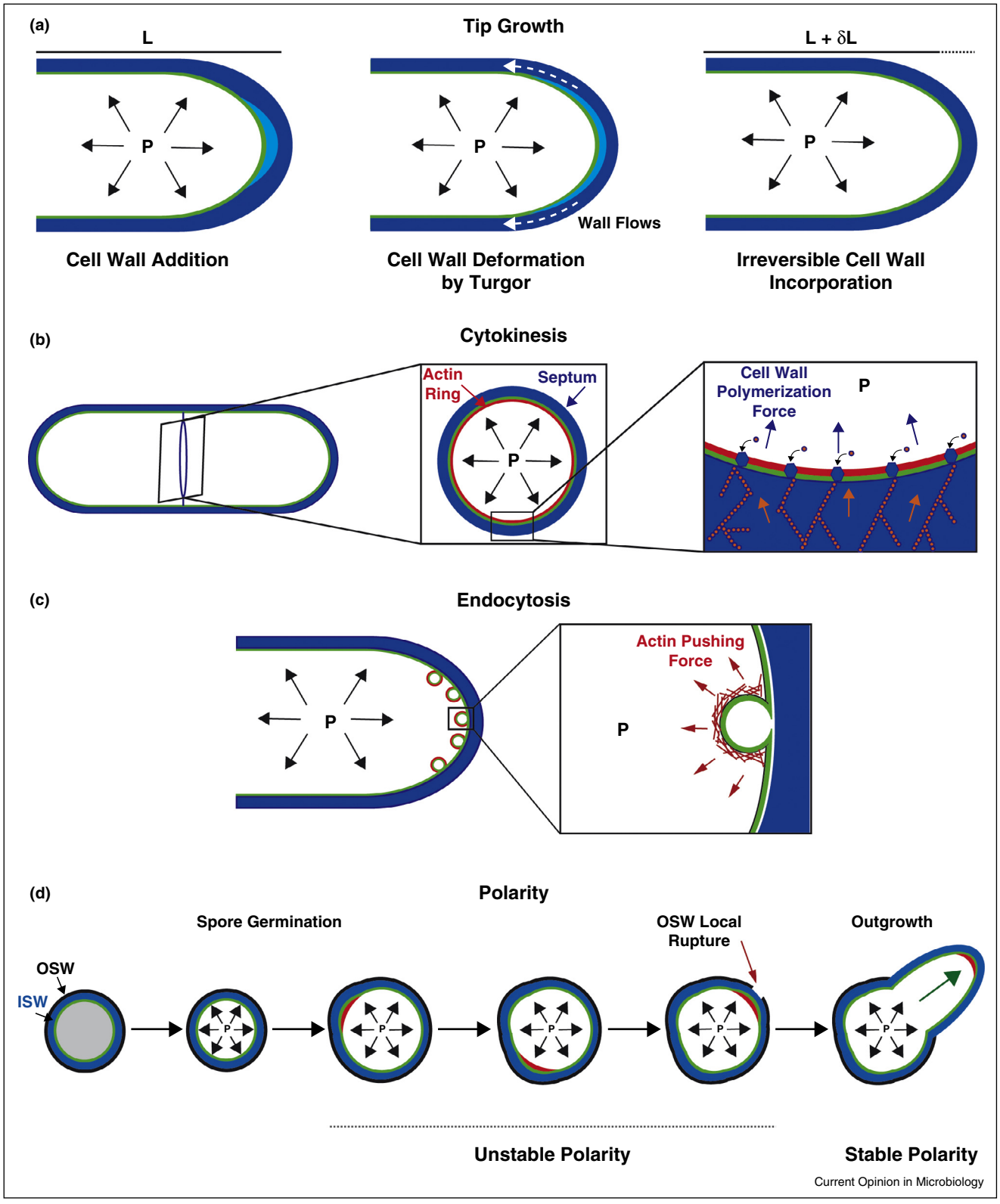

Influence of cell mechanics on fission yeast growth, division, endocytosis and polarization. **(a)** During tip elongation, cell wall is added at cell tip, and strained by the work of turgor and becomes irreversibly deformed for cell length addition. Maintenance of a constant cell wall thickness implies cell wall flows from the tip to cell sides. **(b)** Mechanical considerations in fission yeast cytokinesis. During cytokinesis, the acto-myosin ring

These mathematical models can make interesting predictions on cell diameters, exact tip shapes, or the dependence of elongation rates on mechanical values. For instance, a simple scaling model can recapitulate the variation of cell size observed among many walled cells based solely on their mechanical properties [23]. The probably most complete model adapted to fission yeast tip growth incorporates a spatial distribution of wall synthesis directly correlated with GTP-Cdc42 concentration at cell tips. This model makes important tests on the stability conditions required to maintain a straight rod-shape axis and a fixed diameter over generations of dividing cells, and predicts the existence of complex feedbacks between cell geometry and Cdc42-based polarity [93••].

Role of cell mechanics in endocytosis and cytokinesis

How might other mechanically-driven process, like cytokinesis and endocytosis may adapt to the particular mechanical properties of fission yeast or other walled cells? During cytokinesis, for instance, a conserved acto-myosin contractile ring attached beneath the plasma membrane has long been thought to provide the mechanical force to drive membrane ingression [94,95]. However, simple calculations suggest that the mechanical work exerted by the ring can only account for a small fraction (around 1%) of the work needed to overcome internal turgor pressure [96•]. Recent studies indeed indicate that reducing turgor yields faster constriction rates, and that once cytokinesis has initiated, the ring may become dispensable for membrane ingression and septum completion [43,96•]. This work suggests that most of the mechanical work may be generated by septum assembly, rather than the ring, shifting an important paradigm for cell division in yeast (Figure 3b). The function of the ring, could be instead to keep an homogenous septum assembly around the cell equator, a process plausibly regulated by a curvature-dependent septum assembly mechanism [97••].

Endocytosis, also involves local inward deformation of the plasma membrane to invaginate vesicles with a typical size of tens of nm. This process requires the subsequent assembly of various coat proteins, such as clathrin, myosin and BAR-proteins [98]. Although actin is dispensable for endocytosis in animal cells, it is strictly required in yeast [99]. Two recent studies, one performed in budding yeast [99] and one in fission yeast [100•], suggest that endocytosis also works against turgor, and that actin polymerization around endocytic vesicles generate the necessary forces to overcome turgor (Figure 3c). One set of striking evidence supporting these claims is to show that a reduction in turgor can rescue the defects of endocytic mutants and the requirement for actin. Altogether these data suggest that the regulation of these essential processes may have evolved along with extreme variations in cellular mechanics.

Cell mechanics and polarity

Cell mechanics may also influence cellular spatial organization. Recent studies in migrating animal cells have for instance suggested that surface mechanics, regulated by changes in the actin cortex or membrane tension, could contribute to cell polarization and directed migration [101,102]. Similarly, polarized walled cells such as fungi or plant roots can exhibit thigmotropism, a process during which polarity reorients as a consequence of mechanical contact with a physical barrier [103,104]. In fission yeast, a recent study investigating how initially round spores define their very first polar growth axis provides initial evidence that similar mechanical-polarity crosstalk may exist in these cells [13••]. A very intriguing observation of this work was to find that single polarity domains, built around active Cdc42, spontaneously polarize in germinating spores, but first exhibit a long unstable phase of successive assembly and disassembly, to eventually stabilize to promote polar tip extension at outgrowth. Interestingly, this switch in polarized behavior was found to be concomitant with the opening of the outer spore wall at the site of outgrowth (Figure 3d). By combining mathematical models and laser ablation of the spore wall, this study demonstrates that the spore wall has destabilizing effects on polarity. When the rigid spore wall is intact it acts as a barrier that hinders growth and destabilizes polarity, and opening of the spore wall (either naturally or with a laser) is sufficient to stabilize polarity. These data suggest the existence of feedback systems between wall mechanics and polarity machineries. By considering and testing different hypothesis of feedback (surface curvature, stress in the wall, among others), the authors propose that a positive feedback between growth and polarity, in which polarity localizes growth and more surface growth tend to maintain polarity in place, can explain polarity stabilization in outgrowing spores. Future work should reveal how these feedbacks may be regulated, and if they have relevance to other cellular states and cell types.

(Figure 3 Legend Continued) is surrounded by the septum. Forces generated by cell wall assembly (orange arrows) in the septum may support ring progression against high turgor pressure (adapted from [96•]). **(c)** Mechanical considerations in fission yeast endocytosis. (Left) Endocytic vesicles at cell tips; (Right) Close up on a single vesicle: invagination of the plasma membrane may be driven by a branched actin network that polymerizes and pushes against the membrane and cell wall (red arrows) to overcome turgor pressure (adapted from [100•]). **(d)** Cell mechanics and polarization in fission yeast spores. In spores the inner wall (ISW) is surrounded by a particular rigid outer spore wall (OSW) which may mechanically confine spores. Upon germination single polarity domains (red patch) assemble and disassemble around the spore surface promoting local growth sites that fail to progress. When spores have grown enough, the OSW ruptures at the site of the polarity domain; and this opening releases the hindering effect of the OSW, and polarity becomes stable for outgrowth and polar tip extension (adapted from [13••]).

Conclusion

The contribution of cell mechanics to morphogenesis, is becoming more and more appreciated in different fields, from bacterial growth to embryonic development and tissue homeostasis [1,105]. In fission yeast, which is probably the most established system to link gene function and cell shape, the role of turgor and cell wall mechanics remain surprisingly understudied. This is in contrast with the literature in plants, bacteria and other fungal cells, which have long focused on the mechanics of the wall and turgor for describing morphogenesis. A key endeavor of future studies in fission yeast, will thus be to document how cytoskeletal organization, and more generally gene function, ultimately contribute to pattern and regulate cellular mechanics. Given the genetic power of this system, and its quantitative growth and shape habits, we foresee that it could serve as a novel standard for establishing the biomechanical rules controlling the morphogenesis of single walled cells.

Acknowledgments

We thank Arezki Boudaoud for suggestions and careful reading of the manuscript. Our laboratory is supported by the CNRS, and grants from the FP7 CIG program, the ITN 'FungiBrain' and the 'Mairie de Paris emergence' program.

References and recommended reading

Papers of particular interest, published within the period of review, have been highlighted as:

- • of special interest
- •• of outstanding interest

1. Heisenberg CP, Bellaiche Y: **Forces in tissue morphogenesis and patterning**. *Cell* 2013, **153**:948-962.
2. Lecuit T, Lenne PF: **Cell surface mechanics and the control of cell shape, tissue patterns and morphogenesis**. *Nat Rev Mol Cell Biol* 2007, **8**:633-644.
3. Paluch E, Heisenberg CP: **Biology and physics of cell shape changes in development**. *Curr Biol* 2009, **19**:R790-R799.
4. Salbreux G, Charras G, Paluch E: **Actin cortex mechanics and cellular morphogenesis**. *Trends Cell Biol* 2012, **22**:536-545.
5. Stewart MP, Helenius J, Toyoda Y, Ramanathan SP, Muller DJ, Hyman AA: **Hydrostatic pressure and the actomyosin cortex drive mitotic cell rounding**. *Nature* 2011, **469**:226-230.
6. Bastmeyer M, Deising HB, Bechinger C: **Force exertion in fungal infection**. *Annu Rev Biophys Biomol Struct* 2002, **31**:321-341.
7. Boudaoud A: **An introduction to the mechanics of morphogenesis for plant biologists**. *Trends Plant Sci* 2010, **15**:353-360.
8. • Minc N, Boudaoud A, Chang F: **Mechanical forces of fission yeast growth**. *Curr Biol* 2009, **19**:1096-1101.

This paper uses microfabricated chambers as force sensors to provide the very first measurements of turgor pressure and cell wall elastic modulus in fission yeast.

9. Beauzamy L, Derr J, Boudaoud A: **Quantifying hydrostatic pressure in plant cells by using indentation with an atomic force microscope**. *Biophys J* 2015, **108**:2448-2456.
10. Harold FM: **To shape a cell: an inquiry into the causes of morphogenesis of microorganisms**. *Microbiol Rev* 1990, **54**:381-431.
11. Harold FM: **Force and compliance: rethinking morphogenesis in walled cells**. *Fungal Genet Biol* 2002, **37**:271-282.
12. Chang F, Huang KC: **How and why cells grow as rods**. *BMC Biol* 2014, **12**:54.
13. •• Bonazzi D, Julien JD, Romao M, Seddiki R, Piel M, Boudaoud A, Minc N: **Symmetry breaking in spore germination relies on an interplay between polar cap stability and spore wall mechanics**. *Dev Cell* 2014, **28**:534-546.

This manuscript documents the mechanobiology of growing and polarizing spores, and demonstrates novel feedbacks between the mechanics of the cell wall, cell growth and the stability of polarity machineries.

14. Chang F, Martin SG: **Shaping fission yeast with microtubules**. *Cold Spring Harb Perspect Biol* 2009, **1**:a001347.
15. Mitchison JM, Nurse P: **Growth in cell length in the fission yeast *Schizosaccharomyces pombe***. *J Cell Sci* 1985, **75**:357-376.
16. Chang F, Nurse P: **How fission yeast fission in the middle**. *Cell* 1996, **84**:191-194.
17. Egel R (Ed): *The Molecular Biology of Schizosaccharomyces pombe*. Springer; 2004.
18. Flor-Parra I, Zhurinsky J, Bernal M, Gallardo P, Daga RR: **A Lallzyme MMX-based rapid method for fission yeast protoplast preparation**. *Yeast* 2014, **31**:61-66.
19. Minc N, Bratman SV, Basu R, Chang F: **Establishing new sites of polarization by microtubules**. *Curr Biol* 2009, **19**:83-94.
20. Minc N: **Microfabricated chambers as force sensors for probing forces of fungal growth**. *Methods Cell Biol* 2014, **120**:215-226.
21. Sugawara T, Sato M, Takagi T, Kamasaki T, Ohno N, Osumi M: **In situ localization of cell wall alpha-1,3-glucan in the fission yeast *Schizosaccharomyces pombe***. *J Electron Microsc (Tokyo)* 2003, **52**:237-242.
22. Takagi T, Ishijima SA, Ochi H, Osumi M: **Ultrastructure and behavior of actin cytoskeleton during cell wall formation in the fission yeast *Schizosaccharomyces pombe***. *J Electron Microsc (Tokyo)* 2003, **52**:161-174.
23. Boudaoud A: **Growth of walled cells: from shells to vesicles**. *Phys Rev Lett* 2003, **91**:018104.
24. Dufrene YF: **Towards nanomicrobiology using atomic force microscopy**. *Nat Rev Microbiol* 2008, **6**:674-680.
25. Dufrene YF: **Atomic force microscopy and chemical force microscopy of microbial cells**. *Nat Protoc* 2008, **3**:1132-1138.
26. Zhao L, Schaefer D, Xu H, Modi SJ, LaCourse WR, Marten MR: **Elastic properties of the cell wall of *Aspergillus nidulans* studied with atomic force microscopy**. *Biotechnol Prog* 2005, **21**:292-299.
27. Vella D, Ajdari A, Vaziri A, Boudaoud A: **Indentation of ellipsoidal and cylindrical elastic shells**. *Phys Rev Lett* 2012, **109**:144302.
28. Vella D, Ajdari A, Vaziri A, Boudaoud A: **The indentation of pressurized elastic shells: from polymeric capsules to yeast cells**. *J R Soc Interface* 2012, **9**:448-455.
29. Maitre JL, Niwayama R, Turlier H, Nedelec F, Hiiragi T: **Pulsatile cell-autonomous contractility drives compaction in the mouse embryo**. *Nat Cell Biol* 2015, **17**:849-855.
30. Misra G, Rojas ER, Gopinathan A, Huang KC: **Mechanical consequences of cell-wall turnover in the elongation of a gram-positive bacterium**. *Biophys J* 2013, **104**:2342-2352.
31. Yao X, Jericho M, Pink D, Beveridge T: **Thickness and elasticity of gram-negative murein sacculi measured by atomic force microscopy**. *J Bacteriol* 1999, **181**:6865-6875.
32. Gan L, Chen S, Jensen GJ: **Molecular organization of Gram-negative peptidoglycan**. *Proc Natl Acad Sci U S A* 2008, **105**:18953-18957.
33. Bosch M, Hepler PK: **Pectin methylesterases and pectin dynamics in pollen tubes**. *Plant Cell* 2005, **17**:3219-3226.
34. Perez P, Ribas JC: **Cell wall analysis**. *Methods* 2004, **33**:245-251.
35. Cortes JC, Carnero E, Ishiguro J, Sanchez Y, Duran A, Ribas JC: **The novel fission yeast (1,3)beta-D-glucan synthase catalytic subunit Bgs4p is essential during both cytokinesis and polarized growth**. *J Cell Sci* 2005, **118**:157-174.

36. Hochstenbach F, Klis FM, van den Ende H, van Donselaar E, Peters PJ, Klausner RD: **Identification of a putative alpha-glucan synthase essential for cell wall construction and morphogenesis in fission yeast**. *Proc Natl Acad Sci U S A* 1998, **95**:9161-9166.

37. Katayama S, Hirata D, Arellano M, Perez P, Toda T: **Fission yeast alpha-glucan synthase Mok1 requires the actin cytoskeleton to localize the sites of growth and plays an essential role in cell morphogenesis downstream of protein kinase C function**. *J Cell Biol* 1999, **144**:1173-1186.

38. Cortes JC, Ishiguro J, Duran A, Ribas JC: **Localization of the (1,3)beta-D-glucan synthase catalytic subunit homologue Bgs1p/Cps1p from fission yeast suggests that it is involved in septation, polarized growth, mating, spore wall formation and spore germination**. *J Cell Sci* 2002, **115**:4081-4096.

39. Martin V, Garcia B, Carnero E, Duran A, Sanchez Y: **Bgs3p, a putative 1,3-beta-glucan synthase subunit, is required for cell wall assembly in *Schizosaccharomyces pombe***. *Eukaryot Cell* 2003, **2**:159-169.

40. Duenas-Santero E, Martin-Cuadrado AB, Fontaine T, Latge JP, del Rey F, Vazquez de Aldana C: **Characterization of glycoside hydrolase family 5 proteins in *Schizosaccharomyces pombe***. *Eukaryot Cell* 2010, **9**:1650-1660.

41. de Medina-Redondo M, Arnaiz-Pita Y, Clavaud C, Fontaine T, del Rey F, Latge JP, Vazquez de Aldana CR: **beta(1,3)-glucanosyltransferase activity is essential for cell wall integrity and viability of *Schizosaccharomyces pombe***. *PLoS One* 2010, **5**:e14046.

42. Cortes JC, Konomi M, Martins IM, Munoz J, Moreno MB, Osumi M, Duran A, Ribas JC: **The (1,3)beta-D-glucan synthase subunit Bgs1p is responsible for the fission yeast primary septum formation**. *Mol Microbiol* 2007, **65**:201-217.

43. Munoz J, Cortes JC, Sipiczki M, Ramos M, Clemente-Ramos JA, Moreno MB, Martins IM, Perez P, Ribas JC: **Extracellular cell wall beta(1,3)glucan is required to couple septation to actomyosin ring contraction**. *J Cell Biol* 2013, **203**:265-282.

44. Cortes JC, Sato M, Munoz J, Moreno MB, Clemente-Ramos JA, Ramos M, Okada H, Osumi M, Duran A, Ribas JC: **Fission yeast Ags1 confers the essential septum strength needed for safe gradual cell abscission**. *J Cell Biol* 2012, **198**:637-656.

45. Martin-Cuadrado AB, Duenas E, Sipiczki M, Vazquez de Aldana CR, del Rey F: **The endo-beta-1,3-glucanase eng1p is required for dissolution of the primary septum during cell separation in *Schizosaccharomyces pombe***. *J Cell Sci* 2003, **116**:1689-1698.

46. Dekker N, Speijer D, Grun CH, van den Berg M, de Haan A, Hochstenbach F: **Role of the alpha-glucanase Agn1p in fission-yeast cell separation**. *Mol Biol Cell* 2004, **15**:3903-3914.

47. •• Dudin O, Bendezu FO, Groux R, Laroche T, Seitz A, Martin SG: **A formin-nucleated actin aster concentrates cell wall hydrolases for cell fusion in fission yeast**. *J Cell Biol* 2015, **208**:897-911.
This work evidences the existence of a specialized actin structure ('actin aster') which allows to focus secretion machineries to the exact contact point of fusing mating partners in fission yeast. A function of this structure may be to properly pattern degradation and synthesis of the walls for fusion.

48. Garcia I, Tajadura V, Martin V, Toda T, Sanchez Y: **Synthesis of alpha-glucans in fission yeast spores is carried out by three alpha-glucan synthase paralogues, Mok12p, Mok13p and Mok14p**. *Mol Microbiol* 2006, **59**:836-853.

49. Martin V, Ribas JC, Carnero E, Duran A, Sanchez Y: **bgs2+, a sporulation-specific glucan synthase homologue is required for proper ascospore wall maturation in fission yeast**. *Mol Microbiol* 2000, **38**:308-321.

50. Liu J, Tang X, Wang H, Balasubramanian M: **Bgs2p, a 1,3-beta-glucan synthase subunit, is essential for maturation of ascospore wall in *Schizosaccharomyces pombe***. *FEBS Lett* 2000, **478**:105-108.

51. de Medina-Redondo M, Arnaiz-Pita Y, Fontaine T, Del Rey F, Latge JP, Vazquez de Aldana CR: **The beta-1,3-glucanosyltransferase gas4p is essential for ascospore wall maturation and spore viability in *Schizosaccharomyces pombe***. *Mol Microbiol* 2008, **68**:1283-1299.

52. Arellano M, Cartagena-Lirola H, Nasser Hajibagheri MA, Duran A, Henar Valdivieso M: **Proper ascospore maturation requires the chs1+ chitin synthase gene in *Schizosaccharomyces pombe***. *Mol Microbiol* 2000, **35**:79-89.

53. Arellano M, Duran A, Perez P: **Localisation of the *Schizosaccharomyces pombe* rho1p GTPase and its involvement in the organisation of the actin cytoskeleton**. *J Cell Sci* 1997, **110(Pt 20)**:2547-2555.

54. Nakano K, Arai R, Mabuchi I: **Small GTPase Rho5 is a functional homologue of Rho1, which controls cell shape and septation in fission yeast**. *FEBS Lett* 2005, **579**:5181-5186.

55. Rincon SA, Santos B, Perez P: **Fission yeast Rho5p GTPase is a functional paralogue of Rho1p that plays a role in survival of spores and stationary-phase cells**. *Eukaryot Cell* 2006, **5**:435-446.

56. Perez P, Rincon SA: **Rho GTPases: regulation of cell polarity and growth in yeasts**. *Biochem J* 2010, **426**:243-253.

57. Arellano M, Coll PM, Perez P: **RHO GTPases in the control of cell morphology, cell polarity, and actin localization in fission yeast**. *Microsc Res Tech* 1999, **47**:51-60.

58. Calonge TM, Nakano K, Arellano M, Arai R, Katayama S, Toda T, Mabuchi I, Perez P: ***Schizosaccharomyces pombe* rho2p GTPase regulates cell wall alpha-glucan biosynthesis through the protein kinase pck2p**. *Mol Biol Cell* 2000, **11**:4393-4401.

59. Toda T, Dhut S, Superti-Furga G, Gotoh Y, Nishida E, Sugiura R, Kuno T: **The fission yeast pmk1+ gene encodes a novel mitogen-activated protein kinase homolog which regulates cell integrity and functions coordinately with the protein kinase C pathway**. *Mol Cell Biol* 1996, **16**:6752-6764.

60. Sanchez-Mir L, Soto T, Franco A, Madrid M, Viana RA, Vicente J, Gacto M, Perez P, Cansado J: **Rho1 GTPase and PKC ortholog Pck1 are upstream activators of the cell integrity MAPK pathway in fission yeast**. *PLoS One* 2014, **9**:e88020.

61. Ma Y, Kuno T, Kita A, Asayama Y, Sugiura R: **Rho2 is a target of the farnesyltransferase Cpp1 and acts upstream of Pmk1 mitogen-activated protein kinase signaling in fission yeast**. *Mol Biol Cell* 2006, **17**:5028-5037.

62. •• Kono K, Saeki Y, Yoshida S, Tanaka K, Pellman D: **Proteasomal degradation resolves competition between cell polarization and cellular wound healing**. *Cell* 2012, **150**:151-164.
In this paper, the authors use a localized laser to fragilize the cell wall in budding yeast and show that this leads to the degradation of polarity sites and *de novo* assembly of sites of actin nucleation and myosin recruitment at the site of damage.

63. Villar-Tajadura MA, Coll PM, Madrid M, Cansado J, Santos B, Perez P: **Rga2 is a Rho2 GAP that regulates morphogenesis and cell integrity in *S. pombe***. *Mol Microbiol* 2008, **70**:867-881.

64. Arellano M, Duran A, Perez P: **Rho 1 GTPase activates the (1-3)beta-D-glucan synthase and is involved in *Schizosaccharomyces pombe* morphogenesis**. *EMBO J* 1996, **15**:4584-4591.

65. Arellano M, Valdivieso MH, Calonge TM, Coll PM, Duran A, Perez P: ***Schizosaccharomyces pombe* protein kinase C homologues, pck1p and pck2p, are targets of rho1p and rho2p and differentially regulate cell integrity**. *J Cell Sci* 1999, **112(Pt 20)**:3569-3578.

66. Ribas JC, Roncero C, Rico H, Duran A: **Characterization of a *Schizosaccharomyces pombe* morphological mutant altered in the galactomannan content**. *FEMS Microbiol Lett* 1991, **63**:263-267.

67. Flor-Parra I, Bernal M, Zhurinsky J, Daga RR: **Cell migration and division in amoeboid-like fission yeast**. *Biol Open* 2014, **3**:108-115.

68. Hersen P, McClean MN, Mahadevan L, Ramanathan S: **Signal processing by the HOG MAP kinase pathway**. *Proc Natl Acad Sci U S A* 2008, **105**:7165-7170.

69. Ohmiya R, Yamada H, Nakashima K, Aiba H, Mizuno T: **Osmoregulation of fission yeast: cloning of two distinct genes encoding glycerol-3-phosphate dehydrogenase, one of which is responsible for osmotolerance for growth**. *Mol Microbiol* 1995, **18**:963-973.

70. Degols G, Shiozaki K, Russell P: **Activation and regulation of the Spc1 stress-activated protein kinase in *Schizosaccharomyces pombe***. *Mol Cell Biol* 1996, **16**:2870-2877.

71. Shiozaki K, Russell P: **Cell-cycle control linked to extracellular environment by MAP kinase pathway in fission yeast**. *Nature* 1995, **378**:739-743.

72. Perez P, Cansado J: **Cell integrity signaling and response to stress in fission yeast**. *Curr Protein Pept Sci* 2010, **11**:680-692.

73. Shiozaki K, Shiozaki M, Russell P: **Heat stress activates fission yeast Spc1/StyI MAPK by a MEKK-independent mechanism**. *Mol Biol Cell* 1998, **9**:1339-1349.

74. Morigasaki S, Ikner A, Tatebe H, Shiozaki K: **Response regulator-mediated MAPKKK heteromer promotes stress signaling to the Spc1 MAPK in fission yeast**. *Mol Biol Cell* 2013, **24**:1083-1092.

75. Morigasaki S, Shiozaki K: **Phosphorelay-dependent and -independent regulation of MAPKKK by the Mcs4 response regulator in fission yeast**. *Commun Integr Biol* 2013, **6**:e25020.

76. Samejima I, Mackie S, Fantes PA: **Multiple modes of activation of the stress-responsive MAP kinase pathway in fission yeast**. *EMBO J* 1997, **16**:6162-6170.

77. Nguyen AN, Ikner AD, Shiozaki M, Warren SM, Shiozaki K: **Cytoplasmic localization of Wis1 MAPKK by nuclear export signal is important for nuclear targeting of Spc1/Sty1 MAPK in fission yeast**. *Mol Biol Cell* 2002, **13**:2651-2663.

78. Chen D, Toone WM, Mata J, Lyne R, Burns G, Kivinen K, Brazma A, Jones N, Bahler J: **Global transcriptional responses of fission yeast to environmental stress**. *Mol Biol Cell* 2003, **14**:214-229.

79. Aiba H, Yamada H, Ohmiya R, Mizuno T: **The osmo-inducible gpd1+ gene is a target of the signaling pathway involving Wis1 MAP-kinase kinase in fission yeast**. *FEBS Lett* 1995, **376**:199-201.

80. Shiozaki K, Russell P: **Conjugation, meiosis, and the osmotic stress response are regulated by Spc1 kinase through Atf1 transcription factor in fission yeast**. *Genes Dev* 1996, **10**:2276-2288.

81. Tatebayashi K, Tanaka K, Yang HY, Yamamoto K, Matsushita Y, Tomida T, Imai M, Saito H: **Transmembrane mucins Hkr1 and Msb2 are putative osmosensors in the SHO1 branch of yeast HOG pathway**. *EMBO J* 2007, **26**:3521-3533.

82. Tatebayashi K, Yamamoto K, Nagoya M, Takayama T, Nishimura A, Sakurai M, Momma T, Saito H: **Osmosensing and scaffolding functions of the oligomeric four-transmembrane domain osmosensor Sho1**. *Nat Commun* 2015, **6**:6975.

83. Posas F, Wurgler-Murphy SM, Maeda T, Witten EA, Thai TC, Saito H: **Yeast HOG1 MAP kinase cascade is regulated by a multistep phosphorelay mechanism in the SLN1-YPD1-SSK1 "two-component" osmosensor**. *Cell* 1996, **86**:865-875.

84. Batiza AF, Schulz T, Masson PH: **Yeast respond to hypotonic shock with a calcium pulse**. *J Biol Chem* 1996, **271**:23357-23362.

85. Berrier C, Besnard M, Ajouz B, Coulombe A, Ghazi A: **Multiple mechanosensitive ion channels from *Escherichia coli*, activated at different thresholds of applied pressure**. *J Membr Biol* 1996, **151**:175-187.

86. Nakayama Y, Iida H: **Organellar mechanosensitive channels involved in hypo-osmoregulation in fission yeast**. *Cell Calcium* 2014, **56**:467-471.

87. Nakayama Y, Yoshimura K, Iida H: **Organellar mechanosensitive channels in fission yeast regulate the hypo-osmotic shock response**. *Nat Commun* 2012, **3**:1020.

88. Barba G, Soto T, Madrid M, Nunez A, Vicente J, Gacto M, Cansado J: **Activation of the cell integrity pathway is channelled through diverse signalling elements in fission yeast**. *Cell Signal* 2008, **20**:748-757.

89. Madrid M, Soto T, Khong HK, Franco A, Vicente J, Perez P, Gacto M, Cansado J: **Stress-induced response, localization, and regulation of the Pmk1 cell integrity pathway in *Schizosaccharomyces pombe***. *J Biol Chem* 2006, **281**:2033-2043.

90. Dumais J, Shaw SL, Steele CR, Long SR, Ray PM: **An anisotropic-viscoplastic model of plant cell morphogenesis by tip growth**. *Int J Dev Biol* 2006, **50**:209-222.

91. Rojas ER, Hotton S, Dumais J: **Chemically mediated mechanical expansion of the pollen tube cell wall**. *Biophys J* 2011, **101**:1844-1853.

92. Campas O, Mahadevan L: **Shape and dynamics of tip-growing cells**. *Curr Biol* 2009, **19**:2102-2107.

93. •• Drake T, Vavylonis D: **Model of fission yeast cell shape driven by membrane-bound growth factors and the cytoskeleton**. *PLoS Comput Biol* 2013, **9**:e1003287.
This theoretical paper represents the most complete mathematical model for fission yeast cell growth and shape determination. The model makes important prediction for the stability of classical shape phenotypes of wild-types and mutants.

94. Pollard TD, Wu JQ: **Understanding cytokinesis: lessons from fission yeast**. *Nat Rev Mol Cell Biol* 2010, **11**:149-155.

95. Chang F, Woollard A, Nurse P: **Isolation and characterization of fission yeast mutants defective in the assembly and placement of the contractile actin ring**. *J Cell Sci* 1996, **109(Pt 1)**:131-142.

96. • Proctor SA, Minc N, Boudaoud A, Chang F: **Contributions of turgor pressure, the contractile ring, and septum assembly to forces in cytokinesis in fission yeast**. *Curr Biol* 2012, **22**:1601-1608.
This work provides evidence for the provocative idea that the actin ring may not provide enough pulling force for fission yeast cytokinesis, and that septum assembly may generate most of the force for ingression.

97. •• Zhou Z, Munteanu EL, He J, Ursell T, Bathe M, Huang KC, Chang F: **The contractile ring coordinates curvature-dependent septum assembly during fission yeast cytokinesis**. *Mol Biol Cell* 2015, **26**:78-90.
This work which follows upon [96•] introduces an elegant method to monitor ring constriction and septum assembly ends-on, and suggest that the function of the ring in fission yeast cytokinesis may be to maintain an homogenous rate of septum growth around the cell equator.

98. Galletta BJ, Cooper JA: **Actin and endocytosis: mechanisms and phylogeny**. *Curr Opin Cell Biol* 2009, **21**:20-27.

99. Aghamohammadzadeh S, Ayscough KR: **Differential requirements for actin during yeast and mammalian endocytosis**. *Nat Cell Biol* 2009, **11**:1039-1042.

100. • Basu R, Munteanu EL, Chang F: **Role of turgor pressure in endocytosis in fission yeast**. *Mol Biol Cell* 2014, **25**:679-687.
Following up on previous work in budding yeast [99], this paper shows that turgor pressure opposes forces of actin polymerization in fission yeast endocytosis.

101. Houk AR, Jilkine A, Mejean CO, Boltyanskiy R, Dufresne ER, Angenent SB, Altschuler SJ, Wu LF, Weiner OD: **Membrane tension maintains cell polarity by confining signals to the leading edge during neutrophil migration**. *Cell* 2012, **148**:175-188.

102. Charras G, Paluch E: **Blebs lead the way: how to migrate without lamellipodia**. *Nat Rev Mol Cell Biol* 2008, **9**:730-736.

103. Brand A, Vacharaksa A, Bendel C, Norton J, Haynes P, Henry-Stanley M, Wells C, Ross K, Gow NA, Gale CA: **An internal polarity landmark is important for externally induced hyphal behaviors in Candida albicans**. *Eukaryot Cell* 2008, **7**:712-720.

104. Migliaccio F, Piconese S: **Spiralizations and tropisms in Arabidopsis roots**. *Trends Plant Sci* 2001, **6**:561-565.

105. Persat A, Nadell CD, Kim MK, Ingremeau F, Siryaporn A, Drescher K, Wingreen NS, Bassler BL, Gitai Z, Stone HA: **The mechanical world of bacteria**. *Cell* 2015, **161**:988-997.

106. Campas O, Rojas E, Dumais J, Mahadevan L: **Strategies for cell shape control in tip-growing cells**. *Am J Bot* 2012, **99**:1577-1582 http://dx.doi.org/10.3732/ajb.1200087.

ANNEX 2

Procédé de mesure en temps réel de l’epaisseur de la paroi et ses applications

ANNEX 2

PROCEDE DE MESURE EN TEMPS REEL DE L'EPAISSEUR DE LA PAROI ET SES APPLICATIONS

La présente invention se rapporte au domaine de l'industrie en biotechnologie, dont la portée d'application est aussi bien dans le secteur de la santé, de l'agro-industrie que de la recherche. La présente invention propose plus particulièrement une nouvelle méthode pour mesurer l'épaisseur de la paroi cellulaire de cellules à paroi, ainsi que sa mise en œuvre dans diverses applications.

A la différence des cellules animales, les cellules de champignons, de bactéries, d'archées, de plantes et d'algues sont protégées par une paroi cellulaire plus ou moins rigide constituée principalement de chaînes sucrées, qui entoure leur membrane plasmique (Davi *et al.,* 2015). Cette paroi permet non seulement de définir la forme de ces cellules, de supporter leur structure, de transporter des substances et de diffuser des gaz entre l'environnement extérieur et l'intérieur de ces cellules et de cellule à cellule, mais aussi de réguler la pression osmotique de manière à éviter les pertes d'eau et à empêcher la rupture de ces cellules due la pression de turgescence qu'elles contiennent, et de les protéger contre les agressions extérieures, telles que les infections et le stress mécanique.

En raison du rôle protecteur joué par cette paroi, en particulier chez les microbes potentiellement pathogènes que constituent les bactéries et champignons, la paroi cellulaire est l'une des cibles privilégiées des antibiotiques et antifongiques en développement. Cependant, l'émergence de résistance aux drogues conventionnelles, telles que la pénicilline, nécessite d'identifier de nouveaux composés permettant de lutter efficacement contre ces pathogènes.

Cette paroi est activement construite par les cellules à l'aide d'enzymes de synthèse et de remodelage de la membrane, qui secrètent les chaînes sucrées, et est principalement composée de polysaccharides réticulés et/ou de glycoprotéines. En fonction des espèces et du cycle cellulaire, elle est en outre capable de changer de composition et d'épaisseur, cette dernière pouvant ainsi varier entre 10 et 500nm.

L'épaisseur de cette paroi cellulaire est un élément essentiel et critique, non seulement pour le mode de vie de ces cellules, mais également pour leur survie. En effet, il a été observé qu'une paroi trop fine induit la lyse cellulaire, tandis qu'une paroi trop épaisse peut confiner mécaniquement la cellule et l'empêcher de croître ou de se diviser (Davi *et al.*, 2015 ; Chang *et al.*, 2014). Des défauts d'épaisseur de paroi sont également associés à des changements de formes et de fonctions drastiques.

A ce jour, la seule méthode permettant d'observer la paroi cellulaire et de mesurer son épaisseur est la microscopie électronique à transmission (plus connue sous l'abréviation TEM en anglais) (Osumi *et al.*, 1998). Cette méthode requiert toutefois de fixer les cellules, et donc de les tuer, ce qui donc empêche toute observation dynamique de la paroi, et donc de suivi de son développement dans le temps. Elle est en outre coûteuse, laborieuse, et prône à artefacts. A titre illustratif, un protocole typique d'imagerie de la paroi cellulaire par microscopie électronique nécessite entre 5 et 7 jours de préparation de l'échantillon. Il est également très difficile d'observer la paroi dans le plan de symétrie des cellules en raison des coupes devant être effectuées dans le cadre de cette méthode.

Il existe donc un besoin urgent de développer une nouvelle méthode d'imagerie de la paroi cellulaire, permettant de mesurer son épaisseur sans présenter ces inconvénients, et ainsi de suivre en temps réel son développement, aussi bien à des fins de recherche fondamentale que pour identifier de nouveaux agents susceptibles d'altérer son épaisseur, plus particulièrement destinés à lutter contre les microbes pathogènes.

La présente invention répond à ces besoins.

Les Inventeurs ont en effet mis au point un procédé innovant d'imagerie en microscopie à haute résolution, dont les étapes permettent de mesurer, avec précision, fiabilité et à moindre coût, l'épaisseur de la paroi cellulaire en temps réel, chez des cellules vivantes possédant une paroi. Pour ce faire, les faces interne et externe de la paroi cellulaire sont tout d'abord chacune marquées par un marqueur détectable distinct afin de différencier ces faces, puis la cellule ainsi marquée est imagée par un dispositif optique, en particulier par un microscope photonique confocal. La distance entre ces deux marqueurs, correspondant à l'épaisseur de la paroi, est ensuite déterminée automatiquement par analyse de l'image acquise avec le dispositif optique Il est alors possible de générer automatiquement des cartes spatiales de l'épaisseur tout autour de la cellule. Le procédé de l'invention peut en outre intégrer une méthode de correction des aberrations chromatiques générées par le dispositif optique. Le procédé de l'invention permet ainsi de mesurer localement, mais aussi globalement, l'épaisseur la paroi cellulaire avec une résolution dans le plan de l'ordre de la cinquantaine de nanomètres et une précision sur la mesure d'épaisseur de +/- 10nm, et d'étudier des cellules en pleine croissance.

Ce procédé a été validé avec succès chez deux espèces de champignons : la levure fissipare *Schizosaccarhomyces pombe* et le champignon pathogène *Candida Albicans*. Sa versatilité a en outre été illustrée par les Inventeurs, qui démontrent ici que le procédé

de l'invention est également applicable pour mesurer les changements d'épaisseur consécutifs au traitement par des drogues et dans des mutants de la synthèse de paroi. Ainsi, au-delà des informations précieuses sur la physiologie de cellules à paroi, le procédé de l'invention peut être utilisé pour cribler des composés candidats de type fongicides ou bactéricides ciblant la paroi cellulaire, avec des applications importantes dans le domaine de la santé et de l'agriculture.

La présente invention propose donc un nouveau procédé *in vitro* de mesure en temps réel de l'épaisseur de la paroi cellulaire de cellules à paroi, ainsi que ses applications.

DESCRIPTION DETAILLEE DE L'INVENTION

Sauf indication contraire, les termes scientifiques et techniques utilisés dans le cadre de la présente invention auront les significations qui sont communément admises par l'homme du métier.

Par « paroi cellulaire », on entend désigner ici une structure extracellulaire entourant plus particulièrement les cellules de champignons, bactéries, archées, plantes et/ou algues. La paroi cellulaire est plus précisément située à l'extérieur de la membrane de ces cellules (plus communément appelée membrane plasmique ou membrane cytoplasmique), et est ainsi en contact avec le milieu extracellulaire. Elle permet de par sa rigidité non seulement de soutenir la structure de la cellule mais également de la protéger, en jouant notamment un rôle de filtre au regard du milieu extracellulaire et en faisant obstacle à l'expansion cellulaire lorsque l'eau pénètre dans la cellule (i.e. par osmorégulation). Elle assure également une certaine plasticité ou élasticité qui est nécessaire à la croissance et à la division cellulaire. Cette paroi est généralement constituée de polysaccharides et/ou de peptides/protéines (glycosylé(e)s ou non glycosylé(e)s), qui sont préférablement entrelacés par de l'hydrogène et/ou des liaisons covalentes. La composition de cette paroi varie néanmoins d'une espèce cellulaire à l'autre : à titre purement illustratif et non limitatif, la paroi cellulaire des champignons comprend principalement de la chitine mais également des glucanes et des mannoprotéines (Perez et Ribas, 2004; Ruiz-Herrera, 2012); celle des bactéries à Gram positif principalement des peptidoglycanes (Seltmann *et al*., 2002 ; Silhavy *et al*., 2010); celle des bactéries à Gram négatif principalement des protéines (Seltmann *et al*., 2002 ; Silhavy *et al*., 2010); celles d'archées principalement des glycoprotéines, protéines de couches S, pseudopeptidoglycanes et/ou des polysaccharides (König *et al*., 2010 ; Meyer

et al., 2014); celle des plantes majoritairement de la cellulose et de la pectine (d'où son appellation paroi pectocellulosique) (Rose, 2009 ; Keegstra *et al.,* 2010); et celle des algues des glycoprotéines et/ou des polysaccharides (e.g. cellulose), ou de l'acide silicique (Domozych *et al*., 2012).

Par « épaisseur de la paroi cellulaire », on entend désigner ici la dimension de la paroi telle que définie ci-dessus, mesurée par l'écart ou la distance entre ses deux faces principales, plus ou moins parallèles, et dénommées ici face interne et face externe de la paroi cellulaire. Dans le contexte de la présente invention, cette épaisseur est préférablement déterminée en nanomètres.

Par « face externe de la paroi cellulaire », il faut comprendre ici la partie de la paroi cellulaire qui est du côté extérieur de la cellule, tandis que la « face interne de la paroi cellulaire » désigne la partie de la paroi cellulaire qui est du côté intérieur de la cellule.

Par « marqueur détectable » ou « label détectable », on entend désigner ici une substance ou une molécule, naturelle ou synthétique, qui peut être détectée par un dispositif optique approprié, en particulier, dans le contexte de la présente invention, par un dispositif optique à haute résolution.

De manière préférée, ce marqueur est un « marqueur luminescent », c'est-à-dire un marqueur qui, suite à une excitation (par exemple de nature lumineuse, chimique, enzymatique, etc) émet une radiation lumineuse à une longueur d'onde donnée, dite lumière d'émission ou radiation lumineuse d'émission. Un exemple particulièrement préféré de marqueur luminescent selon l'invention est un marqueur fluorescent.

Par « marqueur fluorescent » ou « fluorophore », il faut comprendre ici un marqueur luminescent coloré, qui absorbe de l'énergie lumineuse à une longueur d'onde donnée (dite lumière d'excitation, ou encore radiation lumineuse d'excitation ou d'absorption) et la restitue sous forme de lumière fluorescente à une autre longueur d'onde (dite lumière d'émission, ou radiation lumineuse d'émission). Un marqueur fluorescent émet une radiation lumineuse dite rapide, c'est-à-dire une radiation lumineuse dont le temps de vie est généralement de l'ordre de 10^{-10} à 10^{-5} secondes, préférablement de 10^{-9} à 10^{-6} secondes. Les marqueurs fluorescents pouvant être utilisés dans le cadre de la présente invention peuvent être de nature protéique ou non protéique, tels que décrits ci-après.

Le terme « dispositif optique à haute-résolution » désigne ici un dispositif optique pourvu d'une source de lumière, typiquement de lumière monochromatique, et dont la résolution latérale est d'environ 200 nm. De manière préférée, la résolution latérale dudit dispositif est comprise entre environ 150 nm et 250 nm, préférablement entre environ 170 nm et environ 230 nm, et encore plus préférablement entre environ 190 nm et environ

210 nm. Ce dispositif doit être à même de détecter les marqueurs de l'invention, en collectant par exemple sous forme d'image la radiation lumineuse émise par les marqueurs luminescents. Dans le cas où le marqueur luminescent utilisé dans le procédé de l'invention est un marqueur fluorescent, ce dispositif doit être également capable d'exciter ledit marqueur, en émettant une lumière d'excitation adéquate qui sera absorbée ledit marqueur : ce type de dispositif optique est plus connu sous le nom de microscope à fluorescence. Le microscope photonique est un dispositif optique particulièrement préféré de l'invention, tel qu'exposé ci-dessous.

Le terme « environ » signifie que les valeurs indiquées sont approximatives, et plus particulièrement qu'une variation de ces valeurs de plus ou moins 5 % peut être tolérée. Préférablement, la variation tolérée est de plus ou moins 4%, plus préférablement de plus ou moins 3%, 2%, 1%, et le plus préférablement de plus ou moins 0,5%.

D'autres définitions sont données ci-après dans la description.

Les Inventeurs ont développé un procédé nouveau et innovant permettant de mesurer en temps réel l'épaisseur de la paroi cellulaire de cellules à paroi. Ce procédé est non seulement rapide et facile à mettre en œuvre, mais également précis, robuste et versatile. Il permet notamment de mesurer l'épaisseur de la paroi cellulaire avec une précision de l'ordre de 10 nm, localement, aussi bien dans des cellules vivantes que dans des cellules mortes, pouvant être issues de différentes espèces cellulaires à paroi. Cette mesure locale appliquée tout le long du contour de la cellule peut par ailleurs permettre d'obtenir une mesure globale de l'épaisseur de la paroi, en moyennant par exemple plusieurs mesures locales.

Ainsi, dans un premier aspect, la présente invention propose un procédé *in vitro* pour mesurer en temps réel l'épaisseur de la paroi cellulaire de cellules à paroi, comprenant:

a) fournir au moins une cellule isolée ayant une paroi cellulaire, la face externe de ladite paroi cellulaire étant marquée avec au moins un premier marqueur détectable, et la face interne de ladite paroi cellulaire étant marquée avec au moins un second marqueur détectable, lesdits marqueurs étant distincts l'un de l'autre ;
b) imager ladite cellule et détecter lesdits marqueurs à l'aide d'un dispositif optique à haute-résolution, préférablement à l'aide d'un microscope photonique ;
c) déterminer la distance entre ledit premier marqueur sur la face externe et ledit second marqueur sur la face interne, mesurant ainsi l'épaisseur de la paroi cellulaire.

Par « cellule isolée », il faut comprendre que la cellule étudiée a été séparée de son environnement naturel, et des composants de celui-ci. Ainsi, tel qu'indiqué ci-dessus, le procédé de l'invention est réalisé « *in vitro* », c'est-à-dire en dehors du modèle biologique, en laboratoire, par exemple en milieu artificiel en observant la cellule sur une lame de verre ou tout autre matériel de laboratoire approprié, selon des protocoles bien connus de l'homme du métier (Gupta *et al.*, 2012).

La cellule isolée peut être une cellule vivante, c'est-à-dire une cellule capable de se diviser dans des conditions de culture *in vitro.* Tel qu'indiqué ci-après, le procédé de l'invention permet précisément d'évaluer la viabilité de la cellule étudiée.

Selon un mode de réalisation préféré, la cellule à paroi cellulaire imagée est sélectionnée dans le groupe consistant en les cellules de champignons, de bactéries, d'archées, de plantes et d'algues. De manière préférée, lesdits champignons, bactéries, archées, plantes et/ou algues sont unicellulaires.

Ces espèces cellulaires à paroi sont bien connues de l'homme du métier, et ne sont donc pas détaillées plus avant ici. Celles-ci peuvent être aisément identifiées, notamment selon les critères taxonomiques établis dans l'art tel que ceux de Ruggiero *et al.* (2015). Il est à noter que le procédé de l'invention ne peut pas être réalisé sur des cellules animales (parmi lesquelles les cellules humaines), ni sur des bactéries de type mycoplasme, puisque ces cellules sont dépourvues de paroi. Par ailleurs, si la cellule à paroi selon l'invention est une bactérie, ladite bactérie n'est préférablement pas une bactérie Gram négatif.

De manière encore préférée, la cellule à paroi cellulaire imagée est une cellule de champignon. Des exemples de cellules de champignons particulièrement préférées selon l'invention, néanmoins non limitatifs, sont les cellules de levure, telle que *Schyzosaccharomyces pombe*, et les cellules de *Candica albicans*, qui sont illustrés dans les exemples décrits ci-après.

La cellule à paroi peut être imagée à l'aide de tout dispositif optique à haute-résolution approprié, en particulier par un microscope photonique. Ces dispositifs sont bien connus de l'homme du métier, et incluent, sans limitation, le microscope en champ clair, le microscope en champ sombre, le microscope en lumière polarisée, le microscope à fluorescence, le microscope à contraste de phase (y compris de type interférentiel), le microscope confocal, le microscope à statif inversé, et leur combinaison (Paddock, 2014).

De manière préféré, le microscope photonique à haute-résolution utilisé dans le procédé de l'invention est un microscope confocal.

Un « microscope confocal » est un microscope optique qui a la propriété de réaliser des images de très faible profondeur de champ (environ 400 nm). En positionnant le plan focal de l'objectif à différents niveaux de profondeur dans l'échantillon, il permet de réaliser des séries d'images à partir desquelles on peut obtenir une représentation tridimensionnelle de l'objet. Une image est ensuite recomposée par ordinateur. Ce microscope, qui comprend typiquement une source de lumière monochromatique (e.g. lampe à mercure ou laser), peut en outre utiliser plusieurs rayons de lumière monochromatique de manière simultanée, ce qui permet d'observer plusieurs endroits de l'échantillon (ici la cellule) à la fois.

Des exemples de microscopes confocaux pouvant être utilisés dans le procédé de l'invention sont le microscope confocal à disque rotatif, le microscope confocal à balayage laser (CLSM), ou encore le microscope confocal spectral (ou chromatique).

Le microscope confocal à disque rotatif (ou disque de Nipkov) est ici particulièrement préféré, car il permet de maximiser la résolution spatiale tout en limitant le bruit de fond. Il peut en outre être aisément couplé à un détecteur de manière à pouvoir numériser l'image de la cellule observée.

Un « microscope confocal à disque rotatif » comporte un disque perforé tournant, comme par exemple un disque de Nipkov, et permet de réaliser des images en temps réel ainsi que la scrutation en simultanée de plusieurs endroits. Le disque perforé tournant de ce microscope tourne typiquement à 25 tours par seconde. Il comporte une pluralité de trous, typiquement de 30 à 200. Chaque trou est placé à une distance décroissante du centre, ce qui permet d'analyser l'image ligne par ligne. Un détecteur placé derrière le disque mesure les variations d'intensité de la lumière qui peuvent alors être transmises à un appareil récepteur distant. Avec ce procédé, l'image est alors composée d'autant de lignes que le disque est percé de trous.

Le détecteur utilisé dans le microscope confocal à disque rotatif peut être une caméra à transfert de charge (CCD « Charge Coupled Device »), qui mesure et numérise l'intensité lumineuse. De manière préférée, ledit détecteur est une caméra à transfert de charge à multiplication d'électrons (EM-CCD). Un « EM-CCD » est un dispositif à transfert de charge dans lequel un registre de gain est placé entre le registre à décalage et l'amplificateur de sortie. Le registre de gain est divisé en un grand nombre d'étages de gain. A chaque étage de gain, les électrons sont multipliés par ionisation par impact d'une manière similaire à une diode à avalanche.

Il est entendu que dans le cas où les marqueurs luminescents de l'invention sont des marqueurs fluorescents, le dispositif optique à haute-résolution de l'invention est également un microscope à fluorescence. De manière préférée, ledit dispositif est un microscope confocal à fluorescence, et avantageusement, un microscope confocal à disque rotatif et à fluorescence.

L'homme du métier comprendra aisément que les marqueurs utilisés dans le procédé de l'invention pour marquer respectivement la face externe et la face interne de la paroi cellulaire sont distincts, de manière à pouvoir différencier ces deux faces. Pour ce faire, des marqueurs luminescents émettant des radiations lumineuses de différente longueur d'onde peuvent être utilisés.

Ainsi, selon un mode de réalisation préféré, ledit premier marqueur détectable (i.e. marquant la face externe de la paroi) est un marqueur luminescent émettant une radiation lumineuse dans une première gamme de longueur d'onde, et ledit second marqueur détectable (i.e. marquant la face interne de la paroi) est un marqueur luminescent émettant une radiation lumineuse dans une seconde gamme de longueur d'onde distincte de la première gamme de longueur d'onde.

Le terme « longueur d'onde » (λ) signifie la distance parcourue dans le vide par une radiation lumineuse (ou onde lumineuse) durant un temps T appelé période. Les longueurs d'onde de la lumière visible sont typiquement comprises entre environ 400 nm et environ 760 nm. Par exemple, la longueur d'onde d'une radiation lumineuse violette est typiquement comprise entre environ 380 nm et environ 449 nm, celle d'une radiation lumineuse violette/bleue (majoritairement/minoritairement) entre environ 449 nm et environ 466 nm, celle d'une radiation lumineuse bleue entre environ 466 nm et environ 483 nm, celle d'une radiation lumineuse bleue/verte (majoritairement/minoritairement) entre environ 483 et environ 490 nm, celle d'une radiation lumineuse verte/bleue (majoritairement/ minoritairement) entre environ 490 nm et environ 510 nm, celle d'une radiation lumineuse verte entre environ 510 nm et environ 541 nm, celle d'une radiation lumineuse verte/jaune (majoritairement/minoritairement) entre environ 541 nm et environ 573 nm, celle d'une radiation lumineuse jaune/verte (majoritairement/minoritairement) entre environ 573 nm et environ 575 nm, celle d'une radiation lumineuse jaune entre environ 575 nm et environ 579 nm, celle d'une radiation lumineuse jaune/orangée (majoritairement/minoritairement) entre environ 579 nm et environ 584 nm, celle d'une radiation lumineuse orangée/jaune (majoritairement/minoritairement) entre environ 584 nm et environ 588 nm, celle d'une radiation lumineuse orangée entre environ 588 nm et environ 593 nm, celle d'une radiation lumineuse orangée/rouge

(majoritairement/minoritairement) entre environ 593 nm et environ 605 nm, celle d'une radiation lumineuse rouge/orangée (majoritairement/ minoritairement) entre environ 605 nm et environ 622 nm, et celle d'une radiation lumineuse rouge entre environ 622 nm et environ 700 nm. Ainsi, à chaque couleur dite spectrale correspond une longueur d'onde précise.

Par « longueur d'onde distincte », on désigne donc des longueurs d'onde dont le spectre est distinct, par exemple celles telles que définies ci-dessus.

A titre purement illustratif, et non limitatif, l'homme du métier pourra par exemple sélectionner un premier marqueur luminescent émettant une radiation lumineuse rouge, telle qu'une radiation dont la longueur d'onde est préférablement comprise environ 622 nm et environ 700 nm, et un second marqueur luminescent émettant une radiation lumineuse verte, telle qu'une radiation dont la longueur d'onde est préférablement comprise entre environ 510 nm et environ 541 nm, ces longueurs d'ondes étant distinctes l'une de l'autre.

De manière préférée, le premier et le deuxième marqueur détectables utilisés pour marquer la paroi cellulaire sont des marqueurs fluorescents, tels que définis ci-dessus. Ces marqueurs peuvent être de nature protéique ou non protéique.

Le terme « protéique » (qualifiant les protéines), « peptidique » (qualifiant les peptides) ou « polypeptidiques » (qualifiant les polypeptides) fait référence ici à une séquence d'acides aminés joints par des liaisons peptidiques (-NHCO-), quelle que soit sa longueur, qui peut être d'origine naturelle ou synthétique, et qui peut jouer un rôle structurel et/ou fonctionnel dans une cellule *in vitro* et / ou *in vivo*.

Les marqueurs fluorescents de nature protéique sont bien connus de l'homme du métier, et incluent, sans limitation, les protéines fluorescentes vertes (plus connues sous le nom de GFPs), les protéines fluorescentes rouges (plus connues sous le nom de RFPs) ou oranges, les protéines fluorescentes cyans (plus connues sous le nom de CFPs), les protéines fluorescentes bleues (plus connues sous le nom de BFPs) ou violètes, et les protéines fluorescentes jaunes (plus connues sous le nom de YFPs).

Ces protéines émettent une radiation lumineuse de longueur d'onde correspondant, dans une certaine mesure, à la couleur désignée par leur nom. Elles ont été décrites de manière extensive dans la littérature, et sont pour la plupart disponibles commercialement ou peuvent être aisément produites par l'homme du métier (Shaner *et al*., 2005 ; Day *et al*., 2009 ; Zimmer, 2015a ; Zimmer, 2015b ; voir également le site internet du Nikon Imaging Center/Université de Californie, San Francisco qui répertorie les propriétés de ces protéines, ainsi que le tableau 1 ci-dessous).

Des exemples de telles protéines fluorescentes, incluent, sans limitation, les protéines de fluorescence verte GFP*av* (provenant d'*Aequoria Victoria*), EGFP, TagGFP, TagGFP2, TurboGFP, CopGFP, AceGFP, mUKG, superfolder GFP, Emerald, Azami Green (AG), ZsGreen, mWasabi, Clover, mNeonGreen, NowGFP, mClover3, Sapphire, T-Sapphire; les protéines de fluorescence rouge ou orange Kusabira-Orange, mOrange, mOrange2, mKOk, mKO2, tdTomato, DsRed, TagRFP, TagRFP-T, mRuby, mRuby2, mTangerine, mApple, mStrawberry, FusionRed, mCherry, J-Red, mNectarine, mRuby3, mKeimaRed, mBeRFP, LSS-mKAte2, LSS-mKate1, LSSmOrange, mKate2, HcRed-Tandem, mPlum, mRaspberry, mNeptune, NirFP, TagRFP657, TagFRP675, mCardinal, iFP1.4, iFP713 (iRFP), iRFP670, iRFP682, iRFP702, iRFP720, iFP2.0, mIFP ; les protéines de fluorescence cyan ECFP, mCFPm, Cerulean, mCerulean3, SCFP, SCFP3A, CyPet, mTurquoise, mTurquoise 2, TagCFP, AmCyan, mTFP1, Midoriishi cyan, Aquamarine; les protéines de fluorescence bleue ou violette EBFP, EBFP2, Azurite, mKalama1, TagBFP, mTagBFP, mTagBFP2, Sirius les protéines de fluorescence jaune EYFP, TagYFP, TurboYFP, ZsYellow, PhiYFP, Topaz, Venus, SYFP2, Citrine, mCitrine, Ypet, SYFP, IanFRP-ΔS83, mPapaya1, mAmetrine.

Le tableau 1 ci-après répertorie les marqueurs fluorescents protéiques de l'invention, avec leurs longueurs d'onde d'excitation et d'émission.

Tableau 1. Marqueurs fluorescents protéiques selon l'invention

Protéine fluorescente	**Longueur d'onde d'excitation (λex) à pH7 (nm)**	**Longueur d'onde d'émission (λem) à pH7 (nm)**	**Référence**
Fluorescence verte émise (GFPs)			
GFP*av*	395	509	Prendergast *et al*., 1978
EGFP	488	507	Yang *et al*., 1996
TagGFP	482	505	Xia *et al*., 2002
TagGFP2	483	506	Subach *et al*., 2008
TurboGFP	482	502	Evdokimov *et al*., 2006
CopGFP	482	502	Shagin *et al*., 2004
AceGFP	480	505	Gurskaya *et al*., 2003
muKG	483	499	Tsutsui *et al*., 2008
superfolder GFP	485	510	Pédelacq *et al*., 2005
Emerald	487	509	Cubitt *et al*., 1998
Azami Green (AG)	492	505	Karazawa *et al*., 2003
mWasabi	493	509	Ai *et al*., 2008a
Clover	505	515	Lam *et al*., 2012

Protéine fluorescente	Longueur d'onde d'excitation (λex) à pH7 (nm)	Longueur d'onde d'émission (λem) à pH7 (nm)	Référence
mNeonGreen	506	517	Shaner *et al*., 2013
ZsGreen	493	505	Matz *et al*., 1999
NowGFP	494	502	Sarkisyan *et al*., 2015
mClover3	506	518	Bajar *et al*., 2016
Sapphire	399	511	Cubitt *et al*., 1998
T-Sapphire	399	511	Zappata-Homer *et al*., 2003
Fluorescence rouge émise (incluant le orange et infra-rouge) (RFPs)			
Kusabira-Orange	548	559	Karasawa *et al*., 2004
mOrange	548	562	Shaner *et al*., 2004
mOrange2	549	565	Shaner *et al*., 2008
mKOk	551	563	Tsutsui *et al*., 2008
mKO2	551	565	Sakaue-Sawano *et al*., 2008
tdTomato	554	581	Shaner *et al*., 2004
DsRed	556	586	Clontech
TagRFP	555	584	Merzlyak *et al*., 2007
TagRFP-T	555	584	Shaner *et al*., 2008
mRuby	558	605	Kredel *et al*., 2009
mRuby2	559	600	Lam *et al*., 2012
mTangerine	568	585	Shaner *et al*., 2004
mApple	568	592	Shaner *et al*., 2008
mStrawberry	574	596	Shaner *et al*., 2004
FusionRed	580	608	Shemiakina *et al*., 2012
mCherry	587	610	Shaner *et al*., 2004
J-Red	584	610	Evrogen
mNectarine	558	578	Johnson *et al*., 2009
mRuby3	558	592	Bajar *et al*., 2016
mKeimaRed	440	620	Kogure *et al*., 2006
mBeRFP	446	611	Yang *et al.,* 2013
LSS-mKAte2	460	605	Piatkevich *et al*., 2010
LSS-mKate1	463	624	Piatkevich *et al.,* 2010
LSSmOrange	437	572	Shcherbakova *et al*., 2012
mKate2	588	633	Shcherbo *et al*., 2009
HcRed-Tandem	590	637	Fradkov et al., 2002

Protéine fluorescente	Longueur d'onde d'excitation (λex) à pH7 (nm)	Longueur d'onde d'émission (λem) à pH7 (nm)	Référence
mPlum	590	649	Wang *et al*., 2004
mRaspberry	598	625	Wang *et al*., 2004
mNeptune	600	650	Lin *et al*., 2009
NirFP	605	670	Shcherbo *et al*., 2010
TagRFP657	611	657	Morozova *et al*., 2010
TagFRP675	598	675	Piatkevich *et al*., 2013
mCardinal	604	659	Chu *et al*., 2014
iFP1.4	684	713	Shu *et al*., 2009
iFP713 (iRFP)	690	708	Filonov *et al*., 2011
iRFP670	643	670	Shcherbakova *et al*., 2013
iRFP682	663	682	Shcherbakova *et al*., 2013
iRFP702	673	702	Shcherbakova *et al*., 2013
iRFP720	702	720	Shcherbakova *et al*., 2013
iFP2.0	690	711	Yu *et al*., 2014
mIFP	683	704	Yu *et al*., 2015
Fluorescence cyan émise (CFPs)			
ECFP	433	475	Heim *et al*., 1994
mCFPm	433	475	Zacharias *et al*., 2002
Cerulean	433	475	Rizzo *et al*., 2004
mCerulean3	433	475	Markwardt *et al*., 2011
SCFP	433	474	Kremers *et al*., 2006
SCFP3A	433	474	Kremers et al., 2006
CyPet	435	477	Nguyen *et al*., 2005
mTurquoise	434	474	Goedhardt *et al*., 2010
mTurquoise 2	434	474	Goedhardt *et al*., 2012
TagCFP	458	480	Xia *et al*., 2002
AmCyan	458	489	Matz *et al*., 1999
mTFP1	462	492	Ai *et al*., 2006
Midoriishi cyan	470	496	Karasawa *et al*., 2004
Aquamarine	430	474	Erard *et al*., 2013
Fluorescence bleue émise (BFPs)			
EBFP	380	460	Yang *et al*., 1998
EBFP2	383	448	Ai *et al*., 2007
Azurite	383	450	Mena *et al*., 2006

Protéine fluorescente	Longueur d'onde d'excitation (λex) à pH7 (nm)	Longueur d'onde d'émission (λem) à pH7 (nm)	Référence
mKalama1	385	456	Ai *et al*., 2007
TagBFP	402	457	Subach *et al*., 2008
mTagBFP	399	456	Subach *et al*., 2008
mTagBFP2	399	454	Subach *et al*., 2011
Sirius	355	424	Tomosugi *et al*., 2009
Fluorescence jaune émise (YFPs)			
EYFP	513	527	Orm *et al*., 1996
TagYFP	508	524	Xia *et al*., 2002
TurboYFP	525	538	Shagin *et al*., 2004
ZsYellow	529	539	Matz *et al*., 1999
PhiYFP	525	537	Shagin *et al*., 2004
Topaz	514	527	Han *et al*., 2002
Venus	515	528	Nagai *et al*., 2002
SYFP2	515	527	Kremers *et al*., 2006
Citrine	516	529	Griesbeck *et al*., 2001
mCitrine	516	529	Griesbeck *et al*., 2001
Ypet	517	530	Nguyen *et al*., 2005
SYFP	515	527	Kremers *et al*., 2006
IanFRP-ΔS83	521	592	Pletnev *et al*., 2013
mPapaya1	530	541	Hoi *et al*., 2013
mAmetrine	406	526	Ai *et al*., 2008b

Les protéines fluorescentes particulièrement préférées selon l'invention sont les protéines fluorescentes vertes et les protéines fluorescentes rouges, et plus particulièrement EGFP et mCherry, respectivement. L'EGFP est la protéine fluorescente la plus préférée de l'invention, elle permet un repliement de la protéine plus rapide et une excitation à 488nm, permettant l'usage d'un laser Argon.

Les marqueurs fluorescents de nature non-protéique sont également bien connus de l'homme du métier, et sont disponibles commercialement. Il s'agit généralement de petites molécules, dont le poids moléculaire peut varier typiquement de 200 à 1000 Daltons, et qui sont donc de taille inférieure à celle des protéines fluorescentes susmentionnées.

Des exemples de tels marqueurs fluorescents non protéiques incluent, sans limitation, le DiBAC (bis-(1,3-dibutylbarbituric acid) trimethine oxonol) et ses dérivés (Haupt *et al*., 2014), les dérivés de xanthène tels que la fluorescéine et l'isothyocyanate de fluorescéine (FITC), les rhodamines (e.g. rhodamine 110, rhodamine 123, rhodamine 5 GLD, rhodamine 6G, rhodamine B, rhodamine B 200, rhodamine B extra, rhodamine BB, rhodamine BG, rhodamine green, rhodamine red, rhodamine *wt*) et ses dérivés (e.g. tétraméthyl rhodamine isothyocyanate plus connu sous le nom de TRITC, 6-carboxyrhodamine 6G, X-rhodamine), les oregon green (e.g. oregon green 488, oregon green 500, oregon green 514), l'éosine, et le Texas red; les dérivés de cyanine tels que l'indocarbocyanine (Cy3) et son dérivé Cy3.18, l'indodicarbocyanine (Cy5) et ses dérivés Cy 5.5. et Cy5.18, l'indotricarbocyanine (Cy7) l'oxacarbocyanine (Cy2), la thiacarbocyanine, et la mérocyanine; les dérivés de squaraine ; les dérivés de naphthalène tels que le dansyl (e.g. 5-(dimethylAmino)naphthalene-1-sulfonyl chloride ou -sulfonamide) et prodan (N,N-dimethyl-6-propionyl-2-naphthylamine); les dérivés de coumarine tels que l'amino-coumarine, la 7-hydroxy-4méthyl-coumarine, la 7-amino-4méthyl-coumarine, et la méthyl-coumarine ; les dérivés d'oxadiazole tels que le pyridyloxazole, et le nitrobenzoxadiazole; les dérivés de pyrène tels que le marqueur cascade blue ; les dérivés d'oxazine tels que les marqueurs Nile red, et oxazine 170; et les dérivés d'arylméthine tels que l'auramine. Les marqueurs fluorescents non protéiques de l'invention incluent également les marqueurs commercialisés AlexaFluor, Fluoprobes, Dyelight, Seta, SeTau et SRFluor. Les marqueurs AlexaFluor sont ici particulièrement préférés ; ils incluent, sans limitation, les marqueurs AlexaFluor 350, 405, 430, 488, 500, 514, 532, 546, 568, 594, 610, 633, 647, 660, 680, 700, 750 et 790.

Le tableau 2 ci-après répertorie les marqueurs fluorescents non protéiques de l'invention, avec leurs longueurs d'onde d'excitation et d'émission.

Tableau 2. Marqueurs fluorescents non protéiques selon l'invention

Marqueur fluorescent non protéique	Longueur d'onde d'excitation (λex) à pH7 (nm)	Longueur d'onde d'émission (λem) à pH7 (nm)	Référence
DiBAC	490	516	CAS#1779-25-5; Haupt *et al*., 2014
fluorescéine	494	512	CAS#2321-07-5
FITC	495	512	CAS#3326-32-7
rhodamine 110	496	520	CAS#13558-31-1
rhodamine 123	511	534	CAS#62669-70-9
rhodamine 5 GLD	470	565	Chemical Book #CB2116215 Pylam products company, Inc.
rhodamine 6G	526	555	CAS#989-38-8
rhodamine B	540	625	CAS#81-88-9
rhodamine B 200	523-557	595	CAS#3520-42-1
rhodamine B extra	550	605	CAS#81-88-9
rhodamine BB	540	580	CAS#509-34-2
rhodamine BG	540	572	CAS#12220-18-7
rhodamine green	502	527	CAS#189200-71-3
rhodamine red	570	590	ThermoFisher Scientific #S6366
rhodamine *wt*	530	555	CAS#37299-86-8
TRITC	557	576	CAS#80724-20-5
6-carboxyrhodamine 6G	525	547	Shanghai DiBai Chemicals Co., Ltd.
X-rhodamine	580	605	CAS # 198978-94-8
oregon green 488	496	524	CAS#195136-58-4
oregon green 500	503	522	Fritz *et al*., 2009
oregon green 514	511	530	ThermoFisher Scientific #D7176
Éosine Y	525	545	CAS#17372-87-1
Texas red	596	615	CAS#82354-19-6
indocarbocyanine (Cy3)	550	570	CAS#146397-20-8
Cy3.18	554	568	Mujumdar *et al*.,

Marqueur fluorescent non protéique	**Longueur d'onde d'excitation (λex) à pH7 (nm)**	**Longueur d'onde d'émission (λem) à pH7 (nm)**	**Référence**
			1993
indodicarbocyanine (Cy5)	640	660	CAS#146368-14-1
Cy5.5	675	695-700	CAS#172777-84-3
Cy5.18	649	666	Mujumdar *et al*., 1993
indotricarbocyanine (Cy7)	710	805	CAS#943298-08-6
oxacarbocyanine (Cy2)	494	512	CAS#260430-02-2
thiacarbocyanine	545	570	CAS#905-97-5
mérocyanine	530	580	CAS#58823-12-4
dérivés de squaraine	630-670	650-700	Cornellissen-Gude *et al*., 1997
Dansyl chloride	340	578	CAS#605-65-2
prodan	360	520	CAS#70504-01-7
amino-coumarine	350	445	CAS#19063-57-1
7-hydroxy-4méthyl-coumarine	360	455	Sherman *et al.*, 1968
7-amino-4méthyl-coumarine	351	430	CAS#26093-31-2
méthylcoumarine	384	469	CAS#92-48-8
pyridyloxazole	410	550–570	CAS#74718-16-4
nitrobenzoxadidole	460-470	510-650	Herman, 2001
cascade blue	400	425	CAS#61725-40-4
Nile red	515-530	525-605	CAS#7385-67-3
oxazine 170	625	550-580	CAS#62669-60-7
auramine	460	550	CAS#2465-27-2
AlexaFluor 350	346	442	CAS#244636-14-4
AlexaFluor 405	401	421	CAS#467233-94-9
AlexaFluor 430	431	540	ThermoFisher Scientific #A10169
AlexaFluor 488	495-492	519-520	CAS#247144-99-6
AlexaFluor 500	503	525	CAS#798557-08-1
AlexaFluor 514	517	542	CAS#798557-07-0
AlexaFluor 532	531-532	553-554	CAS#247145-11-5
AlexaFluor 546	556-557	572-573	CAS#247145-23-9

Marqueur fluorescent non protéique	Longueur d'onde d'excitation (λex) à pH7 (nm)	Longueur d'onde d'émission (λem) à pH7 (nm)	Référence
AlexaFluor 568	577-578	603	CAS#247145-38-6
AlexaFluor 594	590-594	617-618	CAS#247145-86-4
AlexaFluor 610	610	629	CAS#900528-62-3
AlexaFluor 633	632	650	CAS#477780-06-6
AlexaFluor 647	647	666	CAS#400051-23-2
AlexaFluor 660	668	698	CAS#422309-89-5
AlexaFluor 680	679	702	CAS#422309-67-9
AlexaFluor 700	696	719	CAS#697795-05-4
AlexaFluor 750	752	776	CAS#697795-06-5
AlexaFluor 790	782	804	CAS#950891-33-5

Les marqueurs fluorescents non protéiques particulièrement préférés selon l'invention sont AlexaFluor 647, Alexa Fluor 594, TRITC, FITC, et DiBAC, plus préférablement AlexaFluor 647, TRITC et DiBAC (qui a l'avantage de se lier à la membrane cellulaire), et encore plus préférablement AlexaFluor 647 et TRITC. En effet, le marqueur DiBAC a l'avantage de s'insérer spécifiquement dans la membrane plasmique de la cellule à paroi, sans nécessité de couplage à une autre molécule ; tandis que les marqueurs de type AlexaFluor et TRITC sont des fluorophores brillants ayant une bonne stabilité temporelle.

Tel qu'indiqué ci-dessus, le premier et le second marqueur luminescent doivent être sélectionnés de sorte que la longueur d'émission de leur radiation lumineuse soit distincte, ceci afin de pouvoir différentier la face externe de la face interne de la paroi à l'aide du dispositif optique de l'invention.

De manière préférée, un des marqueurs luminescents est sélectionné parmi la protéine fluorescente verte EGFP et le DiBAC, tandis que l'autre marqueur luminescent est sélectionné parmi AlexaFluor 647 et AlexaFluor 594, ces marqueurs ayant permis de différencier avec succès les deux faces de la paroi.

De manière encore préférée, le premier marqueur luminescent (i.e. marquant la face externe de la paroi) est sélectionné parmi la protéine fluorescente verte EGFP et le DiBAC, tandis que le second marqueur luminescent (i.e. marquant la face interne de la paroi) est sélectionné parmi AlexaFluor 647 et AlexaFluor 594, ces marqueurs ayant permis de différencier avec succès la face externe de la face interne de la paroi.

Une fois que la sélection des marqueurs de l'invention est opérée, le marquage de la paroi cellulaire peut être effectué de différentes manières selon la nature desdits marqueurs : en modifiant génétiquement la cellule de sorte que celle-ci exprime par exemple une protéine fluorescente de l'invention sur l'une ou l'autre des faces de sa paroi, et/ou en conjuguant l'un des marqueurs luminescents de l'invention (de nature protéique ou non protéique) à une molécule capable de se lier à l'une ou l'autre face de la paroi, à une molécule faisant partie intégrante de ladite face, voire même en utilisant un marqueur capable de s'ancrer directement dans l'une ou l'autre face de sa paroi.

L'homme du métier est à même de réaliser ce type de marquage, à l'aide de techniques bien connues de biologie moléculaire et/ou de conjugaison physicochimique (Sambrook *et al*., 2012; Wong *et al.*, 2011; Hermanson, 2013).

Selon un mode de réalisation préféré, le premier marqueur luminescent est couplé à une molécule capable de se lier à la face externe de la paroi cellulaire.

Par « couplé », ou « conjugué », on entend ici que le marqueur luminescent est lié à ladite molécule, de manière directe ou indirecte, par tout moyen approprié, par exemple par tout moyen biologique ou physicochimique. Cette liaison est en outre préférablement covalente, de sorte que la liaison entre ledit marqueur et ladite molécule confère un marquage stable pour imager la cellule.

Si le marqueur luminescent, en particulier fluorescent, et ladite molécule sont tous deux de nature protéique, ledit marqueur peut être préférablement directement lié à ladite molécule, en formant par exemple une protéine de fusion avec ladite molécule. Une telle protéine de fusion peut être produite par des techniques d'ingénierie par recombinaison et des techniques d'expression dans des microorganismes appropriés (Sambrook *et al*., 2012).

De manière alternative, et ce quel que soit la nature protéique ou non protéique du marqueur et/ou de ladite molécule, ledit marqueur pourra être lié de manière indirecte à ladite molécule, par exemple par l'intermédiaire d'un « espaceur ». Par « espaceur », on entend ici tout agent chimique ou biologique, naturel ou synthétique, capable de coupler deux molécules entre elles. Les espaceurs dits chimiques sont bien connus de l'homme du métier, et sont typiquement des chaînes de polymères de longueur variée, comprenant des groupes réactifs et au moins un atome, préférablement au moins un atome de carbone. Les espaceurs dits biologiques sont quant à eux typiquement des séquences d'acides nucléiques et/ou d'acides aminés de longueur variée, comprenant au moins un acide nucléique et/ou un acide aminé. Ces espaceurs, et les méthodes de couplage ont été décrites de manière extensive dans la littérature, notamment par Chen *et al.* (2013)

ainsi que dans Thermo Scientific: Crosslinking Technical Handbook (2015).

Par « molécule capable de se lier à la face externe de la paroi cellulaire », on entend désigner ici toute molécule, naturelle ou synthétique, qui présente une affinité pour la face externe de la paroi cellulaire et est donc capable de se lier à celle-ci. L'affinité d'une molécule envers une cible d'intérêt peut être évaluée en mesurant la constante de dissociation Kd et/ou la constante d'association Ka tel que notamment décrit par Wild (2013).

De manière préférée, la molécule capable de se lier à la face externe de la paroi cellulaire est une lectine. Les lectines sont des protéines qui se lient spécifiquement à certaines structures oligosaccharidiques (Horisberger *et al.*, 1985). Les Inventeurs ont ici découvert que de telles lectines peuvent être utilisées pour lier le premier marqueur luminescent de l'invention aux polysaccharides, et/ou aux peptides/protéines glycosylé(e)s présents dans la paroi cellulaire de la cellule étudiée.

Des exemples de lectines pouvant être utilisées dans le contexte de la présente invention, incluent, sans limitation, les lectines se liant spécifiquement aux motifs de type galactose et/ou à la N-acétylgalactosamine telles que les lectines GS-I (lectines de *Griffonia simplicifolia* incluant GS-IB4, GS-IA4, GS-IA3B, GS-IA2B2, et GS-IAB3), RCA (également connue sous le nom de ricine, phytoagglutinine, toxoalbumine ou RCA120), PNA (lectine d'arachide), SBA (lectine de soja), DBA (lectine de Dolichos), MPA (lectine d'oranger des osages), AIL (Jacaline), BPA (lectine d'arbre d'orchidée), et VVL (lectine de vesce velue); les lectines se liant spécifiquement à l'acide sialique et/ou à la N-acétylglucosamine telles que les lectines WGA (lectine du blé), GS-II (lectine de *Griffonia simplicifolia*), SNA (lectine du sureau), et MAL (lectine de *Maackia amurensis*); les lectines se liant spécifiquement au mannose telles que les lectines ConA (Concanavaline A), LCH (lectine de lentille), et GNA (lectine de perce-neige) ; et les lectines se liant spécifiquement au fucose telles que les lectines UEA (lectine de l'ajonc), et AAL (lectine d'*Aleuria aurantia*). Ces lectines sont disponibles dans le commerce, optionnellement liées à un marqueur fluorescent qui est de nature non protéique, tels que ceux décrits dans le tableau 2 ci-dessus (e.g. AlexaFluor, FluoProbes, etc).

Le tableau 3 ci-après répertorie les lectines de l'invention, et leurs propriétés.

Tableau 3. Lectines selon l'invention

Lectine	Organisme d'origine	Motif du ligand préféré	Référence
Affinité pour les motifs de type galactose et/ou N-acétylgalactosamine			
GS-IB4	*Griffonia simplicifolia*	α-D-galactosyl	Sigma Aldrich #L2380 (*); ThermoFisher Scientific #I32450 (*)
GS-IA4	*Griffonia simplicifolia*	N-acetyl-D-galactosamine	Wu *et al.*,1996 (*)
GS-IA3B	*Griffonia simplicifolia*	N-acetyl-D-galactosamine; α-D-galactosyl	voir ci-dessus (*)
GS-IA2B2	*Griffonia simplicifolia*	N-acetyl-D-galactosamine; α-D-galactosyl	voir ci-dessus (*)
GS-IAB3	*Griffonia simplicifolia*	résidus α-D-galactosyl ; N-acetyl-D-galactosamine	voir ci-dessus (*)
RCA	*Ricinus communis*	Galβ1-4GlcNAcβ1-R	Sigma Aldrich #L7886
PNA	*Arachis hypogaea*	Galβ1-3GalNAcα1-Ser/Thr	Chacko *et al.*, 2001
SBA	*Glycine max*	N-acetyl- D -galactosamine	Sigma Aldrich #L2650
DBA	*Dolichos Biflorus*	N-acetyl-D-galactosamine	Hormia *et al.*,1988
MPA	*Maclura pomifera*	alpha-galactose	Kresch *et al.*, 1991
AIL	*Artocarpus integrifolia*	(Sia)Galβ1-3GalNAcα1-Ser/Thr	Sastry *et al.*, 1986
BPA	*Bauhinia purpurea*	N-acetyl-D-galactosamine and D-galactose	Sigma Aldrich #L6013
VVL	*Vicia villosa*	GalNAcα-Ser/Thr	Vector Laboratories #B-1235
Affinité pour les motifs de type acide sialique et/ou N-acétylglucosamine			
WGA	*Triticum vulgaris*	GlcNAcβ1-4GlcNAcβ1-4GlcNAc ; Neu5Ac (acide sialique)	Sigma Aldrich #L9640
GS-II	*Griffonia simplicifolia*	N-acetylglucosamine	Zhu *et al.*,1996
SNA	*Sambucus nigra*	Neu5Acα2-6Gal(NAc)-R	Sigma Aldrich #L6890
MAL	*Maackia amurensis*	Neu5Ac/Gcα2-3Galβ1-4GlcNAcβ1-R	Sigma Aldrich #L8025

Affinité pour les motifs de type mannose			
ConA	*Canavalia ensiformis*	α-D-mannosyl et α-D-glucosyl ; structures ramifiées d'α-mannosyl (type riche en α-mannose, ou type hybride et bi-antennaire de N-Glycans complexes)	Sigma Aldrich #C2272
LCH	*Lens culinaris*	région de base fucosylée des N-Glycans complexes bi- et tri-antennaires	Sigma Aldrich #L9267
GNA	*Galanthus nivalis*	Mannose	Barre *et al*.,2001
Affinité pour les motifs de type fucose			
EAU	*Ulex europaeus*	Fucα1-2Gal-R	Vector Laboratories #B-1065
AAL	*Aleuria aurantia*	Fucα1-2Galβ1-4(Fucα1-3/4)Galβ1-4GlcNAc ; R2-GlcNAcβ1-4(Fucα1-6)GlcNAc-R1	Fujihashi *et al*.,2003

Les lectines citées dans le tableau 3 ci-dessus peuvent se lier à la paroi cellulaire de tout type de cellule à paroi choisie dans le groupe des champignons, des bactéries, des archées, des plantes et des algues, selon le type de motifs de sucre présent à la surface de ladite cellule.

Les lectines particulièrement préférées selon l'invention sont les lectines GS-IB4 et WGA, pour lesquelles le marquage de la face externe de la paroi a été réalisé avec succès par les Inventeurs pour les cellules de champignons tels que *Schyzosaccharomyces pombe* et *Candida albicans*, respectivement.

De manière encore préférée, le premier marqueur luminescent est le marqueur fluorescent AlexaFluor 647 couplé à la lectine GS-IB4, ou le marqueur fluorescent AlexaFluor 594 couplé à la lectine WGA, pour lesquels le marquage de la face externe de la paroi a été réalisé avec succès par les Inventeurs pour les cellules champignons tels que *Schyzosaccharomyces pombe* et *Candida albicans*, respectivement.

Le premier marqueur luminescent peut être préférablement apporté à la cellule de manière externe à ladite cellule, lorsque celui-ci est couplé à une molécule capable de se lier à la face externe de la paroi cellulaire. Ainsi, la cellule à imager n'a pas à être génétiquement modifiée pour exprimer ledit premier marqueur.

Pour ce faire, la cellule à paroi est préférablement placée dans un dispositif de culture comprenant le premier marqueur luminescent. De manière encore préférée, ledit dispositif est préférablement alimenté en continu avec ledit premier marqueur luminescent.

Ce dispositif de culture peut être par exemple une plaque d'agar, c'est-à-dire un milieu de culture cellulaire gélosé, contenant le premier marqueur luminescent ; ou une chambre microfluidique dans laquelle est apporté, préférablement en continu, un milieu de culture cellulaire contenant le premier marqueur luminescent. Ces dispositifs de culture sont bien connus de l'homme du métier (Weibel *et al.*, 2007; Charvin *et al*., 2008).

Un dispositif de culture particulièrement préféré selon l'invention est la chambre microfluidique. Celle-ci permet en effet un approvisionnement constant du marqueur luminescent de l'invention lorsque celui-ci est couplé à une molécule capable de se lier à la face externe de la paroi, et par conséquent d'observer la radiation lumineuse dudit marqueur sur une longue période de temps.

La concentration du premier marqueur luminescent de l'invention dans le milieu de culture dudit dispositif peut être préférablement comprise entre environ 0,10 µg/mL et environ 100 µg/mL, plus préférablement entre environ 0,25 µg/mL et environ 50 µg/mL, plus préférablement entre environ 0,50 µg/mL et environ 25 µg/mL, et encore plus préférablement entre environ 1 µg/mL et environ 10 µg/mL. De manière préférée entre toutes, ladite concentration du premier marqueur luminescent dans ledit milieu est d'environ 5 µg/mL.

Selon un mode de réalisation préféré, le second marqueur luminescent (i.e. marquant la face interne de la paroi) est couplé à une protéine de la membrane cellulaire, ou à une molécule capable de se lier à la membrane cellulaire, ou est capable de se lier à la membrane cellulaire.

Les définitions données ci-avant concernant le couplage de molécules s'appliquent pour le second marqueur luminescent *mutatis mutandis*.

Par « membrane cellulaire », on entend désigner ici la structure cellulaire constituée de lipides qui sépare le milieu intracellulaire de la paroi cellulaire, et qui est généralement juxtaposée à cette dernière. Cette membrane est plus connue sous le nom de membrane plasmique chez les champignons, archées, plantes et bactéries, sauf chez les bactéries Gram négatives où elle est qualifiée de membrane interne. Il est entendu que ce terme se

réfère ici à la membrane cellulaire de la cellule à imager.

Par « protéine de la membrane cellulaire », on entend désigner ici toute protéine faisant naturellement partie intégrante de ladite membrane.

Dans le cadre de la présente invention, la protéine de la membrane cellulaire est préférablement sélectionnée dans le groupe constituée par les protéines membranaires de champignons telles que Psy1, Pma1, Syb1, Pom1, Mod5 et leurs homologues ; les protéines membranaires des bactéries telles que PhoE, ScryY, BtuB, FhuA, OmpA, OmpT, NaIP, OmPIA, FadL et leurs homologues ; les protéines membranaires d'archées telles que Rho, ArtA, Sec11a, Sec11b, FtsY et leurs homologues ; les protéines membranaires de plantes telles que BP-80 (VSR1), PRK1, PRK2, SCAMPs (e.g. SCAMP1) et leurs homologues ; et les protéines membranaires d'algues telles que Toc159, prostaglandines (e.g. PGE2) et leurs homologues.

Par « homologue », on entend ici une protéine présentant une homologie de structure. L'homme du métier est à même d'identifier les homologues des protéines susmentionnées, en fonction de l'espèce cellulaire imagée, en effectuant par exemple une recherche d'homologie de séquence.

Le tableau 4 ci-après répertorie les protéines membranaires de l'invention.

Tableau 4. Protéines membranaires selon l'invention

Cellule de l'invention	Protéine membranaire	Exemples de Référence (UniProtKB; espèce cellulaire)
champignons	Psy1	Q9USH7 (*Schyzosaccharomyces pombe*)
	Pma1	P09627 (*Schyzosaccharomyces pombe*)
	Syb1	Q92356 (*Schyzosaccharomyces pombe*)
	Pom1	Q09690 (*Schyzosaccharomyces pombe*)
	Mod5	O59740 (*Schyzosaccharomyces pombe*)
bactéries	PhoE	Q01605 (*Citrobacter freundii*)
	ScrY	W9B4Y7 (*Klebsiella pneumoniae*)
	BtuB	O52903 (*Citrobacter freundii*)
	FhuA	R4Y5U8 (*Klebsiella pneumoniae*)
	OmpA	K0BWP3 (*Pasteurella multocida*)
	OmpT	A0A0K0PL05 (*Escherichia coli*)
	OmPIA	Q9Z4N8 (*Enterobacter agglomerans*)
	FadL	B3G3J3 (*Vibrio alginolyticus*)
archées	Rho	B7A688 (*Thermus aquaticus*)
	ArtA	D4GUZ4 *(Haloferax volcanii)*

Cellule de l'invention	Protéine membranaire	Exemples de Référence (UniProtKB; espèce cellulaire)
	Sec11a	D4GUC5 *(Haloferax volcanii)*
	Sec11b	D4GYJ8 *(Haloferax volcanii)*
	FtsY	P83749 (*Thermus aquaticus*)
plantes	BP-80 (VSR1)	P93026 (*Arabidopsis thaliana*)
	PRK1	C0LGU0 (*Arabidopsis thaliana*)
	PRK2	Q84JQ4 (*Arabidopsis thaliana*)
	SCAMP1	Q9SKT3 (*Arabidopsis thaliana*)
algues	Toc159	- (*Laminaria japonica*)
	PGE2	- *(Laminaria japonica*)

La protéine membranaire particulièrement préférée selon l'invention est la protéine Psy1 et ses homologues, le marquage de la membrane cellulaire ayant été réalisé avec succès par les Inventeurs avec cette protéine pour les cellules de champignons tels que *Schyzosaccharomyces pombe*.

L'homme du métier comprendra aisément que, lorsqu'une protéine membranaire est utilisée pour le marquage de la face interne de la paroi, le second marqueur luminescent est préférablement une protéine fluorescente, telle que décrite ci-dessus. Ledit marqueur et ladite protéine membranaire peuvent ainsi être préférablement sous la forme d'une protéine de fusion, qui peut être produite par des techniques d'ingénierie par recombinaison bien connues dans l'art, puis exprimée directement dans la cellule de l'invention par des techniques d'expression conventionnelles (Sambrook ***et al.***, 2012). Selon ce mode de réalisation, la cellule de l'invention est ainsi génétiquement modifiée avec ladite protéine de fusion.

De manière encore préférée, le second marqueur luminescent est la protéine fluorescente EGFP couplée à la protéine Psy1 ou à l'un de ses homologues, ou la protéine fluorescente mCherry couplée à la protéine Psy1 ou à l'un de ces homologues, le marquage de la membrane cellulaire ayant été réalisé avec succès par les Inventeurs pour les cellules de champignons tels que *Schyzoaccharomyces pombe*. Les Inventeurs ont en effet observé que ces marqueurs luminescents émettent une radiation lumineuse forte et homogène, facile à imager. De manière préférée entre toutes, le second marqueur luminescent est la protéine fluorescente GFP couplée à la protéine Psy1, en particulier pour imager les cellules de champignons tels que *Schyzosaccharomyces pombe.*

De manière alternative, tel qu'indiqué ci-dessus, le second marqueur luminescent peut être couplé à une molécule capable de se lier à la membrane cellulaire.

Par « molécule capable de se lier à la membrane cellulaire », on entend désigner ici toute molécule, naturelle ou synthétique, qui présente une affinité pour la membrane cellulaire et est donc capable de se lier à celle-ci.

De manière préférée, la molécule capable de se lier à la membrane cellulaire est un polypeptide comprenant ou consistant en au moins un domaine de liaison aux lipides. Ces domaines de liaison aux lipides sont en effet hydrophobes et chargés, et peuvent donc s'ancrer directement dans les lipides de la membrane.

Des exemples de domaine de liaison aux lipides pouvant être préférablement utilisés dans le cadre de la présente invention, incluent, sans limitation, les domaines CaaX (où a est un acide aliphatique et X est n'importe quel acide aminé) (SEQ ID NO :1) tel que le domaine de séquence SEQ ID NO :2 , les domaines de myristoylation tels que le domaine de séquence SEQ ID NO :3, les domaines PH (« Pleckstrin homology ») tels que ceux de référence Pfam PF00169, les domaines BAR (Bin1/Amphiphysin/Rsv167) tels que ceux de référence Pfam PF03114, les domaines FYVE (Fab1, YOTB, Vac1, EEA1) tels que ceux de référence Pfam PF01363, les domaines PX (se liant aux phosphoinositides) tels que ceux de référence Pfam PF00787, et les domaines ENTH (« Epsin N-Terminal Homology ») tels que ceux de référence Pfam PF01417. L'homme du métier est à même d'identifier les polypeptides comprenant ces domaines de liaison, par exemple à l'aide de la base de données Pfam, et/ou de la base de données CGDB, toutes deux disponibles sur internet (Hurley et al., 2000).

Le tableau 5 ci-après répertorie les domaines de liaison aux lipides de l'invention.

Tableau 5. Domaines de liaison aux lipides selon l'invention

Exemples de domaine de liaison aux lipides	Exemples de protéine contenant ce domaine	Référence (Pfam)	Cellule de l'invention
CaaX (SEQ ID NO:1)			
SEQ ID NO:2	Cdc42	-	champignons, plantes, algues
myristoylation			
SEQ ID NO:3	MARCKS	-	champignons, plantes, algues, bactéries
PH			
-	Bem2	PF00169	champignons, plantes,algues,Bactéries
BAR			
-	Cdc15	PF03114	champignon, plantes, algues
Exemples de domaine de liaison aux lipides	**Exemples de protéine contenant ce domaine**	**Référence (Pfam)**	**Cellule de l'invention**
FYVE			
-	ZFYVE1	PF01363	champignons, plantes, algues, bactéries, archées
PX			
-	NCF1	PF00787	champignons, plantes, algues
ENTH			
-	EPN1	PF01417	champignons, plantes, algues

Le domaine de liaison particulièrement préféré selon l'invention est le domaine de liaison CaaX, le marquage de la face interne de la paroi ayant été réalisé avec succès par les Inventeurs avec un polypeptide comprenant ce domaine pour les cellules de champignons tels que *Candida albicans*, en particulier avec le polypeptide Rac1.

L'homme du métier comprendra aisément que, lorsqu'un polypeptide comprenant ou consistant en au moins un domaine de liaison aux lipides est utilisé pour le marquage de la face interne de la paroi, le second marqueur luminescent est préférablement une protéine fluorescente, telle que décrite ci-dessus. Ledit marqueur et ledit polypeptide peuvent ainsi être préférablement sous la forme d'une protéine de fusion, qui peut être produite par des techniques d'ingénierie par recombinaison bien connues dans l'art, puis exprimée directement dans la cellule de l'invention par des techniques d'expression conventionnelles (Sambrook *et al*., 2012). Selon ce mode de réalisation, la cellule de l'invention est ainsi génétiquement modifiée avec ladite protéine de fusion.

De manière encore préférée, le second marqueur luminescent est la protéine fluorescente EGFP couplée au domaine C-terminal de la protéine Rac1 (i.e. CtRac1, de séquence SEQ ID NO :4), le marquage de la face interne de la paroi ayant été réalisé avec succès par les Inventeurs pour les cellules de champignons tels que *Candida albicans*.

De manière encore alternative, tel qu'indiqué ci-dessus, le second marqueur luminescent peut être capable de se lier à la membrane cellulaire.

En d'autres termes, un tel marqueur ne nécessite pas d'être couplé à une quelconque autre molécule pour se lier à la membrane cellulaire. Des exemples de marqueurs luminescents capables de se lier à la membrane cellulaire incluent, sans limitation, le DiBAc (bis-(1,3-dibutylbarbituric acid) trimethine oxonol) et ses dérivés tels que décrits dans le tableau 2 ci-dessus.

Le second marqueur luminescent peut être préférablement apporté à la cellule de manière externe à ladite cellule, lorsque celui-ci est capable de se lier lui-même à la membrane cellulaire. Ainsi, la cellule à imager n'a pas à être génétiquement modifiée pour exprimer ledit second marqueur.

Pour ce faire, la cellule à paroi est préférablement placée dans un dispositif de culture comprenant le second marqueur luminescent. De manière encore préférée, ledit dispositif est préférablement alimenté en continu avec ledit second marqueur luminescent.

Ce dispositif de culture peut être par exemple une plaque d'agar, c'est-à-dire un milieu de culture cellulaire gélosé, contenant le second marqueur luminescent ; ou une chambre microfluidique dans laquelle est apporté, préférablement en continu, un milieu de culture cellulaire contenant le second marqueur luminescent.

Un dispositif de culture particulièrement préféré selon l'invention est la chambre microfluidique. Celle-ci permet en effet un approvisionnement constant du marqueur luminescent de l'invention lorsque celui-ci est capable de se lier lui-même à la face interne de la paroi, et par conséquent d'observer la radiation lumineuse dudit marqueur

sur une longue période de temps.

La concentration du second marqueur luminescent de l'invention dans le milieu de culture dudit dispositif peut être préférablement comprise entre environ 0,05 µg/mL et environ 500 µg/mL, plus préférablement entre environ 0,5 µg/mL et environ 50 µg/mL, plus préférablement entre environ 1 µg/mL et environ 5 µg/mL. De manière préférée entre toutes, ladite concentration du premier marqueur luminescent dans ledit milieu est d'environ 2,5 µg/mL.

Selon un mode de réalisation préféré, le premier et le second marqueur luminescent sont apportés à la cellule de manière externe à ladite cellule, lorsque ceux-ci sont respectivement couplés à une molécule capable de se lier à la face externe de la paroi et capable de se lier directement à la membrane cellulaire.

Selon un mode de réalisation particulièrement préféré de l'invention : la cellule à paroi est un champignon, préférablement *Schyzosaccharomyces pombe* ou *Candida albicans* ; le premier marqueur luminescent (i.e. marquant la face externe de la paroi) est un marqueur fluorescent couplé à une lectine, préférablement AlexaFluor 647 couplé à la lectine GS-IB4 ou AlexaFluor 594 couplé à la lectine GS-IB4 ; et le second marqueur luminescent (i.e. marquant la face interne de la paroi) est un marqueur fluorescent couplé à une lectine, préférablement la protéine fluorescente EGFP couplée à Psy1 ou à CtRac1.

Par exemple, la cellule à paroi est *Schyzosaccharomyces pombe* ; le premier marqueur luminescent est AlexaFluor 647 couplé à la lectine GS-IB4 ; et le second marqueur luminescent est la protéine fluorescente EGFP couplée à Psy1.

Alternativement, la cellule à paroi est *Candida albicans* ; le premier marqueur luminescent est AlexaFluor 594 couplé à la lectine GS-IB4 ; et le second marqueur luminescent est la protéine fluorescente EGFP couplée à CtRac1.

L'analyse de l'image de la cellule à paroi obtenue par le dispositif optique à haute-résolution peut être effectuée en détectant la radiation lumineuse émise par les marqueurs de l'invention, en chaque point du contour de la cellule.

Ainsi selon un mode de réalisation préféré, l'étape c) de détermination de la distance entre le premier marqueur et le second marqueur comprend :

i) détecter, dans une direction perpendiculaire à la tangente à la paroi cellulaire en un point de ladite paroi, un premier maximum de radiation lumineuse dans ladite première gamme de longueur d'onde et un second maximum de radiation lumineuse dans ladite seconde gamme de longueur d'onde, la distance entre le premier et le second marqueur en ce point étant définie comme la distance entre le premier et le second maximum de radiation lumineuse ; et

ii) optionnellement, répéter l'étape i) en une pluralité de points de la paroi cellulaire.

A cet effet, en chaque point du contour de la cellule correspondant à un pixel, est définie la tangente au contour de la cellule ainsi que la direction perpendiculaire à ladite tangente.

Pour chacune des deux gammes de longueur d'onde émises par les marqueurs de l'invention, l'intensité de la radiation lumineuse dans la gamme de longueur d'onde est mesurée le long d'un segment ayant une direction perpendiculaire à ladite tangente. Le segment a une taille modulable, mais qui est généralement fixée à 4 µm (93 px).

Pour détecter un maximum de l'intensité de la radiation lumineuse dans la gamme de longueur d'onde, l'intensité de la radiation lumineuse dans la gamme de longueur d'onde est préférablement modélisée sous la forme d'une gaussienne. Le maximum de radiation lumineuse dans la gamme de longueur d'onde est défini comme le maximum de la gaussienne. Les première et seconde gammes de longueur d'onde peuvent par exemple être celles telles que définies ci-dessus.

L'épaisseur de la paroi locale, qui correspond à la distance entre le premier et le second marqueur en ce point est définie comme la distance entre le premier et le second maximum de radiation lumineuse.

Le procédé d'analyse d'image permet ainsi une mesure de l'épaisseur de la paroi résolue au pixel près, c'est-à-dire avec une précision de plus ou moins 10 nm.

L'étape i) peut être répétée en une pluralité de points de la paroi cellulaire ; en particulier l'étape i) peut être répétée en chaque pixel de l'image correspondant au contour de la cellule. Ceci permet de déterminer l'épaisseur de la paroi en fonction de la position autour de la cellule qui peut être représentée sur un graphique (Figure 1D) ou par le biais d'une carte couleur (Figure 1E).

Il est possible d'effectuer des mesures moyennées sur une partie de la cellule et moyennant l'épaisseur mesurée sur une section du contour de la cellule. Cette étape de mesure d'une moyenne permet de supprimer les erreurs de mesure locales.

Du fait d'aberrations chromatiques associées à tous les systèmes de microscopie optique à haute-résolution, en particulier à fluorescence, les images venant de la ligne correspondant à la radiation lumineuse du premier marqueur et de la ligne correspondant à la radiation lumineuse du second marqueur ne sont généralement pas exactement alignées. Cet effet crée des décalages qui peuvent donner lieu à des asymétries dans la carte d'épaisseur de la paroi qui ne correspondent pas à la réalité biologique.

Les déformations et en particulier les aberrations chromatiques qui peuvent créer des décalages dans le plan ou en profondeur des deux signaux peuvent être compensées par une étape de calibration. Cette étape de calibration peut comprendre les étapes suivantes :

α) imager un élément ponctuel irradiant dans plusieurs longueurs d'onde connues ;

β) analyser les radiations détectée dans ces longueurs d'onde pour définir une carte des déformations ; et

γ) compenser ces déformations dans les images acquises.

L'étape α) peut en particulier consister à imager un élément d'une taille inférieure au pixel tel qu'une bille d'un diamètre de 0,2 µm irradiant dans plusieurs longueurs d'onde connues (par exemple bleu, vert, rouge et infrarouge).

L'étape α) peut également consister à imager une cellule marquée avec deux marqueurs luminescents émettant une radiation de longueur d'onde différente, en particulier à l'aide de marqueurs luminescents couplés à des molécules capables de se lier à la face externe de la paroi cellulaire, tels que des marqueurs fluorescents distincts couplés à une lectine.

L'étape β) d'analyse des radiations détectée permet plus précisément d'établir une carte des déformations optiques. En effet, les signaux aux différentes longueurs d'onde devraient, par construction, être parfaitement alignés, puisqu'ils émanent du même point. La déformation optique en un point est définie comme le décalage entre les signaux détectés aux différentes longueurs d'onde. Le décalage moyen en chaque point est mesuré sur un certain nombre de mesure (par exemple, 20).

Au cours de l'étape γ) la carte des déformations optiques définie à l'étape β) peut être utilisée pour corriger les images acquises et donc les mesures d'épaisseur. Les mesures d'épaisseur de paroi sont ainsi corrigées en fonction du décalage mesuré à l'étape β) (Figures 2A et 2B).

Selon un mode de réalisation préféré, les différentes étapes de l'analyse d'image du procédé de l'invention sont exécutées au moyen d'instructions de code de programme.

En conséquence, un autre aspect de l'invention porte sur un produit programme d'ordinateur, ce programme étant susceptible d'être mis en œuvre dans les moyens de traitement ou un système informatique, ce programme comportant des instructions de code adaptées à la mise en œuvre d'un procédé selon l'invention tel que décrit ci-dessus.

Ce programme peut utiliser n'importe quel langage de programmation, et être sous la forme de code source, code objet, ou de code intermédiaire entre code source et code objet, tel que dans une forme partiellement compilée, ou dans n'importe quelle autre forme

souhaitable. L'invention vise aussi un support d'informations lisible par un ordinateur, et comportant des instructions d'un programme d'ordinateur tel que mentionné ci-dessus. Le support d'informations peut être n'importe quelle entité ou dispositif capable de stocker le programme. Par exemple, le support peut comporter un moyen de stockage, tel qu'une ROM, par exemple un CD ROM ou une ROM de circuit microélectronique, ou un autre moyen d'enregistrement. D'autre part, le support d'informations peut être un support transmissible tel qu'un signal électrique ou optique, qui peut être acheminé via un câble électrique ou optique, par radio ou par d'autres moyens. Alternativement, le support d'informations peut être un circuit intégré dans lequel le programme est incorporé, le circuit étant adapté pour exécuter ou pour être utilisé dans l'exécution du procédé en question.

Le procédé de l'invention peut être mis en œuvre pour étudier la physiologie de la cellule à paroi. Il est en effet bien connu de l'homme du métier que l'épaisseur de la paroi reflète la viabilité de la cellule, et conditionne sa croissance, son homéostasie ainsi que sa polarité (Davi *et al.*, 2015).

Ainsi, selon un autre aspect, l'invention porte sur un procédé *in vitro* pour évaluer en temps réel la viabilité cellulaire, la synthèse de la paroi cellulaire, la morphogénèse cellulaire, l'homéostasie de la paroi cellulaire et/ou la polarité de cellules à paroi, comprenant:

a) mesurer en temps réel l'épaisseur de la paroi cellulaire d'au moins une cellule isolée selon le procédé de l'invention tel que décrit ci-dessus; et

b) évaluer la viabilité cellulaire, la synthèse de la paroi cellulaire, la morphogénèse cellulaire, l'homéostasie de la paroi cellulaire et/ou la polarité de ladite cellule, en fonction de l'épaisseur de la paroi cellulaire mesurée à l'étape a).

Le terme « viabilité cellulaire » signifie ici la capacité de la cellule à se diviser dans des conditions de culture *in vitro.* Ainsi, une épaisseur de la paroi trop faible, par exemple inférieure à 20% de la valeur normale, ou trop importante, par exemple supérieure à 300% de la valeur normale, mesurée en un seul point ou plusieurs points du contour de la cellule est indicative d'une faible viabilité de la cellule.

Lorsque la cellule imagée est vivante, la synthèse de sa paroi, sa morphogénèse, l'homéostasie de la paroi et/ou sa polarité peuvent être étudiées grâce au procédé de l'invention.

Par « synthèse de la paroi cellulaire », on entend désigner ici le processus physiologique par lequel se forme et évolue la paroi cellulaire d'une cellule à paroi, lors de la croissance de ladite cellule. Les Inventeurs ont en effet observé la formation de la paroi en temps réel chez des cellules sphéroplastées (i.e. sans paroi), et ce sur plusieurs

heures, grâce au procédé de mesure de l'épaisseur de la paroi selon l'invention.

Par « morphogénèse cellulaire », on entend désigner ici le processus physiologique de développement d'une cellule dans le temps. Ce phénomène recouvre, entre autres, la croissance cellulaire et la division cellulaire. Les Inventeurs ont en effet démontré qu'il était possible d'observer les variations spatio-temporelles de l'épaisseur de la paroi d'une cellule vivante, et de suivre ainsi dans le temps la croissance de cette dernière ainsi que sa division, grâce au procédé de mesure de l'épaisseur de la paroi selon l'invention.

Par « homéostasie de la paroi cellulaire », on entend désigner ici le processus physiologique permettant de maintenir l'épaisseur moyenne de la paroi de la cellule constante.

La « polarité cellulaire » désigne quant à elle les différences spatiales dans la forme et la structure d'une cellule. Ainsi, une épaisseur locale de la paroi de 50% de la valeur normale est indicative de default de polarité et par conséquent de sécrétion vectorielle de matériel dans la paroi.

Le procédé de l'invention peut être également mis en œuvre pour identifier des cellules à paroi résistantes à un agent ou combinaison d'agents capables de modifier l'épaisseur de la paroi cellulaire. Le procédé de l'invention permet ainsi d'identifier plus particulièrement la résistance à des antibiotiques, phénomène qui est responsable de milliers de morts chaque année.

Ainsi, selon un autre aspect, l'invention concerne un procédé *in vitro* pour déterminer la résistance de cellules à paroi envers un agent ou combinaison d'agents capables de modifier l'épaisseur de la paroi cellulaire, comprenant :

a) mesurer en temps réel l'épaisseur de la paroi cellulaire d'au moins une cellule isolée selon le procédé de l'invention tel que décrit ci-dessus, en présence d'un agent ou combinaison d'agents capables de modifier l'épaisseur de la paroi cellulaire et optionnellement en absence dudit agent ou de ladite combinaison d'agents ;
b) déterminer si l'épaisseur de la paroi cellulaire est modifiée par ledit agent ou ladite combinaison d'agents ; et
c) optionnellement, déterminer la résistance de la cellule envers l'agent ou combinaison d'agents capables de modifier l'épaisseur de la paroi cellulaire.

En particulier, la non-modification de l'épaisseur de la paroi de la cellule est indicative que la cellule est résistante audit agent ou combinaison d'agents, tandis que la modification de l'épaisseur de la paroi de ladite cellule est indicative que la cellule est sensible, et donc non-résistante, audit agent ou combinaison d'agents.

Dans le contexte de la présente invention, la résistance est plus particulièrement évaluée envers des agents capables de diminuer l'épaisseur de ladite paroi, et encore plus avantageusement pour une cellule à paroi pathogène, telle qu'une cellule de bactérie ou une cellule de champignon.

Les agents capables de diminuer l'épaisseur de la paroi cellulaire d'une bactérie (antibactériens, bactériostatiques ou bactéricides) ou d'un champignon (antifongiques, fongistatiques ou fongicides) sont bien connus de l'homme du métier, et ont été décrits dans la littérature, notamment par Perlin *et al.* (2015).

La cellule à paroi peut quant à elle être isolée d'un sujet infecté par ladite cellule, par exemple à partir d'un échantillon biologique prélevé chez ce sujet. De manière préférée, ledit sujet est un animal, tel que l'homme, ou une plante.

Le procédé de l'invention peut être aussi mis en œuvre pour créer ou adapter un régime de traitement permettant de lutter contre des cellules à paroi pathogènes, notamment en fonction de la résistance ou de la non-résistance (i.e. sensibilité) de la cellule à paroi à un agent thérapeutique ou susceptible d'être thérapeutique.

Ainsi, selon un autre aspect, l'invention concerne un procédé pour déterminer ou adapter un régime thérapeutique destiné à un sujet infecté par une cellule à paroi pathogène, comprenant :

a) déterminer la résistance d'au moins une cellule à paroi isolée dudit sujet envers un agent ou combinaison d'agents capables de modifier l'épaisseur de la paroi cellulaire, selon le procédé tel que décrit ci-dessus; et
b) déterminer ou adapter un régime de traitement en fonction de la résistance ou de la non-résistance de la cellule à paroi envers ledit agent ou ladite combinaison d'agents, telle que déterminée à l'étape a).

Le terme « traitement » désigne ici aussi bien le type de traitement (i.e. l'agent ou la combinaison d'agents et son mode d'administration), que la dose, le rythme d'administration et/ou la durée du traitement qui est fourni au sujet. La dose, le rythme d'administration et/ou la durée du traitement peut varier, en fonction du stade de la pathologie et du type de traitement sélectionné. Les agents susceptibles d'être utilisés dans le régime de traitement sont soit ceux connus par l'homme du métier pour lutter contre ladite cellule pathogène, ou ceux susceptibles d'être identifiés par le procédé de criblage de l'invention.

Ici, le régime de traitement est déterminé ou adapté et optionnellement administré au sujet en fonction de la résistance ou de la non-résistance de la cellule à paroi envers ledit agent ou combinaison d'agents. En particulier, si la cellule est résistante audit agent

ou combinaison d'agents, le traitement sera préférablement stoppé et échangé par un traitement alternatif plus approprié. En revanche, si la cellule est non-résistante (i.e. est sensible) audit agent ou combinaison d'agents, le traitement pourra être soit sélectionné pour la première fois, soit continué. L'homme du métier est à même de déterminer ou d'ajuster le type de traitement avec la dose, le rythme d'administration et/ou la durée du traitement, en fonction de la résistance ou de non-résistance de la cellule.

Le procédé de l'invention peut être aussi mis en œuvre pour identifier de nouvelles molécules capables de modifier l'épaisseur de la paroi de cellules pourvues de paroi, en particulier pathogènes, et donc nuisibles à l'environnement et/ou à la santé. Ceci est particulièrement utile en cas de résistance de la cellule à paroi aux agents connus pour altérer la paroi cellulaire.

Ainsi, selon un autre aspect, l'invention concerne un procédé *in vitro* pour cribler des agents capables de modifier l'épaisseur de la paroi cellulaire de cellules à paroi, comprenant :

a) mesurer en temps réel l'épaisseur de la paroi cellulaire d'au moins une cellule isolée selon le procédé de l'invention tel que décrit ci-dessus, en présence d'un agent candidat ou combinaison d'agents candidats et optionnellement en absence dudit agent ou de ladite combinaison d'agents ;
b) déterminer si l'épaisseur de la paroi cellulaire est modifiée par ledit agent ou ladite combinaison d'agents ; et
c) optionnellement, identifier l'agent ou combinaison d'agents capables de modifier l'épaisseur de la paroi cellulaire de ladite cellule.

Dans le contexte de la présente invention, l'identification d'agents capables de diminuer l'épaisseur de la paroi de cellules à paroi pathogènes est préférablement recherchée, telles que des cellules de bactérie et/ou de champignon.

Afin de mettre en œuvre tous les procédés de l'invention, il est en outre particulièrement utile de disposer d'un kit comprenant les composants nécessaires à leur réalisation.

Ainsi, l'invention concerne dans un autre aspect un kit, en particulier pouvant être utilisé dans l'un quelconque des procédés décrits ci-dessus, ledit kit comprenant :

a) un premier marqueur luminescent couplé à une molécule capable de se lier à la face externe de la paroi cellulaire d'une cellule à paroi ; et
b) un second marqueur luminescent couplé à une protéine de la membrane cellulaire de ladite cellule, ou à une molécule capable de se lier à la membrane

cellulaire de ladite cellule, ou est capable de se lier à la membrane cellulaire de ladite cellule.

Les modes de réalisation préférés sont tels que décrits ci-dessus.

De manière optionnelle, ledit kit peut en outre comprendre au moins une cellule à paroi isolée telle que définie ci-dessus, pouvant notamment servir de contrôle, et/ou des instructions pour réaliser ledit procédé.

La présente invention sera mieux comprise à la lumière des exemples ci-après.

DESCRIPTION DES DESSINS

Figure 1. Mesure de l'épaisseur de la paroi cellulaire dans des cellules vivantes par méthode de microscopie photonique. (A) Image initiale d'une cellule de levure exprimant la fusion EGFP-Psy1 (protéine intégrale de la membrane, flèche interne) et marquée avec le couple fluorescent lectine-AlexaFluor-647 sur la face externe de la paroi (flèche externe). (B) Principe de détection locale de l'épaisseur de la paroi : après avoir segmenté le contour de la cellule, des lignes perpendiculaires au contour sont tracées, le long desquelles le signal est analysé. (C) Le long d'une ligne chaque signal est ajusté par une fonction gaussienne. Face interne de la paroi (o), face externe de la paroi (□). La distance entre les deux maximums permet de mesurer une épaisseur de paroi, Δ, à un point de la cellule. (D) et (E) En réitérant cette méthode tout le long du contour de la cellule, des profils ou cartes complètes de l'épaisseur de la paroi dans des cellules vivantes peuvent être établis.

Figure 2. Correction du décalage chromatique et influence du rapport signal/bruit sur la mesure. (A) Cellule contrôle marquée avec des lectines de 2 couleurs différentes et carte de billes multi-spectrales déplacées sur le champ d'observation. (B) Correction du décalage (à gauche avant correction, et à droite après correction). (C) Images synthétiques pour sonder la méthode d'analyse (Panels de gauche). Pics gaussien (Panel du milieu) (Gris clair: membrane ; gris foncé: Lectine). Epaisseur de la paroi autour de la cellule (Panel de droite). (D) Cellule synthétique ayant deux régions avec des signaux d'intensité différentes (Panels de gauche). Pics gaussien (Panel du milieu) (Gris clair : face interne de la paroi ; gris foncé: face externe de la paroi). Epaisseur de la paroi autour de la cellule (Panel de droite). (E) Diagramme résumant les effets du signal/ bruit sur la mesure de l'épaisseur. La zone délimitée par le trait noir correspond aux valeurs typiques

dans nos mesures. (F) Evolution de la valeur moyenne de l'épaisseur de la paroi en fonction du rapport signal sur bruit.

Figure 3. Comparaison de la méthode de l'invention avec celle réalisée par microscopie électronique à transmission (MET). (A) Distributions de valeurs moyennes de l'épaisseur de la paroi cellulaire mesurée par la méthode de l'invention (ronds, à gauche) et par microscopie électronique à transmission (carrés, à droite). (B) CLEM (« Correlative Ligth Electron Microscopy ») permettant de visualiser l'épaisseur locale de la paroi cellulaire par la méthode de l'invention (panels du haut) et par microscopie électronique (panels du bas). Images originales (panels de gauche). Cartes de la paroi (panels de droite). (C) Comparaison entre les deux mesures pour la cellule présentée en B (ronds : mesure par la méthode de l'invention ; triangles : mesure par microscopie électronique à transmission, i.e.MET). (D) Analyse de corrélation entre les deux méthodes obtenues par CLEM pour 15 régions sous-cellulaires de taille de 3 micromètres effectués sur 8 cellules individuelles (en abscisse: mesure par microscopie électronique à transmission, i.e. MET; en ordonnée : mesure par la méthode de l'invention). La ligne pointillée indique l'ajustement linéaire de ces données, et sa pente est proche de 1, suggérant une corrélation précise.

Figure 4. Utilisation de la méthode de l'invention pour détecter des variations locales, globales et temporelles d'épaisseur chez la levure, et application chez *Candida Albicans.* (A) Image par microscopie photonique d'une cellule de levure sauvage (panel du haut et à gauche), et carte de sa paroi cellulaire (panel du centre et à gauche), et image d'une cellule de levure mutante fabriquant de la paroi cellulaire 2 à 3 fois plus épaisse par surexpression de la protéine pck2p (panel du haut et à droite) et carte de sa paroi cellulaire (panel du centre et à droite). (Panel du bas) Quantification des épaisseurs moyennes de la paroi de ces deux cellules (à gauche, triangles : cellule de levure sauvage ; à droite, carrés : cellule de levure mutante). (B) Traitement par l'enzyme zymolase d'une cellule de levure sauvage causant une réduction nette de l'épaisseur après 60 min de traitement. Cellule à t=0 (panels de gauche) : image par microscopie photonique (panel du haut), carte de sa paroi (panel du centre) et quantification moyenne de la paroi cellulaire (panel du bas). Cellule traitée par zymolase à t=60 minutes (panels du centre) : image par microscopie photonique (panel du haut), carte de sa paroi (panel du milieu) et quantification moyenne de la paroi cellulaire (panel du bas). Cellule non traitée par zymolase à t=60 minutes (panels de droite) : image par microscopie photonique

(panel du haut), carte de sa paroi (panel du centre) et quantification moyenne de la paroi cellulaire (panel du bas). (C) Comparaison entre une levure sauvage (panels à gauche) et une levure mutante (*cwg1*-1) ayant un défaut de fabrication de la paroi cellulaire et dont la paroi est ainsi 2 fois plus fine (panels à droite) : images représentatives de cellules de levure fixées et imagées en microscopie électronique à transmission (panels du haut), mesure des épaisseurs aux pointes de cellules vivantes (panels du centre), quantification des épaisseurs aux pointes (panels du bas). (D) Dynamique de reformation de la paroi cellulaire chez des sphéroplastes en recouvrement, au cours du temps. Valeurs mesurées de l'épaisseur sur une série de cellules individuelles en fonction du temps (panel de gauche). Images originales (Haut) et cartes d'épaisseur (Bas) pour une série de sphéroplastes en recouvrement. (E) Validation de la méthode de l'invention chez le champignon filamenteux et pathogène *Candida Albicans*. Image par microscopie photonique (panel de gauche), et carte de la paroi cellulaire (panel de droite)

Figure 5. Dynamique spatio-temporelle de la paroi au cours du cycle cellulaire. Photos de films indépendants de 2 cellules de levure fissipare grandissant et se divisant avec une mesure du profil d'épaisseur à différents points dans le temps.

EXEMPLES

1. MATERIEL ET METHODES

1.1. Marquage fluorescent des cellules

La culture des levures fissipare *Schizosaccharomyces pombe* a été effectuée selon des protocoles standards (http://www-bcf.usc.edu/~forsburg/). Les cellules ont été cultivées tout d'abord sur boites d'agar de milieu YE5S, puis en milieu liquide sur la nuit. Les souches utilisées sont décrites dans le Tableau 1. Ces cellules expriment le marqueur de membrane plasmique EGFP-Psy1 ou mCherry-Psy1. Pour marquer l'extérieur de la paroi, la lectine issue de *Griffonia simplificifolia* liée à un fluorophore brillant dans le rouge lointain (Alexa Fluor 647 isolectin GS-IB4, LifeTechnologies) a été ajoutée à une concentration finale de 5µg/ml à partir d'un stock au 200X. Pour tester d'autres combinaisons de couleur, les mêmes lectines conjuguées au TRITC (Tetramethylrhodamine – Sigma) ou FITC (fluorescein isothiocyanate - Sigma) ont également été essayées. L'incubation a été faite sur un rotor pendant 10min; après quoi les cellules ont été placées soit sur un pad 2% agar de YE5S contenant une concentration

de lectine de 5µg/ml. Alternativement, les cellules ont été placées au sein d'une chambre microfluidique, coincées entre une membrane de dialyse et une lamelle (Charvin *et al*., 2008). Ces chambres permettent un échange constant du milieu et donc un approvisionnement constant de lectines fluorescentes.

Les cellules de champignons *Candida Albicans* ont été quant à elles cultivées sur la nuit dans un milieu YEPD+Uri (2% glucose) à 30°C, puis re-diluées pour obtenir une culture ayant une densité optique de 0.6. Pour engendrer la filamentation, ces cellules ont été cultivées dans un milieu contentant 50% de FCS à 37°C, pendant 1 à 2h. La souche utilisée exprime un marqueur de membrane fluorescent construit par la fusion d'une protéine fluorescente verte (EGFP) à l'extrémité C-terminale de la protéine CtRac1 correspondant à SEQ ID NO :4 (voir tableau 6). Pour marquer l'extérieur de la paroi, la lectine WGA couplée à Alexa594 (Life) a été ajoutée à une concentration finale de 100 µg/ml.

Tableau 6. Souches de microorganismes utilisées

Souche	**Origine de la cellule imagée**	**Type Sexuel**	**Génotype**	**Autotrophies**
NM 468	*S. pombe*	h+	Leu:EGFP-psy1	Ura-4-D18 Leu-32
NM 469	*S. pombe*	h-	Leu:EGFP-psy1	Ura-4-D18 Leu-32
VD115	*S. pombe*		Leu:EGFP-psy1 cwg1-1 CRIB-tdTomato:ura	Ura-4-D18 Leu-32
VD94	*S. pombe*	h-	ade6:EGFP-psy1 pREP3X-pck2	Ade6 Ura4-D18 Leu-32
PY173	*C. albicans*		RP10::ARG4-pADH1-EGFP-CtRac1	ade2Δ::hisG/ade2Δ::hisG ura3Δ::limm434/ura3Δ::limm434 his1Δ::hisG/his1Δ::hisG arg4Δ::hisG/arg4Δ::hisG ENO1/eno1::ENO1-tetRScHAP4AD-3xHA-ADE2

1.2. Imagerie

Pour maximiser la résolution spatiale et limiter le bruit de fond, un système de confocal à tête « spinning », yokogawa X1, monté sur un statif Nikon Ti, muni d'une caméra EM-CCD couplée à un grossisseur 2.5X, a été utilisé.

Les cellules de levures ont été imagées avec un objectif Nikon 100X 1.4 NA Plan Apo oil, amenant une taille de pixel de 43,1nm. Ce choix a été fixé après essais de nombreux systèmes confocaux droits et d'épifluorescence. Les cellules de *Candida Albicans* ont quant à elles été placées entre lame et lamelle et imagées sur un système de confocal « spinning », avec une taille finale de pixel de 130 nm.

1.3. Analyse et registration des images

L'analyse d'images brutes pour obtenir les mesures locales d'épaisseur de la paroi cellulaire a utilisé une série de scripts développée sur le logiciel MatLab (Mathworks). L'image de la cellule a d'abord été segmentée à l'aide du signal fluorescent émanant de la lectine ou de la membrane. A partir de cette segmentation, des lignes perpendiculaires ont été tracées pour chaque pixel du contour de la cellule. Ces lignes ont une taille modulable, mais qui est généralement fixée à 4 µm (93 px). Le long de chaque ligne, l'intensité des deux signaux fluorescents a été modélisée par des gaussiennes dont le pic est détecté de manière automatique. La distance entre ces deux pics correspond à l'épaisseur de la paroi locale.

Les aberrations chromatiques susceptibles de créer des décalages dans le plan ou en profondeur des deux signaux ont été compensées, soit par l'utilisation de billes (TETRASPECK-microspheres, 0,2 µm, blue/green/red/far red) qui permettent d'établir une carte des déformations, soit en imageant des cellules marquées avec deux lectines de couleurs différentes. Ces cartes ont été utilisées dans le script pour corriger l'analyse de l'épaisseur initiale. Les scripts intégrant ces cartes permettent ainsi d'effectuer des corrections manuelles du de la modélisation sous forme de gaussienne pouvant provenir de signaux aberrants, mais également d'effectuer des mesures moyennées sur une partie de la cellule.

1.4. Microscopie Corrélative

Pour comparer l'épaisseur de la paroi sur les mêmes cellules par la méthode de l'invention à celle réaliser par microscopie électronique à transmission (MET), les cellules ont été marquées comme précédemment décrit et collées sur une boîte de Petri à fond de verre gradué (Ibidi) préalablement traitée à la PolyLysine (1mg/ml pendant 20min).

Les cellules ont été tout d'abord fixées pendant 2h dans du YE5S contenant 2 % de glutaraldehyde à 4°C, puis rincées une fois dans du YE5S et 3 fois dans de l'eau, pour être ensuite imagées en suivant la même procédure que précédemment, tout en prenant soin d'imager les marqueurs de position sur la lame de verre. Les cellules ont alors été refixées pendant 45 min dans une solution d'osmium (2% OsO_4 dans l'eau) dans l'obscurité, rincées 2x dans de l'eau, puis deshydratées dans des solutions successives d'éthanol pendant 5 min à chaque fois (30% , 50% , 70%, 80%, 95% EtOH), suivi par 2x 10min dans 95% EtOH et 3x 6min dans 100% EtOH. Finalement, un rinçage des cellules a été réalisé dans de l'oxyde de propylène pendant 10 minutes, et les cellules ont été incluses dans une solution EPON/oxyde de propylène 1vol/1vol pendant 1h couvertes et 1h sans couvercle. Elles ont ensuite été placées dans de l'EPON pure qui est polymérisée à 60°C pendant 48h. Les boîtes de Petri comprenant ces cellules ainsi traitées ont finalement découpées au microtome, et les coupes placées sur des grilles de microscopie électronique colorées à l'uracil d'acetyl et au citrate de plomb. Finalement, les images ont été acquises sur un Microscope électronique à transmission Tecnai12 (FEI) à 80 kV équipé d'une caméra 1K×1K Keen View (Olympus).

1.5. Recouvrement de sphéroplastes

Des sphéroplastes (cellules sans paroi cellulaire) ont été générés en plaçant des cellules de levure dans une solution contenant 0,1M d'acide citrique 0,1 M de Citrate de Sodium (pH = 5.8) et 1,2 M de Sorbitol et une enzyme de digestion de paroi, Lallzyme MMX (Lallemand), à une concentration de 0.1 g/ml et ce pendant 45 min. Après digestion de la paroi, les cellules ont été observées au microscope pour s'assurer qu'elles aient adoptées une forme ronde. Pour permettre la resynthèse de la paroi, les sphéroplastes ainsi obtenus ont été placés dans du YE5S liquide contenant 1M Sorbitol dans un agitateur à 25°C puis marquées à la lectine à différents temps et imagées au microscope comme décrit ci-dessus.

1.6. Essais à la Zymolyase

Pour partiellement digérer la paroi cellulaire, les cellules étudiées ont été marquées à la lectine et placées dans une solution YE5S contenant 500U/ml de Zymolyase (ZymoResearch).

2. RESULTATS

2.1. Une nouvelle méthode pour imager l'épaisseur de la paroi

A ce jour, la seule méthode connue permettant d'obtenir des informations sur la paroi cellulaire de n'importe quelle espèce à paroi est la microscopie électronique. Cette approche est néanmoins associée à différents artefacts et ne permet pas d'observer cette structure dans des cellules vivantes. La présente méthode permet de pallier à ce besoin. Le concept de l'invention repose en effet sur le marquage des deux côtés de la paroi cellulaire par deux fluorophores de couleurs différentes, et sur l'utilisation de microscopie en super-résolution pour mesurer localement l'épaisseur. La levure *Schizosaccharomyces pombe* a été utilisée ici comme modèle, car il s'agit d'une cellule qui permet aisément les manipulations génétiques, dont la forme stéréotypée de bâtonnet est facile à observer, et dont la paroi cellulaire a été caractérisée dans différentes études (Chang *et al.*, 2009; Davi et al., 2015).

Pour marquer la face interne de la paroi, des protéines ou des colorants qui s'associent à la membrane plasmique juxtaposée à la paroi, ont été utilisés. Différentes protéines ont été testées, parmi lesquelles Pma1, Psy1, et Syb1 (Iwaki *et al.*, 2008; Yamaoka *et al.*, 2013) : la protéine Psy1 qui est une protéine accrochée à la membrane a fourni les meilleurs résultats en terme de force et homogénéité du signal. Les couples de fluorophore-protéines EGFP-Psy1 (émission dans le rouge) et mCherry-psy1 (également émission dans le rouge) ont aussi été testés, menant à une légère préférence pour la EGFP. Par ailleurs, des colorants comme ceux de la famille DiBAc (Haupt *et al.*, 2014), qui s'insèrent spécifiquement dans la membrane plasmique ont été validés et peuvent être envisagés pour marquer la membrane d'autres espèces, en particulier celles qui ne sont pas génétiquement modifiables.

Le marquage de la face externe de la paroi est ici basé sur le fait que des glycoprotéines sont généralement sécrétées sur cette face. La nature glucidique des glycoprotéines est normalement propre à chaque espèce (par exemple, le galactomannan, chez la levure *S. pombe*), et peut être reconnue de manière spécifique par une famille de protéines appelées les lectines (Horisberger *et al.*, 1985). Dans le cadre de l'optimisation de la méthode de l'invention, différents types de lectines ont été testées, et celles issues de *Griffonia simplificifolia* ont été sélectionnées, celles-ci étant déjà disponibles commercialement liées à différent fluorophores (FITC, Tritc ou Alexa 647). Tous les couples de couleurs entre signal membranaire et lectine ont fonctionné pour la mesure, mais pour des raisons d'optimisation du signal et d'analyse, le couple EGFP-Psy1 et

Lectine-Alexa 647 a été préférentiellement sélectionné. Le marquage par la lectine-Alexa 647 a ensuite été optimisé pour obtenir le meilleur signal, sans affecter la croissance cellulaire. Une gamme de concentration de lectine entre 1 et 10 µg/ml a donné en général de bons résultats. Néanmoins, lorsque les cellules grandissent, la nouvelle paroi synthétisée n'est plus marquée par la lectine, et un apport constant de lectine fraiche dans la solution est ainsi nécessaire. Pour cela, de la lectine a été ajoutée directement dans les pads d'agar servant de support à la croissance et à l'imagerie des cellules, ou, alternativement, des chambres à flux microfluidique ont été utilisées dans lesquelles les cellules marquées ont été immobilisées entre une membrane de dialyse et la lamelle du fond de la chambre et apportant en flux continu de la lectine.

Pour imager les cellules, les systèmes de microscopies ont été optimisés pour maximiser les signaux, et dans le même temps obtenir la meilleure résolution spatiale afin de réussir à cartographier de manière aussi précise que possible l'épaisseur de la paroi tout autour de cellules individuelles (voir ci-après). La résolution spatiale dans le plan ainsi déterminée est de 43.1 nm, c'est-à-dire, deux valeurs de résiliation de 43,1 nm ont été distinguées le long du contour de la cellule). Quant à la mesure de l'épaisseur de la paroi cellulaire, celle-ci est plus précisément réalisée à une résolution d'environ 10 nm,

A partir d'une image telle que celle présentée dans la Figure 1A, un processus d'analyse d'images a été implémenté de manière à segmenter le contour de la cellule, puis à tracer des lignes perpendiculaires au contour pour détecter successivement les signaux issus de la lectine et de la membrane (Figure 1B). Ces lignes de 4 µm (93 px) de longueur ont été espacées le long du contour par la taille d'un pixel (43.1nm). Le signal fluorescent a été ajusté le long de chacune de ces lignes par une fonction gaussienne, et dont le centre est détecté, la distance entre les deux pics correspondant à l'épaisseur locale de la paroi. Cette distance a été mesurée avec une précision de +/- 10nm. Ce processus a par la suite été répété tout autour de la cellule pour obtenir l'évolution de l'épaisseur en fonction de la position autour de la cellule qui peut être représentée sur un graphique (Figure 1D), ou par le biais d'une carte reproduisant les couleurs des marqueurs de la face externe et interne de la paroi (Figure 1E).

La force du signal ainsi que la construction de la méthode et des scripts d'analyse, permettent une mesure de l'épaisseur résolue au pixel près.

2.2. Correction des aberrations chromatiques et des différences de signaux

Du fait d'aberrations chromatiques associées à tous les systèmes de microscopie de fluorescence, les images venant de la ligne bleue (utilisée pour imager EGFP-Psy1) et de la ligne rouge lointain (utilisée pour imager la lectine-AlexaFluor-647), n'ont pas été exactement alignées. Cet effet engendre des décalages légers susceptibles de donner lieu à des asymétries dans la carte d'épaisseur de la paroi qui ne correspondent pas à la réalité biologique. Pour pallier àcela, un système d'alignement mesurant précisément le décalage entre les lignes et permettant de compenser ce décalage dans l'analyse a été introduit. Pour ce faire, des cellules marquées avec deux lectines de couleurs différentes ont été utilisés comme calibre : la lectine-FITC (qui fluoresce sur la même ligne que EGFP-Psy1) et la lectine-AlexaFluor-647 (Figure 2A). Ces deux signaux doivent, par construction, être parfaitement alignés. Un décalage moyen sur 20 contrôles a ainsi été mesuré et compensé pour corriger les cartes de paroi. Au cours de l'optimisation, des billes fluorescant dans de multiples longueurs d'onde ont également été utilisées, et ont donné les mêmes résultats (Figure 2A et 2B). Les décalages en profondeur ont également été calibrés donnant des imprécisions inférieures à 10 nm ; et ont donc rentré dans le bruit associé à la méthode.

Les images obtenues fluorescent fortement là où le marqueur est localisé mais également quelque peu à l'intérieur de la cellule et à l'extérieur. Ces signaux de fond, peuvent en principe créer des asymétries dans la détection du centre du pic gaussien, qui pourraient alors créer des biais sur les valeurs des mesures d'épaisseur. Pour sonder ces effets, des simulations ont été effectuées, durant lesquelles des images similaires à celles analysées ont été créées de manière artificielle, mais en générant différents signaux et bruits artificiellement. Ces images artificielles, ont ensuite été analysées par le même procédé d'analyse d'image pour évaluer les erreurs potentielles (Figure 2C et 2D). Ces analyses ont montré que le décalage causé par les variations de bruit de fond est resté négligeable et n'a pas influencé la mesure de manière significative, dans le domaine de signaux typiquement obtenus par la méthode d'imagerie de l'invention (Figure 2E et 2F). Elles permettent par ailleurs de valider la mesure locale, proposée ici, sur des cellules susceptibles de présenter des variabilités de signaux naturels autour de leur contour.

2.3. Validation de la méthode par comparaison à la MET

La méthode de l'invention a été validée tout d'abord en comparant directement les mesures obtenues avec celles de l'état de l'art, qui est basée sur la microscopie électronique. Une première validation a consisté à comparer les mesures moyennées à

l'échelle globale de différentes cellules, obtenues par la méthode de l'invention et par microscopie électronique à transmission (MET). Cette comparaison a montré que les mesures réalisées par la méthode de l'invention possèdent une valeur moyenne, ainsi qu'un bruit reflétant les variations à l'échelle de la population très similaires à celles de la méthode basée sur la MET, validant ainsi la méthode présentée ici (Figure 3A).

L'un des points forts de la présente méthode est qu'elle permet de résoudre spatialement les changements d'épaisseur autour de la cellule. Cette propriété a été vérifiée par des expériences de CLEM (« Correlative Light-Electron Microscopy ») qui ont permis de mesurer, dans la même cellule, l'épaisseur de la paroi par microscopie électronique et par la méthode de l'invention. Ces expériences ont montré une corrélation quasi-parfaite entre les deux mesures, tout autour de chaque cellule (Figure 3B-3D); la différence entre les deux mesures étant plus faible que le bruit associé à la mesure elle-même. Il peut ainsi être conclu que la méthode d'imagerie de l'épaisseur de la paroi sur cellule vivante proposée par la présente invention donne des valeurs locales précises reflétant clairement la biologie du système.

2.4. Validation de la méthode de l'invention dans des conditions de parois défectueuses et d'autres espèces de champignons

Pour établir la souplesse et la robustesse de la méthode de l'invention, celle-ci a été appliquée pour mesurer l'épaisseur de la paroi cellulaire de mutants de levures dont les parois sont plus fines ou plus grosses que des levures sauvages, ou dans des conditions enzymatiques permettant de digérer partiellement la paroi. En effet, un tel mutant et une levure surexprimant la protéine pck2 sont connus pour présenter des parois très épaisses, (Arellano *et al.*, 1999). Avec la présente méthode, des parois de cellules mutantes ayant des épaisseurs allant jusqu'à 800nm (Figure 4A) ont ainsi pu être mesurées. Inversement, des cellules de levure ont été traitées avec des concentrations faibles de Zymolyase, une enzyme capable de digérer la paroi. Au bout d'une heure de traitement, un amincissement conséquent de la paroi a pu être observé avec une réduction typique de 30% de l'épaisseur (Figure 4B). De manière similaire, la méthode de l'invention a permis de détecter des réductions significatives de l'épaisseur à la pointe de cellules de levure dont un allèle *cwg1-1* est défectueux pour la synthèse de la paroi spécifiquement à ladite pointe (Munoz *et al.*, 2013)(Figure 4C). Enfin, la méthode de l'invention a été utilisée pour observer comment les cellules sphéroplastées (i.e. sans paroi) régénèrent leurs parois au cours du temps : cela a permis de montrer qu'une fine couche de paroi d'environ 60nm est tout d'abord déposée, suivi par une re-synthèse rapide de la paroi entre la 9ème heure

et 12ème heure de croissance des sphéroplastes (Figure 4D). Pour conclure, ces données valident la souplesse et l'applicabilité de la méthode pour comprendre des variations locales ou globales de la paroi.

La méthode de l'invention a ensuite été validée dans d'autres espèces. Pour ce faire, une approche similaire a été mise en place pour mesurer l'épaisseur de la paroi au cours de la filamentation chez le champignon pathogène *Candida Albicans*. La face interne de la paroi de ce champignon a été marquée avec une EGFP fusionnée à l'extrémité C-terminale de la protéine Rac1 qui cible la membrane plasmique ; tandis que la lectine WGA- AlexaFluor-594 a été utilisée pour marquer la face externe, car celle-ci reconnait plus spécifiquement la face externe de la paroi chez cette espèce (Figure 4E). Cette expérience a permis d'observer des valeurs similaires à celles reportées dans la littérature (Staniszewska *et al.*, 2012) : la méthode de l'invention peut ainsi s'appliquer à différents types de champignons filamenteux et à d'autres cellules à paroi, telles que les bactéries, les algues, plantes et/ou archées.

2.5. Mesure en « *time-lapse* » de l'évolution de l'épaisseur pendant la croissance de cellules.

La méthode de l'invention permettant de mesurer les valeurs de la paroi dans des cellules vivantes, il a ensuite été étudié si celle-ci permettait également d'obtenir des mesures séquentielles de l'épaisseur de la paroi. Pour faire cette démonstration, des cellules de levures ont été placées sur des pads d'agar dans lesquels de la lectine a été ajoutée, ceci afin d'éviter les effets de dilution du signal associé à la croissance cellulaire, et ainsi pouvoir filmer les cellules avec un intervalle de 30min pendant typiquement 3h. Ces films ont montré que la méthode de l'invention en dynamique demeurait valide et permet d'observer les variations spatio-temporelles de l'épaisseur au cours de la croissance et de la division cellulaire (Figure 5).

3. CONCLUSION

La méthode d'imagerie de la présente invention est une méthode simple, nouvelle et innovante permettant de sonder les propriétés de la paroi cellulaire de cellules possédant une telle paroi. Elle permet de mesurer, avec une précision à ce jour inachevée, l'épaisseur de cette structure essentielle à la survie de ces cellules. L'un des avantages de cette méthode est qu'elle est implémentable avec des systèmes de microscopie disponibles dans la plupart des centres de recherche ou de développement, et qu'elle a donc le potentiel d'être utilisée dans de nombreuses applications. Il s'agit d'une méthode précise, mais également versatile, susceptible d'être appliquée pour mesurer aussi bien l'épaisseur de la paroi de multiples types cellulaires, allant de la levure, au champignon, voire aux bactéries, archées, plantes et algues, que de sonder la réponse de la paroi cellulaire à des drogues, ou encore d'étudier des cellules mutées dont la paroi a été modifiée. Par ailleurs, la paroi cellulaire étant actuellement la cible principale des agents antifongiques, il ne fait aucun doute que la présente méthode présente un important potentiel biomédical et agronomique.

La présente méthode est extrêmement précise car elle fournit une mesure locale, avec une résolution de l'ordre de la cinquantaine de nanomètres, et ne nécessite pas de moyenner des mesures car il n'y a pas de problèmes d'homogénéité dans la mesure de l'épaisseur. Elle permet en outre des observations sur de longues périodes de temps (jusqu'à plusieurs heures), ce qui rend possible des essais sur le long terme.

Enfin, au regard du vaste champ d'applicabilité de cette méthode, de sa souplesse et de sa simplicité, la présente méthode peut être utilisée pour étudier aussi bien les fondamentaux de la synthèse de la paroi cellulaire que pour développer et tester de nouveaux composants détruisant la paroi cellulaire d'organismes non désirables, tels que les antifongiques ou les antibiotiques.

REFERENCES

Ai *et al.* (2007). *Biochemistry;* 46(20): 5904-5910.

Ai *et al.* (2006). *Biochem;* 400(3): 531 -540.

Ai *et al.* (2008a). *BMC Biology*; 6(1): 13.

Ai *et al.* (2008b). *Nature Methods*; 5(5): 401-403.

Bajar *et al.* (2016). *Sci. Rep* ; 6: article number 20889.

Arellano *et al.* (1999). *J Cell Sci*.; 112 (Pt 20):3569-3578.

Barre *et al.* (2001). *Biochimie*; 83(7):645-51.

Chacko *et al.* (2001). *Int J Biol Macromol*.;28(5):365-71.

Chang *et al.*(2014). *BMC Biol*.; 12:54.

Chang *et al.* (2009). *Cold Spring Harb Perspect Biol*.; 1:a001347.

Charvin *et al.* (2008). *PLoS One*; 3:e1468.

Chen *et al.* (2013). *Adv Drug Deliv Rev*; 65(10):1357-1369.

Chu *et al.* (2014). *Nature Methods*; 11 (5): 572-578.

Cornellissen-Gude *et al.* (1997). *J. Phys. Chem. A*; 101 (50), pp 9673–9677.

Cubitt *et al.* (1998). *Methods in Cell Biology*; 58:19-30.

Davi *et al.* (2015). *Curr Opin Microbiol*. 28:36-45.

Day *et al.* (2009). *Chem Soc Rev;* 38(10):2887-921.

Domozych *et al.* (2012). *Front Plant Sci.*; 3:82.

Erard *et al.* (2013). *Mol. BioSyst.*; 9(2): 258-267.

Evdokimov *et al.* (2006). *EMBO Rep*; 7(10): 1006-1012.

Filonov *et al.* (2011). *Nat Biotechnol*; 29(8): 757-761.

Fradkov *et al.* (2002). *Biochem J*.; 368: 17-21.

Fritz J.S. et Gjerde D.T. (2009). Ion chromatography, 4ème édition. Wiley-VCH. ISBN: 978-3-527-32052-3.

Fujihashi *et al.* (2003). *Biochemistry*; 42(38):11093-9.

Goedhart *et al.* (2010). *Nature Methods*; 7(2): 137-139.

Goedhart *et al.* (2012). *Nature Communications*; 3: 751.

Griesbeck *et al.* (2001). *Journal of Biological Chemistry*; 276(31): 29188-29194.

Gupta *et al.* (Ed.) (2012). Laboratory Protocols in Fungal Biology: Current Methods in Fungal Biology. Springer. ISBN-13: 978-1461423553.

Gurskaya *et al.* (2003). *Biochem. J.;* 373: 403-408.

Han *et al*. (2002). *Ann N Y Acad Sci*.; 971: 627-33.

Haupt *et al.* (2014). *PLoS Biol*.; 12(12):e1002029.

Heim *et al.* (1994). *Proceedings of the National Academy of Sciences*; 91 (26): 12501 - 12504.

Herman (2001). *Curr Protoc Cell Biol.*; Appendix 1:Appendix 1E.

Hermanson G.T. (2013). Bioconjugate Techniques, 3ème édition. Elsevier. ISBN: 978-0-12-382239-0.

Hoi *et al.* (2013). *Chemistry & Biology*; 20(10): 1296-1304.

Horisberger *et al.* (1985). *Experientia*; 41:748-750.

Hormia *et al.* (1998). *J Histochem Cytochem.*; 36(10):1231-7.

Hurley *et al.* (2000). *Annu. Rev. Biophys. Biomol*. Struct.; 29:49-79.

Iwaki *et al.* (2008). *Microbiology*; 154:830-841.

Johnson *et al.* (2009). *Journal of Biological Chemistry*; 284(31): 20499-20511.

Karasawa *et al.* (2003). *Journal of Biological Chemistry*; 278(36): 3416734171.

Karasawa *et al.* (2004). *Biochem. J.*; 381 (1): 307-312.

Keegstra *et al.* (2010). *Plant Physiol.*; 154(2):483-486.

Kogure *et al.* (2006). *Nat Biotechnol*; 24(5): 577-581

König H., Claus H., et Varma A. (Ed.) (2010). Prokaryotic Cell Wall Compounds, Structure and Biochemistry. Springer. ISBN 978-642-05061-9.

Kredel *et al.* (2009). *PLoS ONE*; 4(2): e4391.

Kremers *et al.* (2006). *Biochemistry*; 45(21): 6570-6580.

Kresch *et al.* (1991). *Lung* ;169(3):139-51.

Lam *et al.* (2012). *Nature Methods*; 9(10): 1005-1012.

Lin *et al.* (2009). *Chemistry & Biology*; 16(11): 1169-1179.

Markwardt *et al.* (2011). *PLoS ONE*; 6(3): e17896.

Matz *et al.* (1999). *Nat Biotechnol*; 17: 969-973.

Mena *et al.* (2006). *Nat Biotechnol*; 24(12): 1569-1571.

Merzlyak *et al.* (2007). *Nature Methods*; 4(7): 555-557.

Meyer *et al.* (2014). *Microbiologyopen.* ; 3(4): 531-43.

Morozova *et al.* (2010) *Biophysical Journal* ; 99(2): L13-L15.

Mujumdar *et al.* (1993). *Bioconjug Chem*. ;4(2):105-11.

Munoz *et al.*(2013). *J Cell Biol*.; 203:265-282.

Nagai *et al.* (2002). *Nat. Biotechnol.*; 20(1): 87-90.

Nguyen *et al.* (2005). *Nat Biotechnol.*; 23(3): 355-360.

Orm *et al.* (1996). *Science*; 273(5280): 1392-1395.

Osumi *et al.* (1998). *Fungal Genet Biol*. 24:178-206.

Paddock S. W. (Ed.) (2014). Methods in Molecular Biology,Confocal microscopy: Methods and Protocols. Springer

Pédelacq *et al.* (2005). *Nat Biotechnol*; 24(1): 79-88.

Perez, P., and J.C. Ribas (2004). *Methods*; 33:245-251.

Piatkevich *et al.* (2010). *Proceedings of the National Academy of Sciences*; 107(12): 5369-5374.

Piatkevich *et al.* (2013). *Sci. Rep.*; 3: article number 1847.

Pletnev *et al.* (2013). *Acta Crystallogr D Biol Cr;* 69(9): 1850-1860.

Rizzo *et al.* (2004). *Nat Biotechnol* 2004. 22(4): 445-449.

Sakaue-Sawano *et al.* (2008). *Cell*; 132(3): 487-498.

Sarkisyan *et al.* (2015). *Biophysical Journal*; 109(2): 380-389.

Shagin *et al*. (2004). *Mol Biol Evol;* 21: 841-850.

Shaner *et al.* (2004). *Nat Biotechnol*; 22(12): 1567-1572.

Shaner *et al.* (2005). *Nat Methods;* 2(12):905-9.

Shaner *et al.*(2008). *Nature Methods*; 5(6): 545-551.

Shaner *et al.* (2013). *Nature Methods*; 10(5): 407-409.

Shcherbo *et al.* (2009). *Biochem. J.*; 418(3): 567-574.

Shcherbo *et al.* (2010) *Nature Methods*; 7(10): 827-829.

Shcherbakova *et al.* (2012) *J. Am. Chem. Soc.*;134(18): 7913-7923.

Shcherbakova *et al.* (2013). *Nature Methods*; 10(8): 751-754.

Shemiakina *et al.* (2012) *Nature Communications*; 3: 1204.

Shu *et al.* (2009). *Science*;324(5928): 804-807.

Staniszewska *et al.* (2012). *Pol J Microbiol*.; 61:129-135.

Subach *et al.* (2008). *Chemistry & Biology*; 15(10): 1116-1124.

Subach *et al.* (2011). *PLoS ONE*; 6(12): e28674.

Tomosugi *et al.* (2009). *Nature Methods*; 6(5): 351 -353.

Tsutsui *et al.* (2008). *Nature Methods*; 5(8): 683-685.

Xia *et al.* (2002). *Mar Biotechnol.*; 4:155-162.

Yamaoka *et al.* (2013). *Eukaryot Cell*.; 12:1162-1170.

Yang *et al.* (1996). *Nucleic Acids Research*. 24(22): 4592-4593.

Yang *et al.* (2013). *PLoS ONE*; 8(6): e64849.

Yu *et al.* (2014). *Nature Communications*; 5: article number: 3626.

Yu *et al.* (2015). *Nature Methods*; 12(8): 763-765.

Wang *et al.* (2004). *Proceedings of the National Academy of Sciences*; 101 (48): 16745-16749.

Weibel et a*l. (2007). Nat Rev Microbiol.;* 5(3): 209-218*.*

Wild D. (Ed) (2013). The Immunoassay Handbook, 4ème édition. Elsevier. ISBN 9780080970370.

Wong et Jameson (2011). Chemistry of Protein and Nucleic Acid Cross-linking and Conjugation, 2ème édition. CRC Press. ISBN 9780849374913.

Zacharias *et al.* (2002). *Science*; 296:913-916.

Zapata-Hommer *et al.* (2003). *BMC Biotechnology*; 3(1): 5.

Zimmer M. (2015a). Illuminating disease : An introduction to green fluorescent proteins, Oxford University. ISBN-13: 978-0199362813.

Zimmer M. (2015b). Bioluminescence: Nature and Science at Work, Twenty-First Century Books. ISBN-13: 978-1467757843.

Zhu *et al.* (1996). *FEBS Lett*.; 390(3):271-4.

REVENDICATIONS

1. Procédé *in vitro* pour mesurer en temps réel l'épaisseur de la paroi cellulaire de cellules à paroi, comprenant:
   a) fournir au moins une cellule isolée ayant une paroi cellulaire, la face externe de ladite paroi cellulaire étant marquée avec au moins un premier marqueur détectable, et la face interne de ladite paroi cellulaire étant marquée avec au moins un second marqueur détectable, lesdits marqueurs étant distincts l'un de l'autre ;
   b) imager ladite cellule et détecter lesdits marqueurs à l'aide d'un dispositif optique à haute-résolution, préférablement à l'aide d'un microscope photonique ;
   c) déterminer la distance entre ledit premier marqueur sur la face externe et ledit second marqueur sur la face interne, mesurant ainsi l'épaisseur de la paroi cellulaire.

2. Procédé selon la revendication 1, caractérisé en ce que ladite cellule à paroi est sélectionnée dans le groupe consistant en les cellules de champignons, de bactéries, d'archées, de plantes, et d'algues.

3. Procédé selon la revendication 1 ou 2, caractérisé ce que ledit premier marqueur détectable est un marqueur luminescent émettant une radiation lumineuse dans une première gamme de longueur d'onde, et ledit second marqueur détectable est un marqueur luminescent émettant une radiation lumineuse dans une seconde gamme de longueur d'onde distincte de la première gamme de longueur d'onde.

4. Procédé selon la revendication 3, caractérisé en ce que ledit premier et/ou ledit second marqueur luminescent est un marqueur fluorescent préférablement sélectionné parmi :

   - les marqueurs fluorescents protéiques tels que les protéines de fluorescence verte, les protéines de fluorescence rouge ou orange, les protéines de fluorescence cyan, les protéines de fluorescence bleue ou violette, les protéines de fluorescence jaune ; et

   - les marqueurs fluorescents non protéiques tels que le DiBAC (bis-(1,3-dibutylbarbituric acid) trimethine oxonol) et ses dérivés, les dérivés de xanthène, les rhodamines et leurs dérivés, les dérivés de cyanine, les dérivés de squaraine, les dérivés de naphthalène, les dérivés de coumarine, les dérivés d'oxadiazole, les

dérivés de pyrène, les dérivés d'oxazine, les dérivés d'arylméthine, les marqueurs AlexaFluor.

5. Procédé selon la revendication 3 ou 4, caractérisé en ce que :
   - ledit premier marqueur luminescent est un couplé à une molécule capable de se lier à la face externe de la paroi cellulaire ; et/ou
   - ledit second marqueur luminescent est un couplé à une protéine de la membrane cellulaire ou à une molécule capable de se lier à la membrane cellulaire, ou est capable de se lier à la membrane cellulaire.

6. Procédé selon la revendication 5, caractérisé en ce que :
   - ladite molécule capable de se lier à la face externe de la paroi cellulaire est une lectine, préférablement sélectionnée dans le groupe des lectines se liant spécifiquement aux motifs de type galactose et/ou à la N-acétylgalactosamine, des lectines se liant spécifiquement aux motifs de type acide sialique et/ou N-acétylglucosamine, des lectines se liant spécifiquement aux motifs de type mannose, et des lectines se liant spécifiquement aux motifs de type fucose ; et/ou
   - ladite protéine de la membrane cellulaire est sélectionnée dans le groupe constitué par les protéines membranaires de champignons, les protéines membranaires de bactéries, les protéines membranaires d'archées, les protéines membranaires de plantes, les protéines membranaires d'algues, et leurs homologues ; et/ou
   - ladite molécule capable de se lier à la membrane cellulaire est un polypeptide comprenant ou consistant en au moins un domaine de liaison aux lipides tels que ceux appartenant au groupe des domaines CaaX (SEQ ID NO :1), des domaines de myristoylation, des domaines PH, des domaines BAR, des domaines FYVE, des domaines PX, et des domaines ENTH; et/ou
   - ledit marqueur luminescent capable de se lier à la membrane cellulaire est sélectionné parmi le DiBAC et ses dérivés.

7. Procédé selon l'une quelconque des revendications 3 à 6, caractérisé en ce que l'étape c) de détermination de la distance entre le premier marqueur et le second marqueur comprend :
   i) détecter, dans une direction perpendiculaire à la tangente à la paroi cellulaire en un point de ladite paroi, un premier maximum de radiation lumineuse dans ladite première gamme de longueur d'onde et un second maximum de radiation

lumineuse dans ladite seconde gamme de longueur d'onde, la distance entre le premier et le second marqueur en ce point étant définie comme la distance entre le premier et le second maximum de radiation lumineuse ; et

ii) optionnellement, répéter l'étape i) en une pluralité de points de la paroi cellulaire.

8. Procédé *in vitro* pour évaluer en temps réel la viabilité cellulaire, la synthèse de la paroi cellulaire, la morphogénèse cellulaire, l'homéostasie de la paroi cellulaire et/ou la polarité de cellules à paroi, comprenant:

a) mesurer en temps réel l'épaisseur de la paroi cellulaire d'au moins une cellule isolée selon le procédé tel que défini dans l'une quelconque des revendications 1 à 7 ; et

b) évaluer la viabilité, la synthèse de la paroi cellulaire, la morphogénèse, l'homéostasie de la paroi cellulaire et/ou la polarité de ladite cellule, en fonction de l'épaisseur de la paroi cellulaire mesurée à l'étape a).

9. Procédé *in vitro* pour déterminer la résistance de cellules à paroi envers un agent ou combinaison d'agents capables de modifier l'épaisseur de la paroi cellulaire, comprenant :

a) mesurer en temps réel l'épaisseur de la paroi cellulaire d'au moins une cellule isolée selon le procédé tel que défini dans l'une quelconque des revendications 1 à 7, en présence d'un agent ou combinaison d'agents capables de modifier l'épaisseur de la paroi cellulaire et optionnellement en absence dudit agent ou de ladite combinaison d'agents ;

b) déterminer si l'épaisseur de la paroi cellulaire est modifiée par ledit agent ou ladite combinaison d'agents ; et

c) optionnellement, déterminer la résistance de la cellule envers l'agent ou combinaison d'agents capables de modifier l'épaisseur de la paroi cellulaire.

10. Procédé pour déterminer ou adapter un régime thérapeutique destiné à un sujet infecté par une cellule à paroi pathogène, comprenant :

a) déterminer la résistance d'au moins une cellule à paroi isolée dudit sujet envers un agent ou combinaison d'agents capables de modifier l'épaisseur de la paroi cellulaire, selon le procédé tel que défini dans la revendication 9 ; et

b) déterminer ou adapter un régime de traitement en fonction de la résistance ou de la non-résistance de la cellule à paroi envers ledit agent ou ladite combinaison d'agents, telle que déterminée à l'étape a).

11. Procédé *in vitro* pour cribler des agents capables de modifier l'épaisseur de la paroi cellulaire de cellules à paroi, comprenant :

a) mesurer en temps réel l'épaisseur de la paroi cellulaire d'au moins une cellule isolée selon le procédé tel que défini dans l'une quelconque des revendications 1 à 7, en présence d'un agent candidat ou combinaison d'agents candidats et optionnellement en absence dudit agent ou de ladite combinaison d'agents ;

b) déterminer si l'épaisseur de la paroi cellulaire est modifiée par ledit agent ou ladite combinaison d'agents ; et

c) optionnellement, identifier l'agent ou combinaison d'agents capables de modifier l'épaisseur de la paroi cellulaire de ladite cellule.

12. Kit comprenant :

a) un premier marqueur luminescent couplé à une molécule capable de se lier à la face externe de la paroi cellulaire d'une cellule à paroi ; et

b) un second marqueur luminescent couplé à une molécule capable de se lier à la membrane cellulaire de ladite cellule ou à une protéine de la membrane cellulaire de ladite cellule, ou un second marqueur luminescent capable de se lier à la membrane cellulaire de ladite cellule.

13. Utilisation d'un kit tel que défini dans la revendication 12 dans l'un quelconque des procédés tels que définis dans les revendications 1 à 11.

ABREGE

La présente invention se rapporte au domaine de l'industrie en biotechnologie, dont la portée d'application est aussi bien dans le secteur de la santé, de l'agro-industrie que de la recherche. La présente invention propose plus particulièrement une nouvelle méthode pour mesurer l'épaisseur de la paroi cellulaire de cellules à paroi, ainsi que sa mise en œuvre dans diverses applications.

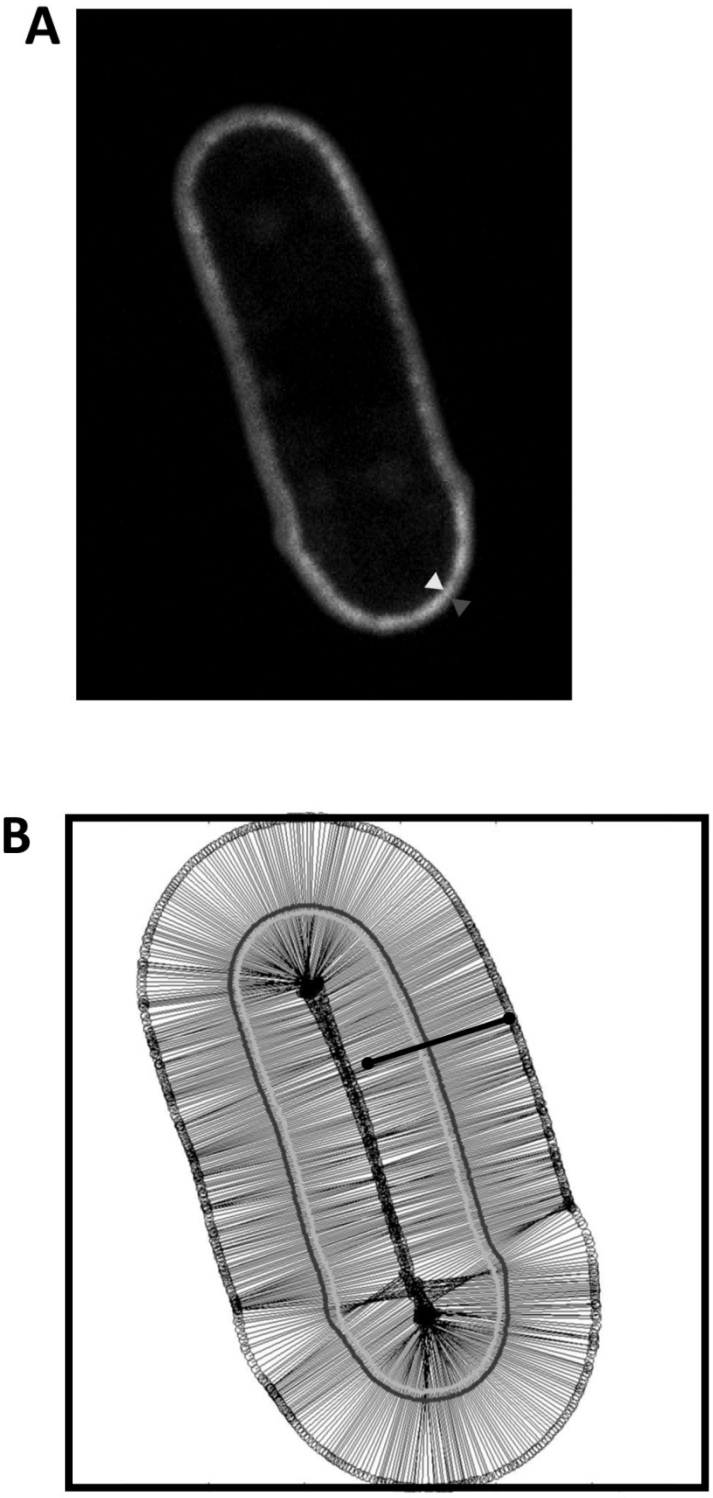

Figure 1

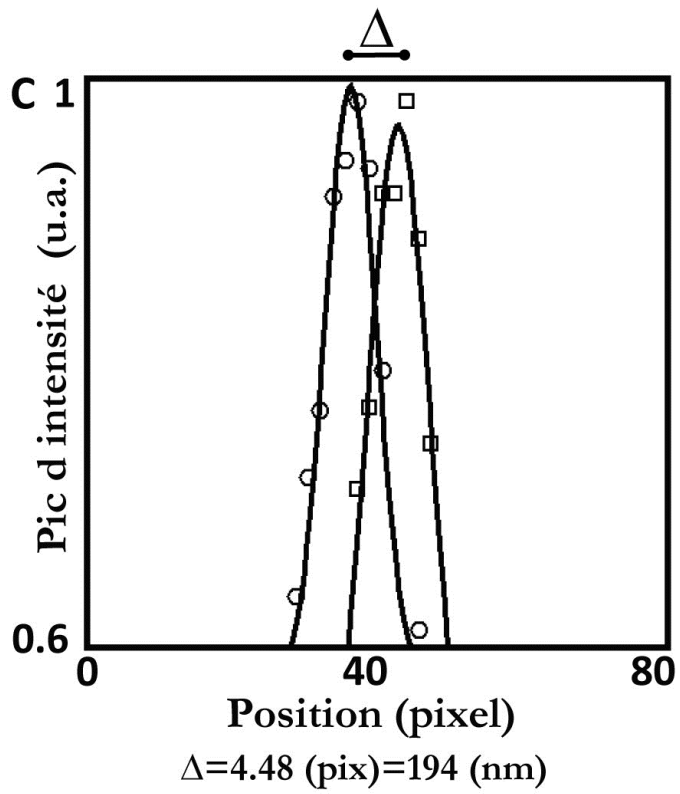

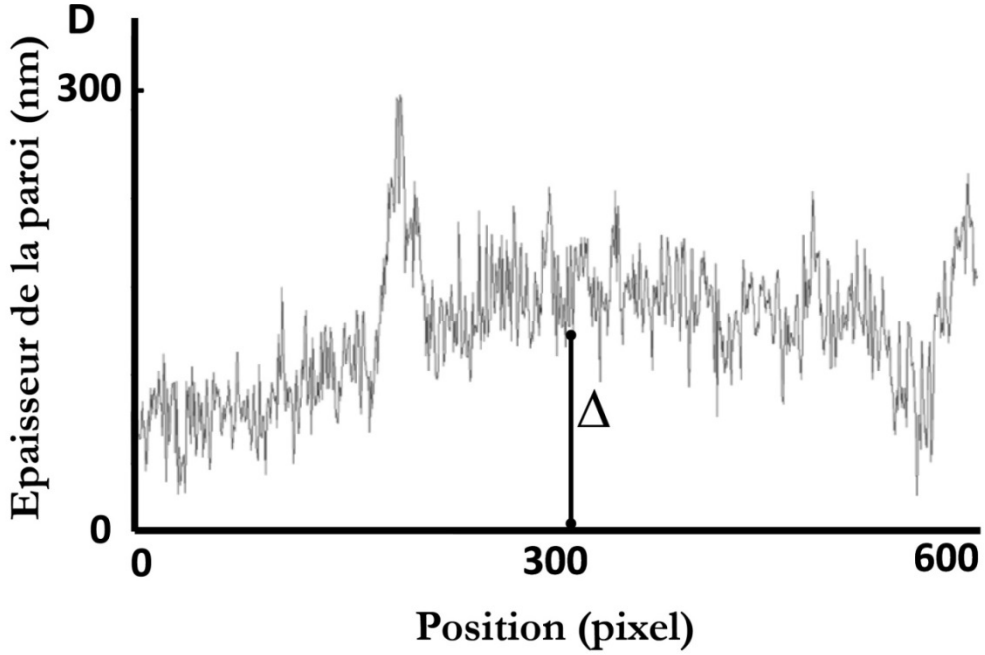

Figure 1 (suite)

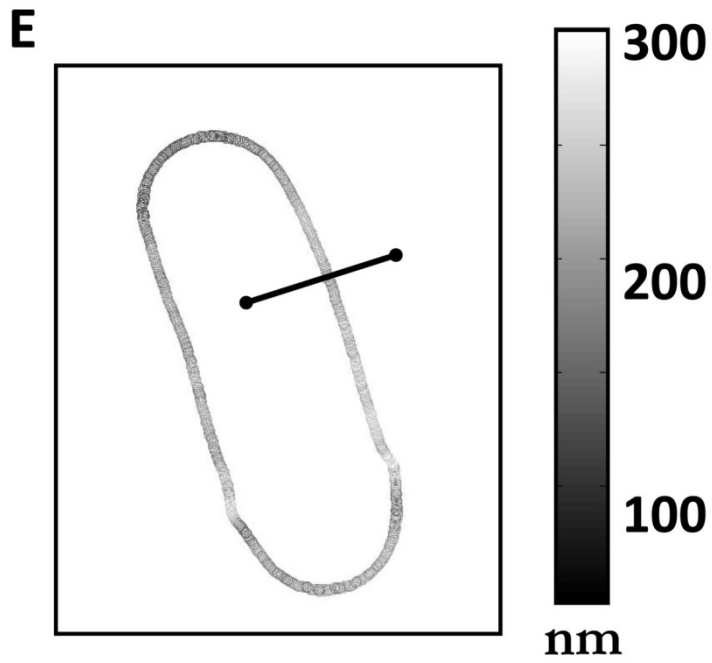

Figure 1 (suite)

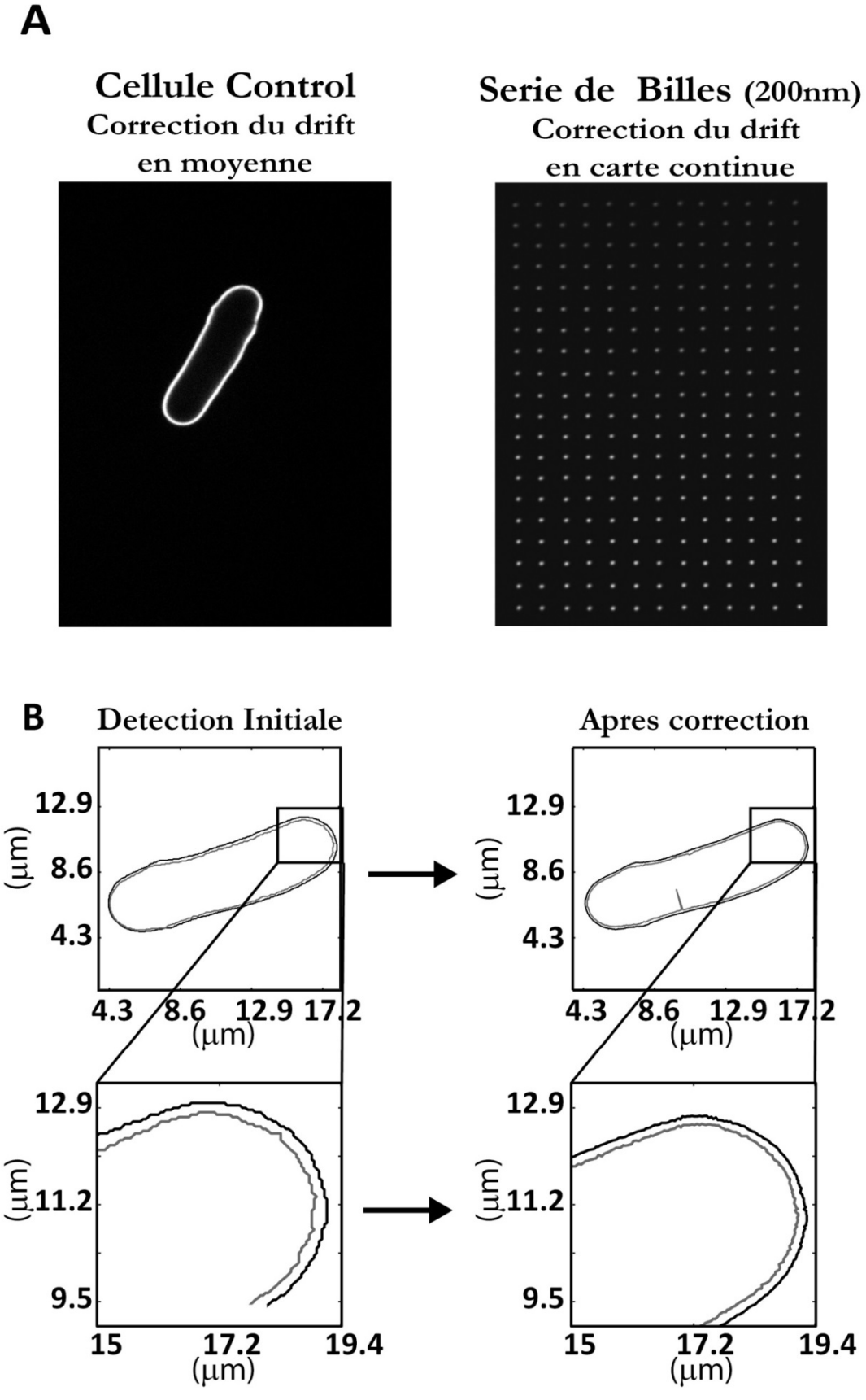
A
Cellule Control
Correction du drift
en moyenne
Serie de Billes (200nm)
Correction du drift
en carte continue
B
Detection Initiale
Apres correction
12.9
8.6
4.3
(µm)
4.3 8.6 12.9 17.2
(µm)
12.9
11.2
9.5
15 17.2 19.4
(µm)

Figure 2

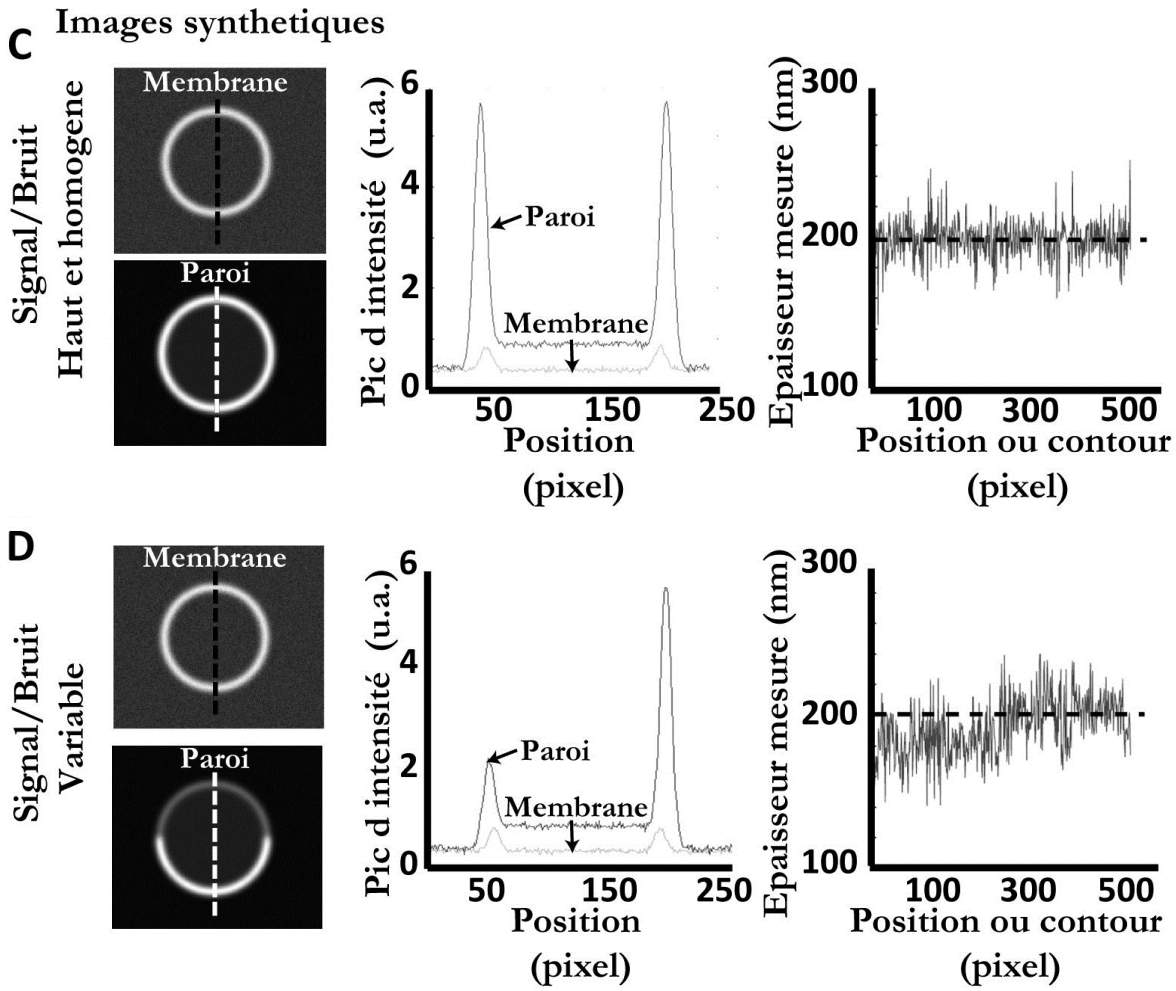

Figure 2 (suite)

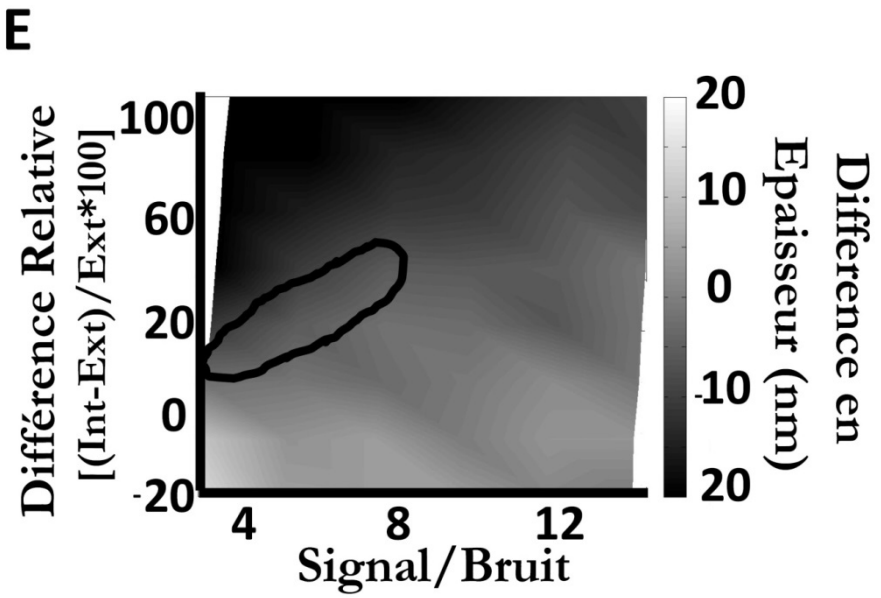

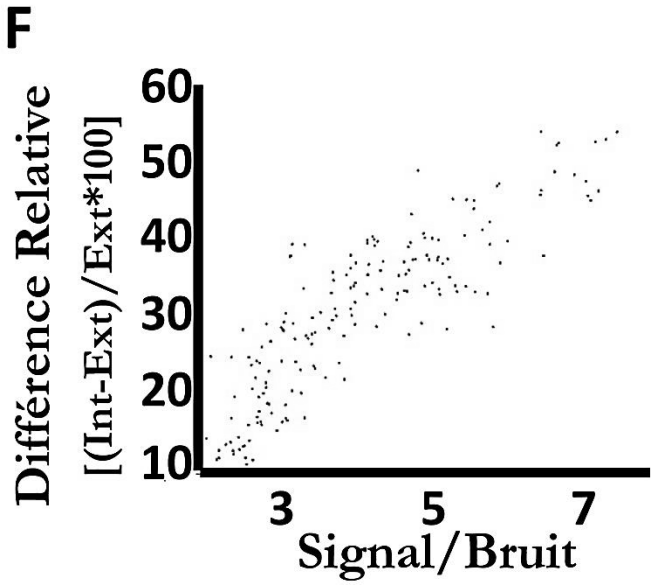

Figure 2 (suite)

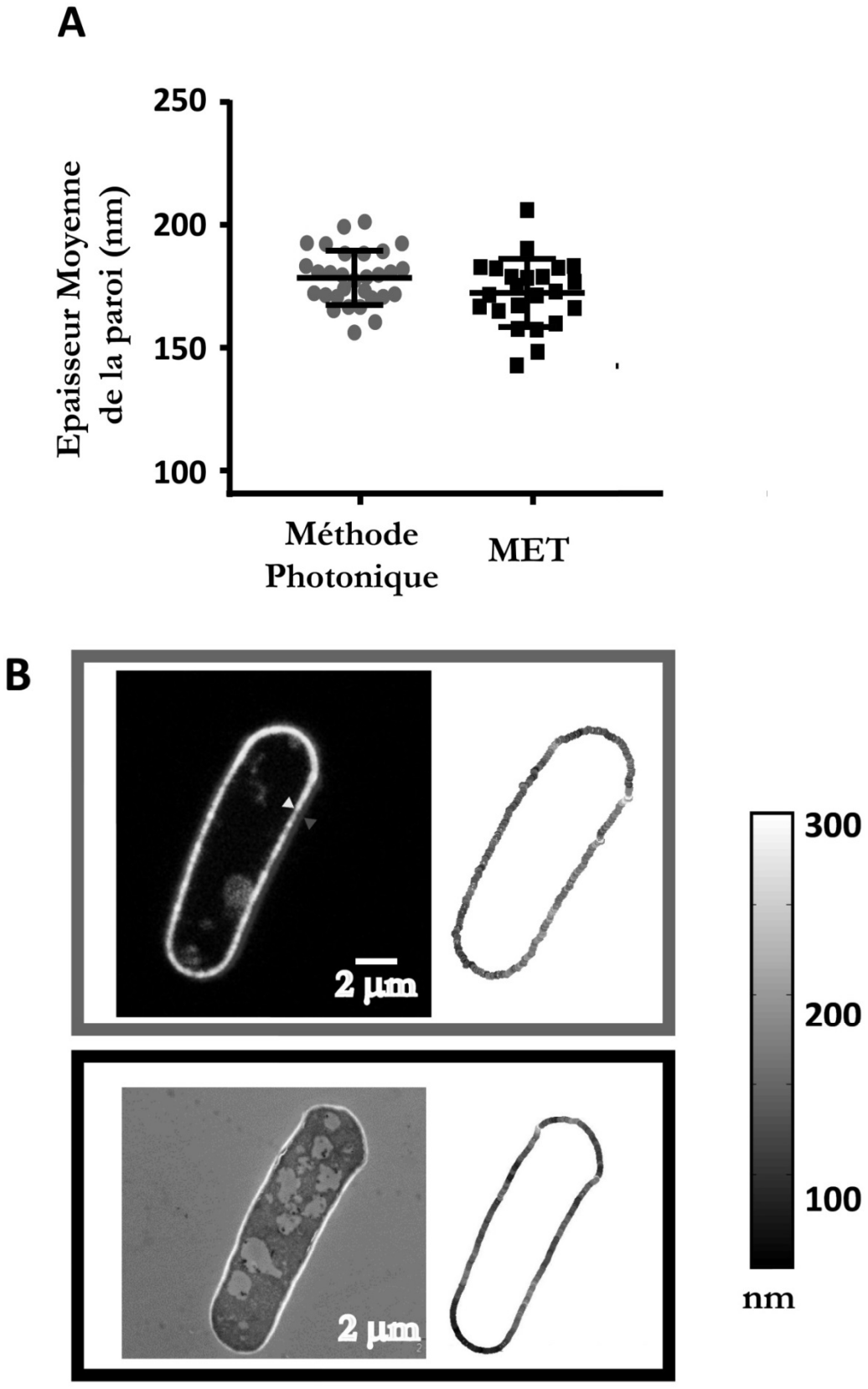
A
250
200
150
100
Epaisseur Moyenne de la paroi (nm)
Méthode Photonique
MET
B
2 µm
2 µm
300
200
100
nm

Figure 3

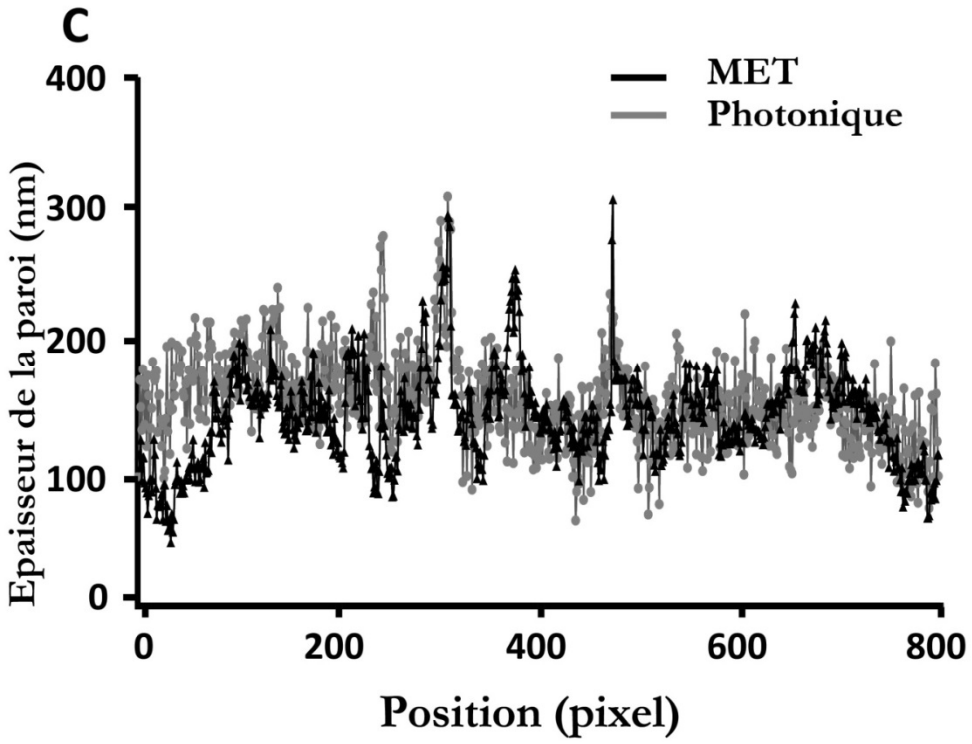

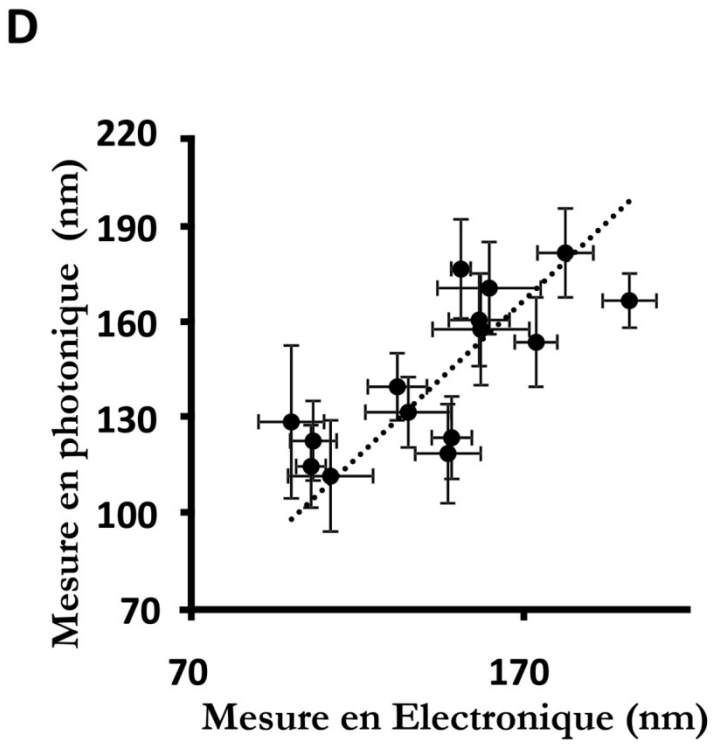

Figure 3 (suite)

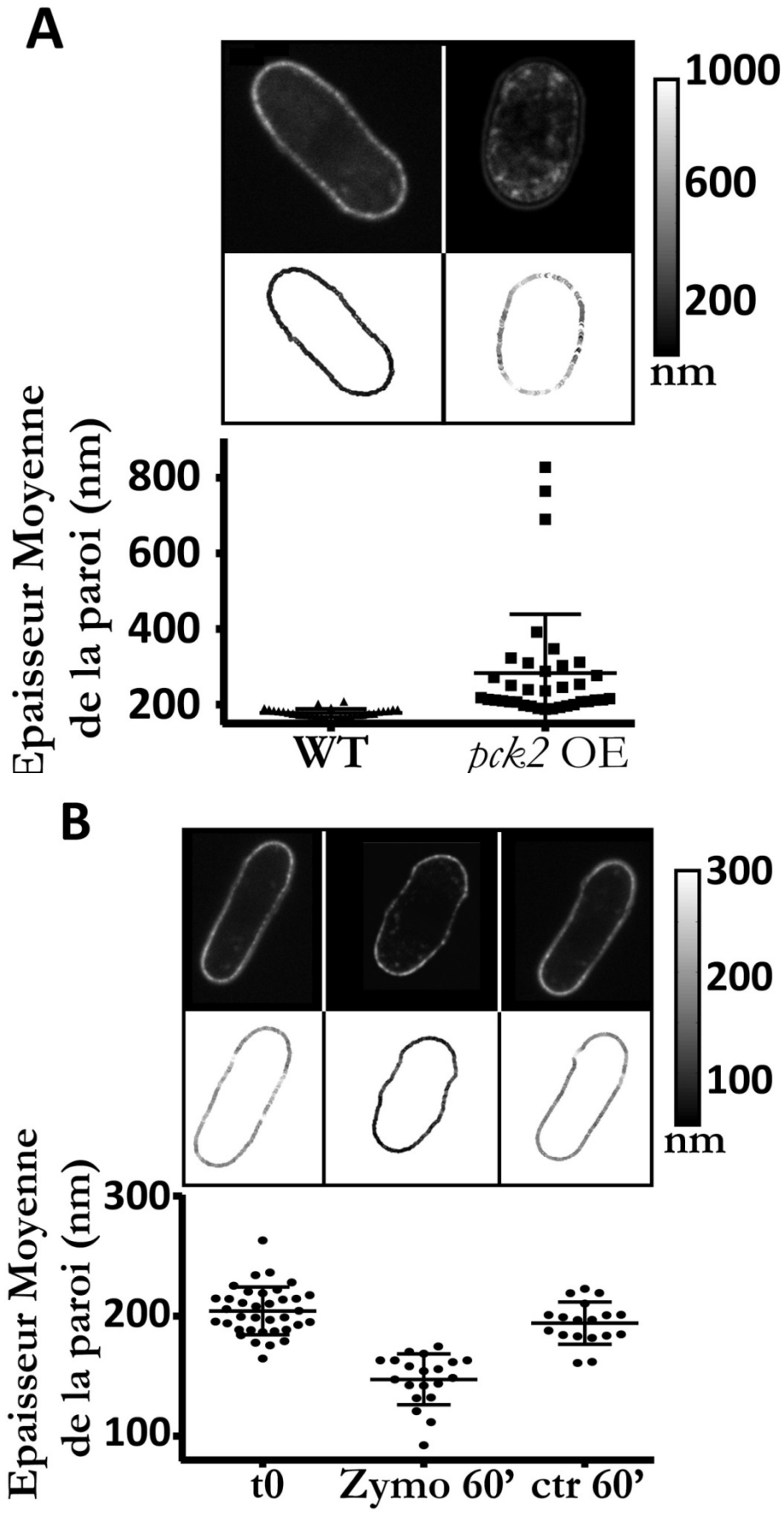
A
1000
600
200
nm
Epaisseur Moyenne de la paroi (nm)
800
600
400
200
WT
pck2 OE
B
300
200
100
nm
Epaisseur Moyenne de la paroi (nm)
300
200
100
t0
Zymo 60'
ctr 60'

Figure 4

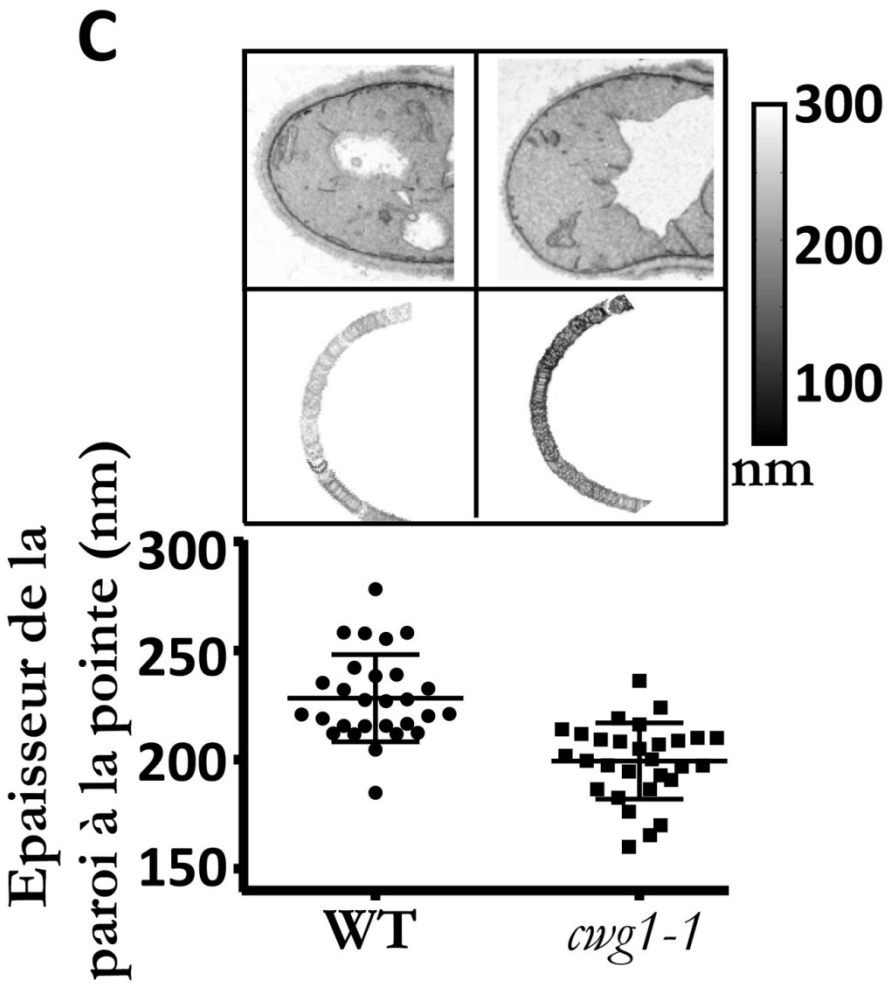

Figure 4 (suite)

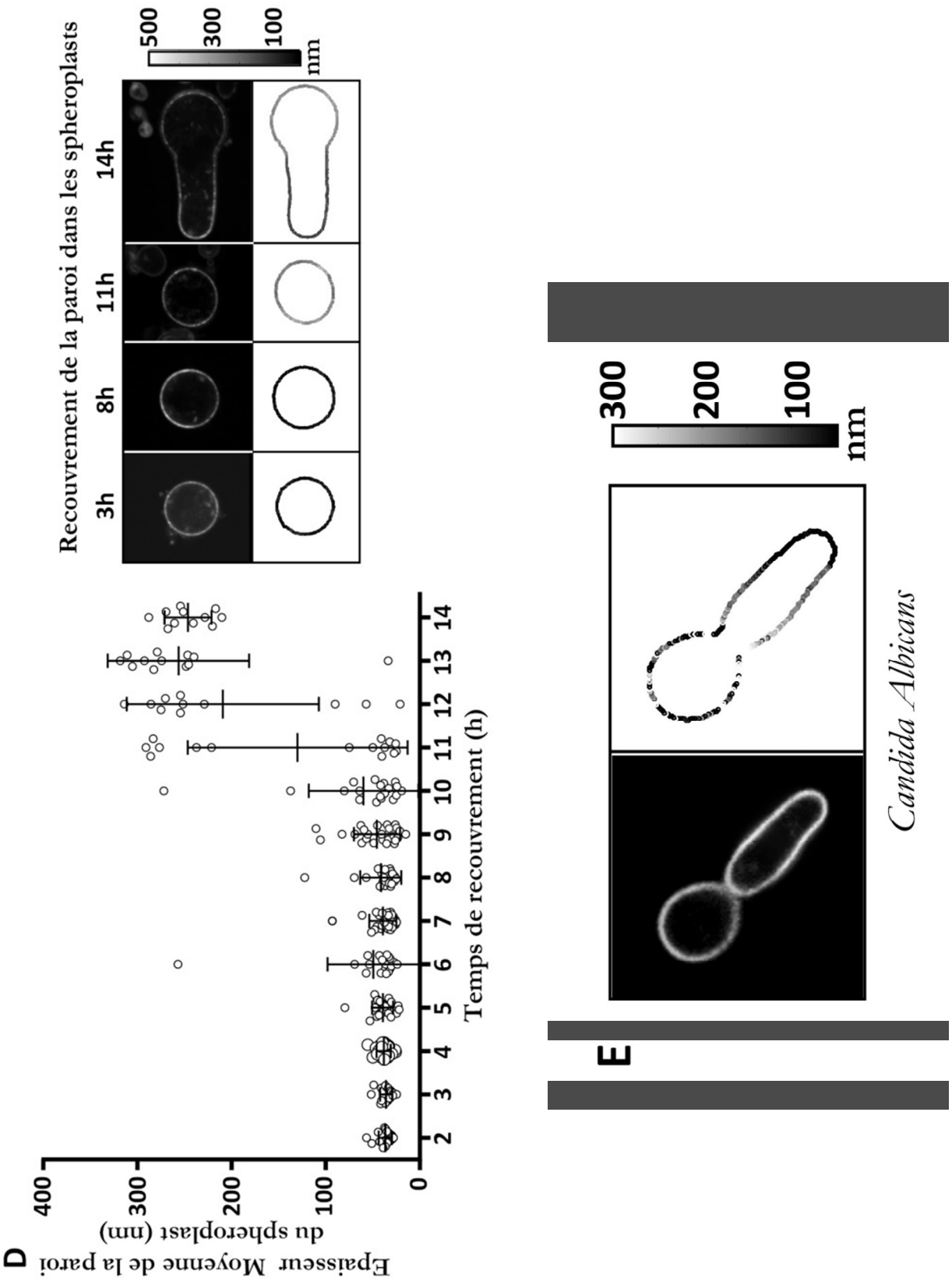

Figure 4 (suite)

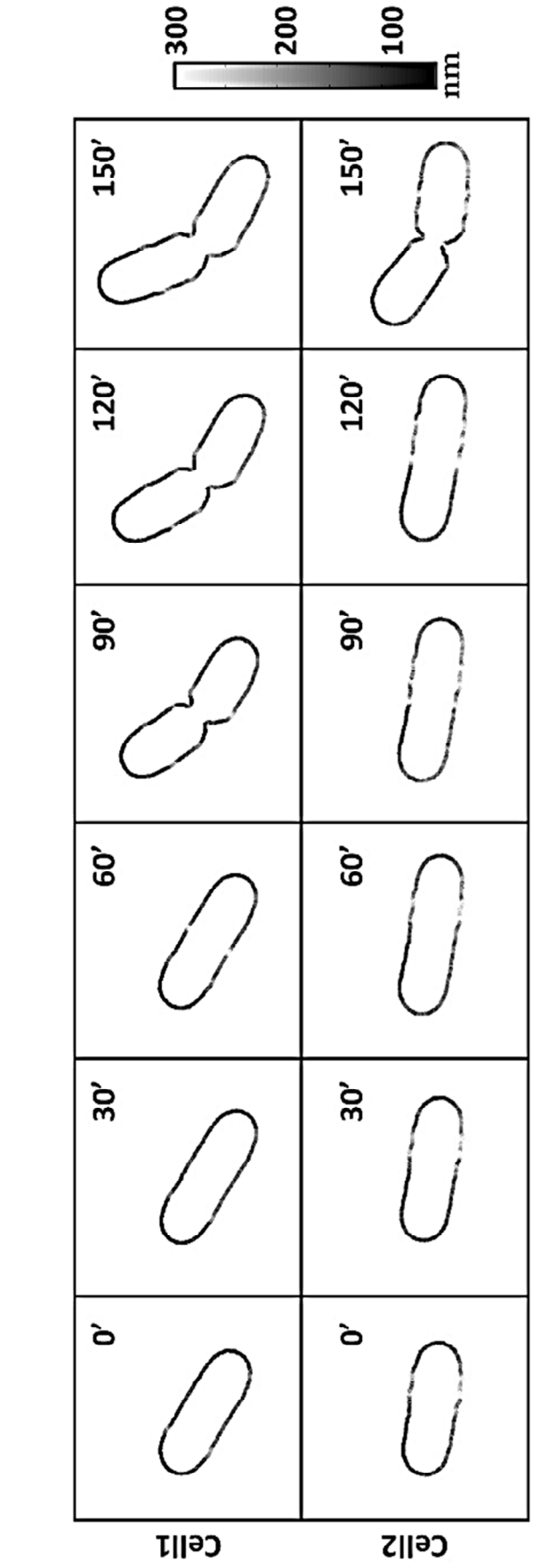

Figure 5

RÉSUMÉ

Dynamique de la paroi cellulaire dans la régulation de la morphogenèse et de la croissance cellulaire

RÉSUMÉ

Introduction et objectifs de l'étude

Les cellules dans la nature se développent avec des formes très différentes et croissent dans des structures profondément diverses, nécessaires pour acquérir et maintenir leur physiologie et leur fonctionnalité. Ces processus sont le résultat de régulations génétiques et biochimiques complexes, qui permettent de réguler la distribution locale des protéines, la synthèse de nouveaux matériaux, la déformation et le remodelage, afin de modifier la mécanique de la surface cellulaire. Toutefois, l'interaction complexe entre ces niveaux de régulation est encore peu claire.

Dans la plupart des organismes vivants, des plantes aux bactéries et aux champignons, la surface cellulaire se compose d'une structure rigide recouvrant les limites des cellules, appelée paroi cellulaire. En raison de sa raideur, les parois des cellules sont souvent appelées coques.

Malgré la rigidité de leurs surfaces, les cellules à paroi peuvent subir des processus très dynamiques de croissance polarisée rapide, de réorientation vers / contre des stimuli et acquièrent des formes profondément différentes, à la fois en tant que cellules individuelles ou dans les tissus.

Des énormes variations morphologiques sont observées chez les bactéries et leur forme a souvent été utilisée pour leur classification. Les bactéries sphériques / en forme de billes sont appelées cocci, mais les cocci peuvent aussi être un peu ovales ou pointues. Les bacilles sont en forme de bâtonnet et ont un rapport longueur / rayon variable. Les tiges plus larges et courtes s'appellent des coccobacilles. Les tiges coudées sont normalement appelées vibrions. Ces cellules de formes simples peuvent souvent se développer dans une structure multicellulaire, sous forme de chaînes ou de carrés. Les spirillia et spirochete sont tous deux caractérisés par une forme en spirale incurvée. Bien que les premières soient rigides, les dernières sont plus flexibles.

Les cellules végétales, dans les tissus, peuvent également acquérir des formes très diverses. Un exemple est le plan très organisé de formes cubiques et rectangulaires, typiques des racines. Un autre bel exemple est celui des cellules pavimenteuses épidermiques des feuilles, dans lesquelles des modèles de croissance multipolaires émergent pour générer des formes cellulaires irrégulières complexes, qui, chez certaines espèces, créent des indentations dans leur paroi cellulaire anticlinale, ce qui a été comparé à un puzzle. Dans le même tissu, des cellules gardiennes beaucoup plus petites, entourent les pores du stomate et sont en forme de rein, pour permettre l’ouverture et la fermeture du stomate nécessaire pour l’échange des gaz.

De plus, parmi les cellules à paroi, la croissance peut être très rapide, comme chez le tube pollinique de Lily, capable de croître à une vitesse supérieure à 10 µm par minute, nécessaire pour fertiliser le gamète femelle.

Les cellules à paroi se caractérisent également par une très forte pression interne de turgescence, qui est le moteur de la croissance. Pour comprendre comment ces cellules acquièrent leur morphologie, nous devons étudier les propriétés et la dynamique de ces deux éléments mécaniques, la paroi cellulaire et la turgescence.

La pression de turgescence interne a été estimée dans des fourchettes comprises entre 0,1 et 2 MPa chez les plantes et les champignons, avec des pics allant jusqu'à 8 MPa dans les appressoria, des structures envahissantes spécifiques de champignons pathogènes filamenteux. Bien que la turgescence soit le moteur efficace de la croissance et de la déformation de la paroi, sa seule contribution ne peut expliquer les formes asymétriques acquises par plusieurs types des cellules à parois, car sa force est égale dans toutes les directions. Par conséquent, pour comprendre la forme polarisée et le mécanisme de croissance de ces cellules, il faut étudier la mécanique de leur paroi cellulaire (Figure R.2).

En effet la paroi modèle littéralement la cellule dessous, comme le montre clairement sa digestion enzymatique dans des conditions osmo-équilibrées: le protoplaste résultant (cellule sans paroi) perd totalement sa morphologie cellulaire en devenant rond, alors qu'une forme «fantôme» intacte est souvent laissés derrière qui n'est rien d'autre que la paroi (Figure R.1).

La paroi cellulaire est composée de différents types de polymères selon le type de cellule, mais en général, les principaux composants structurels sont des chaînes de glucanes et / ou des protéines.

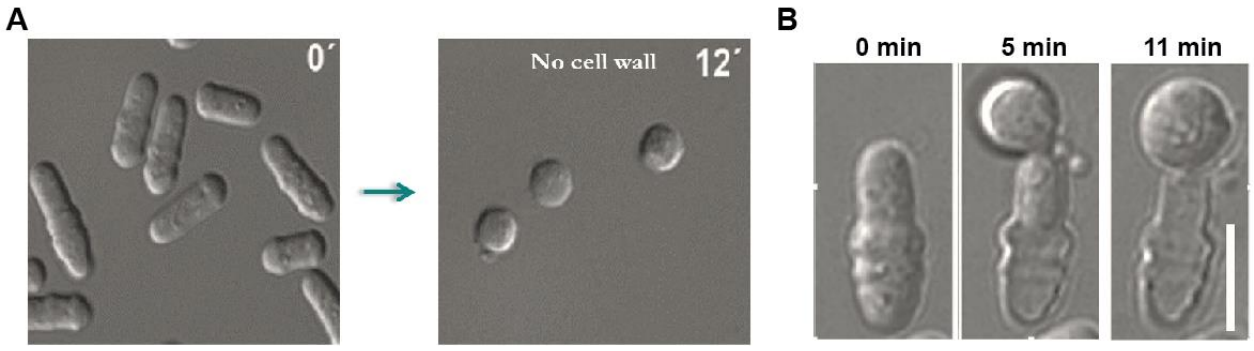

Figure R.1 ***Importance de la paroi cellulaire dans la morphogenèse cellulaire.*** *A. La digestion enzymatique de la paroi cellulaire en condition iso-osmotique conduit à une perte totale de la forme de la cellule. B. Lorsque la paroi est digéré d'un côté, le protoplaste peut sortir, laissant derrière lui une forme de cellule presque intacte, c'est-à-dire la forme de la paroi (Adapté par Flor-Parra et al., 2013).*

Chez les plantes et les champignons les parois sont principalement composées de polysaccharides. Ce sont des chaînes d'unités monosaccharides, liées par des liaisons glycosidiques. Par exemple, les β-glucanes sont créés par des liaisons béta entre le carbone 1 d'un monomère de D-glucose et le carbone 3 du monomère suivant. Les chaînes peuvent également se ramifier, par exemple, dans le gluc-glucane, le groupe OH du carbone 6 peut créer une liaison glycosidique avec un carbone anomère libre d'un nouveau monomère ou d'une nouvelle chaîne D-glucose. Les chaînes parallèles peuvent également interagir par le biais de modifications latérales, créant ainsi des faisceaux parallèles réticulés. Des chaînes de différentes natures peuvent se lier: cette interaction est également appelée cross-link.

La composition et les arrangements de polysaccharides confèrent à la paroi cellulaire ses propriétés mécaniques qui, d'une manière simpliste, peuvent être résumées en épaisseur et en élasticité.

L'épaisseur de la paroi peut varier dans les organismes entre 100 et 500 nm.

L'élasticité est typiquement très élevée, et chez les plantes et les champignons est estimée à des modules d'Young de $10^4/10^5$ Pa.

Après synthèse, la paroi se déforme sous l'effet de la pression de turgescence et, dans certains cas, de l'activité enzymatique, conduisant à sa structure finale (Figure R.2). Dans ces cellules, la croissance cellulaire peut être un processus très dangereux dans les cellules à paroi. Étant donné que la paroi cellulaire maintient la pression de turgescence interne élevée, une expansion incontrôlée de la paroi cellulaire peut entraîner le perçage de la paroi et la lyse cellulaire. Par conséquent, dans ces cellules, la croissance doit s'accompagner d'une interaction complexe entre la distribution locale du matériau, la synthèse des parois, le remodelage et la déformation.

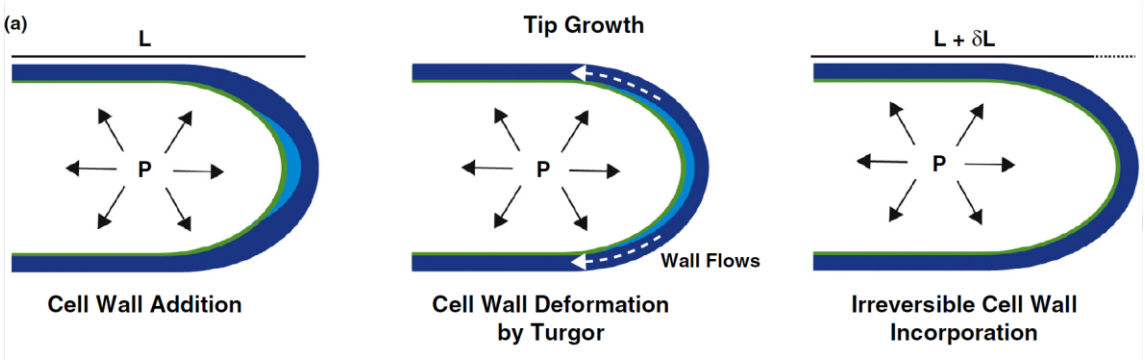

Figure R.2 ***La croissance des cellules à paroi.*** *Au cours de la croissance, du nouveau matériau de paroi (bleu clair) est déposé à la surface de la cellule, puis remodelé par une pression de turgescence interne (P), pour être incorporé de manière irréversible à la structure. Adapté de (Davì et Minc, 2015)*

RÉSUMÉ

De nombreuses études ont focalisé leur attention sur la mécanique de la paroi cellulaire pour comprendre les phénomènes de croissance et de morphogenèse, mais rarement son comportement dynamique a été étudié expérimentalement, principalement en raison du manque de méthodes pour l'imagerie in vivo de la paroi cellulaire. En fait, l'épaisseur de la paroi est normalement en dessous de la résolution de la microscopie optique. L'état de l'art consiste à l'imager par microscopie électronique à transmission, qui est bien sûr un outil puissant, mais puisque il faut fixer l'échantillon, ne donne aucun accès à la dynamique de ses structures.

Pour une meilleure compréhension de cette dynamique, les questions que je voudrais aborder dans mon étude sont les suivantes :

Quel est le comportement dynamique des parois cellulaires ?

Pour répondre à cette question, dans mon travail, je me suis concentré sur un sous-ensemble de cellules à paroi, c'est-à-dire des cellules isolées (ne faisant pas partie d'un tissu), qui poussent par extension de la pointe générant des formes tubulaires et en particulier sur la levure fissipare, *Schizosaccharomyces pombe*, qui parmi elles, est la mieux décrite. Vue que, jusqu'à présent, l'accès à la dynamique des parois cellulaires était très limitée, ma première réalisation a été la mise au point de nouvelles méthodes appropriées pour suivre les paramètres mécaniques de la paroi cellulaire *in vivo*. Cela a permis les toutes premières observations de la dynamique de la paroi cellulaire, montrant que la paroi cellulaire est stable dans les régions stables, mais très variable dans les régions en croissance.

Ces résultats ont conduit aux questions suivantes :

Comment la dynamique de la paroi cellulaire est-elle régulée pour assurer la croissance tout en préservant l'intégrité des cellules ?

Tel que discuté, les cellules de croissance de la pointe sont dans une situation précaire constante, car pendant la croissance, le dépôt de nouveau matériau de paroi doit constamment équilibrer la pression de turgescence interne qui, sans un soutien suffisant, peut provoquer la lyse cellulaire. Pour étudier cet aspect, dans la première partie de mes résultats, j'ai caractérisé la dynamique des parois et les régulateurs de synthèse de paroi dans les cellules sauvages, ainsi que dans les mutants de voies hautement conservées impliquées dans le maintien de l'intégrité cellulaire.

Comment les propriétés mécaniques des parois influencent-elles la forme des cellules ?

En exploitant la forme stéréotypée de la levure de fission, dans la seconde partie de mes résultats, j'ai étudié la corrélation entre les propriétés mécaniques des parois et le diamètre cellulaire, dans différentes conditions de la souche sauvage et chez des dizaines de mutants défectueux en diamètre ou synthèse de paroi. En outre, j'ai observé des changements de diamètre après perturbation des propriétés de la paroi, découvrant un mécanisme supposé de régulation de dimension et intégrité de la cellule.

Le but de ces travaux est de poser les bases de la compréhension de la régulation dynamique des parois cellulaires et de leur influence sur les processus fondamentaux, tels que la croissance et l'établissement de la forme dans les cellules à paroi.

Résultats

1- La mécanosensibilité coordonne dynamiquement la croissance polaire et l'assemblage de la paroi cellulaire pour promouvoir la survie des cellules

Dans ce travail, nous avons développé une nouvelle méthode pour mesurer l'épaisseur de la paroi cellulaire avec une résolution sous-cellulaire dans des cellules vivantes de levure à fission. Cette méthode repose sur l'utilisation de marqueurs fluorescents pour étiqueter la partie interne et externe de la paroi cellulaire. L'utilisation d'une pipeline d'analyse d'images semi-automatisée, permet de mesurer la distance entre les deux fluorophores au bord de la cellule.

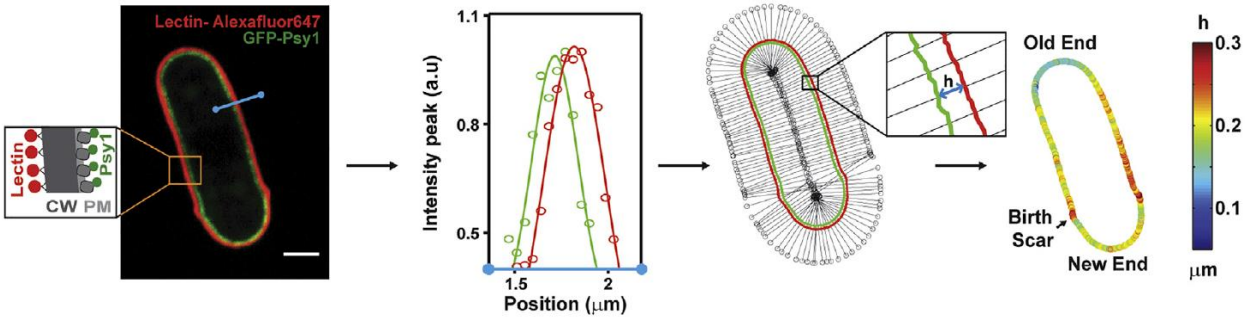

Figure R.3 ***Une méthode pour imager l'épaisseur de la paroi cellulaire autour des cellules vivantes.*** *Image confocale à mi-coupe d'une cellule de levure à fission exprimant GFP-Psy1 (membrane plasmique - PM) et marquée à la lectine-Alexafluor647 (surface externe - CW). Les contours sont déterminés à partir des centres des gaussiens de chaque signal sur la surface de la cellule (ligne bleue). Après l'enregistrement du décalage chromatique, la distance entre les deux contours donnent des mesures d'épaisseur en CW (h). (Droite) Carte de couleur d'épaisseur autour d'une cellule.*

Grâce à cette méthode, nous avons pu observer, pour la toute première fois à notre connaissance, la dynamique de l'épaisseur des parois lors de la croissance polarisée d'un champignon en croissance. Cela a montré que la paroi cellulaire est polarisée, plus fine et plus molle au niveau des sites de croissance.

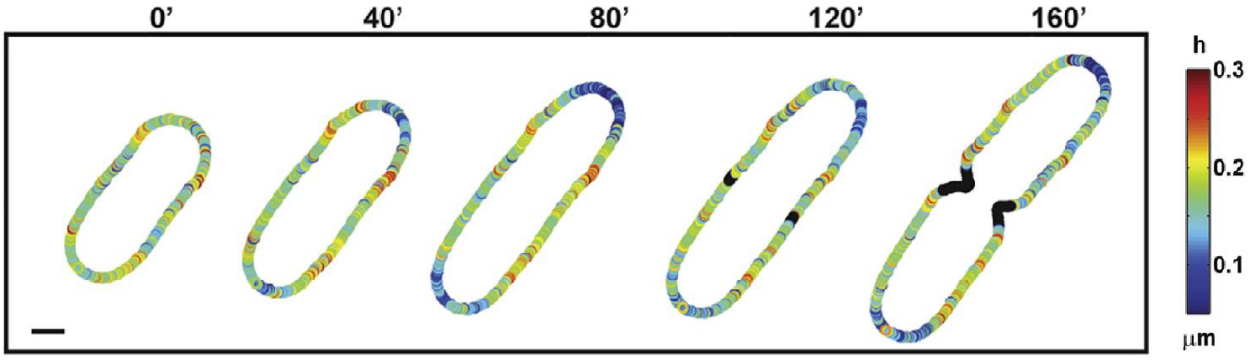

Figure R.4 ***La paroi cellulaire est polarisé et plus fine dans les sites de croissance***. *Laps de temps des cartes d'épaisseur de la paroi d'une cellule en croissance. Les points noirs correspondent aux positions dans lesquelles l'épaisseur ne peut pas être mesurée avec précision*.

À l'aide d'un modèle théorique simple, nous avons pu observer que l'épaisseur des pôles en croissance et le taux de croissance s'influencent négativement, ce qui peut provoquer des événements catastrophiques : par exemple, si la paroi cellulaire est mince, la cellule peut pousser plus vite, cela causera l'amincissement supplémentaire de la paroi, avec un risque élevé de lyse cellulaire.

Afin d'étudier comment les cellules préservent leur intégrité, nous nous sommes concentrés sur la régulation de l'épaisseur de paroi au niveau des pôles en croissance. En observant l'évolution de l'épaisseur de paroi locale dans le temps dans des cellules individuelles, nous avons observé que ce paramètre est très dynamique et présente des phases continues d'amincissement et d'épaississement.

Ces fluctuations se sont révélées être régulées par un mécanisme de mécano-sensation qui détecte la déformation de la paroi et module dynamiquement la synthèse des parois afin de maintenir l'intégrité des cellules. Cette mécano-sensibilité repose sur des composants hautement conservés de la voie de l'intégrité de la paroi cellulaire et les mutants dont la mécano-sensibilité subissent une lyse cellulaire, à la suite d'un amincissement non contrôlé des parois.

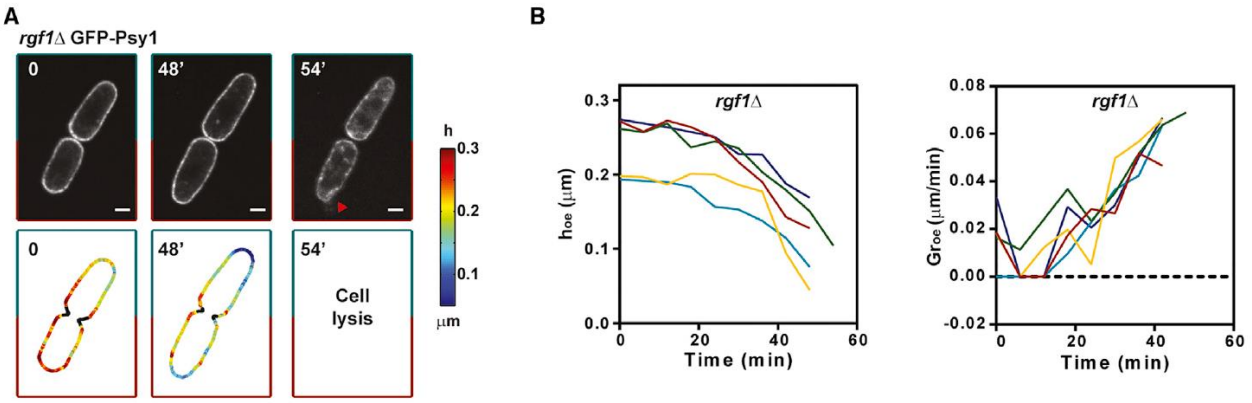

Figure R.5 ***Implication de l'homéostasie de l'épaisseur pour la survie cellulaire pendant la croissance normale***. *A. Laps de temps de GFP-Psy1 et cartes d'épaisseur pour une cellule lysante représentative du souche rgf1Δ, impliqué dans la voi d'integrité de la paroi. La pointe de la flèche pointe vers la membrane qui fuit aux extrémités des cellules après la lyse. B. Evolution de l'épaisseur de l'ancienne extrémité (h_{oe}) et des taux de croissance (Gr_{oe}) chez les cellules lysantes rgf1Δ. Le dernier point est enregistré avant la lyse*.

En conclusion, ces travaux, en fournissant la toute première méthode pour mesurer la dynamique de l'épaisseur des parois cellulaires dans la levure à fission, ont montré que la paroi cellulaire est une structure très dynamique qui doit être régulée avec précision pour maintenir l'intégrité cellulaire.

2- Contrôle mécanique de la forme et de la taille des cellules dans la levure de fission

La détermination de la forme d'une cellule repose en définitive sur les propriétés de sa surface. Tel que discuté, la surface des cellules à paroi est composée d'une couche de polysaccharides, nécessaire pour équilibrer la pression de turgescence interne typique de ces cellules. De nombreux travaux expérimentaux et théoriques ont exploré comment la mécanique des parois peut influencer la morphogenèse cellulaire, mais il manque encore une évaluation systématique des propriétés mécaniques des parois et de leur influence sur la morphologie des cellules individuelles.

Dans ce travail, nous avons élargi la méthode de mesure de l'épaisseur de paroi décrite dans le premier ensemble de résultats, afin d'estimer d'autres paramètres mécaniques de la cellule. À cette fin, nous avons mis en place une ablation par laser permettant de percer des cellules de levure à fission en croissance, provoquant ainsi une lyse et une relaxation des parois cellulaires. En exploitant des règles géométriques simples, en comparant la forme des parois gonflées et relâchées et en les couplant aux valeurs locales de l'épaisseur de la paroi dans l'état turgescent, nous pouvons estimer les valeurs locales du module Young.

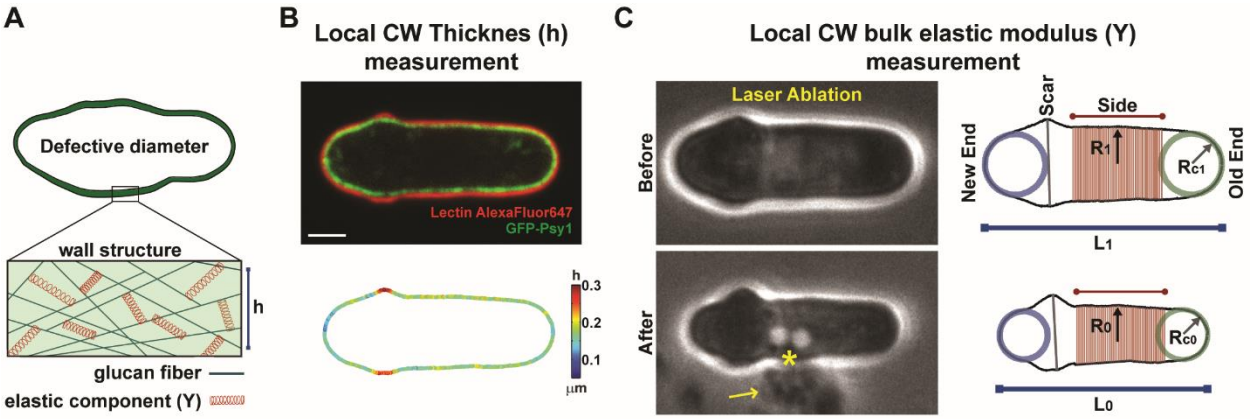

Figure R.6 ***Méthode de mesure des propriétés mécaniques des parois locales dans les cellules de S. pombe.*** *A. Représentation schématique d'une cellule à diamètre variable et zoom sur l'organisation globale de la paroi cellulaire, définissant l'épaisseur (h) et le module d'élasticité global (Y). B. Image fluorescente confocale à mi-coupe d'une cellule exprimant GFP-psy1 et marquée à la lectine-Alexafluor647, et carte d'épaisseur en CW correspondante . C. (Gauche) Méthode permettant d'estimer le module Young de la paroi locale (Y) divisée par la pression de turgescence (P). Images de la même cellule illustrée en B avant (haut) et après (bas) l'ablation au laser. L'étoile indique l'emplacement de l'ablation au laser, la flèche pointant vers un nuage de matériel cytosolique éjecté de la cellule. (Rigth) Les limites des parois cellulaires de la même cellule, obtenues par binarisation du signal lectine-Alexafluor647, avant et après l'ablation, sont utilisées pour calculer les rayons de courbure locaux aux extrémités des cellules et le rayon situé du côté de la cellule, défini comme moyenne sur la région rouge.*

Cette analyse a confirmé que les parois en croissance sont plus molles que les parois stables, mais a montré que le module de paroi est stable pendant le cycle cellulaire des pôles et des côtés en croissance, mais varie considérablement dans les nouveaux pôles.

Nous nous sommes ensuite intéressés à la manière dont la mécanique de la paroi cellulaire peut influencer la détermination de la forme des cellules, en particulier la régulation du diamètre.

Nous avons observé que le module de surface de paroi (produit du module Young et de l'épaisseur) corrèle fortement avec le diamètre local dans différentes conditions de type sauvage et chez plusieurs mutants présentant des défauts de diamètre ou de maintenance, ainsi que chez des mutants de synthèse et remodelage de la paroi.

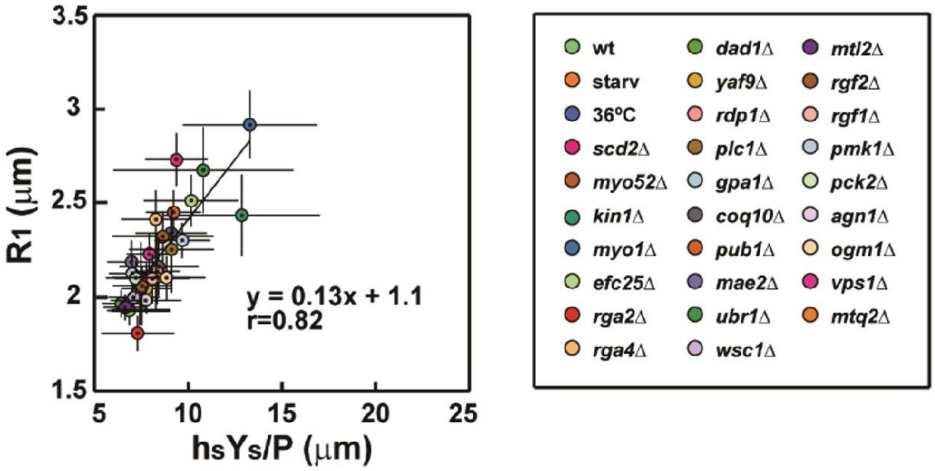

Figure R.7 ***Criblage génétique des paramètres mécaniques en ondes entretenues sur des mutants de diamètre***. *Rayon cellulaire (R1) en fonction du module de surface latérale divisé par P ($Y_s h_s$ / P), dans les conditions et mutants énumérés dans la légende a droite. Chaque souche est représentée par sa valeur moyenne. La ligne est un ajustement linéaire sur les moyennes.*

La perturbation ectopique de la synthèse des parois entraîne des modifications des propriétés mécaniques des parois et une altération simultanée du diamètre.

Notre analyse quantitative révèle que dans toutes les conditions testées, les parois cellulaires se déforment de manière similaire entre les états relâchés et les états turgescents, suggérant une conservation dans les déformations élastiques, qui semblent être un paramètre essentiel pour déterminer la forme des cellules.

Ces résultats élargissent notre compréhension de la manière dont les paramètres mécaniques des parois sont impliqués dans la détermination de la forme cellulaire et peuvent servir de base à une analyse plus poussée visant à comprendre comment ce processus est régulé dynamiquement dans les levures à fission et dans d'autres cellules à paroi.

Discussion

Au cours de mes études de doctorat, j'ai étudié l'influence de la mécanique des parois cellulaires sur la croissance et la morphogenèse de la levure de fission *Schizosaccharomyces pombe*. À cette fin, j'ai développé les toutes premières approches pour évaluer les paramètres mécaniques des parois dans de grandes populations de cellules de levure fissipare vivantes, à l'échelle d'une cellule, avec une résolution subcellulaire. Ces méthodes montrent enfin comment les parois des cellules se comportent de manière dynamique. Grâce à la résolution obtenue, j'ai mis en évidence des interactions complexes entre la mécanique des parois, la croissance et la forme des cellules au niveau d'une cellule, ainsi que des mécanismes de détection mécanique permettant de contrôler la surface de la cellule en préservant son intégrité. Ces résultats montrent que la régulation de la mécanique de surface est essentielle au développement et à la croissance des cellules, et que l'observation systématique de ces paramètres est essentielle pour une compréhension complète de ces processus.

Ce travail jette les bases de la compréhension des règles mécaniques générales régissant les processus complexes tels que la croissance ou l’établissement de la forme dans les cellules a paroi. Il peut également être étendu à la recherche d’autres événements biologiquement pertinents, tels que le tropisme, l’invasion des hôtes, le développement mycélien ou la fertilisation des plantes.

BIBLIOGRAPHY

Abenza, J.F., Couturier, E., Dodgson, J., Dickmann, J., Chessel, A., Dumais, J., and Carazo Salas, R.E. (2015). Wall mechanics and exocytosis define the shape of growth domains in fission yeast. Nature Communications *6*, 8400.

Acevedo, E., Hsiao, T.C., and Henderson, D.W. (1971). Immediate and subsequent growth responses of maize leaves to changes in water status. Plant Physiology *48*, 631-636.

Aghamohammadzadeh, S., and Ayscough, K.R. (2009). Differential requirements for actin during yeast and mammalian endocytosis. Nature Cell Biology *11*, 1039-1042.

Ahmadpour, D., Geijer, C., Tamas, M.J., Lindkvist-Petersson, K., and Hohmann, S. (2014). Yeast reveals unexpected roles and regulatory features of aquaporins and aquaglyceroporins. Biochim Biophys Acta *1840*, 1482-1491.

Akkerman, M., Franssen-Verheijen, M.A., Immerzeel, P., Hollander, L.D., Schel, J.H., and Emons, A.M. (2012). Texture of cellulose microfibrils of root hair cell walls of Arabidopsis thaliana, Medicago truncatula, and Vicia sativa. Journal of Microscopy *247*, 60-67.

Allen, W.E., Zicha, D., Ridley, A.J., and Jones, G.E. (1998). A role for Cdc42 in macrophage chemotaxis. The Journal of Cell Biology *141*, 1147-1157.

Atilgan, E., Magidson, V., Khodjakov, A., and Chang, F. (2015). Morphogenesis of the Fission Yeast Cell through Cell Wall Expansion. Current Biology *25*, 2150-2157.

Banavar, S.P., Gomez, C., Trogdon, M., Petzold, L.R., Yi, T.M., and Campas, O. (2018). Mechanical feedback coordinates cell wall expansion and assembly in yeast mating morphogenesis. PLoS Comput Biol *14*, e1005940.

Bashline, L., Lei, L., Li, S., and Gu, Y. (2014). Cell wall, cytoskeleton, and cell expansion in higher plants. Mol Plant *7*, 586-600.

Bastmeyer, M., Deising, H.B., and Bechinger, C. (2002). Force Exertion in Fungal Infection. Annual Review of Biophysics and Biomolecular Structure *31*, 321-341.

Basu, D., Le, J., Zakharova, T., Mallery, E.L., and Szymanski, D.B. (2008). A SPIKE1 signaling complex controls actin-dependent cell morphogenesis through the heteromeric WAVE and ARP2/3 complexes. Proc Natl Acad Sci U S A *105*, 4044-4049.

Basu, R., Munteanu, E.L., and Chang, F. (2014). Role of turgor pressure in endocytosis in fission yeast. Molecular Biology of the Cell *25*, 679-687.

Beauvais, A., Maubon, D., Park, S., Morelle, W., Tanguy, M., Huerre, M., Perlin, D.S., and Latge, J.P. (2005). Two alpha(1-3) glucan synthases with different functions in Aspergillus fumigatus. Applied and Environmental Microbiology *71*, 1531-1538.

BIBLIOGRAPHY

Beauzamy, L., Nakayama, N., and Boudaoud, A. (2014). Flowers under pressure: ins and outs of turgor regulation in development. Ann Bot *114*, 1517-1533.

Bendezu, F.O., and Martin, S.G. (2010). Actin cables and the exocyst form two independent morphogenesis pathways in the fission yeast. Molecular Biology of the Cell *22*, 44-53.

Bendezu, F.O., and Martin, S.G. (2013). Cdc42 explores the cell periphery for mate selection in fission yeast. Curr Biol *23*, 42-47.

Bendezu, F.O., Vincenzetti, V., and Martin, S.G. (2012). Fission yeast Sec3 and Exo70 are transported on actin cables and localize the exocyst complex to cell poles. PLoS ONE *7*, e40248.

Bendezú, F.O., Vincenzetti, V., Vavylonis, D., Wyss, R., Vogel, H., and Martin, S.G. (2015). Spontaneous Cdc42 Polarization Independent of GDI-Mediated Extraction and Actin-Based Trafficking. PLOS Biology *13*, e1002097.

Benkert, R., and Bentrup, F.W. (1997). The turgor pressure of growing lily pollen tubes Protoplasma *198*, 1-8.

Boisson-Dernier, A., Lituiev, D.S., Nestorova, A., Franck, C.M., Thirugnanarajah, S., and Grossniklaus, U. (2013). ANXUR receptor-like kinases coordinate cell wall integrity with growth at the pollen tube tip via NADPH oxidases. PLOS Biology *11*, e1001719.

Bonazzi, D., Haupt, A., Tanimoto, H., Delacour, D., Salort, D., and Minc, N. (2015). Actin-Based Transport Adapts Polarity Domain Size to Local Cellular Curvature. Current Biology *25*, 2677-2683.

Bonazzi, D., Julien, J.-D., Romao, M., Seddiki, R., Piel, M., Boudaoud, A., and Minc, N. (2014). Symmetry Breaking in Spore Germination Relies on an Interplay between Polar Cap Stability and Spore Wall Mechanics. Developmental Cell *28*, 534-546.

Boudaoud, A. (2003). Growth of Walled Cells: From Shells to Vesicles. Physical Review Letters *91*.

Bowman, S.M., and Free, S.J. (2006). The structure and synthesis of the fungal cell wall. BioEssays *28*, 799-808.

Brand, A. (2012). Hyphal growth in human fungal pathogens and its role in virulence. Int J Microbiol *2012*, 517529.

Brangwynne, C.P. (2011). Soft active aggregates: mechanics, dynamics and self-assembly of liquid-like intracellular protein bodies. Soft Matter *7*, 3052.

Calonge, T.M., Nakano, K., Arellano, M., Arai, R., Katayama, S., Toda, T., Mabuchi, I., and Perez, P. (2000). Schizosaccharomyces pombe rho2p GTPase regulates cell wall alpha-glucan biosynthesis through the protein kinase pck2p. Molecular Biology of the Cell *11*, 4393-4401.

Campàs, O., and Mahadevan, L. (2009). Shape and Dynamics of Tip-Growing Cells. Current Biology *19*, 2102-2107.

Campas, O., Rojas, E., Dumais, J., and Mahadevan, L. (2012). Strategies for cell shape control in tip-growing cells. Am J Bot *99*, 1577-1582.

Cappellaro, C., Mrsa, V., and Tanner, W. (1998). New potential cell wall glucanases of Saccharomyces cerevisiae and their involvement in mating. J Bacteriol *180*, 5030-5037.

CAZY (2018). Glycoside Hydrolase family classification.

Chang, F., and Martin, S.G. (2009). Shaping Fission Yeast with Microtubules. Cold Spring Harbor Perspectives in Biology *1*, a001347-a001347.

Charras, G.T., Coughlin, M., Mitchison, T.J., and Mahadevan, L. (2008). Life and times of a cellular bleb. Biophysical Journal *94*, 1836-1853.

Chaumont, F., Moshelion, M., and Daniels, M.J. (2005). Regulation of plant aquaporin activity. Biol Cell *97*, 749-764.

Chiou, J.G., Balasubramanian, M.K., and Lew, D.J. (2017). Cell Polarity in Yeast. Annual Review of Cell and Developmental Biology *33*, 77-101.

Chugh, P., Clark, A.G., Smith, M.B., Cassani, D.A.D., Dierkes, K., Ragab, A., Roux, P.P., Charras, G., Salbreux, G., and Paluch, E.K. (2017). Actin cortex architecture regulates cell surface tension. Nature Cell Biology *19*, 689-697.

Cortes, J.C.G. (2002). Localization of the (1,3)beta-D-glucan synthase catalytic subunit homologue Bgs1p/Cps1p from fission yeast suggests that it is involved in septation, polarized growth, mating, spore wall formation and spore germination. Journal of Cell Science *115*, 4081-4096.

Cortés, J.C.G., Carnero, E., Ishiguro, J., Sánchez, Y., Durán, A., and Ribas, J.C. (2005). The novel fission yeast (1,3)β-D-glucan synthase catalytic subunit Bgs4p is essential during both cytokinesis and polarized growth. Journal of Cell Science *118*, 157-174.

Cosgrove, D.J. (2016). Plant cell wall extensibility: connecting plant cell growth with cell wall structure, mechanics, and the action of wall-modifying enzymes. Journal of Experimental Botany *67*, 463-476.

Cruz, S., Muñoz, S., Manjón, E., García, P., and Sanchez, Y. (2013). The fission yeast cell wall stress sensor-like proteins Mtl2 and Wsc1 act by turning on the GTPase Rho1p but act independently of the cell wall integrity pathway. MicrobiologyOpen, n/a-n/a.

Das, M., Drake, T., Wiley, D.J., Buchwald, P., Vavylonis, D., and Verde, F. (2012). Oscillatory dynamics of Cdc42 GTPase in the control of polarized growth. Science *337*, 239-243.

Das, M., Nunez, I., Rodriguez, M., Wiley, D.J., Rodriguez, J., Sarkeshik, A., Yates, J.R., Buchwald, P., and Verde, F. (2015). Phosphorylation-dependent inhibition of Cdc42 GEF Gef1 by 14-3-3 protein Rad24 spatially regulates Cdc42 GTPase activity and oscillatory dynamics during cell morphogenesis. Molecular Biology of the Cell *26*, 3520-3534.

Das, M., Wiley, D.J., Chen, X., Shah, K., and Verde, F. (2009). The Conserved NDR Kinase Orb6 Controls Polarized Cell Growth by Spatial Regulation of the Small GTPase Cdc42. Current Biology *19*, 1314-1319.

BIBLIOGRAPHY

Das, M., Wiley, D.J., Medina, S., Vincent, H.A., Larrea, M., Oriolo, A., and Verde, F. (2007). Regulation of Cell Diameter, For3p Localization, and Cell Symmetry by Fission Yeast Rho-GAP Rga4p. Molecular Biology of the Cell *18*, 2090-2101.

Davì, V., and Minc, N. (2015). Mechanics and morphogenesis of fission yeast cells. Current Opinion in Microbiology *28*, 36-45.

Davies, J. (2013). Mechanisms of Morphogenesis - 2nd Edition.

de Medina-Redondo, M., Arnaiz-Pita, Y., Clavaud, C., Fontaine, T., del Rey, F., Latge, J.P., and Vazquez de Aldana, C.R. (2010). beta(1,3)-glucanosyl-transferase activity is essential for cell wall integrity and viability of Schizosaccharomyces pombe. PLoS ONE *5*, e14046.

de Medina-Redondo, M., Arnáiz-Pita, Y., Fontaine, T., del Rey, F., Latgé, J.P., and de Aldana, C.R.V. (2008). The β-1,3-glucanosyltransferase gas4p is essential for ascospore wall maturation and spore viability in Schizosaccharomyces pombe. Molecular Microbiology *68*, 1283-1299.

Deising, H.B., Werner, S., and Wernitz, M. (2000). The role of fungal appressoria in plant infection. Microbes Infect *2*, 1631-1641.

Dekker, N. (2004). Role of the -Glucanase Agn1p in Fission-Yeast Cell Separation. Molecular Biology of the Cell *15*, 3903-3914.

Dekker, N., van Rijssel, J., Distel, B., and Hochstenbach, F. (2007). Role of the alpha-glucanase Agn2p in ascus-wall endolysis following sporulation in fission yeast. Yeast *24*, 279-288.

del Campillo, E., Gaddam, S., Mettle-Amuah, D., and Heneks, J. (2012). A tale of two tissues: AtGH9C1 is an endo-beta-1,4-glucanase involved in root hair and endosperm development in Arabidopsis. PLoS ONE *7*, e49363.

Delauney, A.J., and Verma, D.P. (1993). Proline biosynthesis and osmoregulation in plants. The Plant Journal *4*, 215-223.

Deng, Y., Sun, M., and Shaevitz, J.W. (2011). Direct Measurement of Cell Wall Stress Stiffening and Turgor Pressure in Live Bacterial Cells. Physical Review Letters *107*.

Dichtl, K., Samantaray, S., and Wagener, J. (2016). Cell wall integrity signalling in human pathogenic fungi. Cellular Microbiology *18*, 1228-1238.

Dolan, L., and Langdale, J.A. (2004). New insights into plant development in New England. Development *131*, 5215-5220.

Dotti, C.G., Sullivan, C.A., and Banker, G.A. (1988). The establishment of polarity by hippocampal neurons in culture. J Neurosci *8*, 1454-1468.

Drake, T., and Vavylonis, D. (2013). Model of fission yeast cell shape driven by membrane-bound growth factors and the cytoskeleton. PLoS Comput Biol *9*, e1003287.

Drgonova, J., Drgon, T., Tanaka, K., Kollar, R., Chen, G.C., Ford, R.A., Chan, C.S., Takai, Y., and Cabib, E. (1996). Rho1p, a yeast protein at the interface between cell polarization and morphogenesis. Science *272*, 277-279.

Dudin, O., Bendezú, F.O., Groux, R., Laroche, T., Seitz, A., and Martin, S.G. (2015). A formin-nucleated actin aster concentrates cell wall hydrolases for cell fusion in fission yeast. The Journal of Cell Biology *208*, 897-911.

Duenas-Santero, E., Martin-Cuadrado, A.B., Fontaine, T., Latge, J.P., del Rey, F., and Vazquez de Aldana, C. (2010). Characterization of Glycoside Hydrolase Family 5 Proteins in Schizosaccharomyces pombe. Eukaryotic Cell *9*, 1650-1660.

Dumont, S., and Prakash, M. (2014). Emergent mechanics of biological structures. Molecular Biology of the Cell *25*, 3461-3465.

Dupres, V., Alsteens, D., Wilk, S., Hansen, B., Heinisch, J.J., and Dufrene, Y.F. (2009). The yeast Wsc1 cell surface sensor behaves like a nanospring in vivo. Nat Chem Biol *5*, 857-862.

Dupres, V., Dufrene, Y.F., and Heinisch, J.J. (2010). Measuring cell wall thickness in living yeast cells using single molecular rulers. ACS Nano *4*, 5498-5504.

Dupres, V., Heinisch, J.J., and Dufrene, Y.F. (2011). Atomic force microscopy demonstrates that disulfide bridges are required for clustering of the yeast cell wall integrity sensor Wsc1. Langmuir *27*, 15129-15134.

Ebine, K., and Ueda, T. (2015). Roles of membrane trafficking in plant cell wall dynamics. Front Plant Sci *6*, 878.

Effler, J.C., Kee, Y.S., Berk, J.M., Tran, M.N., Iglesias, P.A., and Robinson, D.N. (2006). Mitosis-specific mechanosensing and contractile-protein redistribution control cell shape. Curr Biol *16*, 1962-1967.

Egel, R. (2004). The Molecular Biology of Schizosaccharomyces pombe - Genetics, Genomics and Beyond, 1 st edition edn.

Encinar del Dedo, J., Duenas, E., Arnaiz, Y., del Rey, F., and Vazquez de Aldana, C.R. (2009). {beta}-glucanase Eng2 is required for ascus wall endolysis after sporulation in the fission yeast Schizosaccharomyces pombe. Eukaryotic Cell *8*, 1278-1286.

Ene, I.V., Walker, L.A., Schiavone, M., Lee, K.K., Martin-Yken, H., Dague, E., Gow, N.A., Munro, C.A., and Brown, A.J. (2015). Cell Wall Remodeling Enzymes Modulate Fungal Cell Wall Elasticity and Osmotic Stress Resistance. mBio *6*, e00986.

Etienne-Manneville, S.a.H., Alan (2002). Rho GTPases in cell biology. Nature *420* 629-635.

Feng, W., Kita, D., Peaucelle, A., Cartwright, H.N., Doan, V., Duan, Q., Liu, M.C., Maman, J., Steinhorst, L., Schmitz-Thom, I.*, et al.* (2018). The FERONIA Receptor Kinase Maintains Cell-Wall Integrity during Salt Stress through Ca(2+) Signaling. Curr Biol *28*, 666-675 e665.

BIBLIOGRAPHY

Flardh, K. (2003). Growth polarity and cell division in Streptomyces. Current Opinion in Microbiology *6*, 564-571.

Flor-Parra, I., Bernal, M., Zhurinsky, J., and Daga, R.R. (2013). Cell migration and division in amoeboid-like fission yeast. Biology Open *3*, 108-115.

Flor-Parra, I., Zhurinsky, J., Bernal, M., Gallardo, P., and Daga, R.R. (2014). A Lallzyme MMX-based rapid method for fission yeast protoplast preparation. Yeast *31*, 61-66.

Formosa, C., Schiavone, M., Martin-Yken, H., Francois, J.M., Duval, R.E., and Dague, E. (2013). Nanoscale effects of caspofungin against two yeast species, Saccharomyces cerevisiae and Candida albicans. Antimicrob Agents Chemother *57*, 3498-3506.

Forterre, Y. (2013). Slow, fast and furious: understanding the physics of plant movements. Journal of Experimental Botany *64*, 4745-4760.

Free, S.J. (2013). Fungal cell wall organization and biosynthesis. Adv Genet *81*, 33-82.

Fujita, M., Fujita, Y., Maruyama, K., Seki, M., Hiratsu, K., Ohme-Takagi, M., Tran, L.S., Yamaguchi-Shinozaki, K., and Shinozaki, K. (2004). A dehydration-induced NAC protein, RD26, is involved in a novel ABA-dependent stress-signaling pathway. Plant J *39*, 863-876.

Gallo Castro, D., and Martin, S.G. (2018). Differential GAP requirement for Cdc42-GTP polarization during proliferation and sexual reproduction. The Journal of Cell Biology.

Galway, M.E. (2006). Root hair cell walls: filling in the framework. Canadian Journal of Botany *84*, 613-621.

Garcia, I., Tajadura, V., Martin, V., Toda, T., and Sanchez, Y. (2006). Synthesis of alpha-glucans in fission yeast spores is carried out by three alpha-glucan synthase paralogues, Mok12p, Mok13p and Mok14p. Molecular Microbiology *59*, 836-853.

Garcia, P. (2006). Rgf1p Is a Specific Rho1-GEF That Coordinates Cell Polarization with Cell Wall Biogenesis in Fission Yeast. Molecular Biology of the Cell *17*, 1620-1631.

Ge, W., Chew, T.G., Wachtler, V., Naqvi, S.N., and Balasubramanian, M.K. (2005). The novel fission yeast protein Pal1p interacts with Hip1-related Sla2p/End4p and is involved in cellular morphogenesis. Molecular Biology of the Cell *16*, 4124-4138.

Geitmann, A., and Ortega, J.K.E. (2009). Mechanics and modeling of plant cell growth. Trends in Plant Science *14*, 467-478.

Geitmann, A., and Parre, E. (2004). The local cytomechanical properties of growing pollen tubes correspond to the axial distribution of structural cellular elements. Sex Plant Reprod *17*, 9-16.

Ghamrawi, S., Gastebois, A., Zykwinska, A., Vandeputte, P., Marot, A., Mabilleau, G., Cuenot, S., and Bouchara, J.P. (2015). A Multifaceted Study of Scedosporium boydii Cell Wall Changes during Germination and Identification of GPI-Anchored Proteins. PLoS ONE *10*, e0128680.

Gierer, A., and Meinhardt, H. (1972). A theory of biological pattern formation. Kybernetik *12*, 30-39.

Goehring, N.W., and Grill, S.W. (2013). Cell polarity: mechanochemical patterning. Trends in Cell Biology *23*, 72-80.

Goldenbogen, B., Giese, W., Hemmen, M., Uhlendorf, J., Herrmann, A., and Klipp, E. (2016). Dynamics of cell wall elasticity pattern shapes the cell during yeast mating morphogenesis. Open Biology *6*.

Goriely, A. (2017). The Mathematics and Mechanics of Biological Growth (Springer).

Goriely, A., and Tabor, M. (2006). Estimates of biomechanical forces in Magnaporthe grisea. Mycol Res *110*, 755-759.

Gow, N.A.R., Latge, J.P., and Munro, C.A. (2017). The Fungal Cell Wall: Structure, Biosynthesis, and Function. Microbiol Spectr *5*.

Green, P.B. (1968). Growth Physics in Nitella: a Method for Continuous in Vivo Analysis of Extensibility Based on a Micro-manometer Technique for Turgor Pressure. Plant Physiology *43*, 1169-1184.

Hamann, T. (2015). The Plant Cell Wall Integrity Maintenance Mechanism—Concepts for Organization and Mode of Action. Plant and Cell Physiology *56*, 215-223.

Hao, N., Behar, M., Parnell, S.C., Torres, M.P., Borchers, C.H., Elston, T.C., and Dohlman, H.G. (2007). A systems-biology analysis of feedback inhibition in the Sho1 osmotic-stress-response pathway. Curr Biol *17*, 659-667.

Harris, S.D. (2008). Branching of fungal hyphae: regulation, mechanisms and comparison with other branching systems. Mycologia *100*, 823-832.

Hayashi, M., and Maeda, T. (2006). Activation of the HOG pathway upon cold stress in Saccharomyces cerevisiae. J Biochem *139*, 797-803.

Hedhly, A., Hormaza, J.I., and Herrero, M. (2005). The effect of temperature on pollen germination, pollen tube growth, and stigmatic receptivity in peach. Plant Biol (Stuttg) *7*, 476-483.

Heinisch, J.J., Dupres, V., Alsteens, D., and Dufrene, Y.F. (2010a). Measurement of the mechanical behavior of yeast membrane sensors using single-molecule atomic force microscopy. Nature Protocols *5*, 670-677.

Heinisch, J.J., Dupres, V., Wilk, S., Jendretzki, A., and Dufrene, Y.F. (2010b). Single-molecule atomic force microscopy reveals clustering of the yeast plasma-membrane sensor Wsc1. PLoS ONE *5*, e11104.

Herzog, S., Schumann, M.R., and Fleissner, A. (2015). Cell fusion in Neurospora crassa. Current Opinion in Microbiology *28*, 53-59.

Hochstenbach, F., Klis, F.M., van den Ende, H., van Donselaar, E., Peters, P.J., and Klausner, R.D. (1998). Identification of a putative alpha-glucan synthase essential for cell wall construction and morphogenesis in fission yeast. Proc Natl Acad Sci U S A *95*, 9161-9166.

Hohmann, S. (2002). Osmotic adaptation in yeast--control of the yeast osmolyte system. Int Rev Cytol *215*, 149-187.

BIBLIOGRAPHY

Horisberger, M., and Rouvet-Vauthey, M. (1985). Cell wall architecture of the fission yeast Schizosaccharomyces pombe. Experientia *41*.

Horisberger, M., and Vonlanthen, M. (1977). Location of mannan and chitin on thin sections of budding yeasts with gold markers. Arch Microbiol *115*, 1-7.

Howard, R.J., Ferrari, M.A., Roach, D.H., and Money, N.P. (1991). Penetration of hard substrates by a fungus employing enormous turgor pressures. Proc Natl Acad Sci U S A *88*, 11281-11284.

Humbel, B.M., Konomi, M., Takagi, T., Kamasawa, N., Ishijima, S.A., and Osumi, M. (2001). In situ localization of beta-glucans in the cell wall of Schizosaccharomyces pombe. Yeast *18*, 433-444.

Irazoqui, J.E., Gladfelter, A.S., and Lew, D.J. (2003). Scaffold-mediated symmetry breaking by Cdc42p. Nature Cell Biology *5*, 1062-1070.

Ivakov, A., and Persson, S. (2013). Plant cell shape: modulators and measurements. Front Plant Sci *4*, 439.

Jiang, L., Yang, S.L., Xie, L.F., Puah, C.S., Zhang, X.Q., Yang, W.C., Sundaresan, V., and Ye, D. (2005). VANGUARD1 encodes a pectin methylesterase that enhances pollen tube growth in the Arabidopsis style and transmitting tract. The Plant Cell *17*, 584-596.

Jiang, Y., Lahlali, R., Karunakaran, C., Kumar, S., Davis, A.R., and Bueckert, R.A. (2015). Seed set, pollen morphology and pollen surface composition response to heat stress in field pea. Plant Cell Environ *38*, 2387-2397.

Karsenti, E. (2008). Self-organization in cell biology a brief history. Nature Reviews Molecular Cell Biology *9*, 255–262.

Katayama, S., Hirata, D., Arellano, M., Perez, P., and Toda, T. (1999). Fission yeast alpha-glucan synthase Mok1 requires the actin cytoskeleton to localize the sites of growth and plays an essential role in cell morphogenesis downstream of protein kinase C function. The Journal of Cell Biology *144*, 1173-1186.

Kelly, F.D., and Nurse, P. (2011a). De novo growth zone formation from fission yeast spheroplasts. PLoS ONE *6*, e27977.

Kelly, F.D., and Nurse, P. (2011b). Spatial control of Cdc42 activation determines cell width in fission yeast. Molecular Biology of the Cell *22*, 3801-3811.

Kim, S.J., and Brandizzi, F. (2014). The plant secretory pathway: an essential factory for building the plant cell wall. Plant Cell Physiol *55*, 687-693.

Kincaid, M.M., and King, S.J. (2006). Motors and their tethers: the role of secondary binding sites in processive motility. Cell Cycle *5*, 2733-2737.

Kirchhelle, C., Chow, C.-M., Foucart, C., Neto, H., Stierhof, Y.-D., Kalde, M., Walton, C., Fricker, M., Smith, Richard S., Jérusalem, A*., et al.* (2016). The Specification of Geometric Edges by a Plant Rab GTPase Is an Essential Cell-Patterning Principle During Organogenesis in Arabidopsis. Developmental Cell *36*, 386-400.

Kopecek, P., and Raclavsky, V. (1999). Comparison of chitin content in the apical and distal parts of fungal hyphae in Basidiobolus ranarum, Neurospora crassa and Coprinus sterquilinus. Folia Microbiol (Praha) *44*, 397-400.

Kotake, T., Li, J., Takahashi, M., and Sakurai, M. (2000). Characterization and function of wall-bound exo-β-glucanases of Lilium longiflorum pollen tubes. Sex Plant Reprod *13*, 1-9.

Lancelle, S.A., and Hepler, P.K. (1988). Cytochalasin-induced ultrastructural alterations in Nicotiana pollen tubes. Protoplasma *[Supp\. 2]*, 65-75.

Lancelle, S.A., and Hepler, P.K. (1992). Ultrastructure of freeze-substituted pollen tubes of Lilium longitlorum. Protoplasma *167*, 215-230.

Landrein, B., and Hamant, O. (2013). How mechanical stress controls microtubule behavior and morphogenesis in plants: history, experiments and revisited theories. Plant J *75*, 324-338.

Laporte, D., Courtout, F., Pinson, B., Dompierre, J., Salin, B., Brocard, L., and Sagot, I. (2015). A stable microtubule array drives fission yeast polarity reestablishment upon quiescence exit. The Journal of Cell Biology *210*, 99-113.

Latge, J.P., and Beauvais, A. (2014). Functional duality of the cell wall. Current Opinion in Microbiology *20*, 111-117.

Lazzaro, M.D., Donohue, J.M., and Soodavar, F.M. (2003). Disruption of cellulose synthesis by isoxaben causes tip swelling and disorganizes cortical microtubules in elongating conifer pollen tubes. Protoplasma *220*, 201-207.

Lee, H.U., Park, J.B., Lee, H., Chae, K.S., Han, D.M., and Jahng, K.Y. (2010). Predicting the chemical composition and structure of Aspergillus nidulans hyphal wall surface by atomic force microscopy. J Microbiol *48*, 243-248.

Levayer, R., and Lecuit, T. (2012). Biomechanical regulation of contractility: spatial control and dynamics. Trends in Cell Biology *22*, 61-81.

Lew, R.R. (2011). How does a hypha grow? The biophysics of pressurized growth in fungi. Nat Rev Microbiol *9*, 509-518.

Li, R., and Gundersen, G.G. (2008). Beyond polymer polarity: how the cytoskeleton builds a polarized cell. Nat Rev Mol Cell Biol *9*, 860-873.

Lichius, A., Goryachev, A.B., Fricker, M.D., Obara, B., Castro-Longoria, E., and Read, N.D. (2014). CDC-42 and RAC-1 regulate opposite chemotropisms in Neurospora crassa. Journal of Cell Science *127*, 1953-1965.

Lin, D., Edwards, A.S., Fawcett, J.P., Mbamalu, G., Scott, J.D., and Pawson, T. (2000). A mammalian PAR-3-PAR-6 complex implicated in Cdc42/Rac1 and aPKC signalling and cell polarity. Nature Cell Biology *2*, 540-547.

BIBLIOGRAPHY

Ma, H. (2005). Surface ultrastructure and elasticity in growing tips and mature regions of Aspergillus hyphae describe wall maturation. Microbiology *151*, 3679-3688.

Ma, H., Snook, L.A., Kaminskyj, S.G., and Dahms, T.E. (2005). Surface ultrastructure and elasticity in growing tips and mature regions of Aspergillus hyphae describe wall maturation. Microbiology *151*, 3679-3688.

Madrid, M., Jimenez, R., Sanchez-Mir, L., Soto, T., Franco, A., Vicente-Soler, J., Gacto, M., Perez, P., and Cansado, J. (2014). Multiple layers of regulation influence cell integrity control by the PKC ortholog Pck2 in fission yeast. Journal of Cell Science *128*, 266-280.

Maeda, Y., Kashiwazaki, J., Shimoda, C., and Nakamura, T. (2009). The Schizosaccharomyces pombe syntaxin 1 homolog, Psy1, is essential in the development of the forespore membrane. Biosci Biotechnol Biochem *73*, 339-345.

Martin-Cuadrado, A.B. (2003). The endo-beta-1,3-glucanase eng1p is required for dissolution of the primary septum during cell separation in Schizosaccharomyces pombe. Journal of Cell Science *116*, 1689-1698.

Martin, S.G. (2015). Spontaneous cell polarization: Feedback control of Cdc42 GTPase breaks cellular symmetry. BioEssays *37*, 1193-1201.

Martin, S.G., and Arkowitz, R.A. (2014). Cell polarization in budding and fission yeasts. FEMS Microbiology Reviews *38*, 228-253.

Martin, S.G., McDonald, W.H., Yates, J.R., and Chang, F. (2005). Tea4p Links Microtubule Plus Ends with the Formin For3p in the Establishment of Cell Polarity. Developmental Cell *8*, 479-491.

Martin, S.G., Rincon, S.A., Basu, R., Perez, P., and Chang, F. (2007). Regulation of the formin for3p by cdc42p and bud6p. Molecular Biology of the Cell *18*, 4155-4167.

Martin, V., Garcia, B., Carnero, E., Duran, A., and Sanchez, Y. (2003). Bgs3p, a Putative 1,3- -Glucan Synthase Subunit, Is Required for Cell Wall Assembly in Schizosaccharomyces pombe. Eukaryotic Cell *2*, 159-169.

Martin, V., Ribas, J.C., Carnero, E., Duran, A., and Sanchez, Y. (2000). bgs2+, a sporulation-specific glucan synthase homologue is required for proper ascospore wall maturation in fission yeast. Molecular Microbiology *38*, 308-321.

McFarlane, H.E., Doring, A., and Persson, S. (2014). The cell biology of cellulose synthesis. Annu Rev Plant Biol *65*, 69-94.

McKenna, S.T., Kunkel, J.G., Bosch, M., Rounds, C.M., Vidali, L., Winship, L.J., and Hepler, P.K. (2009). Exocytosis Precedes and Predicts the Increase in Growth in Oscillating Pollen Tubes. The Plant Cell *21*, 3026-3040.

Mendrinna, A., and Persson, S. (2015). Root hair growth: it's a one way street. F1000Prime Rep *7*, 23.

Merlini, L., Dudin, O., and Martin, S.G. (2013). Mate and fuse: how yeast cells do it. Open Biology *3*, 130008-130008.

Merlini, L., Khalili, B., Dudin, O., Michon, L., Vincenzetti, V., and Martin, S.G. (2018). Inhibition of Ras activity coordinates cell fusion with cell-cell contact during yeast mating. The Journal of Cell Biology *217*, 1467-1483.

Milani, P., Braybrook, S.A., and Boudaoud, A. (2013). Shrinking the hammer: micromechanical approaches to morphogenesis. Journal of Experimental Botany *64*, 4651-4662.

Minc, N., Boudaoud, A., and Chang, F. (2009a). Mechanical Forces of Fission Yeast Growth. Current Biology *19*, 1096-1101.

Minc, N., Bratman, S.V., Basu, R., and Chang, F. (2009b). Establishing New Sites of Polarization by Microtubules. Current Biology *19*, 83-94.

Mishra, M., Huang, J., and Balasubramanian, M.K. (2014). The yeast actin cytoskeleton. FEMS Microbiology Reviews *38*, 213-227.

Mitchison, J.M. (1957). The growth of single cells. I. Schizosaccharomyces pombe. Exp Cell Res *13*, 244-262.

Mitchison, J.M. (1990). The fission yeast, Schizosaccharomyces pombe. BioEssays : news and reviews in molecular, cellular and developmental biology *12*, 189-191.

Mogilner, A., Allard, J., and Wollman, R. (2012). Cell polarity: quantitative modeling as a tool in cell biology. Science *336*, 175-179.

Mollet, J.C., Leroux, C., Dardelle, F., and Lehner, A. (2013). Cell Wall Composition, Biosynthesis and Remodeling during Pollen Tube Growth. Plants (Basel) *2*, 107-147.

Monshausen, G.B., and Gilroy, S. (2009). Feeling green: mechanosensing in plants. Trends in Cell Biology *19*, 228-235.

Mooren, O.L., Galletta, B.J., and Cooper, J.A. (2012). Roles for actin assembly in endocytosis. Annual Review of Biochemistry *81*, 661-686.

Moskalenko, S., Henry, D.O., Rosse, C., Mirey, G., Camonis, J.H., and White, M.A. (2002). The exocyst is a Ral effector complex. Nature Cell Biology *4*, 66-72.

Mouyna, I., Hartl, L., and Latgé, J.-P. (2013). β-1,3-glucan modifying enzymes in Aspergillus fumigatus. Frontiers in Microbiology *4*.

Mouyna, I., Morelle, W., Vai, M., Monod, M., Lechenne, B., Fontaine, T., Beauvais, A., Sarfati, J., Prevost, M.C., Henry, C*., et al.* (2005). Deletion of GEL2 encoding for a beta(1-3)glucanosyltransferase affects morphogenesis and virulence in Aspergillus fumigatus. Molecular Microbiology *56*, 1675-1688.

Muñoz, J., Cortés, J.C.G., Sipiczki, M., Ramos, M., Clemente-Ramos, J.A., Moreno, M.B., Martins, I.M., Pérez, P., and Ribas, J.C. (2013). Extracellular cell wall β(1,3)glucan is required to couple septation to actomyosin ring contraction. The Journal of Cell Biology *203*, 265-282.

BIBLIOGRAPHY

Munoz, S., Manjon, E., Garcia, P., Sunnerhagen, P., and Sanchez, Y. (2014). The checkpoint-dependent nuclear accumulation of Rho1p exchange factor Rgf1p is important for tolerance to chronic replication stress. Molecular Biology of the Cell *25*, 1137-1150.

Nakamura, T., Nakamura-Kubo, M., Hirata, A., and Shimoda, C. (2001). The Schizosaccharomyces pombe spo3+ gene is required for assembly of the forespore membrane and genetically interacts with psy1(+)-encoding syntaxin-like protein. Molecular Biology of the Cell *12*, 3955-3972.

Nakayama, Y., Hirata, A., and Iida, H. (2014). Mechanosensitive channels Msy1 and Msy2 are required for maintaining organelle integrity upon hypoosmotic shock inSchizosaccharomyces pombe. FEMS Yeast Research *14*, 992-994.

Nakayama, Y., and Iida, H. (2014). Organellar mechanosensitive channels involved in hypo-osmoregulation in fission yeast. Cell Calcium *56*, 467-471.

Nedelec, F.J., Surrey, T., Maggs, A.C., and Leibler, S. (1997). Self-organization of microtubules and motors. Nature *389* 305-308.

Newcomb, E.H., and Bonnett, H.T. (1965). Cytoplasmic Microtubule and Wall Microfibril Orientation in Root Hairs of Radish. The Journal of Cell Biology *27*, 575-589.

Newell-Litwa, K.A., Horwitz, R., and Lamers, M.L. (2015). Non-muscle myosin II in disease: mechanisms and therapeutic opportunities. Dis Model Mech *8*, 1495-1515.

Obara, T., Nakafuku, M., Yamamoto, M., and Kaziro, Y. (1991). Isolation and characterization of a gene encoding a G-protein alpha subunit from Schizosaccharomyces pombe: involvement in mating and sporulation pathways. Proc Natl Acad Sci U S A *88*, 5877-5881.

Oikawa, A., Lund, C.H., Sakuragi, Y., and Scheller, H.V. (2013). Golgi-localized enzyme complexes for plant cell wall biosynthesis. Trends in Plant Science *18*, 49-58.

Orlando, K., and Guo, W. (2009). Membrane organization and dynamics in cell polarity. Cold Spring Harbor Perspectives in Biology *1*, a001321.

Osumi, M. (2012). Visualization of yeast cells by electron microscopy. Microscopy *61*, 343-365.

Osumi, M., Yamada, N., Kobori, H., Taki, A., Naito, N., Baba, M., and Nagatani, T. (1989). Cell wall formation in regenerating protoplasts of Schizosaccharomyces pombe: study by high resolution, low voltage scanning electron microscopy. J Electron Microsc (Tokyo) *38*, 457-468.

Otsubo, Y., and Yamamoto, M. (2012). Signaling pathways for fission yeast sexual differentiation at a glance. Journal of Cell Science *125*, 2789-2793.

Paluch, E., and Heisenberg, C.-P. (2009). Biology and Physics of Cell Shape Changes in Development. Current Biology *19*, R790-R799.

Panadero, J., Pallotti, C., Rodriguez-Vargas, S., Randez-Gil, F., and Prieto, J.A. (2006). A downshift in temperature activates the high osmolarity glycerol (HOG) pathway, which determines freeze tolerance in Saccharomyces cerevisiae. J Biol Chem *281*, 4638-4645.

Pandey, A., Roca, M.G., Read, N.D., and Glass, N.L. (2004). Role of a mitogen-activated protein kinase pathway during conidial germination and hyphal fusion in Neurospora crassa. Eukaryotic Cell *3*, 348-358.

Park, S., Szumlanski, A.L., Gu, F., Guo, F., and Nielsen, E. (2011). A role for CSLD3 during cell-wall synthesis in apical plasma membranes of tip-growing root-hair cells. Nature Cell Biology *13*, 973-980.

Park Talaro, K., and Talaro, A. (2001). Foundations in Microbiology, 4th edn (The McGraw−Hill Companies, 2002).

Pauling, L., Itano, H.A., Singer, S.J., and Wells, I.C. (1949). Sickle Cell Anemia, a Molecular Disease. Science *110*, 543-548.

Perez, P., and Ribas, J.C. (2004). Cell wall analysis. Methods *33*, 245-251.

Perez, P., and Rincón, Sergio A. (2010). Rho GTPases: regulation of cell polarity and growth in yeasts. Biochemical Journal *426*, 243-253.

Perozo, E., Kloda, A., Cortes, D.M., and Martinac, B. (2002). Physical principles underlying the transduction of bilayer deformation forces during mechanosensitive channel gating. Nat Struct Biol *9*, 696-703.

Philip, B., and Levin, D.E. (2001). Wsc1 and Mid2 are cell surface sensors for cell wall integrity signaling that act through Rom2, a guanine nucleotide exchange factor for Rho1. Molecular and Cellular Biology *21*, 271-280.

Pierson, E.S., Miller, D.D., Callaham, D.A., van Aken, J., Hackett, G., and Hepler, P.K. (1996). Tip-localized calcium entry fluctuates during pollen tube growth. Dev Biol *174*, 160-173.

Pollard, T.D. (2007). Regulation of actin filament assembly by Arp2/3 complex and formins. Annual Review of Biophysics and Biomolecular Structure *36*, 451-477.

Porat-Shliom, N., Milberg, O., Masedunskas, A., and Weigert, R. (2013). Multiple roles for the actin cytoskeleton during regulated exocytosis. Cell Mol Life Sci *70*, 2099-2121.

Prats, E., Gay, A.P., Mur, L.A., Thomas, B.J., and Carver, T.L. (2006). Stomatal lock-open, a consequence of epidermal cell death, follows transient suppression of stomatal opening in barley attacked by Blumeria graminis. Journal of Experimental Botany *57*, 2211-2226.

Proctor, Stephen A., Minc, N., Boudaoud, A., and Chang, F. (2012). Contributions of Turgor Pressure, the Contractile Ring, and Septum Assembly to Forces in Cytokinesis in Fission Yeast. Current Biology *22*, 1601-1608.

Proseus, T.E., and Boyer, J.S. (2006). Calcium pectate chemistry controls growth rate of Chara corallina. Journal of Experimental Botany *57*, 3989-4002.

Proseus, T.E., and Boyer, J.S. (2008). Calcium pectate chemistry causes growth to be stored in Chara corallina: a test of the pectate cycle. Plant Cell Environ *31*, 1147-1155.

Rojas, E., Theriot, J.A., and Huang, K.C. (2014). Response of Escherichia coli growth rate to osmotic shock. Proc Natl Acad Sci U S A *111*, 7807-7812.

Rojas, Enrique R., Hotton, S., and Dumais, J. (2011). Chemically Mediated Mechanical Expansion of the Pollen Tube Cell Wall. Biophysical Journal *101*, 1844-1853.

Rojas, E.R., and Huang, K.C. (2018). Regulation of microbial growth by turgor pressure. Current Opinion in Microbiology *42*, 62-70.

Rounds, C.M., and Bezanilla, M. (2013). Growth mechanisms in tip-growing plant cells. Annu Rev Plant Biol *64*, 243-265.

Saito, H., and Posas, F. (2012). Response to hyperosmotic stress. Genetics *192*, 289-318.

Saito, H., Yoshioka, Y., Yokoi, M., and Yamada, J. (1990). Distinct Gelation Mechanism between Linear and Branched (1-]3)-Beta-D-Glucans as Revealed by High-Resolution Solid-State C-13 Nmr. Biopolymers *29*, 1689-1698.

Sajiki, K., Hatanaka, M., Nakamura, T., Takeda, K., Shimanuki, M., Yoshida, T., Hanyu, Y., Hayashi, T., Nakaseko, Y., and Yanagida, M. (2009). Genetic control of cellular quiescence in S. pombe. Journal of Cell Science *122*, 1418-1429.

Salbreux, G., Charras, G., and Paluch, E. (2012). Actin cortex mechanics and cellular morphogenesis. Trends in Cell Biology *22*, 536-545.

Sanati Nezhad, A., and Geitmann, A. (2013). The cellular mechanics of an invasive lifestyle. Journal of Experimental Botany *64*, 4709-4728.

Sandini, S., La Valle, R., De Bernardis, F., Macri, C., and Cassone, A. (2007). The 65 kDa mannoprotein gene of Candida albicans encodes a putative beta-glucanase adhesin required for hyphal morphogenesis and experimental pathogenicity. Cellular Microbiology *9*, 1223-1238.

Sapala, A., Runions, A., Routier-Kierzkowska, A.L., Das Gupta, M., Hong, L., Hofhuis, H., Verger, S., Mosca, G., Li, C.B., Hay, A.*, et al.* (2018). Why plants make puzzle cells, and how their shape emerges. Elife *7*.

Sevilla, M.J., and Odds, F.C. (1986). Development of Candida albicans hyphae in different growth media--variations in growth rates, cell dimensions and timing of morphogenetic events. J Gen Microbiol *132*, 3083-3088.

Siderius, M., Van Wuytswinkel, O., Reijenga, K.A., Kelders, M., and Mager, W.H. (2000). The control of intracellular glycerol in Saccharomyces cerevisiae influences osmotic stress response and resistance to increased temperature. Molecular Microbiology *36*, 1381-1390.

Sinha, A.K., Jaggi, M., Raghuram, B., and Tuteja, N. (2011). Mitogen-activated protein kinase signaling in plants under abiotic stress. Plant Signal Behav *6*, 196-203.

Sokabe, M., Sawada, Y., and Kobayashi, T. (2015). Ion Channels Activated by Mechanical Forces in Bacterial and Eukaryotic Cells. Subcell Biochem *72*, 613-626.

Steudle, E., and Zimmermann, U. (1974). Determination of the hydraulic conductivity and of reflection coefficients in Nitella flexilis by means of direct cell-turgor pressure measurements. Biochimica et Biophysica Acta (BBA) - Biomembranes *332*, 399-412.

Stewart, M.P., Helenius, J., Toyoda, Y., Ramanathan, S.P., Muller, D.J., and Hyman, A.A. (2011). Hydrostatic pressure and the actomyosin cortex drive mitotic cell rounding. Nature *469*, 226-230.

Stone, B. (2006). Callose and related glucans. Encyclopedia of life sciencecallose and related glucans.

Sugihara, K., Asano, S., Tanaka, K., Iwamatsu, A., Okawa, K., and Ohta, Y. (2002). The exocyst complex binds the small GTPase RalA to mediate filopodia formation. Nature Cell Biology *4*, 73-78.

Tatebe, H., Nakano, K., Maximo, R., and Shiozaki, K. (2008). Pom1 DYRK Regulates Localization of the Rga4 GAP to Ensure Bipolar Activation of Cdc42 in Fission Yeast. Current Biology *18*, 322-330.

Thompson, D.A.W. (1942). On growth and form.

Tian, G.W., Chen, M.H., Zaltsman, A., and Citovsky, V. (2006). Pollen-specific pectin methylesterase involved in pollen tube growth. Dev Biol *294*, 83-91.

Tinevez, J.Y., Schulze, U., Salbreux, G., Roensch, J., Joanny, J.F., and Paluch, E. (2009). Role of cortical tension in bleb growth. Proc Natl Acad Sci U S A *106*, 18581-18586.

Toya, M., Kobayashi, S., Kawasaki, M., Shioi, G., Kaneko, M., Ishiuchi, T., Misaki, K., Meng, W., and Takeichi, M. (2016). CAMSAP3 orients the apical-to-basal polarity of microtubule arrays in epithelial cells. Proc Natl Acad Sci U S A *113*, 332-337.

Triboulot, Pritchard, and Tomos (1995). Stimulation and inhibition of pine root growth by osmotic stress. New Phytologist *130*, 169-175.

Tu, H., Barr, M., Dong, D.L., and Wigler, M. (1997). Multiple regulatory domains on the Byr2 protein kinase. Molecular and Cellular Biology *17*, 5876-5887.

Turing, A.M. (1953). The chemical basis of morphogenesis. I *B*, 37-72.

Velasquez, S.M., Ricardi, M.M., Dorosz, J.G., Fernandez, P.V., Nadra, A.D., Pol-Fachin, L., Egelund, J., Gille, S., Harholt, J., Ciancia, M*., et al.* (2011). O-glycosylated cell wall proteins are essential in root hair growth. Science *332*, 1401-1403.

Veley, K.M., Marshburn, S., Clure, C.E., and Haswell, E.S. (2012). Mechanosensitive channels protect plastids from hypoosmotic stress during normal plant growth. Curr Biol *22*, 408-413.

Vicente-Manzanares, M., Ma, X., Adelstein, R.S., and Horwitz, A.R. (2009). Non-muscle myosin II takes centre stage in cell adhesion and migration. Nature Reviews Molecular Cell Biology *10*, 778-790.

Vogler, H., Draeger, C., Weber, A., Felekis, D., Eichenberger, C., Routier-Kierzkowska, A.L., Boisson-Dernier, A., Ringli, C., Nelson, B.J., Smith, R.S*., et al.* (2013). The pollen tube: a soft shell with a hard core. Plant J *73*, 617-627.

Vollmer, W., Blanot, D., and de Pedro, M.A. (2008). Peptidoglycan structure and architecture. FEMS Microbiology Reviews *32*, 149-167.

Wedlich-Soldner, R., Altschuler, S., Wu, L., and Li, R. (2003). Spontaneous cell polarization through actomyosin-based delivery of the Cdc42 GTPase. Science *299*, 1231-1235.

Wilson, M.E., Maksaev, G., and Haswell, E.S. (2013). MscS-like mechanosensitive channels in plants and microbes. Biochemistry *52*, 5708-5722.

Wittmann, T., and Waterman-Storer, C.M. (2001). Cell motility: can Rho GTPases and microtubules point the way? Journal of Cell Science *114*, 3795-3803.

Wolf, S., and Greiner, S. (2012). Growth control by cell wall pectins. Protoplasma *249 Suppl 2*, S169-175.

Wood, V., Gwilliam, R., Rajandream, M.A., Lyne, M., Lyne, R., Stewart, A., Sgouros, J., Peat, N., Hayles, J., Baker, S.*, et al.* (2002). The genome sequence of Schizosaccharomyces pombe. Nature *415*, 871-880.

Xu, H., Nobile, C.J., and Dongari-Bagtzoglou, A. (2013). Glucanase induces filamentation of the fungal pathogen Candida albicans. PLoS ONE *8*, e63736.

Yamazaki, H., Tanaka, A., Kaneko, J., Ohta, A., and Horiuchi, H. (2008). Aspergillus nidulans ChiA is a glycosylphosphatidylinositol (GPI)-anchored chitinase specifically localized at polarized growth sites. Fungal Genet Biol *45*, 963-972.

Yanagisawa, M., Zhang, C., and Szymanski, D.B. (2013). ARP2/3-dependent growth in the plant kingdom: SCARs for life. Front Plant Sci *4*, 166.

Yoshida, T., Mogami, J., and Yamaguchi-Shinozaki, K. (2014). ABA-dependent and ABA-independent signaling in response to osmotic stress in plants. Current Opinion in Plant Biology *21*, 133-139.

Zerzour, R., Kroeger, J., and Geitmann, A. (2009). Polar growth in pollen tubes is associated with spatially confined dynamic changes in cell mechanical properties. Dev Biol *334*, 437-446.

Zhao, W., Li, C., Liang, J., and Sun, S. (2014). The Aspergillus fumigatus beta-1,3-glucanosyltransferase Gel7 plays a compensatory role in maintaining cell wall integrity under stress conditions. Glycobiology *24*, 418-427.

Zheng, D., Zhang, S., Zhou, X., Wang, C., Xiang, P., Zheng, Q., and Xu, J.R. (2012). The FgHOG1 pathway regulates hyphal growth, stress responses, and plant infection in Fusarium graminearum. PLoS ONE *7*, e49495.

Zhou, X.L., Stumpf, M.A., Hoch, H.C., and Kung, C. (1991). A mechanosensitive channel in whole cells and in membrane patches of the fungus Uromyces. Science *253*, 1415-1417.

université PARIS-SACLAY
ÉCOLE DOCTORALE
Structure et dynamique des systèmes vivants (SDSV)

Titre : Dynamique de la paroi cellulaire dans la régulation de la morphogenèse et de la croissance cellulaire

Mots clés : Croissance cellulaire, morphogenèse, paroi cellulaire, mécano-sensibilité, levure fissipare, mécanique de surface

Résumé : Les cellules dans la nature se développent avec un large éventail de formes, suivant divers mode de croissance. Malgré l'importance de ces processus fondamentaux, la façon dont les cellules régulent leur croissance et leur morphogenèse reste encore mal comprise. Dans cette thèse, j'ai exploré ces aspects, avec une approche principalement biomécanique, en concentrant mes investigations sur des cellules à paroi et en exploitant en particulier la levure fissipare *Schizosaccharomyces pombe*. J'ai d'abord développé de nouvelles méthodes pour mesurer les paramètres mécaniques clés de la paroi cellulaire in vivo, ce qui a permis les premières observations de la dynamique des parois cellulaires, pendant la croissance. Ceci a révélé que la paroi cellulaire est plus souple et variable dans le temps au niveau des pôles de croissance, et presque stable et plus rigide dans les sites sans croissance. Au cours de l'allongement, il existe une interaction entre la mécanique des parois et la croissance cellulaire, dont le contrôle actif permet l'expansion cellulaire tout en préservant l'intégrité des cellules. De plus, j'ai observé qu'il existe une forte corrélation entre la mécanique des parois cellulaires et la morphologie cellulaire, et que des perturbations des propriétés de la paroi affecte directement l'établissement et la maintenance de la forme. Dans l'ensemble, mes résultats montrent que la régulation de la paroi est fondamentale dans la détermination de la dynamique cellulaire. Globalement, cela suggère que l'observation dynamique de la mécanique de la surface cellulaire est essentielle pour une compréhension complète des processus multifactoriels et complexes comme la croissance et la morphogenèse.

Title : Cell wall dynamics in the regulation of cell morphogenesis and growth

Keywords : Growth, Morphogenesis, Cell Wall, Mechanosensing, Fission Yeast, Surface Mechanics

Abstract : Cells in nature develop in a wide range of forms, following diverse growth patterns. Despite the importance of these fundamental processes, how cells regulate their growth and morphogenesis is still poorly understood. In this thesis, I explored these processes, focusing my investigations on tip growing walled cells and in particular, by exploiting the fission yeast *Schizosaccharomyces pombe*, adopting mainly a biomechanical approach. To this aim, I first developed novel methods to measure key cell wall mechanical parameters in vivo, which allowed the very first observations of cell wall dynamics. This revealed that the cell wall is softer and highly variable at growing poles, and almost stable and stiffer at non-growing sites. During elongation, there is an interplay between wall mechanics and cell growth, whose active control allows cell expansion while preserving cell integrity. In addition, I observed that there is a strong correlation between cell wall mechanics and cell morphology, and ectopic perturbations of wall properties directly affect shape establishment and maintenance. Together my results show that the regulation of wall mechanics is fundamental in the determination of cell dynamics in tip growing walled cells. Moreover, this suggests that dynamic observation of cell surface mechanics is crucial for a complete understanding of multifactorial and complex processes, such as growth and morphogenesis

Université Paris-Saclay
Espace Technologique / Immeuble Discovery
Route de l'Orme aux Merisiers RD 128 / 91190 Saint-Aubin, France